Investigation on the Behavior of Stimuli-Responsive Macromolecules at Nanoemulsion Interface

By

A.W. Zaibudeen

PHYS02 2013 04 008

Indira Gandhi Centre for Atomic Research, Kalpakkam

A Thesis submitted to the
Board of Studies in Physical Sciences
In partial fulfillment of requirements
for the degree of

DOCTOR OF PHILOSOPHY

of

HOMI BHABHA NATIONAL INSTITUTE

August, 2018

Homi Bhabha National Institute

Recommendations of the Viva Voce Board

As members of the Viva Voce Board, we certify that we have read the dissertation prepared by **A.W. Zaibudeen** entitled "**Investigation on the behavior of stimuli-responsive macromolecules at nanoemulsion interface**" and recommend that it may be accepted as fulfilling the thesis requirement for the award of Degree of Doctor of Philosophy.

____**Date:**

Chairman-**Dr. Saroja Saibaba**

____**Date:**

Convener/Guide-**Dr. John Philip**

____**Date:**

Member 1-**V.A. Raghunathan**

____**Date:**

Member 2- **Dr. D. Ponraju**

____**Date:**

Member 3- **Dr. T. R. Ravindran**

____**Date:**

Member 4- **Dr. S. Ningshen**

Final approval and acceptance of this thesis is contingent upon the candidate's submission of the final copies of the thesis to HBNI.

I hereby certify that I have read this thesis prepared under my direction and recommend that it may be accepted as fulfilling the thesis requirement.

Date: **Dr. John Philip**

Place: (Guide)

STATEMENT BY AUTHOR

This dissertation has been submitted in partial fulfillment of the requirements for an advanced degree at Homi Bhabha National Institute (HBNI) and is deposited in the library to be made available to the borrowers under the rules of HBNI.

Brief quotations from this dissertation are allowable without special permission, provided that accurate acknowledgement of the source is made. Requests for permission for extended quotation from or reproduction of this manuscript in whole or in part may be granted by the Competent Authority of HBNI when in his or her judgment the proposed use of the material is in the interest of scholarship. In all other instances, however, permission must be obtained from the author.

(**A.W. Zaibudeen**)

DECLARATION

I, hereby declare that the investigation presented in this thesis has been carried out by me. The work is original and has not been submitted earlier, as a whole or in part, for a degree/diploma at this or any other Institution/University.

(A.W. Zaibudeen)

List of Publications arising from the thesis

Journals

1. “Adsortption of bovine serum albumin at oil-water interface in the presence of polyelectrolytes and nature of interaction forces” **A.W. Zaibudeen,** John Philip, *Colloids Surf.A.* **2019** 566, 38-47.

2. “Temperature and pH sensor using functionalized magnetic nanofluid”, **A.W. Zaibudeen,** John Philip*, Sens. Actuators B.* Chem**. 2018**, 268, 338-349.

3. “Magnetic nanofluid based non-enzymatic sensor for urea detection", **A.W. Zaibudeen,** John Philip*, Sens. Actuators B. Chem.* **2018** *255, 720-728.*

4. “A spectroscopic approach to probe macromolecular conformational changes at interface at different environmental conditions – A case study with PAA adsorbed at liquid interface”, **A.W. Zaibudeen,** John Philip, *J.Mol.Liq.* **2018**, 252, 30-39.

5. “Behavior of strong polyelectrolyte, poly(diallyldimethylammonium chloride) physisorbed at oil-water interface under different environments: A comparison with a weak polyelectrolyte”, **A.W. Zaibudeen,** John Philip, *Colloids Surf. A.* **2018***, 550, 209-221.*

6. “Behavior of weak polyelectrolyte at oil-water interface under different environmental conditions”, **A.W. Zaibudeen,** John Philip*, Colloids Surf. A.* ***2018****, 538, 610-621.*

7. “Thermally tunable grating using thermo-responsive magnetic fluid”, **A.W. Zaibudeen,** John Philip, *Optical Materials.* **2017***, 66, 117-121.*

8. "Multi-stimuli responsive nanofluid with easy to visualize structural color pattern" **A.W. Zaibudeen,** John Philip, *Colloids Surf. A.* **2017**, 538, 98-108.

Conferences

1. **A.W. Zaibudeen,** John Philip, “***Study of macromolecular conformational changes at oil-water interface – A new approach***”, International conference on nanoscience and technology **(ICONSAT – 2018),** Indian Institute of Science and Centre for Nano and Soft Matter Science, Bengaluru, India on March 21st -23rd, **2018**.

2. **A.W. Zaibudeen,** John Philip, “***Spectroscopic detection of urea using magnetic nanoemulsion”*** *International conference on complex fluids (CompFlu-2017*), Indian Institute of Technology Madras (IIT-M), Chennai, India on December 18th – 20th, **2017.**

3. **A.W. Zaibudeen,** John Philip, “***Measurement of inter colloidal interaction force between temperature responsive magnetic nanoemulsion”,*** *International conference on soft materials (ICSM-2016),* Malaviya National Institute of Technology (MNIT), Jaipur, India on December 12th -16th, **2016**.

4. **A.W. Zaibudeen,** John Philip, “***Probing of Intermolecular Force between Nanodroplets using Magnetic Chaining”,*** *International conference on nanomaterials and nanotechnology* ***(Nano-15)”*** KSR college of technology, Trichengode, India on December, 7th – 10th, 2015.

Other Publications (not included in the thesis)

1. “Stability and rheological property of hybrid γ-Al_2O_3 nanofluid with cationic polyelectrolyte additive”, **R. Kiruba, Sithara Vinod, A.W. Zaibudeen, R. Vijay Solomon, John Philip**, *Colloids Surf. A.* ***2018,*** 555, 63-71.

2. “Magnetic hyperthermia in magnetic nanoemulsion: Effect of polydispersity, particle concentration and medium viscosity”, B.B. Lahiri, Surojit Ranoo, **A.W. Zaibudeen,** John Philip, *J. Mag. Mag. Mat.* **2017**, 441, 310-327.

Recognition of the thesis work

1. **Nanotech web technology update,** January 4, 2018 “Simple spectroscopic technique to study polymer behavior at interface**”** (Based on the publication *J.Mol.Liq.* **2018**, 252, 30-39).

2. “Spotting urea in the flash of an eye” Sci-tech News story, The Hindu, January 14, 2018 (Based on the publication *Sens. Actuators B. Chem.* **2018** *255, 720-728).*

3. **Nature India research highlights,** December 22, 2017 “Magnetic nanosensor for detecting urea in human blood” (Based on the publication *Sens. Actuators B. Chem.* **2018** *255, 720-728).*

4. **Highlight Article in Optical Materials, Elsevier Publications** 2017 “The magnetic attraction of a colour-changing thermometer” (Based on the publication *Optical Materials.* **2017***, 66, 117-12).*

5. “Soon, doctors can see a fever” **Sci-tech News story, The Hindu**, April 11, 2017 (Based on the publication *Optical Materials.* **2017***, 66, 117-12).*

(**A.W. Zaibudeen**)

Wholly dedicated to the loving

memory of my father,

Late Mr. A. C. Abdul Wahith

and my loving mother,

Mrs. M.M. Fathimuthu Johara

ACKNOWLEDGEMENTS

At first, I owe my deep sense of gratitude to my thesis supervisor, **Dr. John Philip**. Without his tireless guidance, valuable discussions and suggestions, strong support and warm encouragement, this thesis wouldn’t have emerged. I consider myself fortunate to work with him. I am expecting the guidance and support from him in the future.

My sincere thanks to doctoral committee chairman, **Dr. Saroja Saibaba** and the committee members, **Dr. D. Ponraju** and **Dr. T. R. Ravindran** for their support and valuable suggestions for completing this thesis work.

I would like to thank **Dr. A. K. Bhaduri**, Director, IGCAR and **Dr. G. Amarendra**, Director, Metallurgy and Materials Group for giving an opportunity to carry out Ph.D programme at Indira Gandhi Centre for Atomic Research (IGCAR).

I gratefully acknowledge the help received from **V. Mahendran**, **Leona J. Felicia**, **Anbumozhi Angayarkanni** and **S.S. Pati** for carrying out the experiments, discussions, constant support and advices in the beginning stage of my research work. I thank all my juniors **Sithara Vinod, Amit Kumar Mishra, Dillip Kumar Mohapatra, Surojit Ranoo** and **Manali Nandy** for their help and making my stay in SMARTS peaceful. I express my sincere gratitude towards all other members of **Smart Materials Section (SMARTS)** for their support, kind assistance and help in numerous occasions.

I would like to thanks all of my friends **M. Vairavel, C. Lakshmanan, Nair Radhikesh Raveendran, K.A. Irshad, Nilakanda Meher, Padmalochan Panda, R. Santhosh and N. Karthikeyan** for useful discussion, chatting and making my stay at enclave happy and peaceful.

Finally, I would like to express my sincere gratitude towards my **family members**, especially my father **A.C. Abdul Wahith (late)**, my mother, **M.M. Fathimuthu Johara**,

my brother, **A.W. Sulthan Salaudeen** as well as all other brothers, sisters and cousins of my family for their continued support, love and care in all aspects of my life.

CONTENTS

Chapter 1

Introduction

Chapter 2

Experimental methods

Chapter 3

Behavior of thermo-responsive polymer at the oil-water interface: Effect of temperature and surfactant concentration

Chapter 4

Electro-steric interaction due to weak polyelectrolyte at the oil-water interface under different environmental condition

Chapter 5

Electro-steric interaction due to strong polyelectrolyte, poly(diallyldimethylammonium chloride) physisorbed at the oil-water interface under different environments: A comparison with weak polyelectrolyte

Chapter 6

Competitive adsorption of bovine serum albumin at oil-water interface in the presence of polyelectrolytes

Chapter 7

Novel application of magnetic nanofluid stabilized with different functional groups

Chapter 8

Conclusions and recommendations for future work

SYNOPSIS

Colloidal dispersion is a heterogeneous dispersion of one medium in another medium. Application of colloids such as detergent, paint, pharmaceutical product, food etc prevails in everyday human life. Emulsions are class of colloidal liquid-liquid dispersion, thermodynamically unstable but can be made kinetically stable due to surface active moieties at interface. Ferrofluid emulsions are class of colloids, which are dispersions of magnetically polarizable oil droplets (droplets containing ferro or ferrimagnetic particle in the size range of 5 – 10 nm) in base fluid. They undergo field driven self assembly when magnetic dipole attraction balances repulsive force, property that finds numerous applications in heat transfer, sensor, drug delivery, seals, cell separation etc.

The shelf life of colloidal formulation, including emulsion is determined by the effective interaction or the net forces acting between dispersed particles. If the net interaction force between the dispersed particles is repulsive then the formulation has an extended life. To achieve net repulsive interaction throughout its storage and use, various stabilization approaches such as electrostatic, steric, electro-steric or hard-sphere are attempted using functional groups such as neutral or charged surfactant molecules or nanoparticles. Though the formulations with a superior stability are made by industries using various stabilizing entities and their combinations, the know-how is secretly guarded due to commercial interest. As a result very little details are available in open literature. This is one of the motivations to undertake this work.

The behavior of polyelectrolyte (polymer carrying ionizable group on its backbone) under various environmental conditions is important to fundamentally understand the natural processes such as protein folding, DNA condensation etc.

Interestingly, the adsorption of polyelectrolyte at liquid-liquid interface mimics in vivo condition of charged macromolecule at cell-fluid interface and hence is very important to understand biological phenomenon such as protein aggregation. They are technologically important because of numerous applications in areas such as microcapsule, drug delivery, lubrication, pH gated ionic channel, sensors etc. Therefore, understanding the behavior of polyelectrolyte adsorbed onto a surface or interface is not only important for stabilization of emulsion based products but also useful in understanding biological phenomenon.

Though systematic studies on the behavior of polyelectrolyte under various physicochemical conditions in solution and at surface were carried out, the fundamental understanding of polyelectrolyte behavior at liquid-liquid interface is lacking, though very important for improving the shelf life of colloidal products. Contrary to the interaction forces between solid surfaces in the traditional force measurement techniques, the interaction forces between molecules adsorbed over tiny oil droplets suspended in a fluid are measured using the in-house developed magnetic chaining technique (MCT). The salient feature of MCT is the capability in measuring weak repulsive forces (0.1 pN) between nanodroplets, within 0.2 nm spatial resolution. This technique has been successfully used to study the intermolecular interactions such as electro-static, steric, polymer bridging etc.

The main objective of the present work is to understand the interaction force and the conformational change of neutral and charged macromolecules at oil-water interface under various physio-chemical conditions and its effect on colloidal stability. Another objective of the present work is to develop a simple and cost effective approach for sensing urea, temperature and pH of the body fluid by using suitable nanoemulsions. Thesis consists of eight chapters which are organized as follows:

Chapter 1 deals with a brief introduction to soft materials, magnetic colloids and the interaction forces operating between them. **Chapter 2** explains the preparation of material and the techniques used to characterize them. **Chapter 3** concerns intermolecular interaction due to thermoresponsive polymer, Poly (N-isopropylacrylamide) - (PNIPAM) adsorbed at the oil-water interface under different temperatures and anionic surfactant concentrations. **Chapter 4** deals with a study on the conformational change of adsorbed weak anionic polyelectrolyte, poly(acrylic acid) - (PAA), at oil-in-water interface under different environmental changes such as pH, salt of various concentration and valance and molecular weight. **Chapter 5** deals with the study on a strong polyelectrolyte, poly(diallyldimethylammonium chloride) - PDDA, under different environmental conditions and comparing its behavior with that of a weak polyelectrolyte in the same physiological conditions. **Chapter 6** concerns with the study on the role of low molecular weight protein, Bovine serum albumin - BSA in selective displacement of adsorbed polyelectrolytes at emulsion interface at different solution pH conditions. **Chapter 7** deals with some interesting applications of functionalized magnetic nanoemulsion for sensitive and selective detection of urea of wide concentration range as well as sensing physio-chemical parameters, temperature and pH. **Chapter 8** summarizes the results of this thesis and suggests the future perspectives. The key findings of the thesis are: For PNIPAM stabilized emulsion the decay length (λ) decreased from 12.6 to 7 nm, as the temperature is increased from 5 to 34 °C (below LCST). In the presence of 2 mM of SDS, LCST is increased by 3 ºC and λ decreased from 16.6 to 12.7 nm as the temperature increased from 5 to 38 ºC. pH tunable long range electro-steric interaction is observed for PAA stabilized emulsion where λ was found to be 6.6 nm at pH 3.0 but increases to 28 nm at a pH 11.8. At low salt concentrations, the λ scales with concentration of salt as $\sim \varphi_s^x$, where the exponent x was found to be 0.068, 0.049 and 0.072 for Na^+, Ca^{2+} and Fe^{3+}, respectively. However, at high salt concentrations the λ scales as ~ φ_s^{-y} where the y values were 0.3, 0.26 and 0.17 for Na^+, Ca^{2+} and Fe^{3+}, respectively. λ was found to be ~ 17 nm for PDDA stabilized emulsion between the solution pH 2.5 and 10.0 but decreased to 4 nm at a pH of 12.5 due to enhanced adsorption of OH^-. At low concentration of Na^+, Ca^{2+}, and Fe^{3+} the λ remains constant for PDDA emulsion whereas at high salt concentration of Na^+, Ca^{2+} and Fe^{3+}, λ decreases as $\varphi_s^{-0.4}$, $\varphi_s^{-0.19}$ and $\varphi_s^{-0.15}$, respectively. In the absence of BSA, the λ and ζ of PDDA emulsion was found to be 19 nm and + 56 mV, respectively that changes to 6 nm and + 5 mV at pH 5.2 and 6 nm and -10 mV at pH 7.0 in the presence of BSA. Similarly, in the absence of BSA, λ and ζ of PAA emulsion at pH 3.5 was 15 nm and – 10 mV, respectively but changes to 5 nm and + 38 mV when BSA was present at interface. SDS stabilized emulsion shows a change in Bragg peak wavelength ($\Delta\lambda_{peak}$) of 142 nm that detects urea in the concentration range of 0.003-0.6 g/L. In the case of PAA and F108 stabilized emulsions, the $\Delta\lambda_{peak}$ was 224 and 178 nm that detects urea level of 0.18-33.3 g/L and 2.4-334 g/L, respectively. PAA stabilized emulsion showed a linear detection of normal urea level even in the presence of 130 mM NaCl and 2 mM $CaCl_2$. Similarly, PVA-Vac emulsion showed a linear response in the temperature range 5 to 75 °C. In the presence of 10 mM borax, the temperature range was 5 to 90 °C. Using emulsion stabilized with PAA of 250 and 450 K, pH monitoring in the range of 3 - 11.5 is achieved.

LIST OF FIGURES

LIST OF TABLES

LIST OF ABBREVIATIONS

k_bT	Thermal energy
EIP	Emulsion inversion point
PIT	Phase inversion temperature
OsB	Osmotic brush regime
CI	Counter-ion
SB	Salted brush regime
QNB	Quenched neutral brush
C_{vdw}	Sum of van der Waals interaction
C_{Debye}	Contribution to van der Waals interaction due to Debye
C_{Keesom}	Contribution to van der Waals interaction due to Keesom
C_{London}	Contribution to van der Waals interaction due to London
NaCl	Sodium chloride
$CaCl_2$	Calcium chloride
$FeCl_3 \cdot 6H_2O$	Ferric chloride

$FeSO_4 \cdot 7H_2O$	Ferric sulphate
SDS	Sodium do-decyl sulphate
NP-9	Nonyl phenol ethoxylate
PVA-vac	Poly(vinyl alcohol-vinyl acetate)
PEO-PPO-PEO	Poly(ethylene oxide)-poly(propylene oxide)-poly(ethylene oxide)
PNIPAM	Poly(N-isopropylacrylamide)
PAA	Poly(acrylic acid)
PDDA	Poly(diallyldimethylammonium chloride)
BSA	Bovine serum albumin
MCT	Magnetic Chaining Technique
PALS	Phase analysis light scattering
LCST	Lower critical solution temperature
DLS	Dynamic light scattering
SFA	Surface force apparatus
AFM	Atomic force microscopy
DLVO	Derjaguin-Vervew-Landau-Overbeek
PDI	Polydispersity index
O/W	Oil-in-water
PE	Polyelectrolyte
MW	Molecular weight
PSS	Poly(styrene sulfonate)
CGT	Coil to globule transition
SANS	Small angle neutron scattering
PVA	Poly(vinyl alcohol)
CAC	Critical aggregation concentration

LIST OF SYMBOLS

e	Charge of the electron
Ψ	Potential
$W(h)$	Interaction energy per unit area
F_s	Force per unit
ΔG	Change in Gibb's free energy
ΔS	Entropy of mixing
γ	Interfacial tension
A_{inter}	Interfacial area
g	gravitational acceleration
$\Delta\rho$	Density difference between particle and solvent
η	Viscosity of the solvent
d_{par}	Diameter of the particle
R_h	Droplet radius
V_m	Molar volume of oil phase
R	Gas constant
S_∞	Equilibrium solubility of oil phase in the aqueous phase
D_t	Diffusion co-efficient
κ	Inverse Debye length
A_H	Hamaker constant
l_s	Kuhn length
υ	Excluded volume parameter
h_{pla}	Separation between the plates
H	Hamiltonian of the system
Ω	Grand canonical potential
Γ_{gra}	Grafting density
b_{gra}	Distance between two grafting group
l_b	Bjerrum length

ε	Dielectric constant
a_{mon}	Monomer size
f_{conf}	Elastic force due to stretching of polymer
f_{conc}	Non-electrostatic volume interaction
f_{ion}	Force due to electrostatic interactions between charged units
α	Fraction of charged group
Φ	Polymer volume fraction
φ_s	Concentration of salt
N	Number of monomers or degree of polymerization
α_b	Dissociation constant in the bulk
H^+	Concentration of proton
C_H^*	Solution of H^+ and OH^- at pH = 7
e^{-y}	Potential difference between brush and bulk solution
H_s^{max}	Maximum in the brush thickness
f(x)	Solvation force per unit area
χ	Susceptibility
H_0	External magnetic field
λ_{XR}	Wavelength of X-ray
FWHM	Full width at half maxima
K_{sf}	Crystalline shape factor
d_{int}	Interplanar spacing
θ	Angle of diffraction
A	Absorption co-efficient
I(t)	Scattered intensity at a time t
H_D	Hydrodynamic diameter
U_E	Electrophoretic mobility
I (t+δt)	Scattered intensity recorded after a small time interval δt
τ	Relaxation time

$f(\kappa R_h)$	Henry’s function
M	Magnetic moment
d	Interdroplet distance
λ_{vis}	Wavelength of visible light
μ_0	Magnetic permeability
H_T	Total magnetic field
H_{int}	Field due to magnetic moment of the neighboring droplets in the chain
h	Interdroplet spacing
N_A	Avogadro’s number
R_g	Radius of gyration
R_h	Hydrodynamic radius
$[\eta]$	Intrinsic viscosity
Γ	Fraction of adsorbed segment or degree of surfactant coverage
δ_{eff}	Effective adlayer thickness
δ	Apparent adlayer thickness
Eecc	Eccentricity
R_f	Flory radius
s	Distance between the two grafted points
L	Brush thickness
$2L_0$	First interaction distance
q	Valence of the ion
λ	Decay length
K	Force constant
$\Delta\lambda_{peak}$	Change in Bragg peak wavelength
λ_{peak}	Bragg peak wavelength
b_e	Distance between two charges
U	Coulomb’s energy
ξ_H	Dynamic correlation length

CHAPTER 1

Introduction

1.1 Soft Matter

Soft matter or complex fluid is a class of material that can be easily deformed by thermal fluctuations or external forces. They are macroscopically soft and their properties lies in between that of a simple liquid and crystalline solid [1]. Pierre-Gilles de Gennes coined the word soft matter, is credited as the father of soft matter. The application of soft matter prevails in everyday of human life. E.g. Detergents, paints, plastics, pharmaceutical products, liquid crystal display, food etc. Human body itself composed of soft materials such as biological macromolecules of DNA, polysaccrides, protein etc. Other examples of soft matter are colloids, hydrogel, polymer, surfactant, liquid crystal.

Since the size of fundamental entities of soft matter is in the range of nm to μm, which is ~ 3 – 4 orders of magnitude greater than the atomic system, the number density of soft matter is several orders of magnitude lower that of atomic system (10^{13} cm^{-3} against 10^{22} cm^{-3} for atomic system). This along with the very weak interaction, of the order of thermal energy ~ k_bT, between their fundamental entities gives rise to a very low elastic moduli to soft materials. Besides they lack a long range ordering. Soft matter is non-dissipative, disordered, non-equilibrium, non-linear, thermal and entropic system in nature. Owing to their large relaxation time (10^{-2} s) as compare to atomic material (10^{-11} s) and larger length scale, soft matter system are being used as a model system to study the fundamental phenomenon like glass transition, crystallization etc. One of the interesting properties of soft matter is that their microscopic entities self-assemble or aggregates to form various structures.

1.2 Colloidal dispersion

The term colloid, means glue, was coined by British physicist Thomas Graham in 1861. Colloidal dispersion is a heterogeneous mixture of one materials (dispersed phase) suspended in another (dispersion medium) [2]. Both dispersed phase and dispersion medium can be solid, liquid or gas. The typical length scale of the dispersed phase ranges from a few nm to µm. Some common examples are paints, inks, food products such as mayonnaise, ice-cream and biological fluids such as blood and milk. Depending on the interaction between the dispersed phase and dispersion medium, it is classified as lyophilic or solvent loving and lyophobic or solvent repelling [3]. The effective interaction between colloids can be tailored by changing the environmental conditions such as temperature, pH or salt. One of the major a difference between atomic and colloidal system is size distribution or polydispersity in the latter.

1.3 Emulsion

Emulsion is a thermodynamically unstable biphasic system, usually kinetically stabilized using surface active agents (surfactant) or macromolecules. They are an important class of colloidal dispersion from commercial point of view as well as from scientific point of view due to their ease of preparation, low toxicity, biodegradability, biocompatibility etc [4, 5]. They are metastable colloidal dispersion, formed by mixing two immiscible liquids in the presence of surface active molecules that impart stability at the interface [6]. In general, surfactants are used to provide sufficient stability to emulsions but macromolecules such as polymer, protein [7], lipid or even nanoparticle [8] are also be used to attain long term stability. The role of the stabilizing moiety is to cover the interface and prevent the emulsion from destabilizing, by forming a monolayer of adsorbed molecules, thereby reducing the interfacial tension. The adsorbed surface active moieties impart stability through electrostatic or steric interaction. Natural macromolecules, such as polysaccharides, are also being used to enhance the stability of the emulsion due to their abundant presence, edibility, low toxicity and cost. Recently, stabilization by nanoparticle gained much attention due to strong interfacial stability, ecofriendly, and non-toxic behavior[9]. Double emulsion or multiple emulsion where small droplets are dispersed within the large droplets, are widely used in industrial products such as syrups, taste making, drugs etc.

1.3.1 Preparation of emulsion

Emulsification process can be broadly classified into two categories: high energy and low energy emulsification [6]. High energy emulsification uses significant energy (10^8 to 10^{10} W/Kg) to produce smaller droplet diameter whereas low energy emulsification uses less amount of energy (10^3 to 10^5 W/Kg) to produce smaller droplets by exploiting phase inversion property of the system, without consuming excess energy to produce emulsion [4].

High energy emulsification includes high energy stirring, ultrasonic emulsification, high pressure homogenization microfluidization and membrane emulsification. The first step in preparing emulsion using this technique is to prepare oil-in-water (O/W) macroemulsion by mixing oil, water and surfactant in a simple batch stirrer for sufficient period of time and then passing into a homogenizer where sufficient high energy is applied for a long period of time to convert larger macroemulsion droplets into smaller sized nanoemulsion. This process is repeated for several times, till a uniforms size distribution is attained.

In contrast to high energy homogenization, low energy emulsification begins with W/O macroemulsion which is then converted to an O/W nanoemulsion either by changing the composition or temperature of the system. The most widely used low energy homogenization techniques are emulsion inversion point (EIP) and phase inversion temperature (PIT). In EIP method, the obtained W/O macroemulsion is then phase inverted either by diluting the obtained emulsion with water to converts into O/W nanoemulsion at the inversion point. Similarly in PIT method, W/O macroemulsion is prepared at high temperature and the system is then allowed to cool [10]. Below the PIT, W/O macroemulsion is converted to an O/W nanoemulsion. In both processes at the point of phase inversion, the interfacial energy becomes very low that results in the formation of lower size droplets without much energy penalty.

1.3.2 Mechanism of emulsion destabilization

Emulsions are thermodynamically unstable system and the change in Gibb’s free energy ($\Delta G = \gamma A - T\Delta S$) is greater than 1 where γ is the interfacial tension, A_{inter} is the interfacial area, T is the temperature and ΔS is the entropy of mixing. The droplet size and interfacial charge play an important role in determining the stability of the emulsion [11]. Emulsion degradation happens through various mechanisms, shown in the **Figure 1,** that depends on droplet size distribution and density difference between dispersed phase and dispersion medium. The mechanisms of emulsion degradation are broadly classified into primary and secondary and the physical phenomenon involved in each process is complex in nature. Primary emulsion degradation involves increase in size of the emulsion droplets whereas secondary emulsion degradation results in spatial rearrangement of the droplet with respect to each other. Mechanisms such as coalescence, Ostwald ripening, inversion comes under primary whereas the mechanisms such as aggregation, sedimentation categorized under secondary.

1.3.2.1 Sedimentation

Sedimentation arises from gravitational interaction on the dispersed phase and happens when the density of the dispersed phase is greater than the density of continuous phase. In this process, gravity plays an important role which attracts the particle but the viscous force opposes the movement of particle. The rate of settling of particle is calculated by balancing the hydrodynamic and gravitation force, as described by stokes equation which is given by [11]

$$V_s = \frac{-2\,\Delta\rho g\, d^2}{9\eta} \qquad (1.1)$$

where V_s, is the strokes velocity, g is the gravitational acceleration, $\Delta\rho$ is the difference in density of particle and solvent, d is the diameter of the particle and η is the viscosity of the solvent. Making emulsion with lower sedimentation rates is possible by: (1) Matching the density difference between dispersed and continuous phase. (2) Reducing the droplet size. This is the principle used in formation of nanoemulsion where the droplet size lies between 20 and 200 nm. (3) Use of thickening agents such as high molecular weight polymer to increase the viscosity of the emulsion.

1.3.2.2 Creaming

Creaming is similar to sedimentation but happens in opposite direction where droplets are moving towards the top of the container[12]. It is not breaking of emulsion but a phase separation which is prestage of coalescence. It arises due to density difference between the continuous and dispersed phase, particularly when the density of the dispersed phase is smaller than the density of continuous phase. Creaming can be either problematic or advantageous. Though it is one of the factors that reduce the shelf life of the formulation, yet this phenomenon is exploited in industries for separation process. The mechanisms that are proposed to avoid the sedimentation can also be used to prevent creaming.

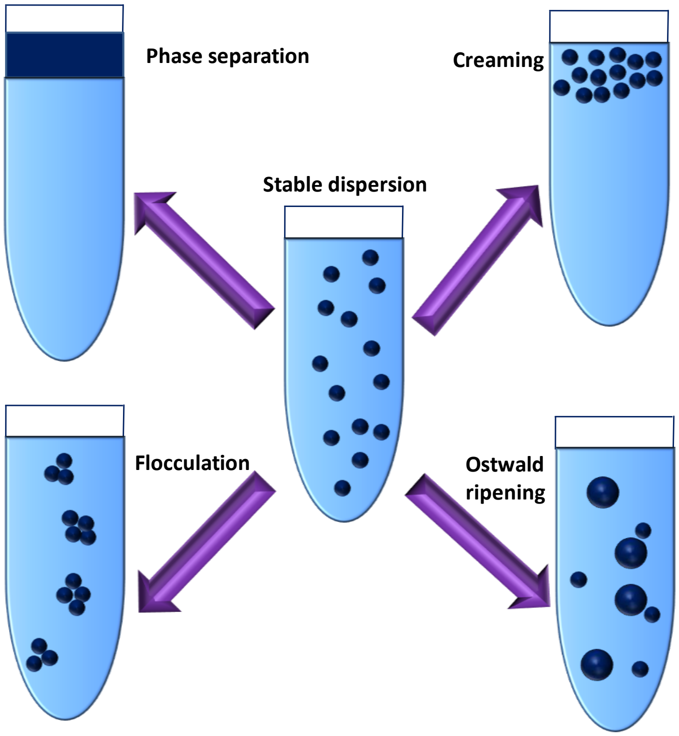

Figure 1.1: Different types of emulsion destabilization process: phase separation, creaming, flocculation and Ostwald ripening.

1.3.2.3 Flocculation

Flocculation, aggregation of droplets into a larger unit without change in primary droplet size, arises when attractive interactions acting within the emulsion (such as van der Waals, hydrophobic) outweigh the repulsive interaction. It can be avoided by suitably using an emulsifier that imparts sufficient stability to the emulsion by adsorbing at the colloidal interface. Surface active moieties such as surfactant or polymer or polyelectrolyte are used as stabilizers that keep the dispersed media far apart through electrostatic or steric or electro-steric interactions, where contribution due to van der Waals and other structural forces such as hydrophobic are negligible. Depending upon the strength of van der Waals force, the emulsion flocculates weakly or strongly. The presence of large number of non-adsorbed surface active species can also flocculate the emulsion via depletion interaction.

1.3.2.4 Ostwald ripening

Ostwald ripening is a degradation process where smaller droplets are diffused in the bulk phase and deposit over larger droplets that results in an overall increase in size of the emulsion droplets with time [13]. It happens due to the difference in chemical potential of the oil phase between different droplets size that has different radius of curvature. This process results in increase in size of the droplets with time. The rate of Ostwald ripening can be described as follows [14]:

$$\frac{d{<}R_h{>}^3}{dt} = \frac{8\gamma V_m S_\infty D}{9RT} \qquad (1.2)$$

Here R_h, γ, V_m, R, T, S_∞ and D are the droplet radius, interfacial tension, molar volume of oil phase, gas constant, absolute temperature, equilibrium solubility of oil phase in the aqueous phase and translational diffusion co-efficient. Unlike coalescence, no rupture of thin film of the droplets happens in Ostwald ripening. The rate of Ostwald ripening of the droplets i.e. increase in size of the droplets with time can be calculated from the diffusion co-efficient of the droplets, radius of the droplets and the concentration gradient using **equation 2**. The process of Ostwald ripening in monodisperse nanoemulsion is very often neglected due to extremely small and uniform droplet size but has a serious problem in macroemulsion where the dispersed phase has high aqueous solubility. Several methods were put forwarded to reduce the rate of Ostwald ripening [11]. One of the important parameter is the addition of second disperse phase that is insoluble in the continuous phase. The second method relies on modification of interface film at oil-water interface that reduce the interfacial tension. By suitably decorating the interface with surfactant or macromolecule that does not desorbs during ripening, the rate of Ostwald ripening could be reduced significantly.

1.3.2.5 Coalescence

This type of destabilization arises when droplets come in contact through flocculation or creaming or Brownian motion and involves rupturing of thin interfacial layer or film around the oil droplet. The formation of thin film results from the adsorption of surfactant or macromolecules which prevents the phase separation. Due to repeated collision between the droplets, thin films around the droplets could rupture that ultimately results in the fusion of droplets which increase the droplets size. As the mechanism progresses with time, complete phase separation of emulsion can occurs. Some mechanisms were proposed to prevent droplet coalescence. Friberg et al[15]. proposed to use a combination of surfactants to produce multilayer's that wrap the droplets so that the rupturing of interfacial films and hence the van der Waals attraction decreases. The adsorption of such multilayer improves the Gibbs elasticity, surface viscosity and also hinders the diffusion of surfactant film from the interface and therefore lifetime of the emulsion can be enhanced.

1.4 Importance of Interface

The characteristic features of any colloidal dispersion is the large surface to volume ratio of the dispersed particle and the presence of interface between dispersed and continuous phase. The interface is the shared boundary between two immiscible phases and interfacial tension is the force per unit length across the interface of two immiscible liquids that is responsible for instability of the emulsion or colloidal dispersion. The adsorption of surfactant or macromolecule at the interface of the colloidal dispersion can impart electric double layer interaction [16], steric [17] or electro-steric interaction [18] that reduces the interfacial tension and alters the overall behavior of the colloidal dispersion. The presence of a few molecular layers at the interface within a few nanometers ultimately determines the bulk properties of the colloids and the resultant product stability, by altering the particle-particle and particle-solvent interaction, respectively.

1.5 Intermolecular interactions

The shelf life of any formulation, including emulsion, is ultimately determined by the effective interaction or the net forces acting between suspended particles. If the net interaction force between the dispersed particles is repulsive then the formulation has an extended lifetime. To achieve a net repulsive interaction throughout its storage and use, various stabilization approaches such as electrostatic, steric, electro-steric or hard-sphere are attempted using stabilizing group such as surfactant, neutral and charged macromolecule or nanoparticles. More recently, particle stabilization is also attempted widely because of their effectiveness in achieving long term stability. Types of interaction forces that determine the stability of colloidal dispersion are broadly classified into DLVO (Derjaguin-Landau-Verwey-Overbeek) and non-DLVO. DLVO force is the sum of electrostatic and van der Waals forces whereas non-DLVO forces includes steric, electro-steric, structural, hydration, hydrophobic etc and the classification of interaction force is shown schematically in the **Figure 2**.

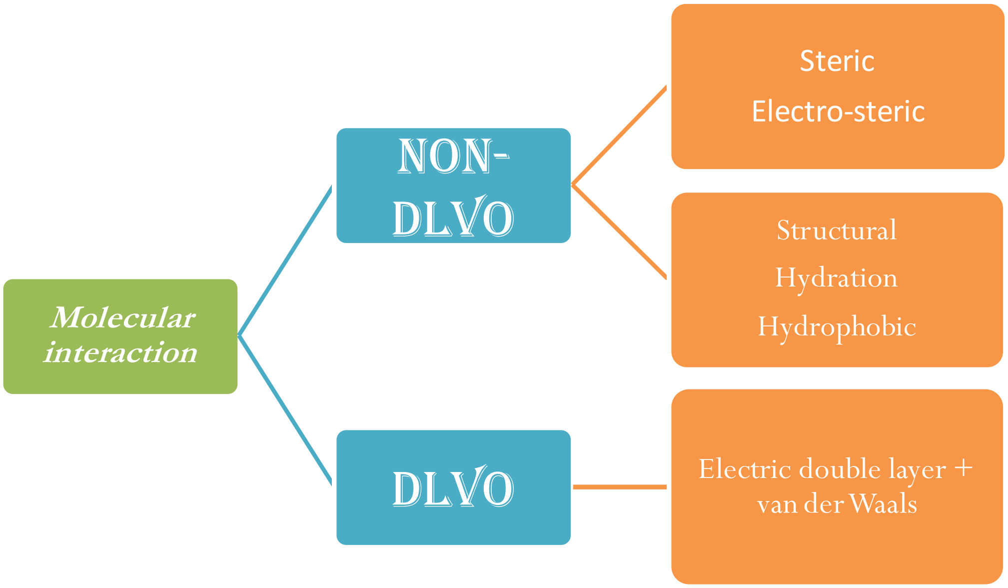

Figure 1.2: Classification of molecular interactions

1.5.1 DLVO theory

It has been known for several decades that aqueous colloidal dispersion coagulate or precipitate upon addition of salt and the process of coagulation progress rapidly with increasing the valence of salt. This process was first explained theoretically by Derjaguin [19] and then Vervew [12], Landau and Overbeek [20] by combining the repulsive electrostatic and attractive van der Waals interaction. This theory is known as DLVO theory that explains the stability of colloidal dispersion and aggregation behavior.

1.5.1.1 Electrostatic stabilization

Electrostatic interaction in an aqueous colloidal system arises due to the existence of charged group on the surface of the particle [21]. Charging of surface takes place either due to dissociation of surface groups or adsorption of charged moieties over a surface. The adsorbed charged moieties give rise to an electric field which attracts the counter-ions that are balanced with the equal number of surface co-ions, as shown in the **Figure 3**.

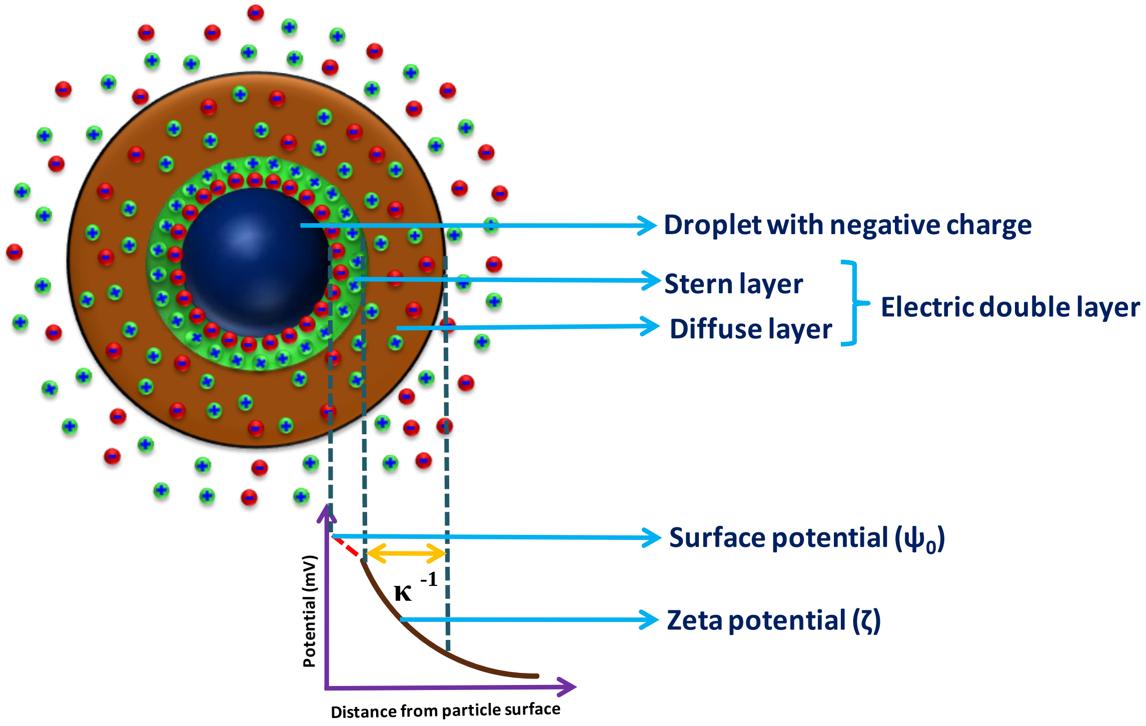

Figure 1.3: Schematic representation of electric double layer and the variation of potential from droplet surface.

The simplest model of electric double layer was proposed by Hermann von Helmholtz who considers the counter-ions are strongly bound to the surface co-ions. Though this model could explain the basic features of charged surface, it failed to explain the capacitance of electric double layer. The theory was modified by Guoy and Chapman [22, 23] who proposed that the thermal fluctuation drive the counter-ions away from the surface and the resultant structure was called diffuse layer and the corresponding potential and ion-distribution was calculated by Debye and Huckel [24]. Otto Stern [25] combined Helmholtz and Guoy-Chapman model and proposed the double layer theory where the counter-ions are strongly bound to the surface is called Stern or Helmholtz layer and ions that are scattered or diffused around the surface is called diffused layer. This layer of surface charge that composed of Stern or Helmholtz and diffuse layer around the surface or particle is called electric double layer.

The counter-ion distribution between the surfaces that carry charges in a pure solvent like water is discussed. Consider a planar charged surface immersed in a solvent like water. In general, the relation between the local charge density (ρ) and potential (ψ) of the surface is expressed as

$$\nabla^2\psi = \frac{\partial^2\psi}{\partial x^2} + \frac{\partial^2\psi}{\partial y^2} \;\; \frac{\partial^2\psi}{\partial z^2} = -\frac{\rho}{\varepsilon\varepsilon_0} \tag{1.3}$$

Here, the local charge density is expressed as

$$\rho = e\,(C^+ - C^-) \tag{1.4}$$

where C^+ and C^- are local cation and anions concentrations. In addition, the solvent contains monovalent salt that exceeds the background ion concentrations, which are related to the local potential via Boltzmann relation as

$$\varphi_s = \varphi_s^0\, e^{-{W_i}/{kT}} \tag{1.5}$$

where $W_i = e\psi$ is the work required to bring the ion from infinite distance to the surface, φ_s^0 is the bulk concentration of salt and k_bT is the thermal energy.

Therefore, the total local charge density that includes the contribution due to cations and anion is expressed as

$$\rho = e\,(C^{+} - C^{-}) = \varphi_s^0 e \left[\exp\left(-{}^{e\psi}/_{k_bT}\right) - \exp\left({}^{e\psi}/_{k_bT}\right)\right] \tag{1.6}$$

Therefore, the potential can be expressed as

$$\nabla^2\psi\,(x,y,z) = \frac{\varphi_s^0 e}{\varepsilon\varepsilon_0}\left[\exp\left({}^{e\psi\,(x,y,z)}/_{k_bT}\right) - \exp\left(-{}^{e\psi\,(x,y,z)}/_{k_bT}\right)\right] \tag{1.7}$$

For a simple case of infinitely extended planar surface, the Poisson-Boltzmann equation can be written as

$$\frac{d^2x}{dx^2} = \frac{\varphi_s^0 e}{\varepsilon\varepsilon_0}\left[\exp\left({}^{e\psi\,(x)}/_{k_bT}\right) - \exp\left(-{}^{e\psi\,(x)}/_{k_bT}\right)\right] \tag{1.8}$$

Since the potential change in y and z direction is zero, their contribution is omitted.

For lower surface potential ($|e\psi| < k_bT$), it is reduced to

$$\frac{d^2\psi}{dx^2} \approx \frac{2\varphi_s^0 e^2}{\varepsilon\varepsilon_0 k_bT}\,\psi \tag{1.9}$$

where ε and ε_0 are dielectric permittivity in medium and free space.

With appropriate boundary conditions, the solution to the linearized Poisson-Boltzmann equation is expressed as follows

$$\psi = \psi_0 \exp(-\kappa x) \tag{1.10}$$

Here, κ^{-1} is the Debye length that quantifies the extension of double layer, which is expressed as

$$\kappa^{-1} = \sqrt{\frac{\varepsilon\varepsilon_0 k_bT}{2\varphi_s^0 e^2}} \tag{1.11}$$

where, φ_s, k_b, T, and e are concentration of electrolyte, Boltzmann constant, temperature and charge of ions. When two charged surfaces approach each other the electric double layer overlaps that result in development of electrostatic repulsive force which is important for stabilizing colloidal dispersion. Using linear approximation and assume low surface potential, the interaction free energy per unit area between identical parallel surfaces of infinitely extended solids, W_{plane} can be expressed as

$$W_{plane} = \frac{64\, \varphi_s^0 k_b T \tanh^2(\frac{e\psi_0}{4k_bT})}{\kappa} e^{-\kappa D} \tag{1.12}$$

Using Derjaguin approximation, the force between two spheres of radius R can be obtained using the following relation as

$$F_{sphere} = \pi R W_{plane} \tag{1.13}$$

For lower surface potential, the force between two spheres is expressed as follows

$$F_{sphere} = 2\pi R \varepsilon \varepsilon_0 \kappa \psi_0^2\, e^{-\kappa D} \tag{1.14}$$

The above equation shows that the double layer interaction energy decay exponentially with distance with a characteristics decay length equals to the Debye length of the double layer.

1.5.1.2 Van der Waals interaction

Van der Waals interaction plays a critical role in intermolecular force and has a universal relevance as it present in any combination of surfaces or molecules and exhibit both long and short range interaction. It arises due to dipolar interaction and named after the great theoretician Johannes Diderik van der Waals. The interactions between molecules in vacuum are of three different types: Ion-dipole (Debye), dipole– dipole (Keesom) interactions, induced dipole – induced dipole (London) interaction. The last interaction is also known as dispersion force or charge fluctuation force. The contribution to the Van der Waal interaction (C_{vdw}) is the sum of interaction of Debye, Keesom and London which is expressed as:

$$V_{vdW}(D) = -\frac{C_{vdW}}{D^6} \quad \text{where } C_{vdW} = C_{Debye} + C_{Keesom} + C_{London} \qquad (1.15)$$

where C_{Debye}, C_{Keesom} and C_{London} are the contribution to the van der Waals interaction due to Debye, Keesom and London. Minus sign arises due to attractive nature of van der Waals interaction. The contribution of dispersion force dominates among all the van der Waals interaction between atoms and molecules that determines the properties such as adhesion, surface tension, wetting, physical adsorption as well as properties of gas, liquids, thin films, strength of solids and flocculation of particle in dispersion, behavior of macromolecules such as polymer, DNA, proteins etc. All three types of interaction contain the same distance dependence and the potential decreases as $1/D^6$.

1.5.1.2.1 Van der Waals interaction between macroscopic bodies

Theoretical description of van der Waals interaction between macroscopic bodies was developed by London, who proposed that dispersion interaction was responsible for the attractive interaction between macroscopic bodies. This idea led Hamaker to develop a microscopic approach that used pair wise addition of force between molecules in an object immersed in a solvent that is not influence by the presence of third molecules.

To calculate the net interaction between object immersed in a solvent, the van der Waals interaction between molecule A and molecule B in an object is expressed as

$$V_{mol/obj}\,(D) = -C_{AB} \iiint \frac{\rho_B}{D^6}\, dV \tag{1.16}$$

Here, C_{AB}, and ρ_B are material specific constant and molecular density of surface B. By using cylindrical polar co-ordinates and assuming that the density of the molecule is constant in the object, the net interaction is expressed as

$$V_{Mol/Obj}\,(D) = -\frac{\pi \rho_B C_{AB}}{6D^3} \tag{1.17}$$

Similarly, the energy of interaction between the two extended solid surfaces of molecular density ρ_A and ρ_B immersed in a solvent is given by

$$V^A\,(D) = -\frac{\pi \rho_A \rho_B C_{AB}}{12D^2} \tag{1.18}$$

By introducing Hamaker constant $A_H = \pi^2 C_{AB} \rho_A \rho_B$, the net interaction energy can be expressed as

$$V^A\,(D) = -\frac{A_H}{12\pi D^2} \tag{1.19}$$

It is to be noted here that the van der Waals interaction between surfaces decreases less steeply than the same force operate between the molecules.

1.5.1.2.2 Lifshiftz theory of van der Waals interaction

The problem with Hamaker approach to estimate the net van der Waals interaction between surfaces was based on pair wise additivity which ignores the role of neighboring atoms that affect the net interaction. But in general, the effective polarizability of any pair of atoms or molecules is affected due to neighboring atom or molecule. Furthermore, additivity cannot hold between the extended bodies interacting in a medium. By taking this into consideration, Lifshitz formulated a theory that ignored the atomic structure and the forces between the large bodies are treated as a continuous media.

The main finding of the Lifshiftz theory was the equation derived as per Hamaker approach remains same as follows:

$$V^A = \frac{A_H}{12\pi x^2} \tag{1.20}$$

Here, A_H is the non-retarded Hamaker constant which is expressed in McLachlan's equation as

$$A = \pi^2 C \rho_1 \rho_2 = \frac{3}{4}\, kT \left(\frac{\varepsilon_1 - \varepsilon_3}{\varepsilon_1 + \varepsilon_3}\right) \left(\frac{\varepsilon_2 - \varepsilon_3}{\varepsilon_2 + \varepsilon_3}\right) + \frac{3h}{4\pi} \int_{\upsilon_1}^{\infty} \left(\frac{\varepsilon_1\,(i\upsilon) - \varepsilon_3(i\upsilon)}{\varepsilon_1\,(i\upsilon) + \varepsilon_3(i\upsilon)}\right) \left(\frac{\varepsilon_2\,(i\upsilon) - \varepsilon_3(i\upsilon)}{\varepsilon_2\,(i\upsilon) + \varepsilon_3(i\upsilon)}\right) d\upsilon \tag{1.21}$$

where ε_1, ε_2 and ε_3 are static dielectric constant of three media and $\varepsilon(i\nu)$ is the value of ε at imaginary frequency.

1.5.1.3 Limitations of electric double layer theory

Though electric double layer theory could explain the observed behavior of colloids under various conditions, yet it suffers several demerits which are as follows:

1. Ion-correlation effect is not included in the mean field theory of Poisson-Boltzmann double layer expression.
2. Specific ion effect is not included.
3. Finite size of the ions was neglected.
4. The theory holds only for small range concentration of salt (< 0.05 M) which limit the application of DLVO theory to a biological medium.

1.5.2 Non-DLVO interaction

While DLVO theory is simple in nature and able to explain the observed stability of colloids, yet the theory was not sufficient to describe the stability of uncharged particle at high salt concentration [26]. Also, it could not explain the behavior of particles or surfaces at very short distance where continuum theories breaks down and interactions such as structural, hydration[27, 28] and hydrophobic force operates which could be oscillatory, repulsive or attractive that are sensitive to the nature of solvent molecules such as size, shape etc. Therefore, depending upon the nature of surface, solvent and moieties adsorbed on the surface, several non-DLVO interactions arise which are described below:

1.5.2.1 Steric interaction

It arises due to adsorption of neutral surfactant or macromolecule such as polymer that can dramatically influence the stability of dispersion. It is the only way of ensuring stability to the dispersion in a non-polar media where electrostatic interaction is absent or extremely weak and van der Waals interaction dominates. The presence of polymer or simple neutral molecule ensures the particle to feel sufficient repulsive force at small interparticle distance such that the outer segments of the polymer overlap. Therefore, the particles covered with polymer maintain sufficient distance between them that give rise to an enhanced stability to the colloidal dispersion.

The assembly of polymer chains end-tethered its one end onto the particle or substrate and the other end float freely is called polymer brush. The polymer can adsorbs on a surface and attains saturation level at very low concentration. In general, the adsorption of polymer can be physical or chemical where in the former case physical force drives the polymer to adsorb at the interface whose energy of detachment is of the order of thermal energy (k_bT) whereas in the latter case, chemical bonding between the molecules and surface is ensured to chemically graft the molecules over a surface whose energy of detachment is very large.

The behavior of polymer under confinement was different from its counter-part in the continuous media that exhibit random walk behavior. Depending upon the number of polymers at the surface the conformation and hence the behavior of the colloidal dispersion changes. When the density of polymer at the surface is very low such that the distance between the tethering groups is greater than the dimension of the adsorbed polymer, it exhibit mushroom conformation. But, when the crowding of polymer at the surface is so dense, the polymers are stretched along the direction normal to the grafting surface so as to avoid overlapping which is called polymer brush.

The theory of steric interaction was quite complex as it depends on various parameters such as reversible or irreversible adsorption of polymer, coverage of the polymer and quality of the solvent [29-31]. To understand the steric interaction, consider polymer brushes grafted at the surface with a grafting density $\Gamma = {}^{1}/_{b_{gra}^{2}}$ where b_{gra} is the distance between the grafting groups on the surface. To find out the thickness of the polymer brush in a good solvent condition it is necessary to consider the contributions due to two forces: repulsive interaction between the polymer segment that force the polymer to stretch away from the surface and the chain elasticity that oppose the polymer stretching. The total force experienced by the chain is given by

$$F_s = \frac{3k_bTL}{Nl_s^2} - \frac{k_bT\nu N^2\Gamma}{2L^2} \qquad (1.22)$$

Here, l_s, ν are Kuhn length and excluded volume parameter. The first term represents the repulsive interaction of polymer segment and second term corresponds to the chains elasticity. At equilibrium and in the absence of external force, the brush thickness is given by

$$L = N\left(\frac{\nu l_s^2\, \Gamma}{6}\right)^{1/3} \tag{1.23}$$

The free energy of surface coated with polymer was calculated by studying the force per unit area (F_s) between two parallel flat surfaces with polymer solution between them which is given by

$$F_s = -< \frac{\partial H}{\partial h_{pla}} > = -\frac{\partial \Omega}{\partial h_{pla}} \tag{1.24}$$

where H is the Hamiltonian of the system, Ω is the grand canonical potential and h_{pla} is the separation between the plates. The theory of steric interaction was studied extensively where Milner [29] used self consistent field theory to describe the behavior of polymer at the surface who showed that the concentration profile of the polymer exhibit parabolic profile and the brush height gradually falls to zero from the maximum at the surface whereas de Gennes[30] used a step function i.e. a flat density profile where the brush height falls abruptly to zero over a narrow region.

When two polymer coated surfaces are bring together such that at distance where polymer brush overlap, the local density of the polymer increases that give rise to a repulsive interaction. Using scaling theory for a homogenous segment concentration profile, the interaction energy per unit area between two parallel plates as obtained by de-Gennes is given by

$$\Pi\left(h_{pla}\right) = k_b T \sigma^{3/2}\left[\left(\frac{2L}{h_{pla}}\right)^{\frac{9}{4}} - \left(\frac{h_{pla}}{2L}\right)^{\frac{3}{4}}\right], \quad h_{pla} < 2L \qquad (1.25)$$

The interaction potential is obtained by integrating the above equation as

$$W\left(h_{pla}\right) = \frac{8\, k_b T H\, \sigma^{3/2}}{35}\left[7\left(\frac{2L}{h_{pla}}\right)^{\frac{5}{4}} + 5\left(\frac{h_{pla}}{2L}\right)^{\frac{7}{4}} - 12\right], \quad h_{pla} < 2L \qquad (1.26)$$

When the parameter $h_{pla}/2L$ is in the range of 0.2 to 0.9, the above expression is simply expressed as follows

$$W\left(h_{pla}\right) = \frac{100\, k_b T}{\pi}\, H\, \sigma^{3/2} e^{-{\pi h_{pla}}/{L}} \qquad (1.27)$$

Therefore, the steric interaction due to polymer decay exponentially with distance with characteristics decay length equals to the extension of the polymer.

1.5.2.2 Electro-steric stabilization

It arises due to adsorption of charged macromolecules that contains ionizable group, thereby dissociates and leaves the charged group over polymer backbone with counter-ions in the solution. Presence of charged macromolecules over a surface gives rise to an electro-steric interaction which contains electrostatic interactions due to dissociated charged moieties and steric interaction due to chain excluded volume interaction. Unlike neutral polymer, the interaction force due to adsorbed polyelectrolyte is highly complicated due to ionized group with associated counter-ions. In general, polyelectrolytes are classified as strong and weak where the former is pH independent and latter is pH dependent.

The interaction force due to polyelectrolyte arises due to combination of electrostatic, conformational entropy of polymer chain, excluded volume interaction, entropy of counter-ions as well as quality of the solvent [32]. In addition to these, other parameters such as pH, temperature, grafting density, electric field [33] etc are also involved in altering the net interaction force due to polyelectrolyte and hence the associated conformational changes. The polyelectrolyte mediated interactions are altered due to variation in charge density of the ionizable group on the polyelectrolyte backbone when they are exposed to different environment conditions. At low or zero salt level, the behavior of polyelectrolyte is controlled by long range electrostatic interaction. However, under complete screening of charge at high salt concentration, short range excluded volume interaction dominates over long range electrostatic force. In addition, counter-ions (CI's) play an important role in swelling and collapse of the charged macromolecules [34, 35]. The adsorption of CI's over the polyelectrolyte can modulate the strength of electrostatic interaction which dictates the chain conformation. The strength of electrostatic interaction of polyelectrolyte is expressed in terms of reduced Bjerrum length as $\overline{l_b} = \frac{l_b}{a_{mon}} = \frac{\beta e^2}{\varepsilon a_{mon}}$ where ε is the dielectric constant, a_{mon} is the monomer size and $\beta = 1/k_bT$. In a good solvent conditions, the CI's are dispersed away from the polyelectrolyte chain but increasing $\overline{l_b}$ leads to attractive interaction between the CI's and polyelectrolyte that favors condensation of CI's on polyelectrolyte backbone [36], which reduces the effective charge density of the polyelectrolyte and hence collapses. By switching over the solvent condition to a poor region, the attractive interaction between the monomer increases, which further collapses the polyelectrolyte. Systematic studies in the past showed the extended to collapse transition of polyelectrolyte under different solvent condition [36-38]. Moreover, the characteristics of the polymer such as molecular weight [39], polydispersity [40] also affect the coil to globule transition of a polyelectrolyte.

1.5.2.2.1 pH mediated polyelectrolyte interaction

Depending upon the nature of polyelectrolyte, the interaction mechanism differs. The rate of dissociation of weak polyelectrolyte varies at different solution pH level. For instance, dissociation of carboxylic acid ($C_6H_5COOH \longrightarrow C_6H_5COO^- + H^+$) happens only at pH > pK_a. Below pK_a, it is highly neutral but dissociates at pH > pK_a due to deprotonation of the carboxyl groups. The fraction of charged monomer or degree of dissociation (α) of the polyelectrolyte depends on the pH of the medium which is calculated as $pH = pK_a + 4.10\,\alpha^{1/3} - \log\left(\frac{(1-\alpha)}{\alpha}\right)$ where pK_a was 4.54 [41] for acrylic acid. This shows that fraction of charged monomer increases with increase in pH of the medium > pK_a. Though it was believed that at pH > pK_a + 1, weak acid dissociate completely, it is applicable only to monomer whereas polyelectrolyte barely reaches only 50 % ionization at this pH. Therefore, enhanced fraction of deprotonated group is observed when the solution pH increases above pK_a. When pH < pK_a only 10% of the surface groups are ionized whereas around 90 % of the surface group are ionized when pH > pK_a. The adsorbed polymer exhibit loop, tail and train structure [42] and the adsorbed layer of the pH responsive polyelectrolyte at interface varies with varying the solution pH [43]. At low pH, the loops and train dominates and the length of the tail segment increases with increasing pH [44].

The interaction force due to adsorbed strong polyelectrolyte is entirely different as it is considered to be pH independent [45, 46]. As the strong polyelectrolyte dissociated completely at all pH range, the brush height of strong polyelectrolyte does not vary with solution pH. But, a recent study showed that the conformation, stiffness, hydration, adhesion, lubricity, protein adsorption of strong polyelectrolyte brush can be pH dependent because of the formation of inter chain hydrogen bonded network between grafted chains and the rearrangement of chain conformation, resulting from pH mediated adsorption of OH^{-} within the polyelectrolyte brush. The formation of such interchain hydrogen bonds between the grafted brushes leads to cross-linking, making them physically stiffer that leads to weakening of electrostatic interaction. Moreover, it was also shown that the mole fraction of adsorbed OH^{-} on the strong polyelectrolyte brush varying with solution pH [47]. In the pH range of 2-7, only few OH^{-} groups were adsorbed on the brush but with increase in pH from 7-12 a strong adsorption of OH^{-} was noticed, particularly between pH 10 and 12.

1.5.2.2.2 Salt mediated polyelectrolyte interaction

The theory of polyelectrolyte conformation in the presence of electrolyte was studied extensively [48-57]. Various models were proposed to explain the conformational change of polyelectrolyte under different environmental conditions. The scaling analysis ignores the details of internal brush structure whereas the brush structure was centre of attention in numerical calculations, which consider the spatial variations within the brush. Analytical self consistent field model deals both the internal brush structure and the average characteristics.

Several theoretical models were used to understand the behavior of polyelectrolyte brush under various physio-chemical conditions. According to mean field model developed by Zhulina et al. [50] the polyelectrolyte brush is assumed to be immersed in an infinite reservoir of water containing fixed amount of monovalent ions, besides H^{+} and OH^{-} . The dimensions of the mobile ions are ignored thereby only the electrostatic contribution is taken into account and the steric interactions are ignored as dilute electrolyte solutions are considered. The equilibrium values of polymer molar concentration, brush height etc, are obtained by balancing various forces acting within the brush immersed in a salt-water solution as

$$f_{conf} = f_{conc} + f_{ion} \qquad (1.28)$$

where f_{conf} is the elastic force arising due to stretching of polymer, f_{conc} is the non-electrostatic volume interaction and f_{ion} is the force due to electrostatic interactions between charged units which are given by is given by

$$\frac{f_{conf}}{kT} = \frac{H}{Na_{mon}^{2}} = \frac{a_{mon}}{\sigma\varphi} \qquad (1.29)$$

$$\frac{f_{conc}}{kT} = \left(\frac{\upsilon\sigma\varphi^{2}}{a_{mon}^{3}}\right) + \left(\frac{w\sigma\varphi^{3}}{a_{mon}^{3}}\right) \qquad (1.30)$$

$$\frac{f_{ion}}{kT} = \sigma\left\{\left[\left(\frac{\alpha\varphi}{a_{mon}^{3}}\right)^{2} + 4\left(C_{H}^{*} + \varphi_{S}\right)\right]^{1/2} - 2\left(C_{H}^{*} + \varphi_{S}\right)\right\} \qquad (1.31)$$

Here α, φ, a$_{mon}$, C_{H}^{*} and φ_{S} is the fraction of charged group, polymer volume fraction, size of the monomer, Solution of H^{+} and OH^{-} at pH = 7 and concentration of salt. The excluded volume interaction for polyelectrolyte is neglected in the theory (i.e. f_{conc} is ignored), such that at equilibrium

$$f_{conf} \approx f_{ion} \qquad (1.32)$$

By equating the force due to electrostatic and elastic (depending upon the amount of salt in the bulk solution), the equilibrium brush height at different concentration of salt is obtained as

$$H = Na_{mon}\alpha^{\,1/2} \qquad \text{when } C_H^* + \varphi_s \ll a_{mon}\varphi/a^3 \qquad (1.33)$$

$$H = N(a_{mon}^2 \alpha_b^2 \sigma^{\,-1} \varphi_s^{-1})^{1/3} \qquad \text{when } \varphi_s \gg \alpha\varphi/a_{mon}^3, C_H^* \qquad (1.34)$$

Here, N and α_b are the number of monomers and dissociation constant in the bulk. **Equation (1.33)** corresponds to the brush height in osmotic brush regime (OsB) where concentration of salt is smaller than immobilized charge density of polyelectrolyte whereas **equation (1.34)** corresponds to salted brush (SB) regime where the salt concentration in the bulk is greater than polyelectrolyte charge density. The brush height in OsB and SB regime is valid for both strong and weak polyelectrolyte. But, in case of weak polyelectrolyte the problem becomes more complicated due to the dependence of dissociation constant (α) on polymer volume fraction (φ) and hence, the brush height in this case was predicted to follow accordingly,

$$H \sim Na_{mon}^{4/3}\sigma^{1/3}\left(\frac{\alpha_b}{1-\alpha_b}\right)^{1/3}([H^+] + \varphi_s)^{1/3} \qquad (1.35)$$

where N is the number of monomers in the brush chain, σ is the graft density, α is the degree of dissociation in the bulk, H^+ is the concentration of proton and φ_s is the concentration of salt. The anomalous behavior of annealed polyelectrolyte brush at low salt concentration is attributed to the increased degree of ionization of brush with increase in salt concentration as given as

$$\alpha = \left(\frac{\alpha_B}{1-\alpha_B}\, a_{mon}\, \sigma \left[C_H^* + \varphi_s\right]\right)^{2/3} \tag{1.36}$$

The scaling relation gives new features on the strong and weak polyelectrolyte brush behavior. At low salt concentration i.e. in osmotic brush regime the brush thickness of weak polyelectrolyte increases with σ and φ_s whereas thickness of strong polyelectrolyte brush is independent of σ and φ_s. When salt concentration is increased the brush enters salted brush regime where the difference between annealed and quenched regime disappear and the thickness of the brush decreases with addition of salt.

Israel's et al. [58] used self consistent mean field theory to describe behavior of anchored weak polyacid where the brush segment was assumed to be a function of local environment and pH of the solutions. Since the degree of dissociation of brush (α) is a function of local pH, there exist a potential difference between the brush and the bulk solution, where the degree of dissociation is α_b. The relation between them, based on two state approximations in a self-consistent mean field theory, was expressed as

$$\alpha = \frac{\alpha_b}{\alpha_b + (1-\alpha_b)e^{-y}} \tag{1.37}$$

where e^{-y} is the potential difference between brush and bulk solution. As the amount of salt increases in the bulk, the difference in proton concentration between the bulk and brush decreases and it vanishes (i.e. $e^{-y} \approx 0$) at a particular salt concentration termed as φ_s^{max}. Consequently, the brush structure expands with the addition of salt till it attains a maximum. Once the concentration of ions inside and outside the brush balances then the polyelectrolyte enters SB regime where $\alpha \approx \alpha_b$. With further addition of salt, the brush thickness decreases with increasing salt concentration due to screening of surface group on the polyelectrolyte backbone. A maximum in the brush thickness is observed during the transition from OsB to SB regimeas given by $H_s^{max} \sim N\,(\alpha_b)^{1/2}$ and the concentrations of salt at which the transition takes place (i.e. φ_s^{max}) is a function of grafting density and bulk dissociation constant α_b as $\varphi_s^{max} \sim \sigma\,(\alpha_b)^{1/2}$. Thus, a weak polyelectrolyte shows a non-monotonic behavior in brush thickness with varying salt concentration (φ_s), due to the potential difference between the bulk and brush which is not fixed but varies with electrolyte concentration in the surrounding medium [59, 60].

Such an anomalous behavior of increasing brush height with increasing ion concentration in OsB regime is a distinct property of a weak polyelectrolyte that arises due to varying degree of dissociation in the presence of salt. Such a response is not observed in strong polyelectrolyte as it dissociates at all pH ranges. Mean field [50] and self consistent field theory [58] predicts that the brush height of a strong polyelectrolyte does not change until the concentration of external ions is equal to the number of CI's inside the brush whereas the anomalous behavior (i.e. increase in polyelectrolyte brush height at low salt concentration) is a characteristics of weak polyelectrolyte [50, 58]. At very low salt concentration, the brush height of the strong polyelectrolyte does not vary with addition of salt and the polyelectrolyte conformation remains unaltered where only slight variation in polyelectrolyte charge distribution was noticed. However, at high salt concentration, the brush enters salted brush (SB) regime where both quenched and annealed polyelectrolyte brush height collapse with increasing salt content. The collapse continues due to decrease in osmotic pressure of the CI's and polyelectrolyte brush neutralizes completely and it enters quenched neutral brush (QNB) regime where it behaves like a neutral polymer brush.

1.5.2.2.3 Polyzwitterion mediated interaction

Polyzwitterion is a special class of polyampholyte which carries equal number of cationic and anionic group on the polymer backbone [61]. In general, the charged groups in polyampholyte are distributed heterogeneously along the polymer backbone where one group outweigh the contribution of others at a particular physiological condition, so that the net charge could be either positive or negative which varies with solution pH and ionic strength. But, in polyzwitterion both charges are present with equal contributions. They are special type of polymer with low amount of production but increased attention were paid when researcher found they are analogous to a biological macromolecules, polyphospolipds that are major constituent of cell membrane.

Due to simultaneous presence of both charges, they exhibit unique behavior in the presence of salt. They adopt collapsed conformation in water but in the presence of salt extended conformation is noticed which is opposite of the polyelectrolyte behavior, therefore termed as “anti-polyelectrolyte effect”. Various models were put forwarded to explain the anti polyelectrolyte effect. This behavior is exploited for various applications, enabling many on/off applications for protein transport, membranes separation, self-cleaning surfaces, controlled release, and lubricant surfaces. The consequence of such effect leads to poor solubility of this polyelectrolyte in water but enhanced solubility can be obtained in salt solution. They are less soluble in water due to strong attractive electrostatic interactions (including charge-charge, charge-dipole, and dipole-dipole interactions) between zwitterionic polymer chains, which causes the collapse of polymer chains [62]. But the solubility increases in salt solution, where the addition of counter ions will screen out such attractive electrostatic interactions that leads to increasing the solubilization of zwitterionic polymers in salt solution [63].

1.5.2.3 Solvation forces

At large distance the force of interaction are governed by continuum DLVO or other non-DLVO interactions such as steric or electro-steric interaction where the intrinsic property of the solvent molecules such as size, shape and chemical nature is not taken into account [21, 64]. But, when two surfaces approach very close distance (~ 1 nm) the continuum theories breaks down and other non-DLVO theory emerges where the interaction force could be either attractive or repulsive or oscillatory which are very sensitive to the shape of the solvent molecules. It also depends on the nature of the surface such as hyrophilicity or hydrophobicity, smooth or rough, amorphous or crystalline etc.

1.5.2.3.1 Oscillatory interaction

DLVO theory of van der Waals and electric double-layer interaction are continuum theories which are described in terms of the bulk properties of the intervening medium such as density ρ, refractive index n, and dielectric permittivity. The oscillatory force was proposed by Derjaguin and Kussakov [65] who assumed that the liquid layer at the interface is different from the bulk. When distance between two surfaces is below a few molecular diameters, the interface experiences a force that arises due to adsorption of solvent molecules on the surface. At very short separation, the layered structure of solvent molecules is influenced by the other surface as a result number density of solvent molecules changes at the interface which gives rise to a force that varies periodically with distance whose periodic length equals to the thickness of the solvent layer. The magnitude of periodically varying force decreases with increasing distance which was calculated using contact value theorem. The force between two similar parallel walls is expressed as

$$f_{osc}\,(x) = f_0 \cos\left(\frac{2\pi x}{d_0}\right) e^{-x}/_{\lambda} \qquad (1.38)$$

where f_{osc}(x) is the solvation force per unit area at a distance x, decay exponentially with a characteristic decay length (λ). The cosine part ensures the force oscillates with distance and exponential part ensures that the force decay rapidly and happens only at short distance.

In addition to the simple molecules, the oscillatory force also occurs in complex liquids such as micelle, lamelle etc whose structures are observed at different length scale. In case of surfactant or lipid solution two different scales are observed: One is due to structure of solvent molecules and other is due to structure and thickness of complex macromolecule. The confinement of such complex macromolecular structures gives rise to oscillatory force that depends on the length scale of the macro structure instead of solvent molecules. The decay length and period of oscillation of such force gives information about the supramolecular structure.

1.5.2.3.2 Hydration interaction

It is a short range force that operate between surfaces or colloids at very small distance that could explain the unexpected stability of particle in high salt media [26], soap films, swelling of clay, interaction of biological membrane etc. Hydration force was proposed based on the experimental observation of swelling of clay and enhanced stability of silica and other dispersion at high salt concentration where the surfaces or particle are supposed to aggregates or coagulate in highly adhesive form according to DLVO theory. The hydration force, in general, can be described by a function as

$$W(D) = W_0 \exp(-\frac{D}{\lambda}) \tag{1.39}$$

where D is the distance between the surface and λ ranges from 0.2 - 10 nm and W_0 depends on the hydration of the surface that usually lies between 10^{-3} – 10 N m^{-1}.

Numerous theories were proposed to explain the observed hydration phenomenon. They were based on the assumption that the structure of water molecule at the surface is different from the bulk. Marcejia and Radic [66] assumed that water molecules are in direct contact with the surfaces are fixed and oriented preferentially which is coupled to the adjacent water molecules. But, later on Cevec et al. [28] used a different approach based on effective orientation field which could change the ordering of water molecules when surfaces comes very close distance rather than fixing the order of water molecules. Such change in the orientation and immobilization of water molecules due to an electric field was observed experimentally and computed using simulation. The force per unit area of the surface was given by

$$f_{hyd} = \frac{E_0^A}{2\lambda_h^{cor}} \frac{1}{cos^2\,(\frac{x}{\lambda_h^{cor}})} \tag{1.40}$$

In the limit of large distance x >> λ_h^{cor}, the force profile follows exponentially decaying function.

1.5.2.3.3 Hydrophobic interaction

The concept of hydrophobic interaction was put forwarded to explain the low solubility and strong attraction that is followed by formation of aggregates between hydrophobic moieties such as hydrocarbon or fluorocarbon chain in aqueous phase. At microscopic level, it plays an important role in determining the protein folding, formation of lipid bilayer and micelle due to surfactant and polymers etc whereas in macroscopic level, the effect can be visualized when mixing oil and water that always results in phase separation due to very large interfacial tension and sudden attraction of hydrophobic surfaces in water.

Evidence for hydrophobic interaction was first given by Israelachvili and Pashley [27] who showed exponentially decaying nature of strong attraction between hydrophobic surfaces in water. Two component of hydrophobic interactions were observed which are described by an exponential function as

$$f(x) = C_1 e^{-x/\lambda_1} - C_2 e^{-x/\lambda_2} \tag{1.41}$$

where the first exponential function is short ranged (1- 2 nm) and the second exponential function is long ranged (100 nm) and the constants (C_l and C_2) are depends on the preparation of surfaces and experimental conditions. Similar to hydration force, different theories were put forwarded to explain the observed hydrophobic behavior. The structure of water molecules at the hydrophobic surfaces is different from bulk and when two surfaces approach closer together, the surface layer overlap and attract each other at very short distance which could explain the short range attraction.

1.6 Magnetic Colloids

Magnetic colloids are suspension of ferro or ferrimagnetic particle, such as Fe_2O_3 or γ - Fe_2O_3, in the size range of 5 – 20 nm that exhibit both liquid and solid property [67]. To prevent aggregation they are functionalized with a surfactant or polymer. They are capable of undergoing reversible phase transformation from fluid to visco-elastic solid by aggregating or self-assembling in the presence of external magnetic field due to dipole-

dipole interaction among the magnetic particle. The field driven structure of the magnetic fluid enable one to manipulate their optical, rheological and thermal properties [68, 69]. Besides, it can also be tailored by suitably functionalizing them with stimuli responsive moieties for real time applications and hence they are classified as smart nanofluids [70]. The dipolar interaction of the ferrofluid results in the formation of linear one dimensional chain like structures in the direction of magnetic field. At higher field strength, lateral coalescence of the chain leads to zippering effect [71] where a strong modification in rheological [72] and thermal properties of the ferrofluids [73, 74] are observed. Because of their tunable optical properties they are exploited for various applications such as magneto-optical wavelength filter [75], sensing [76, 77], device cooling [78, 79], bio-medicine [80, 81], tunable grating [70] etc.

1.6.1 Theoretical background of magnetic colloids

The dispersed magnetic nanoparticles are under Brownian motion with a zero net magnetic moment in the absence of a magnetic field. But, in the presence of magnetic field, they acquire magnetic moment $m = \frac{4}{3}\pi {R_h}^3 \chi H_0$ where R_h is the radius of the particle, χ is the susceptibility and H_0 is the magnitude of external magnetic field that causes the particle to align along the direction of the field with increased anisotropy interaction between two particle as $U_{ij}\left(r_{ij}, \theta_{ij}\right) = \frac{m^2\mu_0}{4\pi}\left(\frac{1-3cos^2_{ij}}{r^3_{ij}}\right)$. The field induced structure evolves when magnetic energy between the particles exceeds that of thermal energy which is expressed in terms of coupling constant $\Lambda = \frac{\pi\mu_0 d^3\chi_2 H_0^2}{72K_bT}$. Only when $\Lambda > 1$, magnetic particle self assemble to form various structure.

1.7 Magnetic nanoemulsion

Magnetic nanoemulsion is a class of magnetic colloids, which is a dispersion of magnetically polarizable oil droplets (droplets containing magnetic particle) in water. Similar to ferrofluid they undergo field driven self assembly when dipole attraction due to magnetic particle inside the oil droplets balances with repulsive force due to adsorbed surface moieties over the droplets that results in significant change in optical properties, which were exploited for real time applications such as cation sensors [82], defect detection [76], glucose sensor [83], urea sensor [84], alcohol sensor [85] etc.

1.8 Motivation of the current work

Though various stabilization techniques are used to obtain colloidal dispersions with an extendable shelf life, each method has its own advantages and disadvantages. Electrostatic stabilization is very sensitive to ionic strength and solvent conditions. In general, polymer or polyelectrolyte based stabilization is widely used in many products to achieve the effective steric or electro-steric repulsive forces. In addition, these macromolecules also act as rheological modifiers to achieve the desired viscosity and flow behavior. Though the above approaches are adopted by industries, a proper scientific understanding of the interaction mechanism of macromolecules especially polyelectrolyte's at interface is still lacking. Such an understanding is absolutely essential to produce durable product formulations with an extended shelf life. Though the formulations with a superior stability are made by industries by using various stabilizing entities and their combination, the know-how is secretly guarded by them due to commercial interest. As a result there are little details available in open literature.

In addition to this, the behavior of polyelectrolyte under various environmental condition is fundamentally important to understand the natural process such as protein folding, DNA condensation, etc. Interestingly, the adsorption of polyelectrolyte at liquid-liquid interface mimics in vivo condition of charged macromolecule at cell-fluid interface and hence is very important to understand the biological phenomenon. They are technologically important because of numerous applications in areas such as microcapsule [86], drug delivery [87], lubrication [88], pH gated ionic channel [89] etc. Therefore, an understanding the behavior of polyelectrolyte adsorbed to a surface or interface is important for stabilization of emulsion based products as well as fundamental understanding of biological macromolecules.

Though systematic studies on the behavior of polyelectrolyte under various physicochemical conditions in solution and at surface were carried out, using surface force apparatus [88, 90], quartz crystal microbalance [91, 92], atomic force microscopy [93], total internal reflection microscopy [94, 95], the fundamental understanding of polyelectrolyte behavior at the liquid-liquid interface at various physio-chemical condition is not explored, though very important for improving the shelf life of colloidal products and surface functionalization. The characteristics of the polyelectrolytes at interfaces are least understood as compared to their behavior in the bulk**.** The direct force measurement techniques were used to study the conformational transition of the adsorbed functional moieties at solid surfaces, other indirect techniques such as nuclear magnetic resonance [96] , vibrational sum frequency [97, 98] small angle neutron scattering [99, 100] were also used to get insight into the molecular properties of the adsorbed polymer under various physio-chemical conditions. The interaction forces measured in the above force measurement techniques are between solid surfaces whereas the present study focus on magnetic chaining technique (MCT) [17, 101, 102] which is capable of measuring interaction forces between molecules adsorbed over tiny emulsion droplets suspended in a fluid as a function of interdroplet distance. The capability of the present approach in measuring weak repulsive forces between nanodroplets < pN, within 0.2 nm spatial resolution (i.e. inter particle distance) is exploited to probe polyelectrolyte driven repulsive interaction and conformation changes [103].

1.9 Objective

The objectives of the present work are:

- ✓ To study the effect of temperatures and surfactant concentration on the neutral thermo-responsive polymer at the oil-water interface and the resultant colloidal stability.
- ✓ To understand intermolecular interaction due to weak polyelectrolyte at different environmental conditions (such as pH, ionic strength) and molecular weight.
- ✓ To understand intermolecular interaction due to strong polyelectrolyte at different environmental conditions (such as pH, ionic strength) and compare its behavior with that of weak polyelectrolyte.
- ✓ To understand the role of protein into emulsion stabilized with a weak and strong polyelectrolyte at different solution pH.
- ✓ To develop a new simple strategy to detect biological analyte, urea and physio-chemical parameter pH and temperature using magnetic nanoemulsions functionalized with different surface active molecules and explore the interaction mechanisms involved.

1.10 Thesis Overview

Thesis consists of eight chapters. **Chapter 1** concerns the introduction to soft matter, classification and preparation methods of specific soft matter systems. The importance of interaction force and the theory of intermolecular interaction are detailed briefly. **Chapter 2** deals about the material and characterization tools used in the present work. Preparation of ferrofluid, ferrofluid emulsion and techniques used to characterize the materials are discussed in detail. **Chapter 3** deals with multi-stimuli responsive nanofluid using thermo-responsive polymer, Poly(N-isopropylacrylamide) – PNIPAM and superparamagnetic nanoparticle. The role of temperature and anionic surfactant of different concentration over intermolecular interaction due to PNIPAM is studied. The change in Bragg spectra at different temperature and anionic surfactant concentrations for PNIPAM stabilized emulsion is studied and the results are compared with intermolecular force measurement and phase contrast optical microscopy image. **Chapter 4** deals with understanding the conformational change of adsorbed weak anionic polyelectrolyte, poly(acrylic acid) - PAA under different environmental changes. The Bragg peak variation and intermolecular force are measured at various pH and salt of various concentration, valance and molecular weight. The swelling and collapse of the adsorbed weak polyelectrolyte under various conditions is compared with the theoretical models. The study shows that the coil to extended transition cannot be observed for PAA of molecular weight < 16.5 kg/mol. **Chapter 5** deals with the studies on a strong polyelectrolyte, poly(diallyldimethylammonium chloride) - PDDA under different environmental conditions and comparison of its behavior with that of weak polyelectrolyte, PAA in the same physiological conditions. Light scattering measurement confirms the presence of a strong and weak polyelectrolyte at emulsion droplets. The change in Bragg peak shift from emulsion stabilized with strong and weak polyelectrolyte was found to affect the conformational change of adsorbed polyelectrolyte and the results are compared with intermolecular force measurement. **Chapter 6** study the role of protein, Bovine serum albumin (BSA) in the selective replacement of adsorbed polyelectrolyte at emulsion interface by BSA. Further, this study shows that protein induces competitive displacement of the adsorbed weak polyelectrolyte at the oil-water interface at different solution pH conditions. A similar competitive displacement was noticed when the interface was decorated with a strong polyelectrolyte (PDDA) followed by competitive adsorption of protein at the oil-water interface. The study shows that irrespective of the nature of polyelectrolyte, whether the adsorbed polyelectrolyte is anionic or cationic, strong or weak with low or high charge density, the added protein molecules displaces the adsorbed polyelectrolyte and occupy the interface. **Chapter 7** deals with some interesting applications of nanoemulsion stabilized with macromolecules. Two different applications were developed using magnetic nanoemulsion by changing the functional groups. First application deals with a urea sensor, using functionalized magnetic nanoemulsion. A highly sensitive and selective detection of urea was exposed by using emulsions decorated with the charged surfactant, neutral and charged macromolecules. The response of the magnetic nanoemulsion to urea is studied by looking at the Bragg peak wavelength changes. The result shows the possibility of selective urea sensing for a wide range of concentrations. Second application concerns the development of temperature and pH sensor using magnetic nanoemulsion that was stabilized with a neutral di-block copolymer and weak polyelectrolyte, independently. The change in Bragg peak shift showed a linear response for temperature even at different pH level, when emulsion is stabilized with a neutral macromolecule and a linear response to pH when emulsion is stabilized with an annealed polyelectrolyte at various temperatures. This study showed a new platform for rapid sensing of temperature and pH, using magnetic nanoemulsion, with appropriate macromolecular functional groups. **Chapter 8** concludes the results of this work and highlights the important findings from all the chapters and suggests the possible future work.

CHAPTER 2

Materials and Experimental Methods

2.1 Materials

2.1.1 Polymers and polyelectrolytes

The neutral polymers used in this study are thermo-responsive polymer, poly(N-isopropylacrylamide) - PNIPAM of average molecular weight 23 kg/mol, di-block copolymer, poly(vinyl alcohol-co-vinyl acetate) - (PVA-vac) of average molecular weight 155 kg/mol and triblock copolymer, poly(ethylene oxide)-poly(propylene oxide)-poly(ethylene oxide) - (PEO-PPO-PEO) of average molecular weight 14.6 kg/mol. The polyelectrolytes used in this study are poly(acrylic acid) - PAA of average molecular weight 15, 250 and 450 kg/mol, poly(diallyldimethylammonium chloride) – (PDDA) of average molecular weight < 100 kg/mol and bovine serum albumin - (BSA) of average molecular weight 66.7 kg/mol. All polymers and polyelectrolytes were obtained from Sigma-Aldrich and used without purification. The molecular structure of the polymers and polyelectrolytes are shown in the **Figure 2.1.**

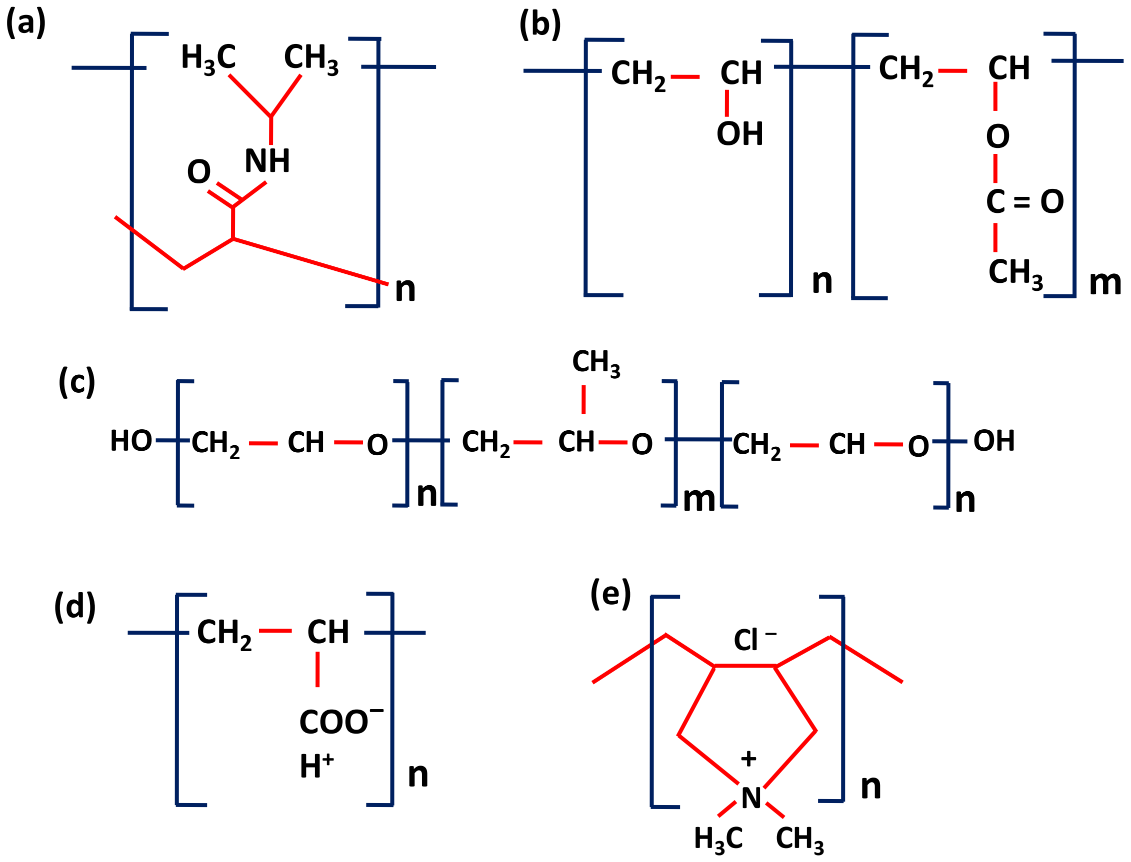

Figure 2.1: Molecular structure of neutral polymers (a) PNIPAM (b) PVA-vac (c) PEO-PPO-PEO and charged polymers (d) PAA and (e) PDDA

2.1.2 Surfactants

Surfactants used in the present study are sodium do-decyl sulphate (SDS), nonyl phenol ethoxylate (NP-9) and oleic acid. They were obtained from sigma-aldrich and used without further purifications. The molecular structure of the surfactants are shown in the **Figure 2.2**

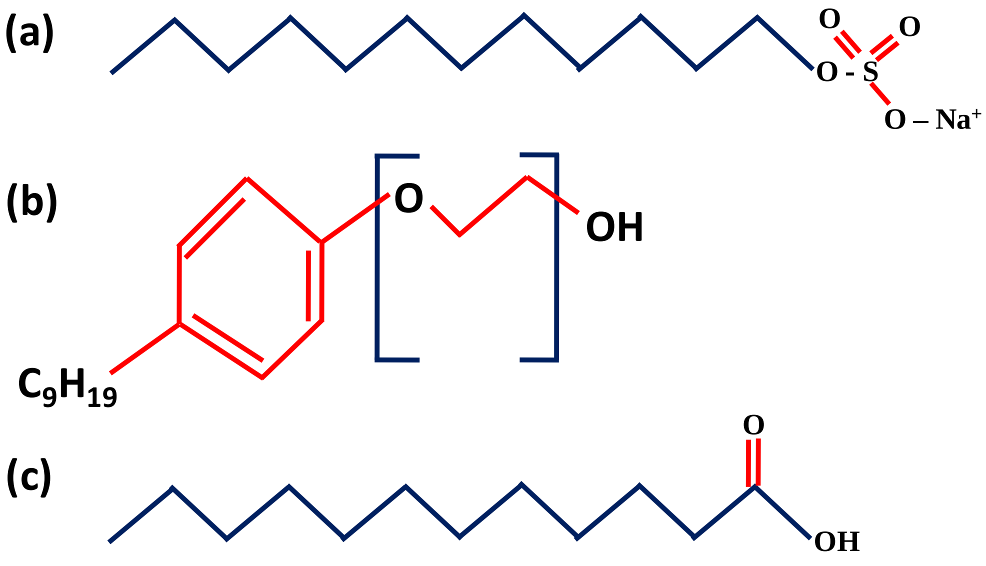

Figure 2.2: Molecular structure of (a) SDS (b) NP-9 and (c) oleic acid.

2.1.3 Salts

Salts used in the present study, sodium chloride (NaCl), calcium chloride ($CaCl_2$), ferric chloride ($FeCl_3·6H_2O$) and ferrous sulphate ($FeSO_4·7H_2O$), are GR grade with 99 % purity. Sodium borate or borax ($Na_2B_4O_7.10H_2O$) was obtained from Agros Organics. The salts were used as such without further purification.

2.1.4 Urea

Urea of average molecular weight 60.06 g/mol was obtained from Merck and also used without further purifications.

2.2 Ferrofluid preparation

Non-aqueous ferrofluid i.e. oleic acid stabilized magnetic nanoparticle dispersed in octane, is prepared through co-precipitation technique [104]. In the present study, the magnetite nanoparticles are prepared by precipitating iron salts (0.8 M $FeCl_3.6H_2O$ and 0.4 M

$FeSO_4.7H_2O$) in acidic medium [104-106]. The iron salt solution were mixed in 1:1 ratio under a constant stirring rate and the solution pH was increased rapidly to 10 by adding ammonium hydroxide till the resultant solution turns black (indicating the formation of magnetite particle). The resultant mixture is digested for 30 minutes, followed by the addition of oleic acid. In order to coat the magnetite particle completely, the solution pH, stirring rate and temperature are maintained constant for another 30 minutes. The vigorous stirring is done to prevent the coagulation of particle. The obtained particles were separated from the dispersion by adding dilute hydrochloric acid. The oleic acid coated particles is collected and washed with water repeatedly till pH of the dispersion reaches 7. After removing the excess ionic salt impurities, the sample is vacuum dried. The resultant oleic acid coated magnetite nanoparticle is dispersed in octane.

2.3 Characterization techniques

2.3.1 Powder X-ray diffraction (XRD)

XRD is a powerful technique, used to obtain the crystal structure, unit cell dimension etc. As the wavelength of X-ray (λ_{XR}) is comparable to the dimension of the atoms, arranged orderly in the crystal, this technique is used to explore the structure of crystalline materials [107]. The basic system comprised of X-ray source, a sample stage, detector and a method to vary θ. The fundamental working principle of XRD is based on the constructive interference between monochromatic X-rays scattered from periodic array of the crystal structure that results in the formation of Bragg peak where the crystalline lattices acts as a three dimension diffraction grating. Cathode ray tubes are used to generate X-rays, which are filtered to obtain monochromatic radiation, collimated and directed to the sample. The interaction of X-ray with the sample results in constructive interference that gives rise to a Bragg spectra, when it meets Bragg's diffractive condition, which relates the interplanar spacing (d_{int}) in a crystalline powder to wavelength (λ_{XR}) of X-ray and angle of diffraction (θ) through $n\lambda_{XR} = 2d_{int}sin\theta$. The strength of the diffraction is quantified through intensity of diffraction maximum. The average crystallite size of the crystal is obtained from peak broadening of the diffraction pattern using Scherer's equation, $B\,(2\theta) = \frac{(K_{sf}*\lambda_{XR})}{(FWHM*cos\theta)}$, where K_{sf} is the crystallite shape factor (whose value is 0.9 for spherical particle) and FWMH is the full width at half maxima of the maximum intensity peak. By analyzing the diffracted X-ray, at all possible angle by rotating the sample, the information of the crystal structure of the material is obtained. In the present study, powder XRD pattern is obtained by using a Rigaku Ultima IV that uses Cu-K_α radiation (λ_{XR} = 1.5416 Å) and record the diffraction pattern in the 2θ range between 20 and 80^0 by varying θ but keeping λ_{XR} fixed. Data acquisition was obtained using PDXL software.

2.3.2 Fourier transforms infrared spectroscopy (FTIR)

FTIR is a non-destructive technique for characterization of materials where the intensity of infrared wavelength of the light absorbed by the molecule as a function of its frequency that is used for determining organic and inorganic materials [108]. The absorbance of IR radiation by a substance happens only when the frequency of the light matches with the vibration or rotation frequency of the molecule. High signal-to-noise ratio, wavenumber precision and multiplex (many scans accomplished in a short period of time) are some of the advantage of FTIR over infrared spectrometers. It is an extension of IR spectroscopy where the additional part includes interferometer which was developed to overcome limitations such as slow scanning process.

The major optical component of FTIR is the interferometer, IR radiation source and a detector. The most commonly used interferometer in any FTIR instruments is Michelson interferometer which consists of beam splitter and mirror. The broad spectrum of IR radiation is collimated and passed into the interferometer and the resultant interferogram signal is passed to the sample which absorbs radiation of certain wavenumber that is measured using a suitable IR detector. The interferogram signal from the sample is decoded into individual frequencies via a well-known mathematical technique called the Fourier transform and then presents the user with the desired spectral information for analysis.

FTIR can be analyzed only for heteronuclear molecules that posses a permanent dipole moment, unlike homonuclear diatomic molecules such as H_2, O_2 where there is no permanent dipole moment change and therefore no absorption of IR radiation. Since no two compounds give the same infrared spectrum, this technique is a finger print of a material. An important advantage of FTIR spectroscopy is that samples of any form such as solid, liquid, air, paste, and film can be studied. Since FTIR is a single beam instrument that measures the background spectrum comprised of water vapor and CO_2 and therefore the spectrum of the sample is obtained by subtracting the obtained spectrum with the contribution due to background spectrum. In the present study, ABB Bomem MB 3000 FTIR spectrometer that produces wavenumber in the range of 400-4000 cm^{-1} with a spectral resolution of 4 cm^{-1} is used.

2.3.3 Thermogravimetric analysis (TGA)

TGA is primarily used to measure change in mass of the substance as a result of decomposition, oxidation or structural transitions as a function of temperature or time under definite and controlled atmosphere of argon or oxygen or nitrogen etc. It can also be used to determine the compositional, thermal and oxidative stabilities of the materials. The basic instrumentation part consists of a sample pan that resides inside a furnace which is programmed to increase temperature linearly with time, where mass of the substance is measured using precision balance under heating or cooling. In the present study, Mettler Toledo TGA-DSC-1, 1100 LF system that operates in the temperature range of 30-1000 ^{0}C with a heating rate of 10 °C/min is used. It gives information about the concentration of nanoparticle from the weight loss profile with temperature.

2.3.4 Vibrating sample magnetometer (VSM)

VSM operates on the principle of Faraday law of induction (i.e. changing magnetic field generates an electric field), in order to measure the magnetic property of the material such as magnetic moment, blocking temperature, susceptibility etc. The instrumentation part comprised of water cooled electromagnet, sample vibrator, sensor (pick-up coil), hall probe and amplifier.

The measurement is carried out by keeping the sample in between the pole pieces of the magnet that produce a constant magnetic field that align the dipole moments or spins of the sample in the direction of magnetic field. Larger magnetic field produces higher magnetic moment in the sample which creates a stray magnetic field around it. As the sample connects to the vibrating exciter that oscillates up and down periodically with relative to a pick-up coil at a definite frequency, the oscillation of the sample changes the magnetic stray field. The change in magnetic field gives rise to an induced electric current that is sensed and collected by the pick-up coils. The magnitude of the induced current is proportional to the magnetization of the sample which is amplified by the trans-impedance amplifier. Lock-in amplifier is employed to collect the signal that is oscillating at the vibrating frequency of the sample and ignore all other stray noises from the environment. In the present study cryo-free VSM (Cryogenics Ltd.), that operate in the field range of ± 2.0 T, is used for magnetic measurements.

2.3.5 Transmission electron microscopy (TEM)

It is one of the important microscopy technique used to probe the structural features of specimen in nano range, posses very high resolution than conventional optical microscope. Unlike optical microscopy, TEM uses high energetic electrons to image the specimen under a high vacuum condition. Since the wavelength of electron is much shorter than the wavelength of visible light, the electron microscopy allows one to investigate the smaller structural features in nano region such as particle size, morphology, crystal structure, chemical composition etc.

The basic features of a TEM consist of source (electron emitter) that could be a tungsten or lanthanum boroxide, three stages of lenses (condenser, objective and projector) and detector. In TEM, high energetic electron beam is accelerated and collimated into small, thin and coherent beam that are projected onto the specimen via condenser lenses. The objective lenses focus the transmitted beam of electron comes from the sample to form an image and the projector lenses expand the beam onto the imaging screen.

When highly energetic electron beam strikes a thin specimen, scattering (elastic, inelastic) and unscattering (transmittance) of electron occurs. The image is formed through the transmitted beam of electrons and the intensity of transmitted electrons is inversely proportional to the thickness of the specimen under investigation. For thicker specimen, lesser electrons are transmitted, therefore the image appear darker and vice-versa. Elastically scattered electrons are collimated (using magnetic lenses) to form the diffraction pattern that contains the crystal structure details of the specimen such as atomic arrangements and phases. In the present study, TEM investigation is carried out using JEOL 2100 high resolution TEM with an acceleration voltage of 200 kV. The sample preparation is carried out by placing a drop of the magnetite dispersion on a carbon coated copper grid (0.3 cm diameter, mesh size of 200 holes/cm) and left it to dry overnight at room temperature.

2.4 Preparation of ferrofluid emulsion

Oil-in-water nanoemulsions were prepared by classical inversion method where water containing anionic surfactant (SDS) and octane containing oleic acid coated Fe_3O_4 nanoparticles of diameter ~10 nm were sheared at the rate of 1500 rpm using IKA homogenizer for 5 minutes [101, 102, 109]. The typical particle loading in the emulsion was about 10 wt%. After this process a polydisperse emulsion, containing droplet size in the range 0.1 to 1 µm, was obtained. By using fractionation approach[110] combined with magnetic separation, highly monodisperse emulsion with polydispersity less than 0.07 was obtained. Here, excess surfactant is added into the continuous medium to induce an attractive interaction between droplets to phase separate the smaller droplets from the larger droplets. The dilute phase is removed and the dense phase is diluted with surfactant solution further and the process is repeated several times to obtain a highly monodisperse emulsion. In the present study, emulsion with an average droplet size of 200 nm, stabilized with SDS, is obtained and schematic representation is shown in the **Figure 2.3**.

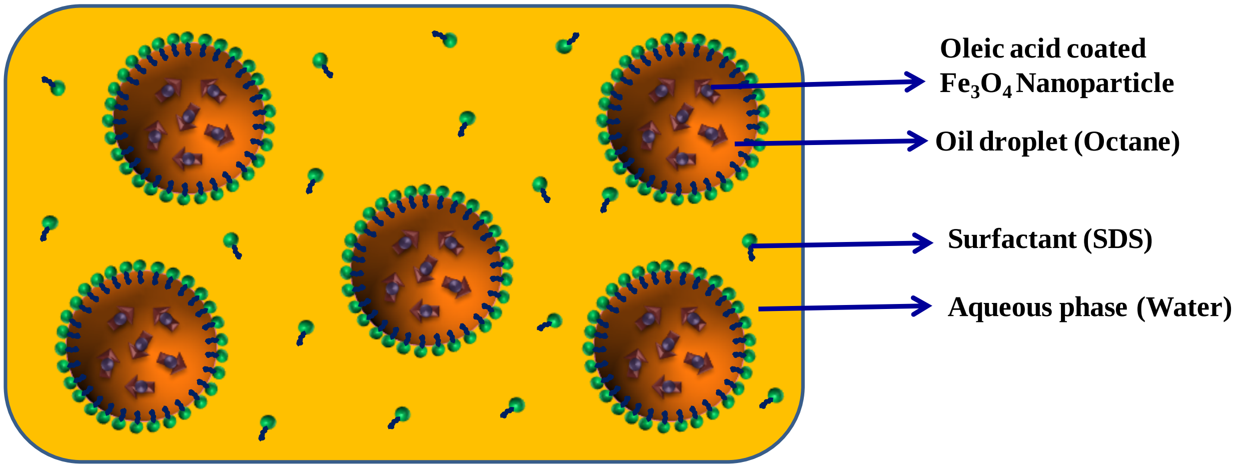

Figure 2.3: Schematic representation of ferrofluid emulsion in the absence of magnetic field

2.4.1 Polymer stabilized ferrofluid emulsion

To functionalize the emulsion with neutral polymers such as PVA-vac, PEO-PPO-PEO and PNIPAM, the concentration of SDS in the SDS stabilized emulsion is reduced by washing it with diluted SDS solution. A strong magnetic field is applied to phase separate the aqueous and organic phase. Every time, the aqueous phase containing excess surfactant was removed and replaced with polymer solution. This process was repeated 3 to 4 times to completely replace the surfactant molecules with polymer. Later, the emulsion was left for 3 days to equilibrate [43, 101, 102, 109, 111, 112].

2.4.2 Polyelectrolyte stabilized ferrofluid emulsion

To stabilize the emulsion with polyelectrolytes (PAA, PDDA and BSA), the SDS stabilized emulsion was initially washed with a lower concentration of SDS (CMC/10), and then with a non-ionic surfactant, nonyl phenol ethoxylate (NP-9). The pH of the emulsion was decreased to neutralize the residual surface charge that is followed by adding polyelectrolyte of required concentration to the emulsion. In the present study, PAA, PDDA and BSA of 0.5 wt. % is added independently and the resultant mixture are left it for 3 days to equilibrate [18, 113, 114].

2.5 Characterization of ferrofluid emulsion

2.5.1 Dynamic light scattering (DLS)

DLS is also known as quasi elastic light scattering or photon correlation spectroscopy, which is a non-destructive technique used to measure the hydrodynamic size of molecules and particles dispersed in a base fluid [115]. It is a homodyne approach that measures the similarity between scattered light intensity from the Brownian motion of the particle at a very short period of time using an autocorrelator. The intensity of the scattered light is completely in phase with each other in the beginning where the autocorrelation function is maximum but later on the scattered light intensity becomes out of phase, which reduces the autocorrelation function.

The measured intensity normalized time correlation function is given by

$$g^2\,(t) = \frac{I\,(t) I\,(t+\delta t)}{I\,(t)^2}, \tag{2.1}$$

where, I(t) is the scattered intensity at a time t and I (t+δt) is the scattered intensity recorded after a small time interval δt which is related to the normalized electric field correlation function, $g^{(1)}\,(t)$ via Siegert's relation,

$$g^{(2)}(t) = 1 + \beta \mid g^{(1)}\,(t) \mid^2 \tag{2.2}$$

where, β is (a constant) characteristic of the instrument, approximately close to one. For monodisperse particles, $g^{(1)}\,(t)$ is a single exponential function given by

$$g^{(1)}\,(t) = exp(-t/\tau) = exp(-D_t q^2 t), \qquad (2.3)$$

where τ is the relaxation time ($\tau = {}^{1}/_{q^2 D_t}$), q is the wave vector of the laser light and D_t is the diffusion coefficient of the dispersed phase. The homodyne correlation function is an exponentially decaying function of time with a time constant τ, from which D_t is obtained. According to Einstein relation, D_t of the particle is related to viscosity of the solvent (η) through stokes approximation (ζ) as

$$D_t = {}^{k_b T}/_{\zeta} \qquad (2.4)$$

which is expressed as $\zeta = 6\pi\eta H_D$, where H_D is the hydrodynamic diameter of the particle.

2.5.2 Electrophoretic measurement

Zeta potential is a measure of potential at the shear plane of electric double layer for a colloidal dispersion, which is widely used to access the stability of colloidal dispersion [116]. The measurement is a heterodyne approach where the intensity of scattered and unscatterd light is combined to measure the particle electrophoretic mobility - U_E (the ratio of migration of velocity component of the particle to the electric field in a given medium).

The measurement was carried out by applying an electric field to liquid medium containing suspended charged particles, such that they are attracted towards the electrode of opposite charge which is opposed by the viscous forces of the dispersing medium. When viscous and electric force on the charged particle are balanced, the particle attains a constant velocity U_E which is related to zeta potential of the suspended particle via Henry equation as, $U_E = \frac{2\varepsilon\zeta f(\kappa R_h)}{3\eta}$, where, ζ is the zeta potential, ε is the dielectric constant, η is the viscosity, κ is inverse Debye length, R_h is the radius of the particle and $f(\kappa R_h)$ is the Henry's function. In the present case, emulsion droplets are dispersed in aqueous water medium, therefore Smoluchowski approximation is used to obtain the zeta potential for which $f(\kappa R_h)$ takes the value of 1.5 whereas for particles in non-aqueous media, Huckel approximation is used where $f(\kappa R_h)$ becomes 1. Particles with zeta potential of greater than |30 mV| are considered to be a stable dispersion.

In the present study, zeta potential is measured using Malvern's Zetasizer-Nano where electrophoretic mobility of the particle is measured using combination of laser Doppler velocimetry and phase analysis light scattering (PALS) which allow one to get the zeta potential for particle with lower mobility with high precision.

2.5.3 Intermolecular force measurement

The intermolecular force measurement is carried out using a custom made force apparatus [102, 109]. It is used to measures weak forces in the range of 10^{-13} to 10^{-11} N, between nanodroplets as a function of distance. The setup comprised of solenoid controlled by a programmable power supply (Agilent Technologies—N5770A), fiber optic based spectrometer (Avaspec, Netherlands), a white light source and a program to compute the net force by taking into consideration of van der Waals and magnetic attraction due to dipolar interactions under a magnetic field. The measurement is performed by keeping the cylindrical glass cuvette containing small quantity (200 uL) of magnetically polarizable monodisperse emulsion inside a solenoid. The sample is illuminated with a white light through optical fibers and the resultant backscattered light is collected and send it to spectrometer which is processed through software AVA-SOFT. Detailed experimental setup and the functioning of intermolecular force measurement were discussed elsewhere [6, 102]. The schematic representation of the force setup is shown in the **Figure 2.4**.

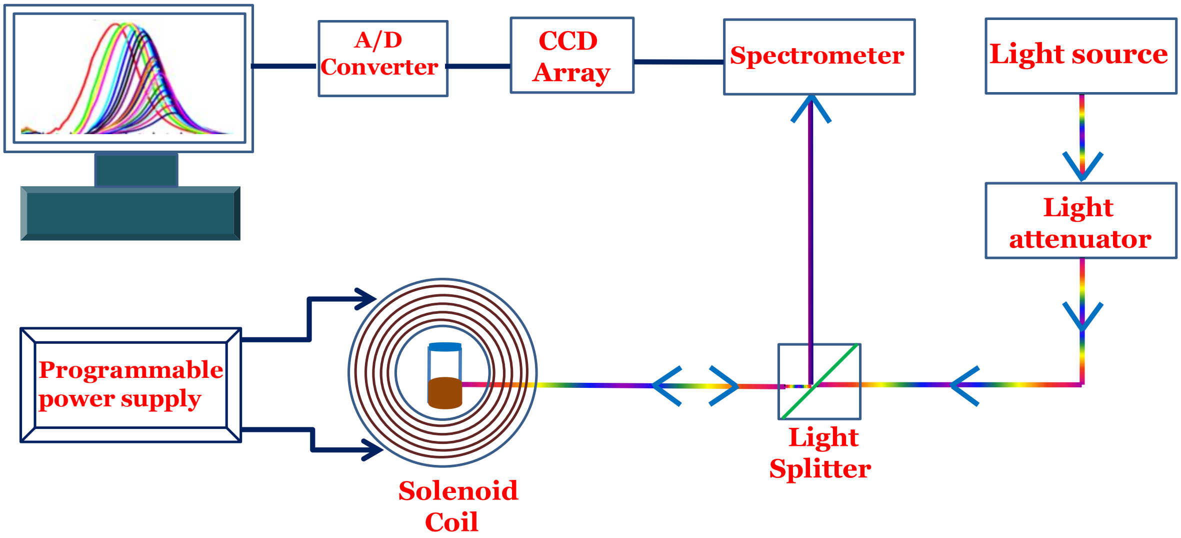

Figure 2.4: Schematic representation of intermolecular force measurement setup.

The interaction force measurement using Magnetic Chaining Technique (MCT) is quite different from the other force measurement techniques such as surface force apparatus, atomic force microscopy, optical tweezer, total internal reflection microscopy where the interaction forces are measured between solid surfaces or between solid and mesoscopic (colloid) surface. In the present force measurement technique, the interaction between molecules adsorbed over magnetically polarizable nanoemulsion droplets is measured as a function of droplet distance. This approach allows measurement of weak repulsive forces (less than a pN) between the nanosized droplets. Due to extremely smaller size of the emulsion droplets, they exhibit a large Laplace pressure and hence are non-deformable. By varying the magnetic field strength, the distance between the droplets are precisely measured.

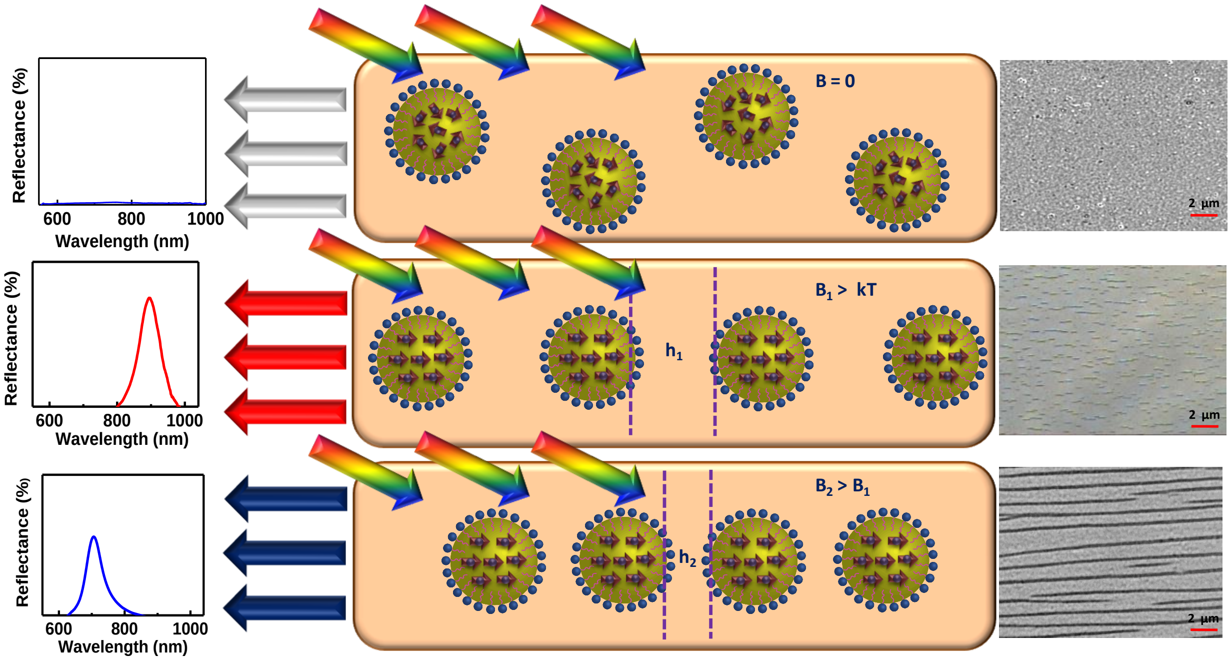

Figure 2.5: Schematic representation of ferrofluid emulsion, the corresponding phase contrast optical microscopy image and Bragg spectra under (a) Zero magnetic energy (b) Magnetic energy (B_1) > thermal energy and (c) At high magnetic energy ($B_1 > B_2$).

The principle of force measurement using MCT is briefly discussed here. The magnetic nanoemulsion is a dispersion of oil droplets, containing superparamagnetic nanoparticle in an aqueous phase. The oil droplets are covered with suitable molecules to prevent aggregation. The droplets are under Brownian motion with zero net magnetic moment, in the absence of magnetic field as shown in the **Figure 2.5 a**. When subjected to a magnetic field, they acquire magnetic moment and undergo disorder to order transition, leading to linear one dimensional (1-D) chains in the direction of applied magnetic field as shown in the **Figure 2.5 b**. With increasing magnetic field, the moment experienced by the droplet increases and hence the spacing between them decreases as shown in the **Figure 2.5 c**. The interdroplet distance (d) within the chain (1-D structures) is measured by shining the emulsion with a white light that results in the formation of Bragg peak spectra (in the visible wavelength ranges) due to diffraction of white light from the ordered structure. The distance between the droplets, with an accuracy of ± 0.2 nm, is obtained from the diffraction condition that is reduced to the first order limit, (d = ${}^{\lambda_{vis}}/_{2 * n}$), where λ_{vis} and n are the wavelength of light and refractive index of the medium, respectively.

The formation of 1-D structure is due to the balance between attractive (due to magnetic nanoparticle and van der Waals) and repulsive forces (due to adsorbed moieties over oil droplets). The attractive force due to magnetic nanoparticle within the chain is given by [117]:

$$F_{chain} = -\sum_{n=1}^{\infty} n \ \frac{6m^2}{(nd)^4} = -\ \frac{1.202}{2\pi\mu_0}\frac{3m^2}{d^4}, \qquad (2.5)$$

where m is the magnetic moment, d is the interdroplet distance, μ_0 is the magnetic permeability of free space. The magnetic moment of the particle is expressed as

$$m = \mu_0 4\,\pi R_h^3 \chi_s H_T/3 \qquad (2.6)$$

Here, μ_0 is the magnetic permeability of free space, R_h is the droplet radius and H_T is the total magnetic field acting on each drop which is sum of external (H_{ext}) and field induced from the magnetic moment of all neighboring droplets in the chain (H_{int}) i.e,. $H_T = H_{ext} + H_{int}$. Here, the internal field, H_{int}, is expressed as

$$H_{int} = 2\sum_{n=1}^{\infty}\frac{2m}{(nd)^3} = 4\,\zeta(3)\,\frac{m}{d^3} \qquad (2.7)$$

The attractive van der Waals forces for spherical particles of diameter 2a is given by

$$F_{vdw}^{att}\,(d) = \frac{AR_h}{12\,(d-2R_h)^2} \tag{2.8}$$

where A_H is Hamaker constant. By making use of the magnetic and van der Waals attractive force equations, the repulsive force between the emulsion droplets for every interparticle spacing is computed. From the attractive component of the forces, the repulsive force component for every interparticle spacing is calculated, by balancing the force equation.

2.5.4 Phase contrast optical microscopy

It is an important light microscopy technique, invented by Frits Zernike in 1932, which allows one to view the transparent and biological specimens by enhancing the contrast of the object by making use of phase shifts in the light passing through the specimen which is converted into amplitude or contrast changes in the image. It helps to see the living object which is difficult to observe in any ordinary light microscope.

The partially coherent beam of light from tungsten-halogen lamp is collimated and collected via collector lens that is passed through the specimen where some light diffracted with a phase difference of λ/4 and others go undeviated. The undeviated and diffracted light is collected and passed into phase plate (a circular plate, containing a groove which is filled with phase advancing or retarding substance) which further induce phase shift of λ/4. Therefore, the image formation through a lens is actually a two stage process where the undiffracted (zero order beam) and diffracted light is collected by the objective which is mixed at the rear focal plane by a phase plate where an extra phase difference is introduced that enhances the brightness of the image. The obtained image is further processed in the intermediate image plane, in order to obtain the phase contrast image that is viewed through an eyepiece. In the present study, the phase contrast optical microscopy is used to observe the order and disorder structures of magnetic nanoemulsion under varying magnetic field and temperature, using Leica DM IRM with a digital camera (JVC) and frame grabber card. The obtained images are processed using Leica Win software.

2.5.5 Capillary viscometer

It is used to determine the viscosity (resistance of the fluid) and hence the radius of gyration of the polymer (R_g) in a base fluid by measuring the time taken by a polymer solution to flow in a capillary of definite diameter and length. From the flow time of solution and solvent in the capillary, the relative viscosity is obtained as given by

$$\eta_r = \frac{t}{t_0}\frac{\rho}{\rho_0} \tag{2.9}$$

Here t, and t_0, are the flow time for solution and solvent and ρ and ρ_0 are density of solution and solvent. The R_g of the polymer in a solution is obtained by first calculating the intrinsic viscosity of the solution which is obtained from the relative viscosity (η_r) and specific viscosity (η_{sp}) of the solution as given

$$[\eta] = \lim_{c\to 0}\frac{\eta_r - 1}{c} = \lim_{c\to 0}\frac{\eta_{sp}}{c} \tag{2.10}$$

where the relative velocity is the ratio of solution viscosity (η_s) to solvent viscosity (η) as $\eta_r = {}^{\eta}/_{\eta_s}$. The interpolation of η_{sp}/c at zero concentration gives intrinsic viscosity of polymer solution. The R_g of the polymer in a base fluid is obtained by calculating the intrinsic viscosity of the solution which is related to molecular weight and Avogadro's number through Einstein-Simha equation [118] as

$$R_h = (\frac{3*MW*[\eta]}{4*\pi*2.5*Na})^{1/3} \qquad (2.11)$$

Here, MW, [η], N_a are molecular weight, intrinsic viscosity and Avogadro number.

2.5.6 Transmittance of polymer solution

The transmittance study is carried out to estimate the lower critical solution temperature (LCST) of polymer solution. With varying temperature, the polymer solution changes from transparent to opaque due to aggregation of polymer. Here, the LCST is determined at the temperature which the transmittance decreases to 50 % during heating or cooling. The measurement is carried out by keeping the polymer solution in a rectangular cuvette which is irradiated with a beam of white light. At first, the transmittance of the reference solvent (water) is measured and then the measurement is carried out for polymer solution so that amount of light transmitted or absorbed by the polymer is obtained. Here, the transmittance is defined as the ratio of amount of light passes through the sample (I) to the original amount of light (I_0) which estimates the relative percentage of light passes through or absorbed by the sample. In the present case, the transmittance study was carried out using a fiber optic spectrometer (Avaspec, Netherlands) with a visible and near infrared light source that measures the fraction of incident light transmitted through the solution. The temperature was varied using a temperature controlled sample compartment (qpod TC 125, Quantum technologies) with a peltier base.

2.6 Characterization of oleic acid stabilized ferrofluid

The characteristics features of oleic acid coated magnetite nanoparticle (Fe_3O_4) dispersed in octane are shown in the **Figure 2.6**. X-ray diffraction (XRD) pattern of ferrite shows the presence of diffraction peak of (220), (311), (400), (422), (511), and (440) that are indexed to an inverse cubic spinel structure of Fe_3O_4 that consists of 1/3 tetrahedral and 2/3 of octahedral interstices (JCPDS file no. 19-0629) as shown in the **Figure 2.6a**. The average crystallite size was ~ 10 nm, obtained from the highest peak intensity of (311) plane [104]. The magnetization study at room temperature shows saturation magnetization of 53 emu/g (**Figure 2.6b)** [104]. The M-H profile shows superparamagnetism of Fe_3O_4 nanoparticle with zero coercivity and remanance. The adsorption of oleic acid on the Fe_3O_4 was confirmed from fourier transform- infrared spectroscopy (FT-IR) study. The formation of peak at 2921 and 2858 cm^{-1} are attributed to the asymmetric and symmetric stretching of methylene group of adsorbed oleic acid whereas the peak at 1458 cm^{-1} is due to asymmetric stretching of carboxylate group of adsorbed oleic acid. The presence of free oleic acid is confirmed through the formation of peak at 1728 cm^{-1}. The stretching of Fe-O bonds of Fe_3O_4 between octahedral and tetrahedral site is confirmed from the peak at 570 cm^{-1}. **Figure 2.6d** shows the weight loss as a function of temperature for oleic acid coated Fe_3O_4 in the range of 30-650 °C, where the weight loss of 25 % is attributed to the removal of functionalized oleic acid on the particle surface. The hydrodynamic diameter of oleic acid capped magnetic nanoparticle was obtained from dynamic light scattering (DLS) is 11 nm as shown in the **Figure 2.6e**, which is quite higher than the crystallite size obtained through XRD as the hydrodynamic size includes the particle size with functional molecules and hydration layers.

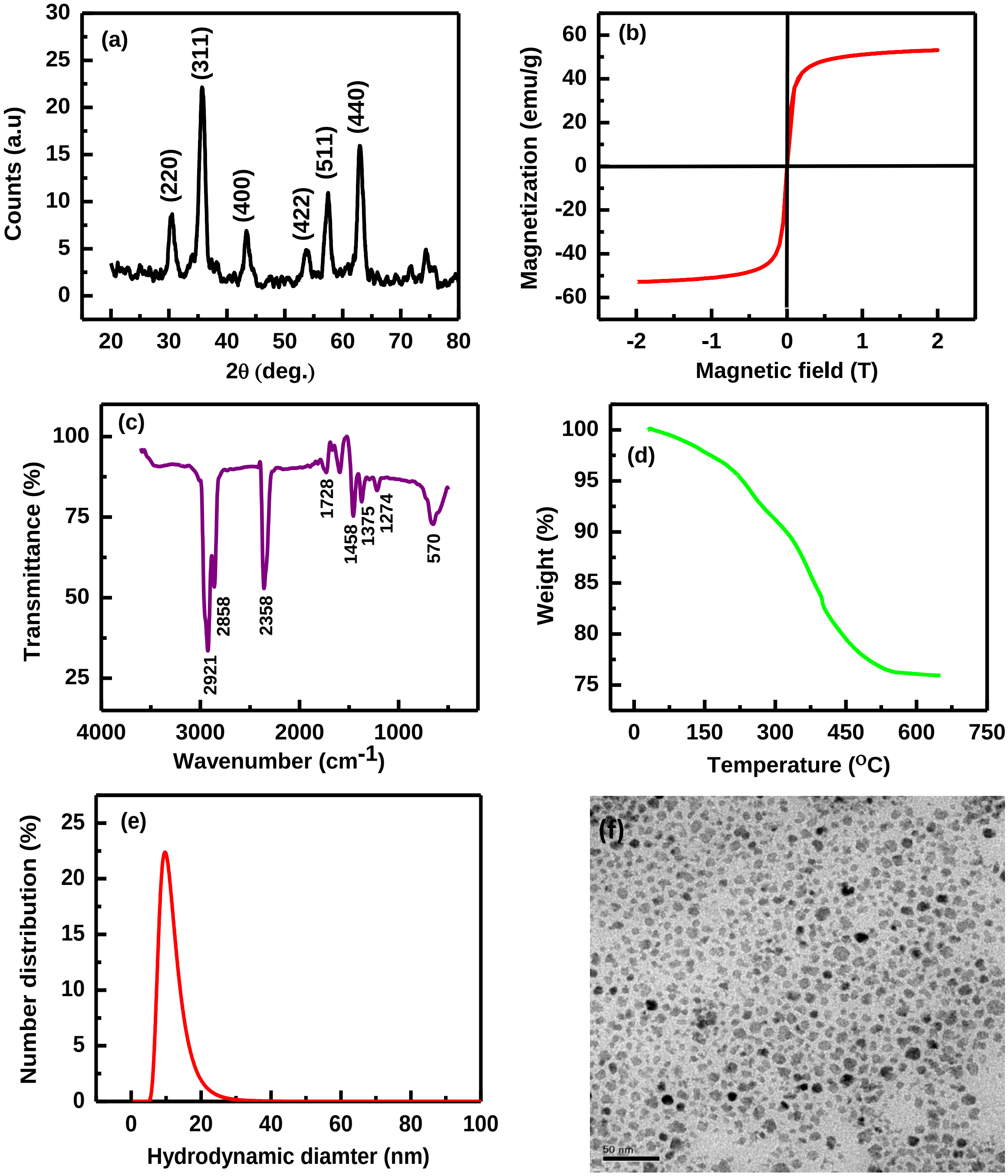

Figure 2.6: (a-d) XRD, VSM, FT-IR and TGA of oleic acid coated magnetic nanoparticle (e) hydrodynamic diameter of magnetic nanoparticle in octane (f) TEM image of magnetic nanoparticle.

The charged carboxylic group of the oleic acid is adsorbed on the magnetite surface through covalent bond whereas the hydro-carbon chain extends into the non-aqueous phase (oil) that gives stability to the fluid through steric interactions thereby preventing the aggregation of the particle through strong van der Waals interaction at lower particle spacing. TEM image of the ferrite is shown in the **Figure 2.6f.**

2.7 Characterization of ferrofluid emulsion through DLS and electrophoretic measurement

Emulsions stabilized with different functional groups were prepared by magnetic decantation process whose hydrodynamic size and zeta potential were measured using Zetasizer nano ZS (Malvern, UK). The obtained values are listed in **Table 2.1**.

Table 2.1: Details of sample with code and their hydrodynamic size, polydispersity and zeta potential as measured through light scattering and electrophoretic measurement.

Sample code	**Sample details**	**Hydrodynamic diameter (nm)**	**Polydispersity Index**	**Zeta potential at pH 7 (mV)**
E_{SDS}	Emulsion stabilized with 0.8 mM SDS	200	0.06	-50
E_{PNI}	Emulsion stabilized with 1 wt.% PNIPAM	255	0.07	-2
$E_{PNI-SDS}$	Emulsion stabilized with 1 wt.% PNIPAM + 2 mM SDS	255	0.07	-5

E_{PLURO}	Emulsion stabilized with 3.5 wt.% PEO-PPO-PEO	242	0.09	-1
E_{PVA}	Emulsion stabilized with 0.66 wt.% PVA-vac	255	0.1	-2
E_{PAA450}	Emulsion stabilized with 0.5 wt.% PAA (450 K)	275	0.2	-58
E_{PAA250}	Emulsion stabilized with 0.5 wt.% PAA (250 K)	260	0.15	-55
E_{PAA15}	Emulsion stabilized with 0.5 wt.% PAA (15 K)	230	0.08	-52
E_{PDDA}	Emulsion stabilized with 0.5 wt.% PDDA	255	0.1	+60
E_{BSA}	Emulsion stabilized with 0.5 wt.% BSA	230	0.09	-10

2.8 Conclusion

The details of the preparation of ferrofluid and ferrofluid emulsion through co-precipitation and high energy emulsification is discussed, respectively. The characterization techniques used such as X-ray diffraction, fourier transform infrared spectroscopy, thermo-gravimetric analysis, vibrating sample magnetometer, transmission electron microscopy, dynamic light scattering, electrophoretic mobility, phase contrast optical microscopy, capillary viscometer and transmittance study is presented. Results of the characterization of iron oxide nanoparticle are presented briefly. The details of magnetic chaining technique are also presented.

CHAPTER 3

Behavior of thermo-responsive polymers at the oil-water interface: Effect of temperature and surfactant concentration

3.1 Introduction

Responsive stimuli materials have been an area of interest in recent years due to their potential applications in smart valve or membrane, tunable optical properties of nanoparticle, metal ion sorption etc [119-124]. For most of these applications, the response of the material to a particular stimulus is achieved using suitable organic moieties. By introducing molecules or materials which respond to more than one stimulus, it is possible to fine tune the behavior of the material with multiple stimuli. Magnetic nanoemulsions are one such response-stimulus materials that has shown to have several interesting applications [76, 125].

The neutral polymers are widely used in the stabilization of dispersions as compared to charged molecules, due to its immunity to pH or ionic strength changes[126]. Poly(N-isopropylacrylamide), PNIPAM is one of the most widely studied systems owing to its thermo responsive behavior close to human body temperature, insensitivity to physio-chemical condition (e.g. pH) and resemblance to biological phenomena, especially protein denaturation. Further, they have a wide range of applications in analyte sensors [127], protein sensor [128], drug delivery [129, 130] and catalysis [131]. The ability of thermo-responsive polymer brushes to tune protein adsorption and cellular adhesion has been exploited in protein separations and tissue engineering [132].

PNIPAM is a water soluble temperature sensitive polymer with an amphiphilic nature due to hydrophilic amide group, hydrophobic carbon backbone and iso-propyl group. It undergoes a coil to globule transition above lower critical solution temperature (LCST) between 32 and 34 °C due to large conformational changes [133-136]. Below LCST, the polymer coil is highly hydrated and swells due to repulsive interaction between the segments. However, above LCST polymer coils are dehydrated leading to a collapsed state due to inter and intra segmental attractive interactions [137]. Studies showed that as the solvency condition changes from good to poor, the polymer chain length is decreased from $N^{3/5}\ to\ N^{1/3}$ [138]. A significantly reduced hydrogen bonding with the PNIPAM was observed above the LCST, resulting in a collapsed polymer conformation [139]. It was shown that the thermo-responsive nature of PNIPAM can be tuned with salt [140], surfactant [141, 142] and other biological molecules [143, 144]. In general, charged surfactants increase LCST due to its favorable interactions with the PNIPAM that favors swelling of the polymers due to increased electrostatic repulsion and inhibit LCST of the polymer-surfactant complex [145-147]. It is also observed that the incorporation of salts can lower the volume phase transition temperature.

Even though there are several studies on temperature induced transition of PNIPAM in aqueous solution using dynamic light scattering (DLS) [136, 148], fluorescence spectroscopy [134, 149] and in solid/water interface using surface force apparatus (SFA) [90], atomic force microscopy (AFM) [150-152] very few studies have reported on the behavior of PNIPAM at liquid-liquid interfaces upon application of temperature stimulus. As the conformation of macromolecules adsorbed at interfaces is altered under various environmental conditions that affects the product quality, an understanding the conformational changes of polymer is important from both the fundamental and practical point of view [153]. Although there are several molecular dynamics simulations studies exist, the experimental studies on the conformational changes of polymers adsorbed on to the colloidal surface are scarce. Therefore, the aim of the present study is (1) to tailor a multi-stimuli emulsion that can respond to both temperature and magnetic stimulus and (2) to study the conformational changes of adsorbed thermo-responsive polymers at the oil-water interfaces by looking at the Bragg peak changes under a constant magnetic force. Further, the manifestation of temperature induced conformational changes of adsorbed PNIPAM chains at the oil-water interfaces is investigated using a simple spectroscopic experimental approach. The interdroplet interactions were successfully tuned using both temperature and magnetic stimuli. This study also gave new insights into the conformational changes of adsorbed polymers.

3.2 Experimental methods and materials

Magnetic nanoemulsions, E_{SDS} (SDS stabilized emulsion) and E_{PNI} (PNIPAM stabilized emulsion) are used in this study. Material preparation and experimental setup are discussed in Chapter II of section 2.4 and 2.5. Intermolecular interactions for E_{SDS} and E_{PNI} at different temperature and SDS concentrations were measured using magnetic chaining technique.

3.3 Results and discussion

3.3.1 Hydrodynamic size and zeta potential of E_{SDS} and E_{PNI} emulsion

The hydrodynamic size distributions of E_{SDS} and E_{PNI} emulsion is shown in the **Figure 3.1a** and the zeta potential distribution of E_{SDS} emulsions is shown in the **Figure**

3.1b. The polydispersity index (PDI) of E_{SDS} emulsion was found to be 0.07, which indicates that the emulsion is fairly monodisperse. The average hydrodynamic diameters of E_{SDS} and E_{PNI} emulsion droplets were 200 and 255 nm, respectively. The average zeta potential was found to be - 46 mV for E_{SDS} emulsion, due to the presence of charged surfactant molecule, SDS (sodium do-decyl sulphate) at the oil-water (O/W) interface. The zeta potential was zero mV for the E_{PNI} emulsion. The increase in hydrodynamic diameter and zero zeta potential of E_{PNI} emulsion confirms the complete coverage of PNIPAM at the oil-water interface.

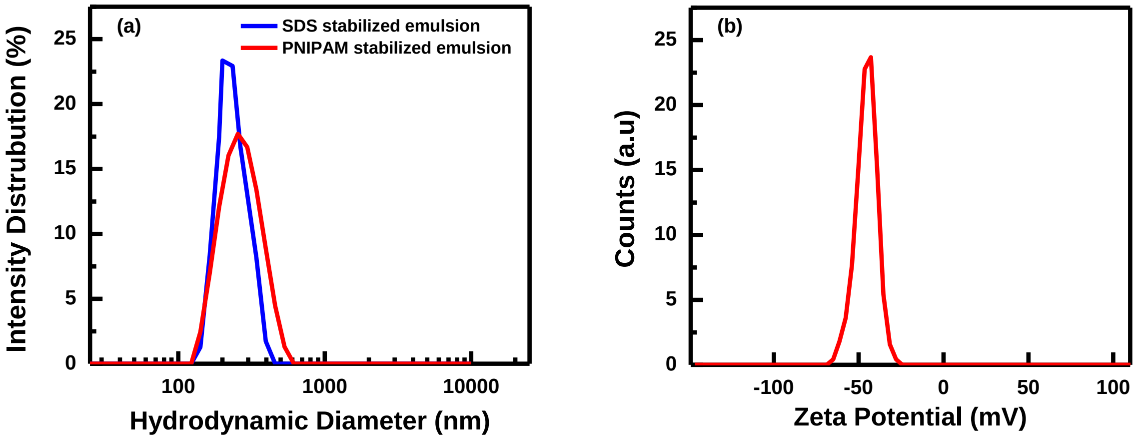

Figure 3.1: (a) Hydrodynamic diameter of E_{SDS} and E_{PNI} emulsion (b) zeta potential of E_{SDS} emulsion.

3.3.2 Tuning lower critical solution temperature (LCST) of PNIPAM solution

Before probing the temperature response of E_{PNI} emulsion, the temperature response and LCST of pure PNIPAM solution is studied. The transmittance of pure PNIPAM solution without and with 2 mM SDS in the temperature range of 25 to 45 °C is shown in **Figure 3.2 a & b.** In the wavelength range of 500-1000 nm and in the temperature range of 5 to 34

°C, the solution was nearly 100% transparent for both cases because of the presence of PNIPAM molecules in the solution whose dimensions are very small as compared to the wavelength of light used[154]. Above LCST the transmittance is nearly 0 % at the lower wavelengths, but the transmittance was slightly more at higher wavelengths (> 600 nm) due to the formation of polymer aggregates, whose size becomes comparable to the wavelength of light used[154]. This observation is in agreement with the decrease in the refractive index with temperature up to LCST and increases above LCST, due to the formation of aggregates[155].

The transmittance of pure PNIPAM solution as a function of temperature, at a wavelength of 550 nm is shown in the **Figure 3.2 c.** For pure PNIPAM solution, the LCST was found to be 35 °C. Below LCST, PNIPAM solution showed nearly 100% transmittances. As the solution temperature was raised above LCST, the polymer started to aggregate and becames a globular structure. Chi Wu et al.[156] showed from FTIR study that below LCST, the carbonyl group (>C=O) is bound to water and no intra-chain bonding exists within amide group (>C=O and H-N). A similar findings on the formation of intramolecular C=O···H-N hydrogen bond in a good solvent by the amide groups of PNIPAM was reported by Yukiteru Katsumoto et al.[137] from the infrared spectroscopy combined with quantum chemical calculations. As the solution temperature increases, the dehydration followed by the formation of new bonding between carbonyl group and heavy water (>C=O···D-O-D) occurs [156], which results in the collapse of polymer and precipitation. This explains the decrease in the light transmittance at higher temperature.

Figure 3.2d shows LCST as a function of SDS concentrations. It can be seen that the LCST is influenced by the SDS monomers in the solution. The inset of **Figure 3.2d (e & f)**

shows the photograph of pure PNIPAM solution at 34 and 35 °C, respectively and **(g-h)** shows the photograph of 1 wt. % PNIPAM+ 2.2 mM SDS solution at 36 and 38 °C, respectively.

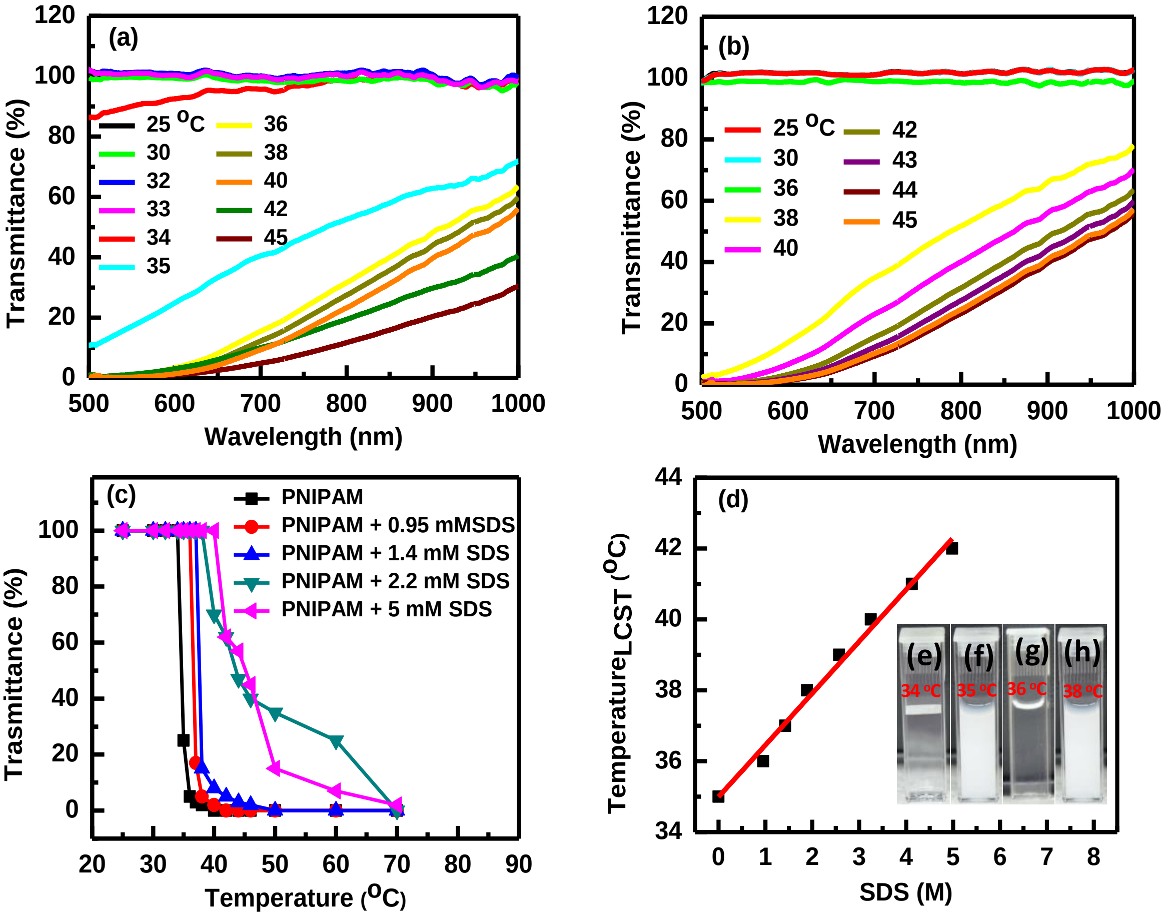

Figure 3.2 : Transmittance from (a) 1 wt % PNIPAM and (b) 1 wt % PNIPAM + 2 mM SDS solution at different temperatures (c) Transmittance from 1 wt % PNIPAM solution at 550 nm for various SDS concentrations and (d) LCST as a function of SDS concentrations at 25 °C. The inset of Figure 3.2d shows the photograph of (e) pure PNIPAM solution at 34 °C (below LCST) (f) at 35 °C (above LCST) (g) 1 wt % PNIPAM+ 2.2 mM SDS solution at 36 °C (below LCST) and (h) at 38 °C (above LCST).

In the presence of SDS (0.95 to 5 mM), LCST increases from 35 to 42 ˚C which is attributed to the hydrophobic interaction between SDS alkyl chain and iso-propyl group of PNIPAM. This results in a polyelectrolyte like structure that increase both the intrinsic viscosity and hydrodynamic size [157]. Therefore, the presence of charged group on the backbone of the PNIPAM inhibits the collapse of the polymer at 35 °C and increases the phase transition temperature. **Figure 3.2d** shows that the LCST increase is almost linear with SDS concentration in the range of 0.95 to 5 mM. Above 5 mM, the exact identification of LCST was difficult due to the sluggish variation in the transmittance. Earlier study showed that below 0.8 mM, there exist a very feeble interaction due to incomplete coverage of SDS molecules on PNIPAM, but above 7 mM no further increase in LSCT is observed, due to the complete coverage of PNIPAM with SDS [157, 158].

3.3.3 Reversible tuning of interdroplet spacing with magnetic field and temperature stimuli.

Figure 3.3a shows that the Bragg spectra for E_{PNI} emulsion are blue-shifted as the temperature increased from 5 to 35 °C. In the above temperature range, the Bragg peak wavelength is shifted from 744 to 714 nm, with a total wavelength shift of 30 nm. The corresponding interdroplet spacing ($h=d-2a$) variation was 9 nm. Above LCST, the Bragg peak was fully collapsed and the reason for this collapse is discussed later. In the presence of 2 mM SDS, the Bragg spectra collapsed only at 38 °C (**Figure 3.3b**), due to SDS-PNIPAM complexes adsorbed at the oil-water interface. The shift in the Bragg peak wavelength, in the temperature range of 5 and 38 °C was drastic as compared to the E_{PNI} emulsion (130 nm against 30 nm).

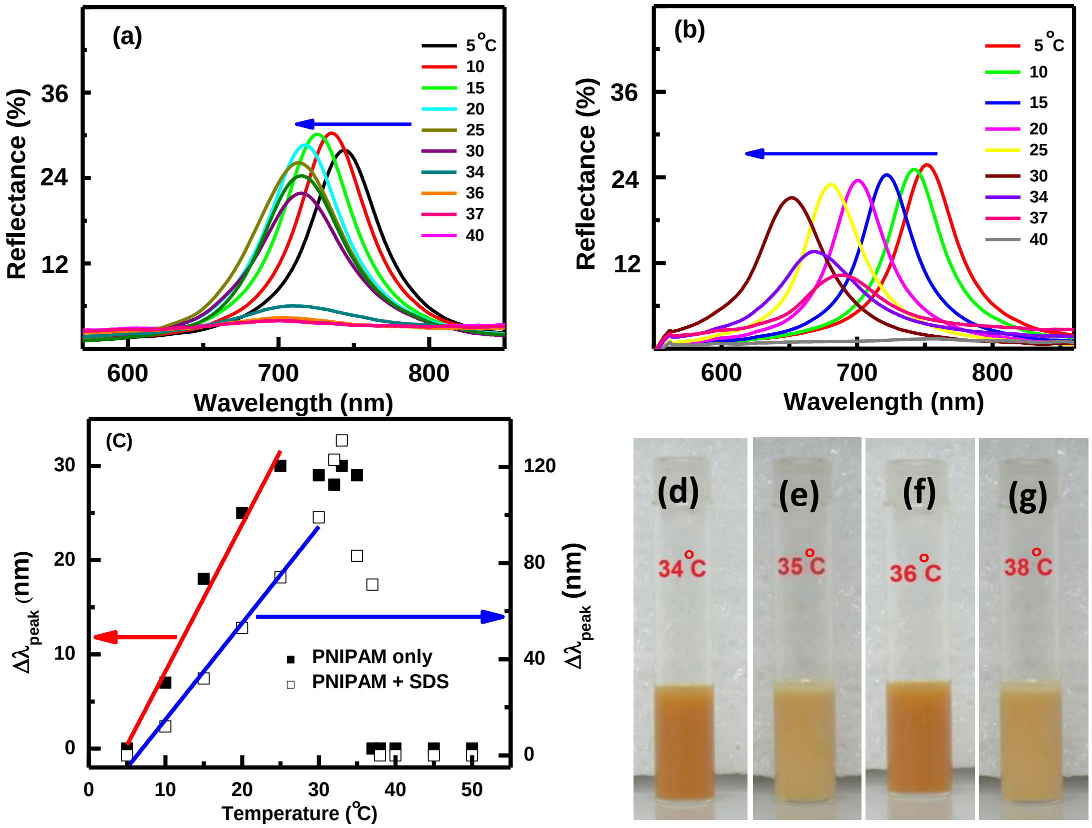

Figure 3.3: The variation of Bragg spectra with temperatures for (a) E_{PNI} (b) $E_{PNI-SDS}$ emulsion. (c) The change in the Bragg peak wavelength (with reference to the Bragg peak at 5 °C) as a function of temperatures for the above two cases and (d-g) Photographs of E_{PNI} and $E_{PNI-SDS}$ emulsion, below and above the LCST.

The interdroplet spacing changes in the above temperature range was 23 nm. Instead of a sharp drop in the case of E_{PNI} emulsion, an increase in the Bragg peak position prior to the complete collapse is observed in the presence of SDS molecules. A fit on the Bragg peak shift data (initial part) of the E_{PNI} and $E_{PNI-SDS}$ emulsion was linear $\Delta\lambda = mx+c$, with slope (m) varying between 1.56 and 4. This showed a better tunability of the inter droplet grating spacing (d spacing) in the presence of SDS molecules in the solution. **Figure 3.3 (d-g)** shows the photographs of E_{PNI} and $E_{PNI\text{-}SDS}$ emulsion below and above the LCST, without the magnetic stimulus.

3.3.4 Temperature dependant interactions without PNIPAM

The details of the force measurement experimental technique are discussed in chapter 2. The intermolecular force profiles for E_{SDS} emulsion as a function of interdroplet spacing for different SDS concentrations is shown in the **Figure 3.4**. In all cases, the pH was maintained at 7. Due to electric double layer at the interface, the force profiles were repulsive and exponentially decaying with interdroplet spacing, in perfect agreement with theory [159, 160]. When the double layer is thin ($\kappa R_h > 5$), the force profile follows the electrostatic double layer equation $F_r(\mathrm{d}) = 4\pi\varepsilon\psi_0^2 R_h^2 [\frac{k}{d} + \frac{1}{d^2}] \exp[-k(d-2R_h)]$, where R_h is the droplet radius, κ is the inverse Debye length, ε is the dielectric permittivity and ψ_0 is the surface potential. When double layer is highly extended ($\kappa R_h < 5$), the electrostatic double layer equation is given by[20]

$$F_r(\mathrm{d}) = 2\pi\varepsilon\psi_0^2 R_h \kappa \frac{\exp[-\kappa(d-2R_h)]}{[1+\exp[-\kappa(d-2R_h)]} \tag{3.1}$$

In the SDS concentration range of 0.2 to 8 mM, the κR_h values were > 5. As expected, the range of repulsion reduces significantly due to screening effect, as the amount of anionic surfactant concentration is increased. As the surfactant concentration is increased from 0.2 to 8mM, the onset of repulsion changes from 78 to 15 nm, respectively and the corresponding Debye length changes from 20.6 to 3 nm.

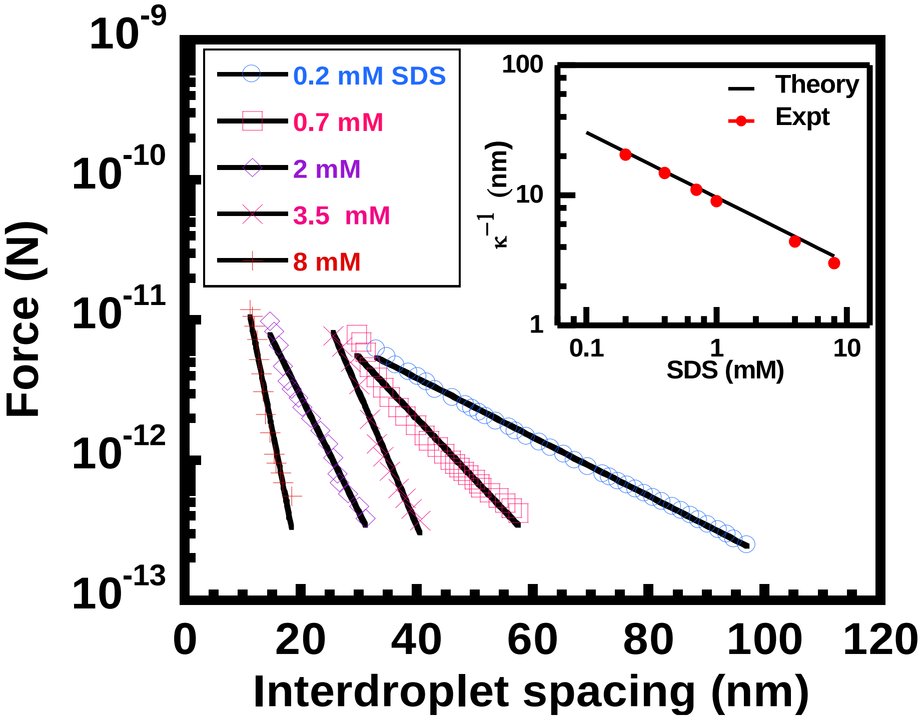

Figure 3.4: Force profile as a function of interdroplet spacing for E_{SDS} emulsion. The inset of the figure shows the Debye length obtained from the fit on the experimental data points (filled circle) and the calculated values (solid line) from the concentration of the surfactant.

The force profiles were fitted with the electrostatic double layer equation and from the slopes of the force profile, Debye length values were evaluated. The Debye length (κ^{-1}) obtained from the slope of the force profiles and the computed values for different surfactant concentrations are shown in the inset of the graph. The solid line shows the best fit. The excellent agreement between the experimental and theoretical Debye length values shows the accuracy and robustness of this approach in probing the electrostatic forces between Brownian colloidal particles.

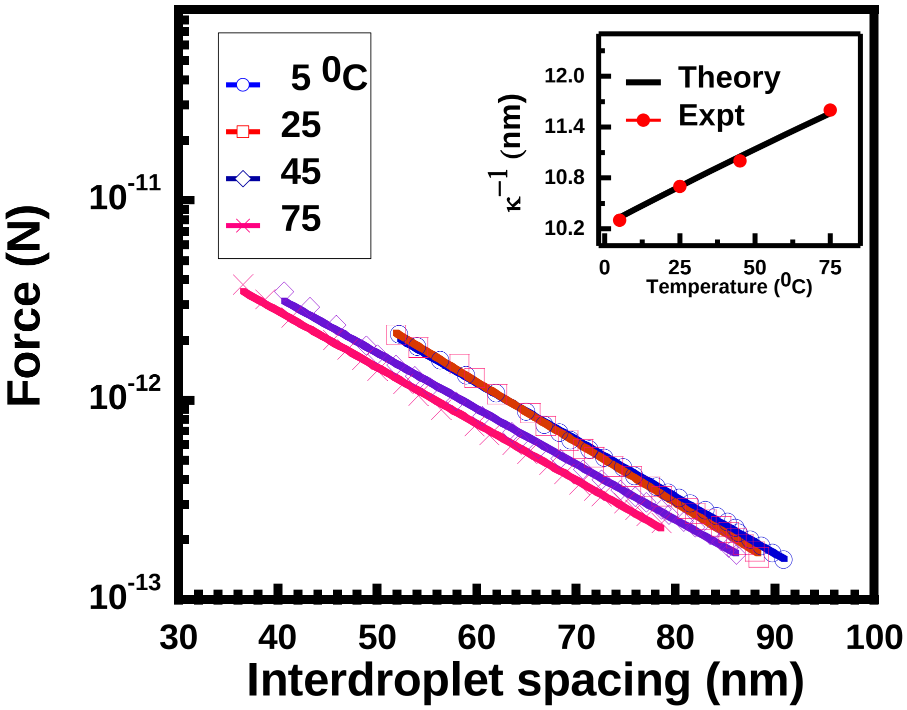

Figure 3.5: Variation of force profile of E_{SDS} emulsion (0.8 mM SDS) at different temperatures. Inset shows the Debye length obtained from the fit on the experimental data points and the calculated values at different temperatures.

Figure 3.5 shows the intermolecular force profiles of E_{SDS} emulsion at 0.8 mM SDS under different temperatures. Only a slight change in the force profiles is observed in the temperature range of 5 to 75 °C. In the above temperature range, κ^{-1} varies only from 10.24 to 11.62 nm. The Debye length obtained from the best fit on force data points and the theoretical values are plotted and shown in the inset of **Figure 3.5.** Again, excellent agreement between the theory and experimental values are seen.

3.3.5 Interactions between PNIPAM covered surfaces below and above LCST

The intermolecular force profile of E_{PNI} emulsion during heating and cooling cycle and the force parameters obtained from the force profiles are shown in the **Figure 3.6 (a –**

d). In all cases, the force profiles were repulsive and decaying exponentially with distance. The zeta potential was nearly zero. The interdroplet separation and the decay length decreased from 82 to 52 nm and 12.6 to 7 nm, respectively as the temperature is increased from 5 to 30 °C. Between 30 and 35 °C, there was a slight increase in both $2L_o$ and decay length. A complete collapse of Bragg peak is observed above 35 °C. The force profiles were reversible during the cooling cycle with a small hysteresis due to conformation changes in the adsorbed polymers at the O/W interface, above the volume phase transition. Such hysteresis was also observed by others [161].

In general, the interaction forces for polymer or weak polyelectrolyte covered surface follows the equation $F(h) = K \exp\left(-\frac{h}{\lambda}\right)$, where the pre-exponential factor, K is the force constant, h is the inter droplet spacing and λ is the decay length of the polymer which is comparable to radius of gyration of polymer in solution [162]. Earlier studies revealed that force profiles follows the theoretical prediction of the mean field and scaling approach [162], which involves three scales; the adsorbed layer thickness λ_{abs}, an adsorption length Z* and the microscopic length "b_{mic}" that is inversely proportional to adsorption strength. In the region of strong adsorption ($\lambda_{abs}/b_{mic} >> 1$), the expression for adsorbed layer thickness, corresponding to the largest loop and tail is $\lambda_{\mathrm{abs}} = \frac{\mathrm{Rg}}{[\mathrm{In}\left(\frac{1}{\varphi_0 \mathrm{v} b_{\mathrm{mic}}^2}\right)]^{1/2}}$, where v is the flory excluded volume parameter and φ_0 is the bulk polymer volume fraction. The above formula indicates that the adsorption thickness is proportional to radius of gyration and is weakly dependent on polymer concentration and adsorption strength. For distance larger than λ, the concentration depends only on the tail section of the polymer and force is always repulsive and decay exponentially with distance. Earlier studies using di-block polymers also confirm that the decay length of the polymer at the O/W interface is comparable to the radius of gyration (R_g) in solution [102].

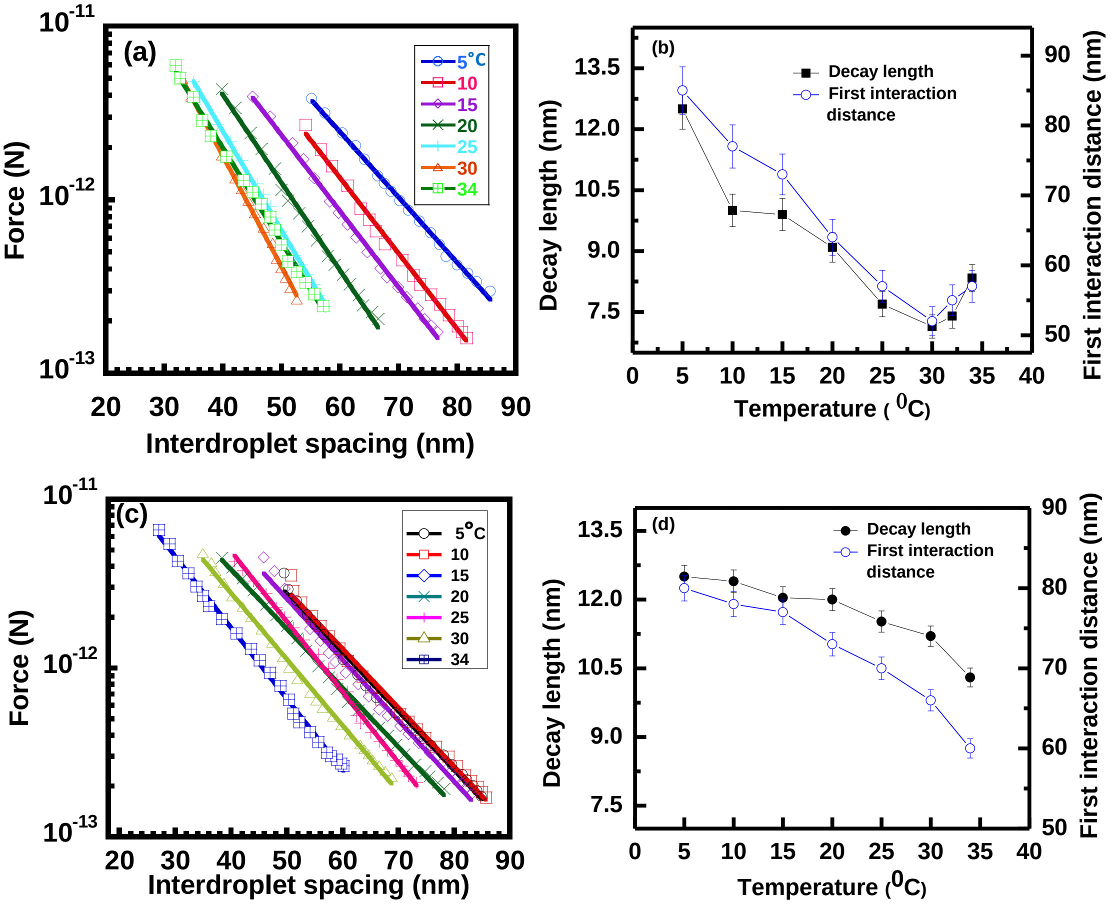

Figure 3.6: Force profiles as a function of interdroplet separation at different temperatures and the force parameters (decay length and $2L_0$) for E_{PNI} emulsion during heating (a & b) and cooling (c & d).

The hydrodynamic radius R_h of the polymer[118] is given by $R_h = \left[\frac{1}{2.5\,N_a}\,\frac{3[\eta]M_w}{4\pi 10^6}\right]^{1/3}$ where N_a is the Avogadro number, $[\eta]$ is the intrinsic viscosity and M_w is the weight average molecular weight of the polymer, respectively. Here, the intrinsic viscosity $[\eta] = 1 + 0.0158\,M_v^{0.72}$ where M_v is the viscosity average molecular weight. The R_g of the polymer solution is related to hydrodynamic radius $\mathrm{R_h}$ as $\mathrm{R_g} = \frac{\mathrm{R_h}}{0.875}$ [118]. In the present study, the value of $\mathrm{R_g}$ for PNIPAM of molecular weight 2.3 x 10^4 was 6.8 nm at room temperature, which was in good agreement with the decay length obtained from the best fit on the force profile of 7 nm.

Earlier studies carried out with PNIPAM of larger molecular weight showed higher radius of gyration (R_g) values. e.g. 58 nm for MW ~ 1.6 x 10^6 by Napper et al.[161]; 60 nm for MW~2.35 x 10^6 by Guangzhao Zhang et al. [163] and 127 nm for a MW ~ 10^7 by Whi Chu et al. [136]. Studies also showed that PNIPAM exhibits both repulsive and attractive interactions depending on the quality of solvent [142, 149]. Below the LCST, they exhibit repulsive interaction due to excluded volume interactions, which becomes attractive above the LCST [135]. For polymer covered surface, the attractive interactions arise due to intersegment attraction, bridging or depletion. In good solvent conditions, intersegment attraction is negligible. Bridging can occur when the surface is not fully covered by the polymer. In the present case, the polymer is in good solvent below 35 °C and hence the coverage at the interface is almost complete. Therefore, both intersegment and bridging should not be significant. Further, as the polymer and droplet concentrations are low, the depletion is unlikely to happen [90]. Then the question is why the Bragg peak disappears above the LCST? It can happen due to two reasons; (1) attractive bridging of the polymer segments of neighboring surfaces, resulting in a huge attractive force and (2) the complete destruction of the droplet ordering. The later possibility is unlikely because the magnetic interaction force is still very significant under the present experimental condition. Therefore, the most likely situation here is the bridging of droplets through adsorbed polymer segments.

The temperature dependent behavior of PNIPAM layers adsorbed to a solid surface from the aqueous solution, studied using surface force apparatus, showed that below LCST, the coverage is low and the PNIPAM adsorbed layer has an open structure with a high content of loops and tails that are highly compressible [90]. Above LCST, polymer segments attract each other, thereby increasing the adsorption strength, leading to a collapse of adsorbed PNIPAM on the surface and to an attraction between the two surfaces [90]. Our observations are consistent with the surface force measurement results, though the interfaces in the two cases are entirely different (i.e. oil-water and solid-water) in these two cases. A molecular dynamics simulation [139] study showed that below LCST, the water molecules form hydrogen bonds with PNIPAM by arranging themselves in an ordered manner around the first hydration layer, resulting in a dominant hydrophilic interactions rather than hydrophobic interactions. However, above LCST the hydrophobic interactions become dominant, resulting in a collapse of PNIPAM. The above study also showed that below and above the LCST, water forms cage-like structures around the hydrophobic groups of PNIPAM, though the cage structures are significantly different below and above the LCST. Simulation studies also showed that the number of water molecules per monomer decreases with an increase in temperature due to an increased entropy of water molecules, that disrupts the cage-like structure. With increase in chain length of PNIPAM, water molecules per monomer decrease due to the slower fluctuation in the mean value of the PNIPAM of higher number of monomers. The simulation studies conclude that solvation dynamics and local structure of water dictates the LCST, as they influence the hydrophilic and hydrophobic interactions significantly. The observed changes in the interdroplet spacing and force parameters are in good agreement with the above simulation results.

To confirm the reversible bridging of polymer covered droplets, phase contrast optical microscopy experiments are performed at different temperatures at a constant magnetic field of 140 Gauss (**Figure 3.7**). The magnetic field induces magnetic dipolar attraction that leads to the formation of 1D chain along the field direction. Below LCST, after the removal of magnetic field, the 1D chains disappears due to the re-dispersion of droplets having high thermal energy (k_bT > Magnetic force). On the contrary above LCST, even after the removal of magnetic field the 1D chain remain because of the bridging of polymers at O/W interfaces. At zero magnetic fields, the chains are flexible without definite alignments which unambiguously confirm the bridging attraction between PNIPAM covered droplets. On lowering temperature below LCST, these flexible chains disappeared due to breaking of bridged polymer segments, which confirms the reversibility of bridging.

From the results of temperature dependent Bragg peak shift, decay length, $2L_0$ change, phase contrast optical microscope image, the confirmation of the adsorbed polymer at the oil interface at different temperatures are schematically shown in **Figure 3.7 (a-d)**. The large Bragg peak shift and $2L_0$ values below LCST (at 5 °C), suggests a highly stretched confirmation of the tail region of the hydrated PNIPAM. At this temperature, the interdroplet separation was ~ 90 nm for a magnetic field of 140 G. As the temperature is increased to 25 ˚C, the interdroplet spacing is reduced to 70 nm for the same magnetic field, indicating a collapse of the tail region due to dehydration of PNIPAM. Further the increase in temperature to 35 °C results in a reduction in the interdroplet separation to 50 nm due to enhanced dehydration, resulting in a further collapse of the adsorbed PNIPAM.

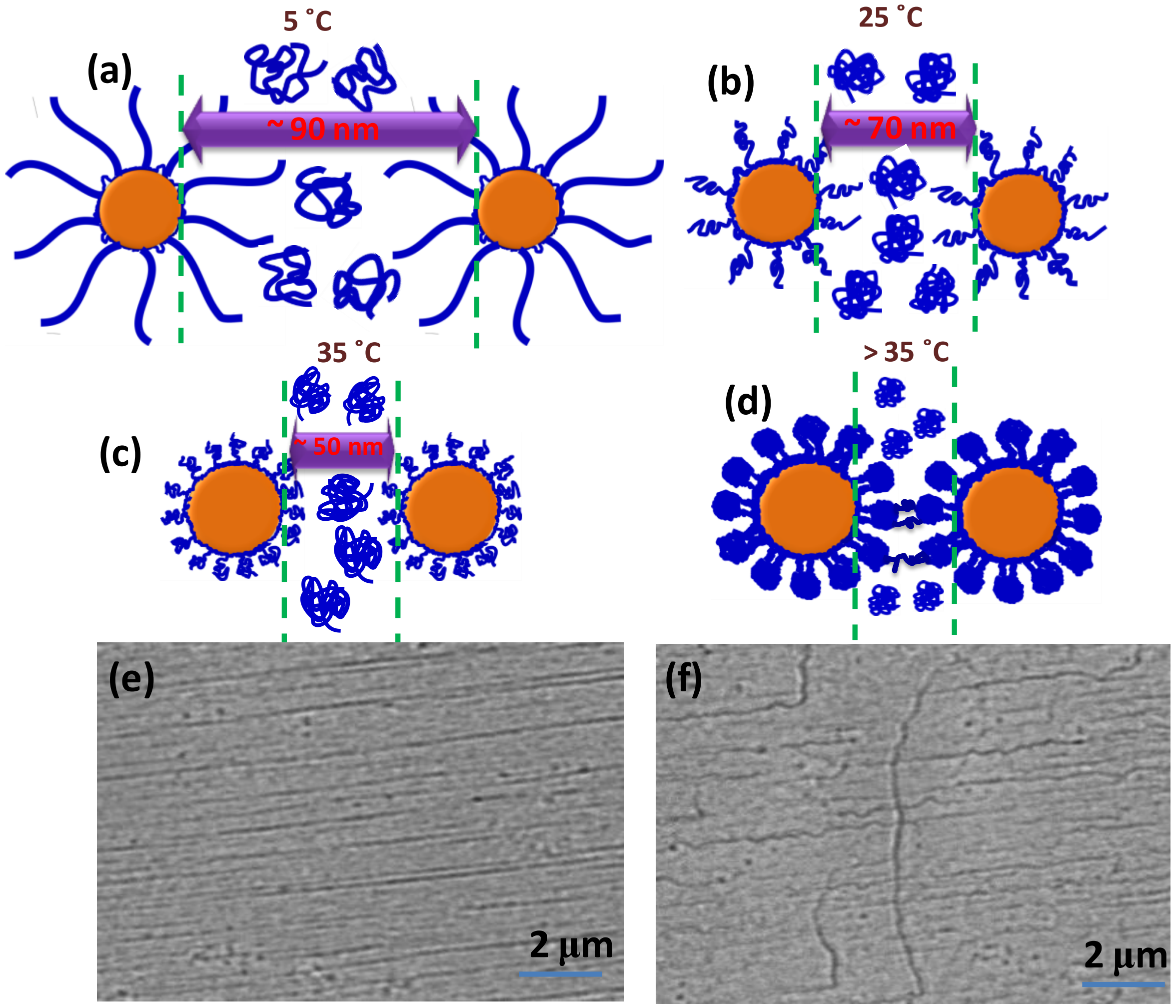

Figure 3.7: Schematics representation of E_{PNI} emulsion at (a) 5 °C (b) 25 °C (c) 35 °C and (d) above 35 °C. (e-f) Phase contrast optical microscopy images of emulsion at (e) T= 25 °C at H = 140 Gauss (f) T= 50 °C after switching off the field.

When temperature is above LCST, PNIPAM becomes more hydrophobic where intersegment as well as intrasegment attraction becomes dominant, resulting in the bridging flocculation. This should be the reason for the disappearance of the Bragg peak. The analytical self-consistent field (SCF) theory calculations by Halperin and Kroger [132] revealed that the brush collapse above LCST favors adsorption because of lowering of the osmotic pressure. Our observation of bridging of the polymer covered surfaces is consistent with the above predictions [132]. Also, the experimental evidence for such brush-to-mushroom transition of PNIPAM layer grafted on a silica surface was provided from AFM imaging by Ishida and Biggs[151] and Satoru Kidoaki et al. [152]

3.3.6 Interactions due to PNIPAM + SDS complex covered surfaces

Figure 3.8 a & b shows the intermolecular force and force parameter for $E_{PNI-SDS}$ emulsion at different temperatures. The force profile shows that in the presence of 2 mM SDS, the onset of interaction is increased throughout the temperature range as compared to E_{PNI} emulsion. Decay length is decreased from 16.6 to 12.7 nm and the first interaction distance is reduced from 115 to 70 nm as the temperature increased from 5 to 38 °C. Furthermore, the LCST is increased by 3 °C, in the presence of 2 mM SDS.

When SDS is added to E_{PNI} emulsion, two possibilities can occur: (a) SDS molecules can replace the adsorbed PNIPAM molecules at the oil/water interface. Such preferential adsorptions are noted in dispersions [164]. (b) SDS can complex with the adsorbed PNIPAM and change their conformation at O/W interface. If we consider the first possibility (i.e. SDS molecule displaces the PNIPAM molecule completely), the zeta potential would have increased to -40 mV and the decay length should have reduced to 7 nm (which is the expected Debye length for the emulsion stabilized with 2 mM SDS concentration). But the measured zeta potential and decay length values were -5 mV and 13.5 nm at room temperature, respectively. This observation clearly ruled out the possibility of complete replacement of PNIPAM by SDS at oil-water interface.

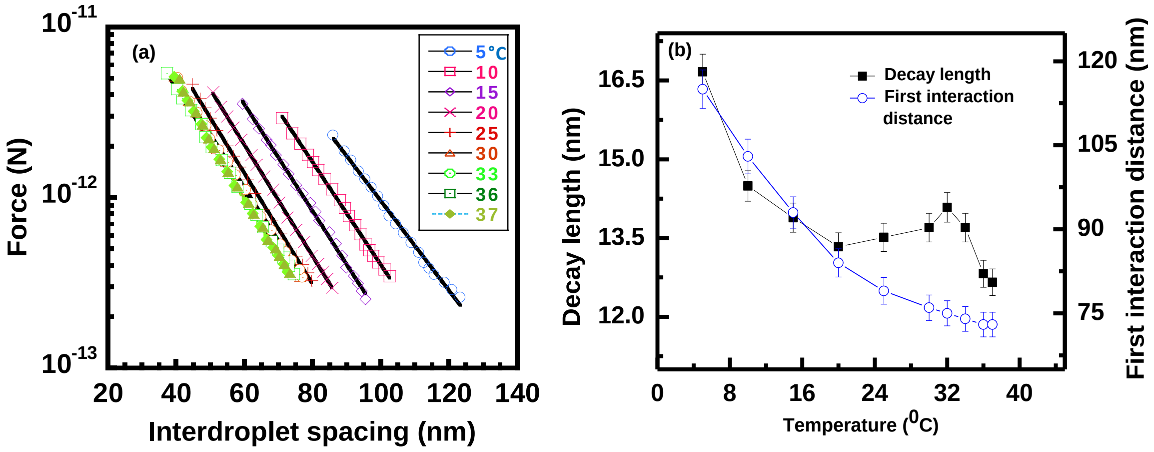

Figure 3.8: (a) Force-distance profiles of $E_{PNI-SDS}$ emulsion at different temperature and (b) force parameters (decay length and $2L_0$) as a function of temperature.

The next possibility is the complexation of SDS molecule with PNIPAM, leading to a polyelectrolyte like structure. For PNIPAM solution of 0.025 wt %, [165] the concentration of surfactant (C_{SDS}) used in this study is higher than the critical aggregation concentration (C_{CAC}). Therefore, SDS modifies the intra and intermolecular interactions of the adsorbed PNIPAM, which significantly change the onset of interaction. The force profiles in **Figure 3.8a** shows that $2L_0$ and λ increased from 72 to 112 nm and 13 to 16.5 nm, respectively when 2 mM SDS is introduced in E_{PNI} emulsion. The increase in the $2L_0$ and λ unambiguously confirm the extended polyelectrolyte like structure of adsorbed PNIPAM due to complexation with SDS molecules. Here, the repulsion between the bound SDS molecules on the backbone of PNIPAM gives rise to an extended conformation. Such complexation in polymers are predicted theoretically [166] and also observed experimentally [102].

The proposed necklace model [166] of PNIPAM-SDS complex, was based on the assumption that bound SDS molecules are wrapped around by PNIPAM chains. The fraction of adsorbed segment (or degree of surfactant coverage) Γ is given by $\Gamma = \frac{\Psi N_{ad}}{N}$, where Ψ is the number of micelle per chain whose value depends on the concentration of SDS. When $C_{SDS} < C_{CAC}$ Ψ is < 1 and for $C_{SDS} > C_{CAC}$, Ψ is > 1. N_{ad} is the number of PNIPAM monomers associated with individual SDS micelles and N is the molecular weight of tethered PNIPAM. According to the binding isotherm equation, as SDS concentration increases the binding isotherm value also increases [147]. The observed increase in the $2L_0$ and λ is a consequence of the increase in the biding isotherm that affects the conformation of the polymer.

Previous studies show that SDS-PNIPAM association prevents interchain aggregation [102, 109, 157]. A similar behavior was observed in E_{PVA} (PVA-vac stabilized) emulsion in the presence of SDS where SDS molecule bound to the PVA group favors a stretched tail like conformation at the oil-water interface [102]. Depending on the concentration of SDS in PNIPAM solutions, three distinct scenario were observed [157]. When SDS concentration was below its critical aggregation concentration (0.86 mM), the addition of SDS do not perturb the PNIPAM and hence very feeble interaction between them is noted. When SDS concentration was between 0.86 and 7 mM, it aggregates on the backbone of PNIPAM, leading to a polyelectrolyte like complex, which results in increased hydrodynamic size of the polymer due to the enhanced intermolecular electrostatic repulsion of the charged complex. When SDS concentration is very high, it saturates the PNIPAM backbone. With increase in temperature from 5 to 40 °C, the spatially extended polymers at O/W interfaces collapses (evident from the reduction in the $2L_0$) because of dehydration of water molecules which eventually increases the adsorption [167]. A similar increase in surface graft density of cationic polyelectrolyte Poly-(L-Lysine)-graft-Polyethylene glycol (PLL-g-PEG) on TiO_2 surface is observed by Ryosuke Ogaki et al. [168] when temperature was increased to 80 °C.

3.4 CONCLUSIONS

A novel multi-stimuli (Thermo-magneto) responsive nanoemulsion is developed and studied the behavior of PNIPAM at the oil-water interface and hence their optical properties under varying temperature and magnetic field. The multi- stimuli thermo-magneto sensitive nanoemulsion are prepared using poly(N-isopropylacrylamide) (PNIPAM), superparamagnetic nanoparticles and oil-in-water emulsion. Below the coil to globule volume phase transition, the interparticle separation of droplets within the self assembled linear array is tuned from 82 to 52 nm by varying the temperature. A small amount of anionic surfactant monomers in E_{PNI} emulsion is found dramatically augment the LCST, the repulsive interaction forces and the interparticle spacing due to strong association of PNIPAM and SDS. These results suggest that by using a combination of PNIPAM and an anionic surfactant the interparticle interactions, volume phase transitions and thermal stability of emulsion can be reversibly tuned. Further, the temperature induced conformational changes of adsorbed PNIPAM chains at the oil-water interface are manifested through a simple spectroscopic experimental approach. The interdroplet interactions are successfully tuned using both the temperature and magnetic stimuli and obtained new insight into the conformational changes of adsorbed polymers. The thermo-magnetic multi-stimuli nanoemulsions should open up many new applications in optical devices (2D and 3D photonic crystals, gratings, body temperature measurement), ion sensors and drug delivery systems.

CHAPTER 4

Electro-steric interaction due to weak polyelectrolyte at the oil-water interface under different environmental condition

4.1 Introduction

Grafting one end of a polyelectrolyte (PE) on a substrate or particle to form a polyelectrolyte brush, has been a topic of intense scientific reserach in the past few decades owing to its potential applications in a wide range of scientific disciplines because of their long range interaction [56, 169]. Recently, responsive switchable surfaces (surface anchored or adsorbed with stimuli responsive polymer) have been shown to have applications in sensors [3, 70], lubrication [88], developing antifouling surfaces [170] etc. In addition to the broad applications of PE, the behavior of PE under various environmental condition is fundamentally important to understand the process such as protein folding [171], DNA condensation [172] etc. Interestingly, the adsorption of PE at the liquid-liquid interface mimics in vivo condition of charged macromolecule at cell-fluid interface and hence is very important to understand biological phenomenon [173].

PE's are unique class of materials, available naturally in the forms of protein, DNA, enzyme, polysaccharides etc. They are broadly classified into two categories: weak or quenched and strong or annealed PE, where the former is highly sensitive to pH due to protonation or deprotonation of surface groups and hence are known as pH responsive polymers whereas the latter is insensitive to pH. The conformational change of a weak PE is entirely different from a strong PE under the same physio-chemical conditions due to the dependence of dissociation constant (α) of weak PE with salt, pH and grafting density. Theoretical [32, 49, 50, 58, 174], simulation [175-178] and experimental [59, 60, 179-181] studies were carried out to understand the conformational changes of PE's at an interface.

In addition to that, the properties of weak PE adsorbed at an interface is different from its properties in bulk (such as the conformation, degree of ionization, wettability etc) solution. The conformational behavior of PE also depends on various conditions like grafting density, salt content, pH, nature of solvent medium, temperature [54, 182-185] etc. For example, the charge density of a grafted PE increases with distance from the substrate level to the end [186]. The physically adsorbed PE undergoes a reversible conformational change (globule to extended transition) under varying pH and ionic strength due to ionization and neutralization of surface carboxyl group (COOH) on the polymer backbone [187, 188]. Recent studies show that a weak polyelectrolyte undergoes a reversible conformational change only above certain molar mass [39] and also exhibits a hysteresis in pH response at certain polydispersity levels of the chains [189]. The present study attempts to gain new insights into the behavior of PE's at interfaces under different environmental conditions.

Here, the behavior of a weak polyelectrolyte, Polyacrylic acid (PAA) adsorbed at the oil-water emulsion interfaces in aqueous media is studied. PAA is a water soluble anionic PE that undergoes reversible conformational transitions under varying pH and ionic strength. At low pH, it is neutral in nature and adopts a compact globule structure but at relatively high pH, they are charged and thus swell because of the ionization of carboxyl group at the backbone of the PE. However, at very low molecular weight, PAA exhibit a pH independent behavior [39].

The main objective of this work is to (1) study the conformational changes of an adsorbed weak PAA at liquid-liquid interface under varying salt and pH (2) compare the scaling exponents with the theoretical prediction and (3) study the effect of salt valence on the conformational change of adsorbed PAA and (4) study the effect of different molecular weight of PAA on the interaction force. To realize the above, we have used a nanoemulsion adsorbed with PAA and studied its behavior under different physiochemical conditions by probing the interdroplet spacing under a given magnetic force and looking at intermolecular force using magnetic chaining technique [102]. These measurements are complemented by light scattering and phase constrast microscospy measurements and finally the results are compared with various established theoreitcal models.

4.2. Materials and methods

Magnetic nanoemulsions, E_{PAA450}, E_{PAA250} and E_{PAA15} (PAA of 450, 250 and 15 K stabilized emulsion) are used in this study. Material preparation and experimental setup are explained in Chapter II, section 2.4.2. Intermolecular interaction for E_{PAA450}, E_{PAA250} and E_{PAA15} emulsion at different pH, salts of various concentrations and valance and PAA of different molecular weight were measured using magnetic chaining technique.

4.3. Results and discussion

4.3.1 Hydrodynamic size and zeta potential of E_{PAA450} emulsion

The hydrodynamic size distribution and zeta potential of E_{PAA450} emulsion at pH of 7 is shown in **Figure 4.1 (a & b)**. The PDI of the emulsion without and with adsorbed PAA is 0.07 and 0.2, respectively. After the stabilization with PAA, the size distribution increased considerably because of larger size and polydispersity of PAA. The average hydrodynamic diameter and zeta potential of the E_{PAA450} emulsion was 260 nm and -47 mV, respectively at this pH. The hydrodynamic diameter and zeta potential for bare emulsion at pH 3.5 (without PAA) was found to be 200 nm and -2 mV, respectively. The increase of hydrodynamic diameter and zeta potential with increasing pH confirms the adsorption of PAA at the oil-water interface. The H_d of the emulsion droplet at the lowest pH (3.0) was found to be 220 nm, which increases to 290 nm as the pH reaches 11.8.

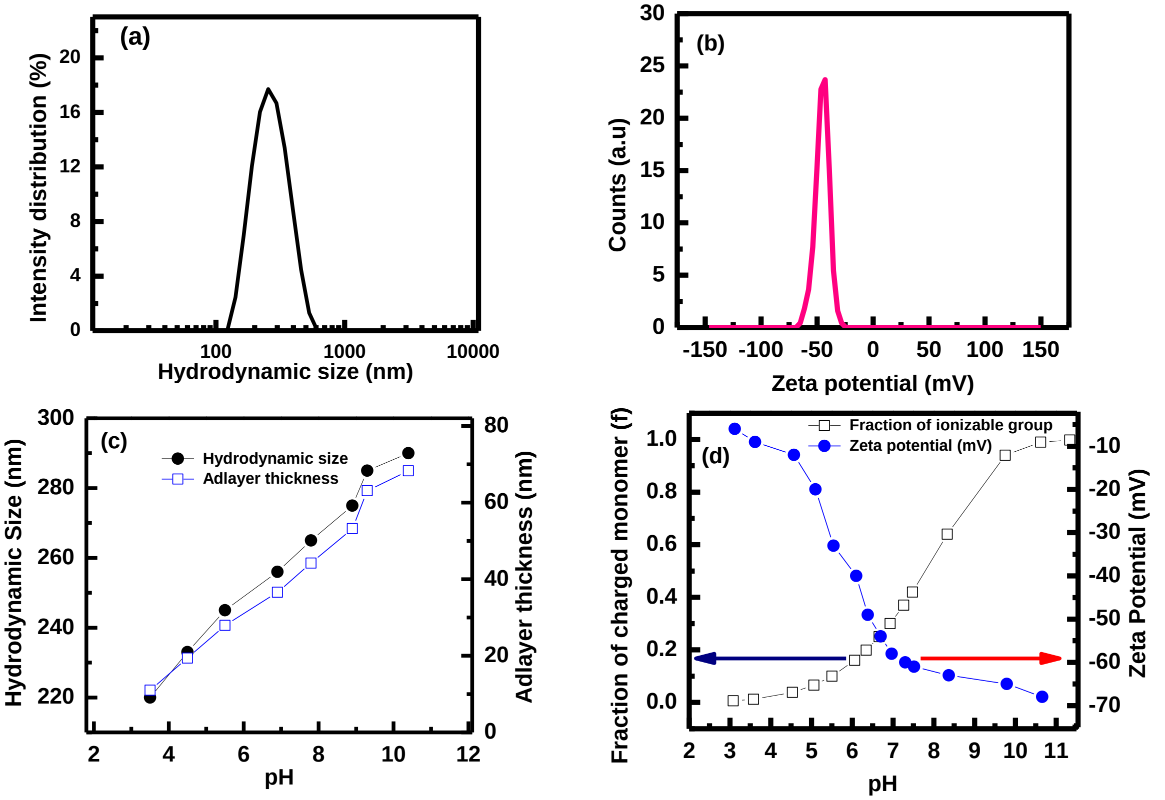

Figure 4.1: (a & b) Hydrodynamic diameter and zeta potential of E_{PAA450} emulsion at pH 7 (c) Variation of hydrodynamic diameter and adsorbed layer (adlayer) thickness for E_{PAA450} emulsion at different pH (d) Variation in fraction of charged monomer on the PAA backbone at different pH and variation in zeta potential for E_{PAA450} emulsion.

The effective adlayer thickness was calculated as $\delta_{eff} = [(R+\delta)^3 - R^3]/3R^2$, where δ is the apparent adlayer thickness and R is the particle radius. The H_d and adlayer thickness measurements were performed at different pH values and the results are shown in the **Figure 4.1c.** The effective adlayer thickness increased from 11 to 68 nm as pH of the medium is increased from 3 to 11.8. Similarly, the zeta potential was increased from -2 mV at pH 3.0 to -70 mV at pH 11.8, due to enhanced dissociation of the carboxyl group of the PAA as shown in the **Figure 4.1d**. The fraction of charged monomer or degree of dissociation (α) is calculated via $pH = pK_a + 4.10\,\alpha^{1/3} - \log\left(\frac{(1-\alpha)}{\alpha}\right)$ [41] where pK_a was 4.54 for acrylic acid [190]. The fraction of charged monomer increases with increase in pH of the medium. **Figure 4.1d** shows the variation of number of ionized group on their backbone with pH. As expected, the fraction of charged monomer and zeta potential increases with increase in pH above pK_a. This shows that PAA adopts a coiled structure at very low charge density (at low pH), where only very few monomers were charged, but it stretches out at higher pH due to enhanced dissociation of carboxyl group on the backbone.

4.3.2 Change in the interdroplet spacing between PAA covered droplets under varying pH

In order to manifest the conformational changes of adsorbed PE under different environmental conditions, the magnetically polarizable emulsion droplets are made to form a stable 1D array by a constant magnetic force, where the equilibrium distance between the droplet depends on the balance between the attractive and repulsive contributions [102, 109]. When the sample is illuminated with a white light, a Bragg peak is observed in the visible wavelength range and the peak position depends on the interdroplet spacing [82, 191]. At pH 3.0 the Bragg peak formed at 645 nm, corresponds to an interparticle spacing of 40 nm.

The competition between the magnetic and surface energy determines the eccentricity (E_{ecc}) of the magnetic nanoemulsion, given as $E_{ecc}^2 = \pi \frac{R_h}{\sigma} M^2$. Here, R_h, σ and M are droplet radius, surface density and magnetization, respectively [117]. For a droplet of radius 200 nm in the presence of magnetic field (250 Oe), the eccentricity (E_{ecc}^2) was calculated as 0.0013. This means it is almost impossible to deform the droplets even at very strong magnetic field, owing to their smaller size, which was also evident in microscopic measurements.

Figure 4.2a shows the Bragg spectra of E_{PAA450} emulsion at a constant magnetic field of 200 G under different pH conditions. At pH 3.5, the Bragg peak is formed at 650 nm, which is red- shifted to 1000 nm as the pH of the medium is increased to 11.8. The change in the Bragg peak under this condition can only be due to the change in the conformation of the adsorbed PAA as a function of pH, as all other conditions (ionic strength, temperature, and applied magnetic force) remains exactly the same. It should be noted that the interdroplet spacing remains constant without any time dependant effect at constant magnetic force and pH. The emulsion was found to be stable against coalescence up to an alkaline pH of 11.8, above which bridged network like structures are observed. The bridged structure is found to be irreversible, unlike the network structure observed in case of E_{PNI} emulsion [43]. It is known that the brush height and fraction of segments in trains, loops, and tails varies with pH. At low pH, the loops and train dominates and the length of the tail segment increases with increasing pH [44]. The coil to extended conformational changes of the adsorbed PAA was found to be highly reversible between pH 3.0 and 11.8, where the Bragg spectra red-shift with increase in pH of the medium and blue-shifts with decrease in pH. The variation in the interdroplet spacing (Δh = 143 nm) between pH of 3.0 and 11.8 (Bragg peak at pH 3.0 is taken as the reference) is shown in the **Figure 4.2b.**

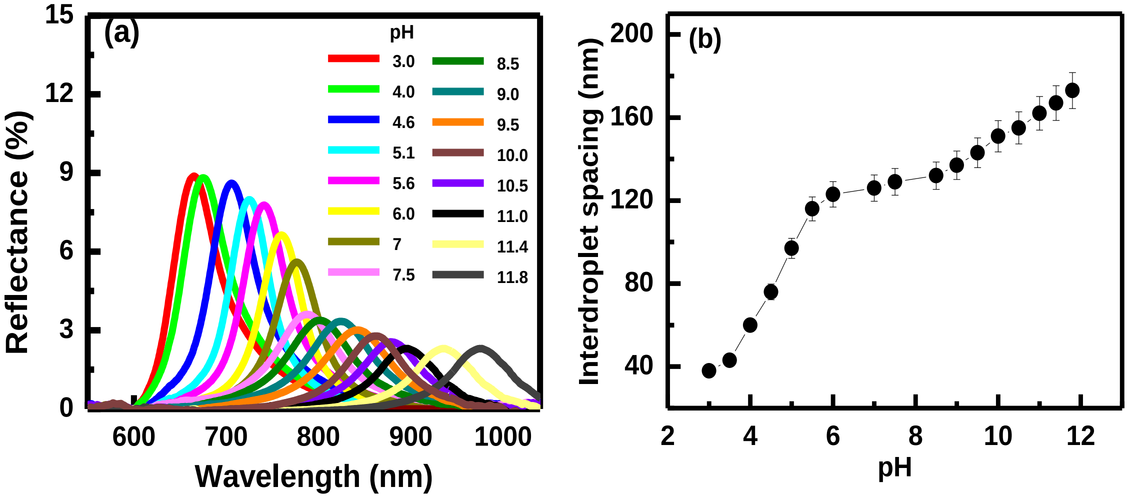

Figure 4.2: (a) Bragg spectra from E_{PAA450} emulsion at various pH. (b) The change in interdroplet spacing (h) as a function of pH from 3 to 11.8.

The increase was steep in the pH range of 3.0 to 6 and from 6 to 9 because of enhanced dissociation of COOH group, whereas the change between 9 and 11.8 was less due to the lower rate of dissociation of backbone functional group (almost dissociates completely at a pH range of ~10).

4.3.3 Forces between PAA covered surfaces under different pH

The swelling and collapse of the adsorbed PE at the oil-water interface is also studied by analyzing the intermolecular forces as a function of pH. The intermolecular forces due to electro-steric interactions follow an exponential decay $F = A \exp(-h/\lambda)$ as shown in the **Figure 4.3a** where the h is the interdroplet spacing and λ is the decay length. The decay length and force magnitude of E_{PAA450} emulsion at different pH are shown in the **Figure 4.3b**. The force profiles were repulsive in nature and decaying exponentially with distance. At pH 3.0 the onset of interaction starts at a lower interdroplet spacing and increases with pH. The λ was found to be 6.6 nm at pH 3.0 but reaches 28 nm at a pH 11.8, with a total variation of 21.4 nm. Almost one order magnitude change in the force magnitude is observed when pH is increased between 3.0 and 11.8, which indicates the pH dependent adsorption strength.

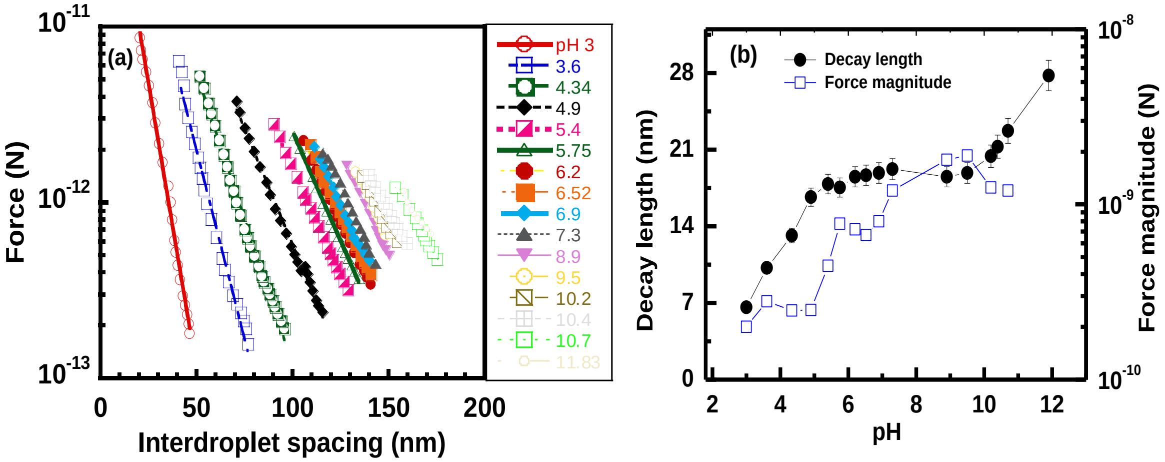

Figure 4.3: (a) Force-distance profile for E_{PAA450} emulsion at different pH values (b) Decay length and force magnitude for the same.

The forces in presence of PE arise from two sources: electrostatic and steric interaction. In the case of anionic PE, at low salt concentration and high pH, long range electrostatic force dominates whereas at high salt concentration and at low pH, short range steric interaction dominates due to screening and protonation of surface charges [192]. The backbone of the PAA carries a carboxylate anion (COOH) group, ionizes into COO^- and H^+ at high pH. At low pH, the PE exhibits a coiled conformation (behaves like a neutral polymer) whereas at high pH, deprotonation of the carboxyl groups of PAA leads to an extended conformation. With increasing pH the degree of ionization increases and the surface of PAA become negative. An earlier study showed that more than 50% of the carboxyl groups on the PAA (Mw = 50,000 g/mol) are negatively charged at pH 7, whereas full ionization occurs at a pH of 11 [193]. Thus the degree of dissociation of COOH on PAA backbone increases with increase in pH of the medium and attains a maximum at pH 11 due to complete dissociation [193]. The force profile starts at lower interdroplet distance at lower pH. The λ of the adsorbed PAA was 6.6 nm, indicating a collapsed conformation at pH=3.0. As the pH increases, the onset of interaction increases, indicating a swelling of the adsorbed PAA. It is well established that polymer exhibits a train, loop and train like conformation at interfaces [21]. At pH 11.8, λ increased to 28 nm, indicating an extended conformation of PAA at the interface. When the polymer is in swollen state, it is expressed in terms of Flory radius $R_f = aN^{0.6}$, whereas in a collapsed state it is $R_f = aN^{0.3}$. According to the above calculation, theoretical value of R_f should be 47.3 and 3.3 nm for PAA (where a = 0.25 nm and N = 6250) whereas the observed experimental values are 28 and 6.6 nm at pH 11.8 and 3, respectively. The experiments carried out using SFA with an end-tethered PAA on mica showed a better agreement between the theory and experiments [194]. The reason for the deviation in our experiment is probably because of physic-sorption of PAA at the oil-water interface. A study by Sparks et al. [180] showed that when PAA adopts an extended conformation at a calcite interface, it displaces twice the water molecules than when it adopts a coiled conformation. The above study also showed that the average number of carboxylic acid (COOH) groups interacting with a surface is ~ 25% of the total number of functional groups in an extended conformation of the polymer but only 14% for a coiled conformation.

The force profile obtained for PAA at low pH (where the electrostatic interaction is negligible), is compared with the Alexander-de-Gennes theory of polymer, $\frac{F(D)}{R} = \frac{100k_bT\ L}{s^3}\exp(-\frac{D}{L})$, where s is the distance between the two grafted points and L is the brush thickness. Using the above equation, the obtained value of s and L for E_{PAA450} are 13.8 and 6.6 nm, respectively. Similar, measurements carried out on PEG-PEI grafted films using AFM colloidal probe technique, in the presence of 50 mM NaCl, showed a complete screening of electrostatic force [195]. The value of s and L obtained in their experiment were 3 and 8 nm, respectively. The force between the PE adsorbed surfaces becomes more complex due to the presence of long range coulomb interaction and counter-ion. At low pH, the role of excluded volume interaction becomes important but at high pH, the electrostatic interaction plays a major role. The increase in droplet distance (due to dissociation of surface group) with increase in pH of the medium can be understood from the increase in force magnitude**.** The force magnitude increases by almost an order of magnitude in the pH range of 3 to 11.8, which shows an enhanced repulsion between the dissociated surface groups. To understand the behavior of adsorbed PAA, the intermolecular forces between the E_{PAA450} emulsion is compared with the theory of PE in a salt free dilute solution [196].

Figure 4.4a shows variation of first interaction distance as a function of pH. It is found that the $2L_0$ increases from 60 to 175 nm as the pH is increased from 3.0 to 11.8. This confirms the swelling or extension of adsorbed the PAA due to increased electrostatic repulsion. According to counter-ion fluctuation theory [197], a weak PE in very dilution limit, the functional backbone are deprotonated and the counter-ion (CI's) occupy the whole volume, resulting in a strong stretching of PE due to electrostatic repulsion. In good solvent conditions and at low electrostatic strength, the PE undergoes stretching where CI's are distributed far away from PE but collapses at high electrostatic strength due to condensation of CI's.

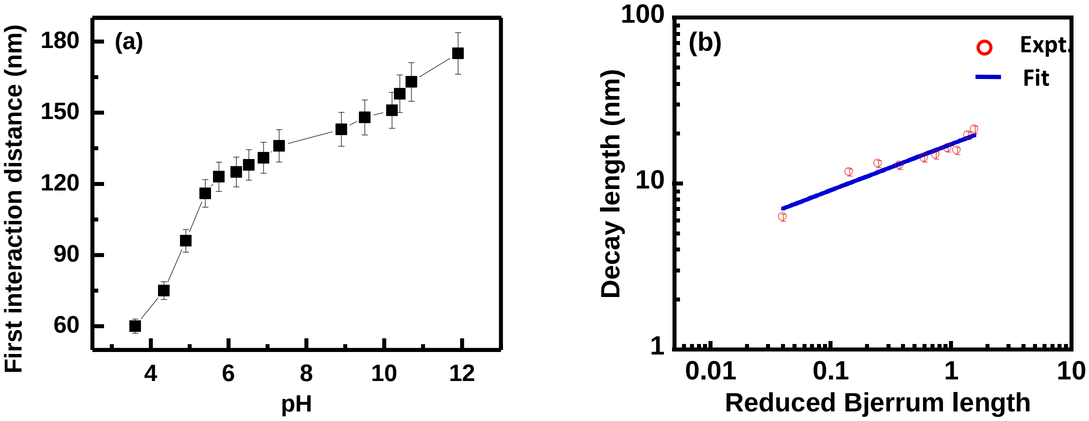

Figure 4.4: (a) First interaction distance ($2L_0$) as a function of pH (b) Decay length Vs reduced Bjerrum length for E_{PAA450} emulsion. The solid line represents the best fit on the experimental data ($\lambda = l_b^{0.21}$ and $R^2 = 0.85$).

The rate of stretching and collapse are understood in terms of radius of gyration (R_g) of the free PE and the reduced Bjerrum length (l_b) as $R_g \sim l_b^{1/3} N$, where N is the degree of polymerization[197] at low electrostatic interaction strength. At high electrostatic interaction strength, $R_g \sim l_b^{-1/2} N^{1/3}$. A recent molecular dynamic simulation study was carried out to probe the flexible PE in a good solvent condition where the collapse of the PE showed two different sub-regime called weak and strong electrostatic regime [35]. In the former case, the collapse rate follows as $R_g \sim l_b^{-1/2} N^{1/3}$ which agree with the counter-ion fluctuation theory but in the latter case, the collapse rate follows $R_g \sim l_b^{-1/5}\ N^{1/3}$ which was explained by including the role of third virial co-efficient into the theory.

Earlier studies showed that for a polymer adsorbed at the oil-water interface, λ is comparable with the R_g of the free polymer in solution [198]. **Figure 4.4b** shows the variation of decay length as a function of reduced Bjerrum length ($\overline{l_b}$). Here, $\overline{l_b} = \frac{\beta e^2}{\varepsilon a_{sp}}$, where β = $(k_bT)^{-1}$, k_b is the Boltzmann constant, T is the temperature and 'a_{sp}' is the average spacing between the charged groups ($a_{sp} = a_{mon} /\alpha$), which is calculated as the ratio of monomer size (a_{mon}) to the degree of dissociation (α). In the present case, 'a_{sp}' (at pH of 7) is found to be 0.56 nm. The exponent was found to be 0.21, against the theoretical prediction of 0.33. The agreement here is remarkable, though the interface in the present case was very much different (liquid-liquid).

4.3.4 Effect of salt on colloidal interaction between PAA covered interfaces

The swelling and collapse of PAA brush adsorbed at the oil-water interface as a function of ionic strength is discussed in this section. The pH of E_{PAA450} emulsion was fixed at 5.0 in all cases. **Figure 4.5 a & c** shows the intermolecular force measurement for PAA covered interface as a function of distance at various concentration of Ca^{2+}. There exist two different regions: in the salt concentration from 0 to 0.1 mM, λ increases from 12 to 17 nm (**Figure 4.5b)**, above this salt concentration, λ decreases from 18 to 6 nm (**Figure 4.5d).**

The theory of PE conformation in the presence of electrolyte was studied extensively [48-51, 199-201]. The theoretical modeling of Zhulina and Israels [50, 58] is based on electro neutrality in the brush layer and force balance in the brush. The brush is assumed to be immersed in an infinite reservoir of water containing fixed amount of ions, whose dimensions are ignored. Therefore, only the electrostatic contribution is taken into account and the steric interactions are ignored as dilute electrolyte solutions are considered.

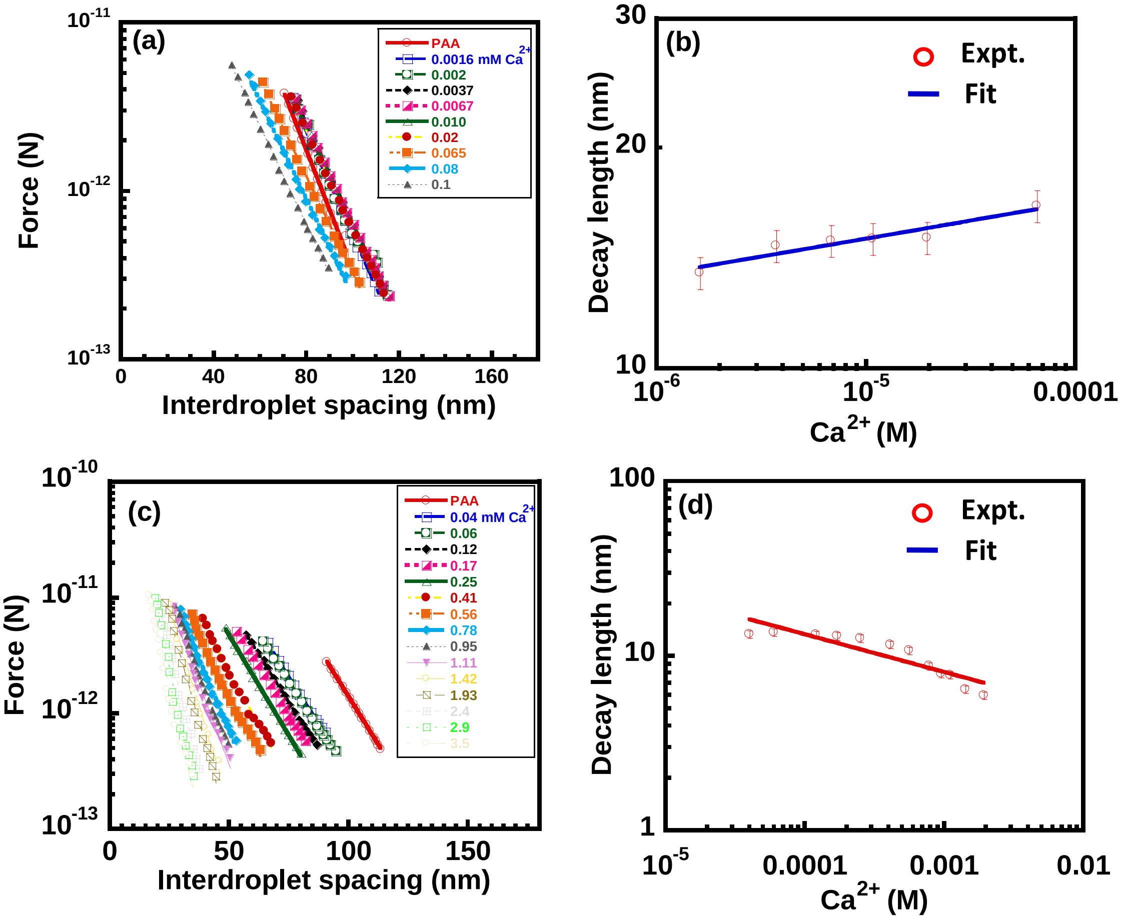

Figure 4.5: (a) Force as a function of distance for E_{PAA450} emulsion at lower Ca^{2+} concentration ranging from 0 to 0.1 mM. (b) Decay length vs. Ca^{2+} concentration. The best fit is shown by the solid line where $\lambda \sim \varphi_s^{0.05}$ and $R^2 = 0.96$ (c & d) Force as a function of distance and decay length for E_{PAA450} emulsion at higher Ca^{2+} concentration ranging from 0.04 to 3.6 mM. The best fit is shown by the solid line where $\lambda \sim \varphi_s^{-0.26}$ and $R^2 = 0.88$.

The equilibrium values of polymer molar concentration, brush height etc, are obtained by balancing various forces acting on grafted chains. The brush height at low salt concentration (Osmotic brush regime) was predicted to follow as $H \sim N a_{mon}^{4/3}\, \sigma^{1/3} \left(\frac{\alpha_b}{1-\alpha_b}\right)^{1/3} ([H^+] +\ \varphi_s)^{1/3}$ and at high salt concentration $H = N(a_{mon}^2 \alpha_b^2 \sigma^{\ -1} \varphi_s^{-1})^{1/3}$, [51] where N is the number of monomers in the brush chain, σ is the graft density, α is the degree of dissociation in the bulk, H^+ is the concentration of proton and φ_s is the concentration of salt. With increase in salt content, the difference in proton concentration between the bulk and brush becomes less and it vanishes at a particular salt concentration termed as φ_s^{max} and the brush thickness during the transition (H_s^{max}) from OsB to SB regime reaches a maximum [58].

Thus, a weak PE shows a non-monotonic behavior in brush thickness with varying salt concentration (φ_s), due to the potential difference between the bulk and brush which is not fixed but varies with electrolyte concentration in the surrounding medium [59, 60]. At very low or no salt in the bulk, the number of protons inside the brush is sufficiently high as compared to bulk, which develops an electrostatic potential between the bulk and brush. Consequently, it responds to an unfavorable electrostatic interaction by dissociating themselves with increase in salt concentration, resulting in an expansion of brush structure. Such an anomalous behavior of increasing brush height with increasing ion concentration in OsB regime is a distinct property of a weak PE, due to varying degree of dissociation. Such a response is not seen in strong PE as it dissociates at all pH ranges.

Now, the theoretically predicted values of brush height are compared with the experimentally obtained decay length values. **Figure 4.5a** shows the intermolecular force measurement for PAA adsorbed at liquid interface at pH 5. The force profiles between the PAA adsorbed surface decay exponentially with distance. In the salt concentration range from zero to 8 μM, though the interdroplet distance decrease with increase in salt concentration, the force profile decay slowly due to swelling of the adsorbed PAA as shown in the **Figure 4.5a**. In the above salt concentration, the PAA is in the OsB regime, where the swelling of the PE with salt (decay length) scales as $\lambda^{0.05}$ whereas theoretically predicted exponent is 0.33 **(Figure 4.5b).** The very low exponent obtained in our experiment may be due to steric interaction[59]. The swelling of PAA happens due to electrostatic interaction between the dissociated monomer and steric interaction between monomer, where the latter contribution is neglected in the scaling theory of Zhulina [50]. Such a lower value of the brush thickness in the OsB regime was observed earlier, where the exponent was found to be 0.1 [59] . Zhang et al. [202] observed a slow expansion rate of the PMMA brush adsorbed on a solid planar surface, which was attributed to the non-inclusion of hydrophobicity of polymer backbone, polydispersity of the chains and three body interaction at higher grafting density in the theory of Zhulina [50].

The force distance profile in the SB regime (at higher Ca^{2+} concentration) and the corresponding decay length variations are shown in **Figure 4.5 c & d,** respectively, where the decay length scales with salt concentration as $\lambda \sim \varphi_S^{-0.26}$. The brush height reaches a maximum value at 9 x 10^{-5} M. The observed exponent of -0.26 was in reasonably good agreement with the scaling law of Zhulina [50]. The force profile decays rapidly with increasing salt content. Though the electrostatic interaction of the adsorbed PAA is screened out in the presence of relatively high salt content, the brush remains stable due to short range excluded volume interaction [203].

4.3.5 Behavior of adsorbed PAA at different pH and trivalent salts concentrations

Figure 4.6a shows the intermolecular force measurement of E_{PAA450} emulsion (pH = 5) at different concentrations of Fe^{3+}. The decay length obtained from the force profiles for different salt concentration is plotted in the **Figure 4.6b.** In the absence of salt, the onset of interaction begins at a higher interdroplet distance. As the salt concentration is increased from 2.5 to 250 μM, the brush collapses with a decay length of $\lambda^{-0.188}$, which is very close to the theoretically predicted collapse of brush height ($H^{-0.14}$) [199] . Force measurements were also carried out at pH 6 and 8 and the decay length values are plotted as a function of salt concentration and are shown in **Figure 4.6 c & d,** respectively. The decay length changes at pH 6 and 8 followed as $\lambda^{-0.19}$ and $\lambda^{-0.17}$, respectively. These results suggest that irrespective of the medium pH, the collapse rate of the adsorbed PAA at liquid-liquid interface is similar.

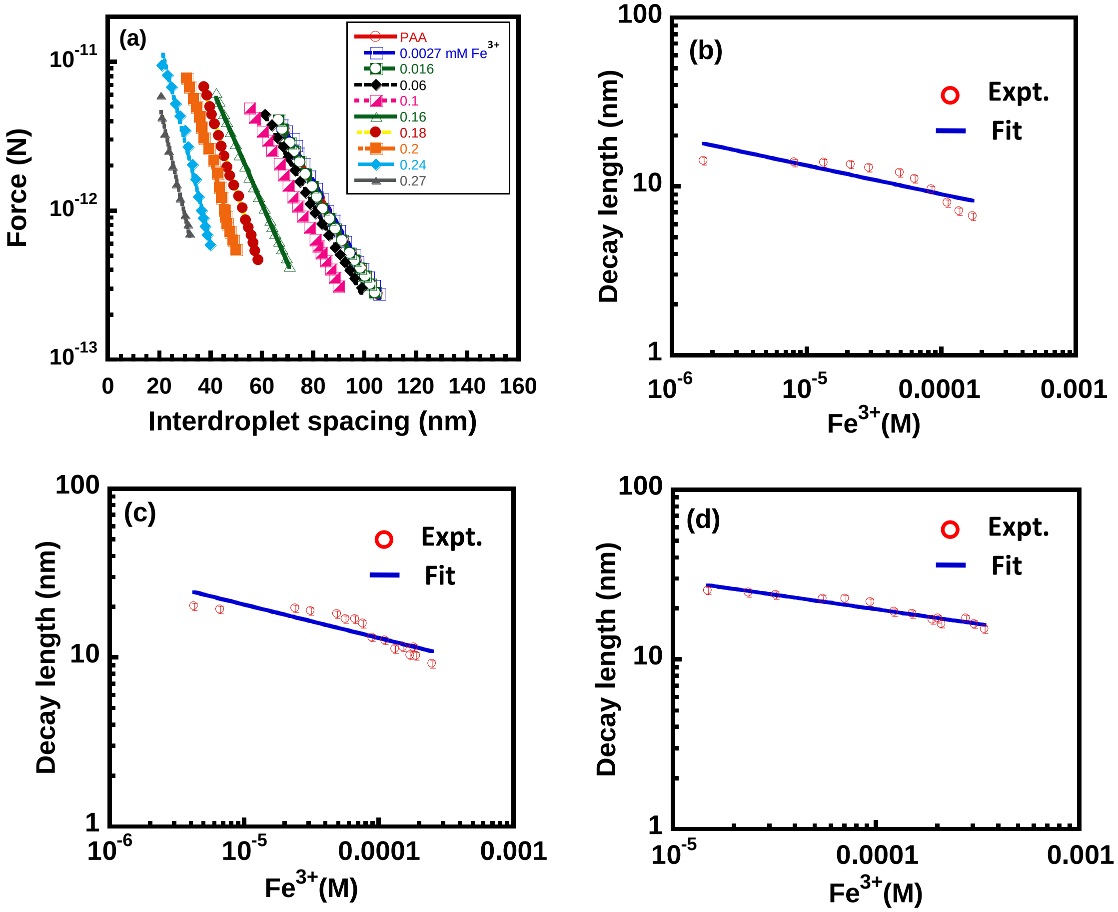

Figure 4.6: (a & b) Force-distance curve of E_{PAA450} emulsion for various concentrations of Fe^{3+} at pH 5 and the corresponding decay length variation. The best fit is shown by the solid line where λ ~ $\varphi_s^{-0.17}$ and $R^2 = 0.83$. (c & d) Decay length of E_{PAA450} emulsion for various concentration of Fe^{3+} at pH 6 and pH 8, respectively, where the decay length scales with concentration of salt as λ ~ $\varphi_s^{-0.196}$ ($R^2 = 0.84$) and λ ~ $\varphi_s^{-0.172}$ ($R^2 = 0.95$).

4.3.6 Effect of salt of different valences on the conformation of adsorbed PAA at interface

To understand the swelling and collapse of the adsorbed PE in the OsB and SB regime for salt of different valences, force measurements (**Figure 4.7)** were performed for E_{PAA450} emulsion at low and high concentrations of Na^+, Ca^{2+} and Fe^{3+} at a fixed pH **.** **Figure 4.7 (a-c) and (d-f)** show the decay length vs. Na^+, Ca^{2+} and Fe^{3+} at low and high concentrations for E_{PAA450} emulsion, respectively. Here, the increase and decrease in the decay length indicate the swelling and collapse of the adsorbed PAA.

During the swelling of the PAA at low salt concentrations, the λ scales with concentration of salt as ~ φ_s^x , where the exponent x was found to be 0.068, 0.049 and 0.072, respectively for Na^+, Ca^{2+} and Fe^{3+}, respectively. These exponents were ~ 20 % of the theoretically predicted value. But, in the high salt concentrations the λ scales as ~ φ_s^{-y} where y values were 0.3, 0.26 and 0.17 for Na^+, Ca^{2+} and Fe^{3+}, respectively. These values are comparable with the theoretical predictions of mono, di and trivalent ions, respectively [199]. According to the scaling theory of Zhulina [199] the brush height variation in the presence of multivalent co-ion and counter-ions become a function of the valence (q). In the presence of low concentration of salt, brush height due to the effect of co-ions is given by $H = a_{mon}^{4/3}\alpha_0^{1/2}\frac{\varphi_H^{\frac{1}{3}}(\varphi_H + q\varphi_S)^{1/3}s^{1/3}}{K_{acid}^{1/6}}N$ where K_{acid} is the acid dissociation constant. At high salt concentration, $H \approx \frac{\alpha_0 N}{q\varphi_S s}$. Therefore, at low salt concentration, the brush height increases with $(q\varphi_s)^{1/3}$, attains a maximum and collapses as $\frac{1}{q\varphi_s}$ at high salt concentration. The effect of counter-ion to the brush height at low and high salt concentration consists of four different regimes where the brush height undergo collapse as $H = a^{2/3}\alpha_0^{2/3}N\ [q(q+1)\varphi_S\, S]^{-1/3}$ at high salt concentration again (SB regime where $\alpha \approx \alpha_0$). In our experiment, it was difficult to distinguish the different regimes due to co-ion and counter-ion effects. However, the swelling rate of PAA remains the same at all valence of salts at low concentration but collapses at high salt concentration where it showed different scaling exponents. This observation was in agreement with the OsB regime but was different from the predicted exponent in the SB regime of co-ion (~ -0.3 against the predicted exponent of -1). In the SB regime of CI, according to theory, the brush height collapse with an exponent of -0.33 for different salt valences. We observed different decay lengths, $\lambda \sim {\varphi_s}^{-0.3}$, ${\varphi_s}^{-0.26}$ and ${\varphi_s}^{-0.17}$ for mono-, di-, and tri-valent ions, respectively. Interestingly, the predicted scaling for the collapse in OsB regime, $H \sim (\varphi_s)^{-1/q+2}$ matches with our experimental observations in the SB regime.

Langevin dynamic simulation of PE brush at various salt concentrations, valence and grafting density, showed that the brush collapse rate was found to vary slowly in monovalent salt solution as $C_S^{-0.15}$, whereas in divalent and trivalent solutions, the brush collapses initially but expands slightly at high concentration due to charge inversion [185]. A neutron reflectivity and surface force measurement study on polystyrene sulfonate (PSS) brush showed a collapse of brush height in presence of monovalent ions in SB regime whereas in the presence of multivalent ions, an abrupt collapse of brush is observed at very low salt concentrations and the effect was found to be reversible [204].

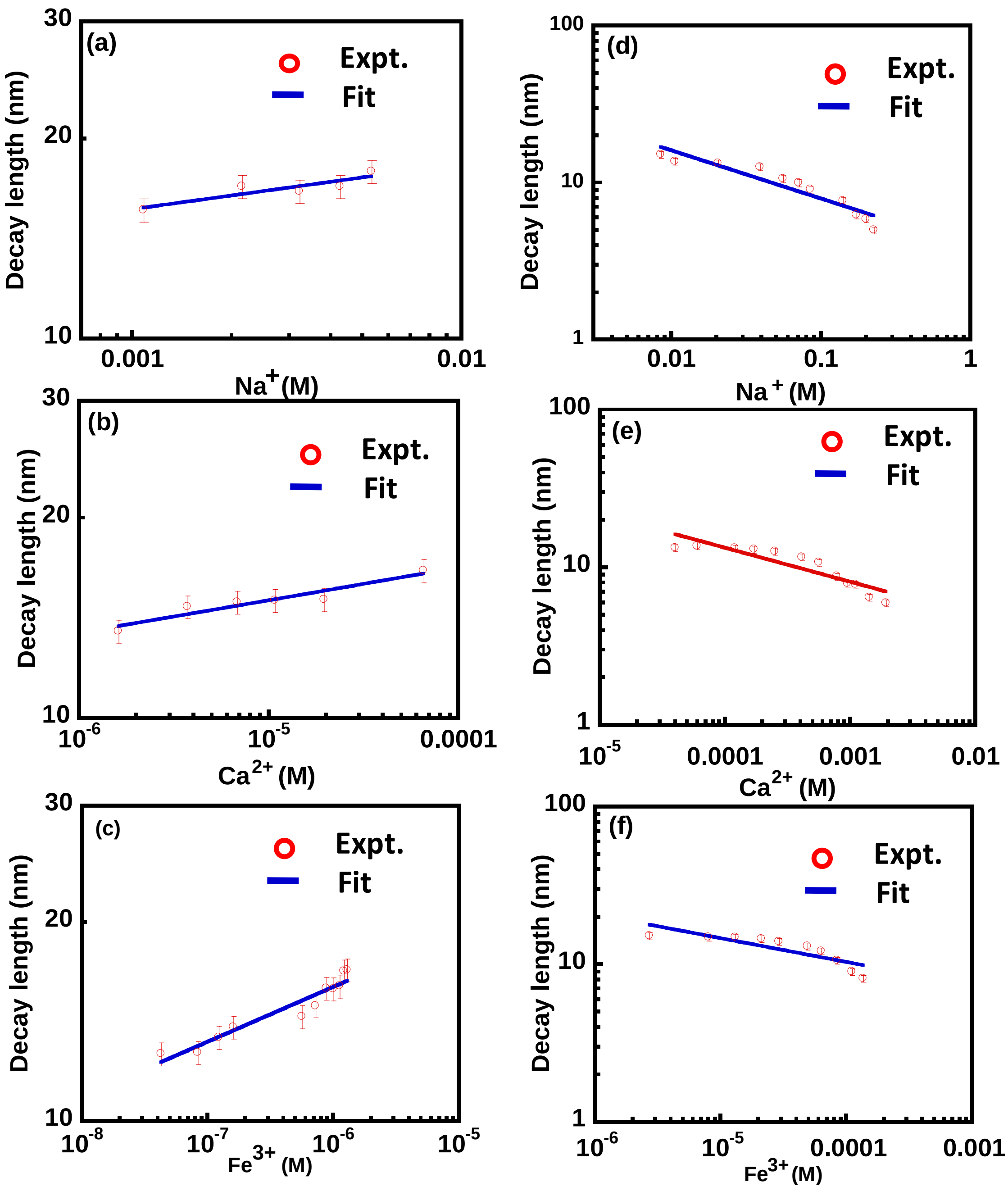

Figure 4.7: The decay length vs. salt concentration for low salt region. The theoretical fit is shown by the solid line. (a) Na^+, **(**λ ~ $\varphi_s^{0.067}$ and $R^2 = 0.89$), (b) Ca^{2+} (λ ~ $\varphi_s^{0.049}$ and $R^2 = 0.95$) and (c) Fe^{3+} (λ ~ $\varphi_s^{0.072}$ and $R^2 = 0.95$). At high salt concentrations (d) Na^+ (λ ~ $\varphi_s^{-0.30}$ and $R^2 = 0.93$), (e) Ca^{2+} (λ ~ $\varphi_s^{-0.27}$ and $R^2 = 0.81$) and (f) Fe^{3+} (λ ~ $\varphi_s^{-0.166}$ and $R^2 = 0.82$).

A study showed that the ion exchange and strong binding of trivalent ion to the end tethered PE leads to lowering of the osmotic pressure in the brush layer when several monovalent CI's are replaced by a single multivalent ion [205]. For divalent (Ca^{2+}) and trivalent ions (Fe^{3+}), the osmotic pressure reduction was twice and thrice, respectively. Experiments were carried out by Farina et al. [55], using surface force apparatus for PE brush immersed in a mixture of mono and trivalent ions (Ru^{3+}) found that at low concentration, the brush structure goes from an extended to a collapsed state without any hysteresis during force measurement but at very high concentration of Ru^{3+}, the PE brush collapse was complete, with an adhesive force between the surfaces during retractions, which was attributed to the uptake of Ru^{3+} ions inside the PE brush.

Though the earlier studies confirm the collapse of PE, the exact role of multivalent ions on conformational changes especially on adhesion forces is still not clear [53, 179]. The theoretically predicted collapse rate of an end tethered PE in multivalent ion solution was found to be very small as compared to the experimental results [54]. According to the predictions of Brettmann et al. [54], the brush height undergoes a first-order transition from an extended state to a collapsed state at a critical multivalent CI concentration. A recent study showed that trivalent ion (spermidine^{3+}) can provoke lateral microphase segregation in DNA brushes, where the collapse of polymer brush was collapsed into octopus-like surface micelles [201].

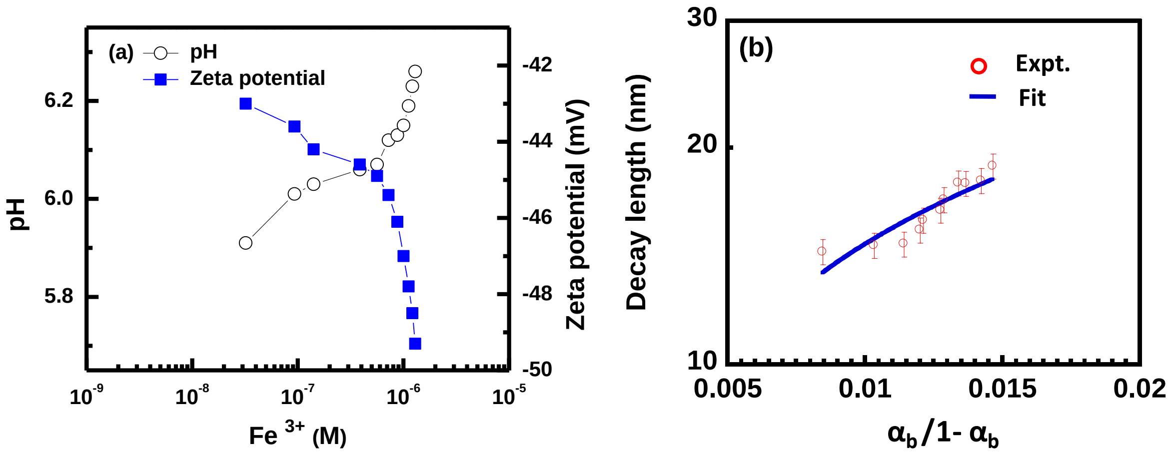

Figure 4.8: (a) Zeta potential and pH for E$_{PAA450}$ emulsion in the presence of Fe^{3+} of 3.2 x 10^{-8} to 1.2 x 10^{-6} M and (b) Variation of decay length (~brush height) as a function of α_b/1-α_b. The best fit on the experimental data is given by $\lambda \sim \left(\frac{\alpha_b}{1-\alpha_b}\right)^{0.54}$ and R^2 = 0.95.

To understand the expansion and collapse of the brush height in the presence of Fe^{3+}, the pH and zeta potential values of E$_{PAA450}$ emulsion at different ion (Fe^{3+}) concentrations were measured. **Figure 4.8a** shows the variation of zeta potential and pH in the OsB regime, where pH of the medium changes from 5.7 to 6.26 and the zeta potential increases from -42 to -50 mV, as the salt concentration is increased from 3.2 x 10^{-8} to 1.2 x 10^{-6} M. The increase in pH of the medium in OsB regime and the corresponding increase in zeta potential (and the first interaction distance) support the argument of expanded brush height. The variation of $\frac{\alpha_b}{1-\alpha_b}$ is plotted against decay length (**Figure 4.8b**), which shows that by increasing the parameter $\frac{\alpha_b}{1-\alpha_b}$, the brush height increases, which is in agreement with the theoretical scaling prediction, where the brush height is given by $H \sim N a_{mon}^{4/3} \sigma^{1/3} \left(\frac{\alpha_b}{1-\alpha_b}\right)^{1/3} ([H^+] + \varphi_s)^{1/3}$. Here, the dissociation constant is measured in the bulk. The observed exponent was 0.54 against the theoretically predicted value of 0.33.

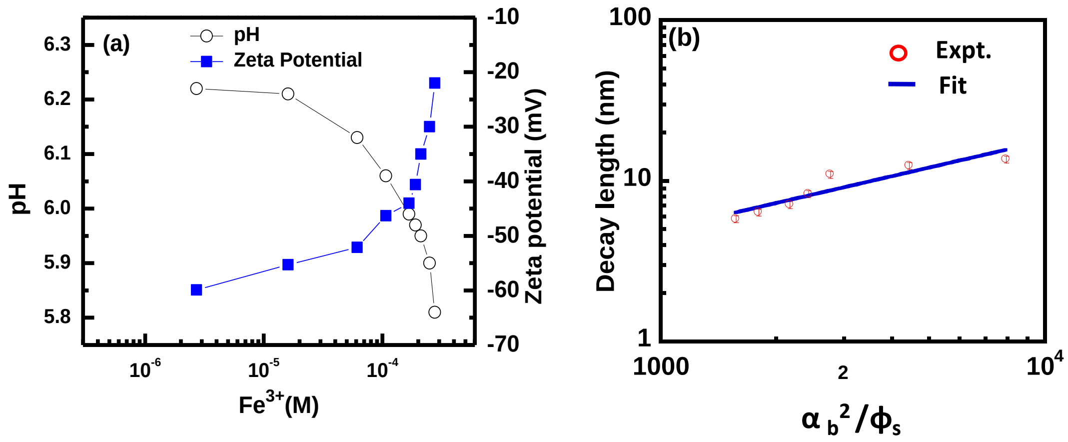

Figure 4.9: (a) Variation of pH and zeta potential for E_{PAA450} emulsion for different trivalent ion concentrations (salted brush regime) (b) Decay length vs. α_b^2/φ_s in the same regime. The theoretical fit is shown by the solid line.

This study was extended for higher salt (Fe^{3+}) concentration to understand the behavior of brush in SB regime. The variation of pH and zeta potential as a function of salt concentration are shown in the **Figure 4.9a.** With increase in salt concentration, the pH of the medium decreases from 6.2 to 5.8 and zeta potential decreases from -58 to -22 mV. This is in agreement with the collapse of brush thickness and the observed decrease in $2L_0$ was opposite to the observed change in OsB regime. The collapse of the brush height in the SB regime is due to neutralization of the COO^- group. We have also plotted the ratio of square of bulk dissociation constant (α_b^2) to the ionic strength (φ_s) against the decay length, proposed by Zhulina [50] $(H = N(a_{mon}^2\alpha_b^2\sigma^{-1}\varphi_s^{-1})^{1/3})$ and is shown in **Figure 4.9b**. The exponent obtained from the best fit (0.52) was higher than the predicted value of 0.33. These experimental results point the fact that the theoretical predictions are fairly accurate in describing the behavior of PE's in solutions under different environmental conditions. The theoretically predicted scaling exponents and the experimentally obtained values in different environmental conditions are tabulated in **Table 4.1.**

Table 4.1: Theoretically predicted scaling exponents and the experimentally obtained values in different environmental conditions.

S.No	Theory	Predicted value	Experimentally obtained value
1.	Counter-ion fluctuation theory [197]	$R_g \sim l_b^{0.33}$	$\lambda \sim l_b^{0.21}$
2.	Mean field theory (The equilibrium brush height in the OsB regime is related to the salt concentration and bulk dissociation constant) [50]	$H \sim (\varphi_s)^{0.33}$	$\lambda \sim (\varphi_s)^{0.05}$
		$H \sim \left(\frac{\alpha_b}{1-\alpha_b}\right)^{0.33}$	$\lambda \sim \left(\frac{\alpha_b}{1-\alpha_b}\right)^{0.54}$
3.	Mean field theory (Equilibrium brush height in the SB regime) [50]	$H = (\varphi_s^{-1})^{0.33}$	$\lambda = (\varphi_s^{-1})^{0.26}$
		$H = (\alpha_b^2 \varphi_s^{-1})^{0.33}$	$\lambda = (\alpha_b^2 \varphi_s^{-1})^{0.52}$
4.	Scaling theory for multivalent ion solution [199]: 1. The contribution of co-ion to the brush height	$H = (\varphi_s)^{1/3}$	Monovalent $\lambda = (\varphi_s)^{0.068}$
			Divalent $\lambda = (\varphi_s)^{0.049}$
			Trivalent $\lambda = (\varphi_s)^{0.07}$
	2. The contribution of counter-ion to the brush height	$H = (\varphi_s)^{-1/q+2}$	
		Monovalent $H = (\varphi_s)^{-0.33}$	Monovalent $\lambda = (\varphi_s)^{-0.30}$
		Divalent $H = (\varphi_s)^{-0.25}$	Divalent $\lambda = (\varphi_s)^{-0.26}$
		Trivalent $H = (\varphi_s)^{-0.2}$	Trivalent $\lambda = (\varphi_s)^{-0.16}$

4.3.7 Effect of Molecular Weight on Polyelectrolyte Conformational changes

One of the universal properties of the responsive polymers was the coil to globule transition (CGT), which was assumed to be independent of their molecular weight. PAA is the one of the response stimuli polymers that undergoes a coil to globule transition (CGT) with a change in pH of the medium. Even at lower molecular weight, PAA is expected to undergo extended rod-like structure when it is in ionized state but exhibits a small globular structure in the neutral state. But, a recent study using fluorescent measurement [39] showed that the CGT of PAA is highly dependent on their molecular weight and only the polymer of higher molecular weight exhibit measurable CGT. To confirm this, we study CGT of PAA of three different molecular weights (15, 250 and 450 K) as a function of pH using the equilibrium force measurement.

Figure 4.10 (a-c) shows the force-distance profile of E_{PAA15}, E_{PAA250} and E_{PAA450} emulsion, respectively as a function of pH. The corresponding decay length (λ) obtained from the slope of the force-distance profile as a function of pH for all molecular weight is shown in the **Figure 4.10d**. The force profiles in all three cases were repulsive in nature and decaying exponentially with distance. For E_{PAA15} emulsion, at pH 3.0, the onset of interaction started at a lower interdroplet spacing and does not show any abrupt variation with increase in pH. The corresponding average λ obtained from the force profile was found to be 3.6 nm at pH 3.3 and remained almost the same even at high pH. Though, the onset of interaction changes slightly with different pH, the slope of the force profile remains the same at all pH level. But, for E_{PAA250} and E_{PAA450} emulsion, there was a dramatic change in force profile and the onset of interaction is found to increase with increase in pH. The λ was found to be 6.0 and

6.6 nm at pH 3.0 but reaches 27 and 31 nm at a pH 11.8, with a total variation in λ of 21.0 and 23.4 nm for E_{PAA250} and E_{PAA450} emulsion, respectively.

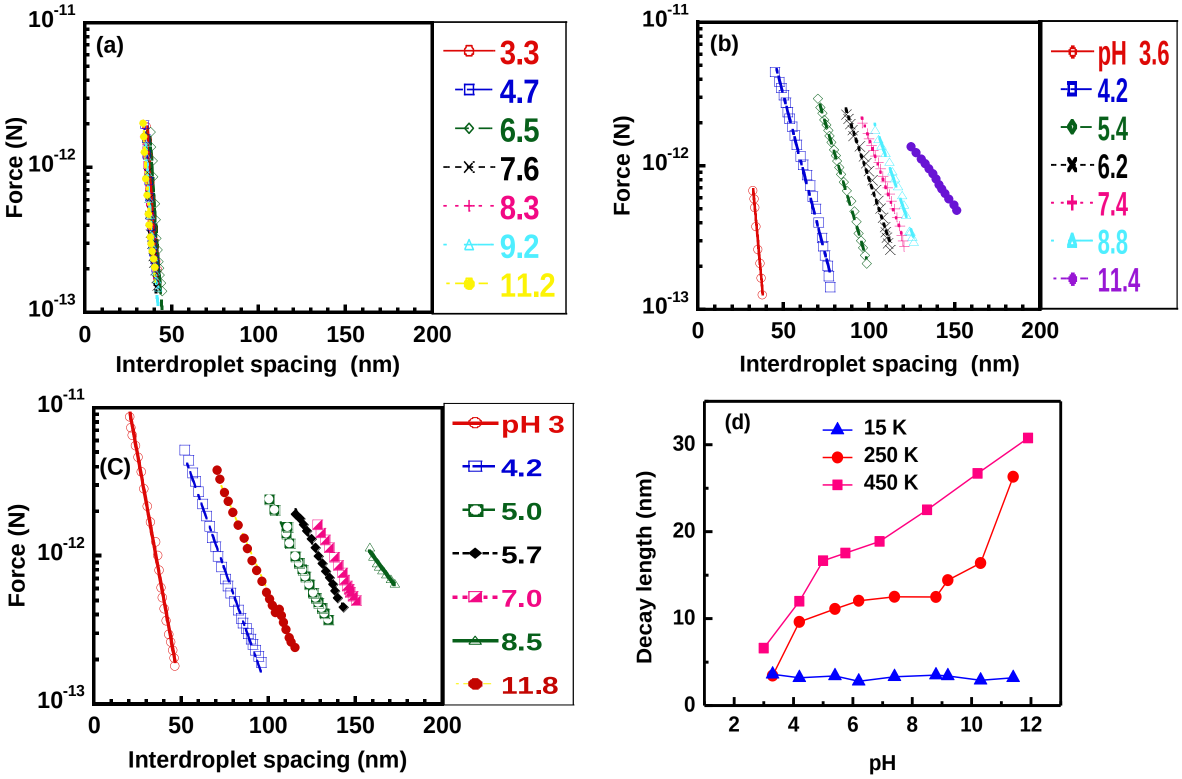

Figure 4.10: Intermolecular force as a function of distance for (a) E_{PAA15} (b) E_{PAA250} and (c) E_{PAA450} emulsion in the pH range from 3 to 11. (d) Decay length of the same as a function of pH.

The role of molecular weight of PAA on the force parameter at different pH value is discussed. The λ value obtained for adsorbed PAA of molecular weight 250 and 450 K at pH ~ 3.0 were found to be 6 and 6.6 nm, respectively, indicating a collapsed conformation of PAA at the O/W interface. As the pH increases, the onset of interaction increases progressively due to swelling of the adsorbed PAA. At pH 11, the λ value increases from 27 to 31 nm, indicating an extended conformation of PAA at the interface. The typical λ where a polymer is adsorbed at an interface is compared to the brush height (L_b) approximated as

$L_b = \Gamma^{1/3} R_f^{5/3}$, where R_f is the Flory radius as per the Alexander's scaling theory [206]. Earlier studies showed that for a polymer adsorbed at the O/W interface, the extension of the polymer (decay length) is comparable with the radius of gyration of the free polymer in solution [109]. By approximately considering the Flory radius and radius of gyration of PE to be same in the present study, the brush height obtained using Alexander theory of polymer is found to be 2.8 and 3.4 nm at low pH and 33 and 47 nm at high pH for PAA of 250 and 450 K, respectively which were quite comparable to the λ values observed in our experiment. The deviation arises at high pH could be because of physisorption of PE at O/W interface. However, for E_{PAA15} the λ variation at low (3.0) and high (11.0) pH were 2.6 and 3.4 nm, respectively. The brush height in a collapsed and extended conformation according to theoretical calculation was found to be 1.2 and 6.1 nm, respectively.

During the onset of globule to extended transition, the product of Bjerrum length and the square of the number of ionized monomers is the same as the Flory radius ($a_{mon}N^{1/2}$) (where a_{mon} is the size of the monomer and N is the degree of polymerization) [39], i.e,. $\frac{(feN)}{4\pi\varepsilon\varepsilon_0 k_b T} = a_{mon}N^{1/2}$. The study showed that below the Flory radius, the excluded volume controls the chain size and the chain adopts a self-avoiding walk. Based on the above calculation, the value of N at which the coil to globule transition takes place was found to be 4.3. But, experimentally only above N = 230, the coil to globule transition was observed, which is more than an order of magnitude greater than the theoretical prediction [39]. The discrepancy was explained by considering the formation of hydrogen bond between the PAA monomers and between the monomer and water. The effective energy of PAA increases with degree of polymerization due to hydrogen bond of neighboring monomers, which is very low for lower molecular weight PAA. It was also found that only above a critical molecular weight, PAA undergoes coil to globule transition whereas PAA chain always exhibit random walk by displaying a swollen behavior at all pH below a critical molecular weight. In the beginning of coil to globule transition, the thermal energy dominates over electrostatic interactions and pH dependence effect disappears.

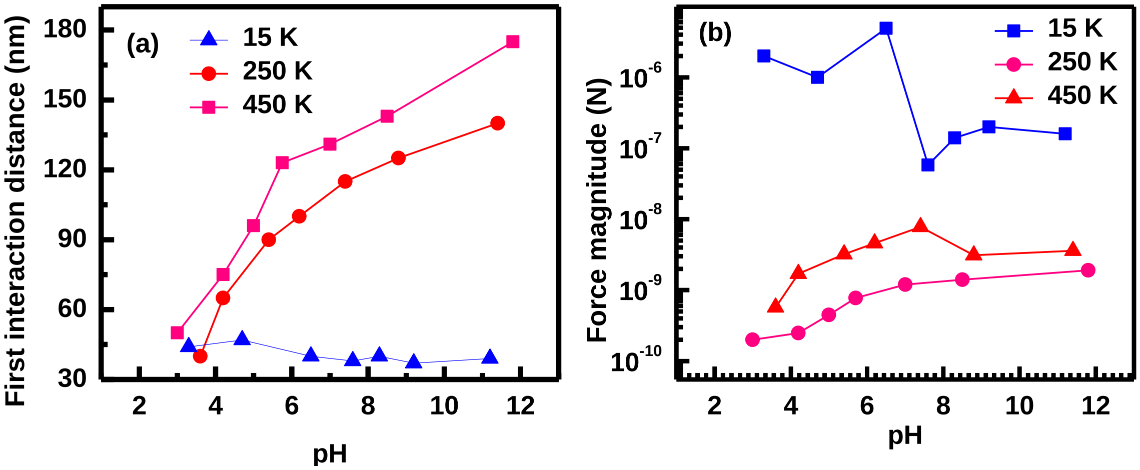

Figure 4.11: (a & b) First interaction distance and force magnitude as a function of pH for E_{PAA15}, E_{PAA250} and E_{PAA450} emulsion.

A study [207] showed a strong molecular weight dependence of fluorescence emission from pyrene labeled PAA of low (2 Kg/mol) and high (450 Kg/mol) molecular weight in aqueous solution due to different degree and level of intra molecular association [207]. We observed almost no change in λ for E_{PAA15} emulsion but a huge change in λ for E_{PAA250} and E_{PAA450} emulsion, which was quite consistent with the earlier works [39, 207]. This observation was further supported by the other force parameters and light scattering measurement of E_{PAA15}, E_{PAA250} and E_{PAA450} emulsion.

To understand the force profile and the adsorbed molecular behavior, first interaction distance ($2L_0$) and force magnitude (K) for E_{PAA15}, E_{PAA250} and E_{PAA450} emulsion were obtained at different pH. **Figure 4.11a** shows variation of $2L_0$ for E_{PAA15}, E_{PAA250} and E_{PAA450} emulsion, respectively as a function of pH. $2L_0$ was 44 nm at pH 3.0 and becomes 39 nm at pH 11.5 for E_{PAA15} emulsion but the values were 40 and 50 nm at pH 3.0 for E_{PAA250} and E_{PAA450} emulsion, respectively and it increased to 140 and 175 nm at pH 11.5. The huge variation in $2L_0$ for higher molecular weight PAA (250 and 450 K) reflects the fact that PAA undergoes significant changes in globule to extended transformation with increase in pH. The stretching of the high molecular weight PAA, as observed from earlier measurement was clearly evident in the $2L_0$ variation also. The enhanced stretching of adsorbed PAA with increase in pH was due to enhanced dissociation of the surface group of PAA (COOH into COO^- and H^+). The swelling or extension of adsorbed PAA was evident from the increase in Bragg peak position, λ and $2L_0$. As PAA exhibits globule structure with no charge at low pH, excluded volume interaction plays an important role but at high pH the electrostatic interaction dominates. The increase in droplet distance (due to dissociation of surface group) with increase in pH of the medium can be understood from the increase in force magnitude as shown in the **Figure 4.11b**. The increase in force magnitude by one order of magnitude between pH 3 and 11.8 for E_{PAA250} and E_{PAA450} emulsion shows an enhanced repulsion between the dissociated surface groups whereas for E_{PAA15} emulsion, the force magnitude change was insignificant.

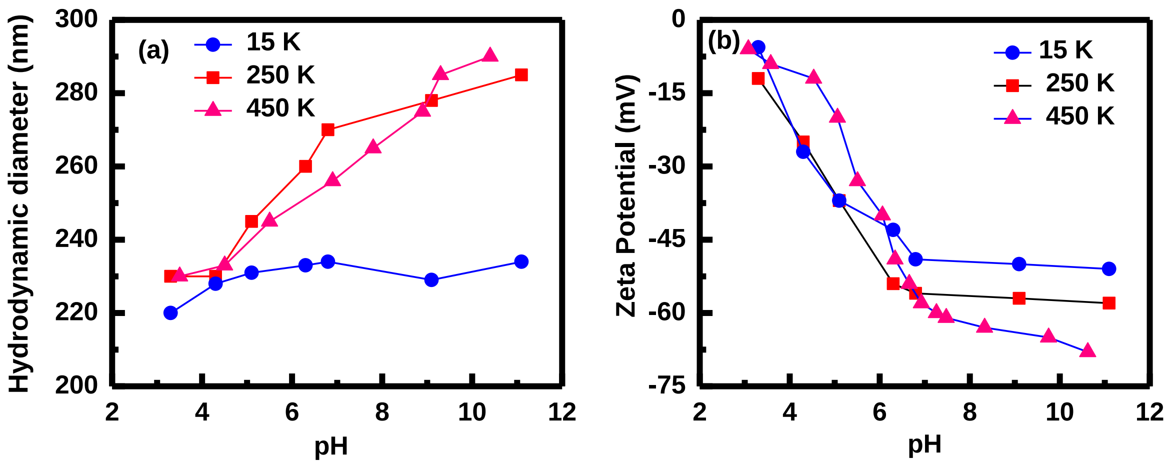

Figure 4.12: (a & b) Hydrodynamic diameter and zeta potential as a function of pH for E_{PAA15}, E_{PAA250} and E_{PAA450} emulsion.

Figure 4.12 (a & b) shows the hydrodynamic diameter and zeta potential of E_{PAA15}, E_{PAA250} and E_{PAA450} emulsion as a function of pH. The average droplet size increases from 200 to 220 nm for E_{PAA15} and 200 to 230 nm for E_{PAA250} and E_{PAA450}, at pH 3.0. The polydispersity index of the E_{PAA250} and E_{PAA450} is 0.15 and 0.2, respectively whereas for E_{PAA15}, the PDI was 0.08. PAA adsorption at O/W interface leads to a significant growth in emulsion droplet size and also the surface charge. The zeta potential was found to be increasing with increasing pH of the medium above pK_a due to ionization of PAA backbone. At low pH (~ 3.0), for PAA of 450 K the zeta potential was -2 mV but increases to -70 mV at pH 12, due to enhanced dissociation of the carboxyl group of the PAA as shown in the **Figure 4.12b.** It was shown that PAA is highly neutral in nature at low pH but attains charged at high pH due to ionization of surface group (COOH) at the polymer backbone above pK_a [190]. The pK_a of adsorbed PAA is found to be different at the end group from the surface [170]. It was shown that the pK_a of the end group is 4.5-4.6 whereas the surface pK_a is 6.4-6.5. In our case, the PAA becomes charged at pH > 4, as observed from zeta potential measurement. It shows that the end groups protrude into the aqueous phase dissociates first.

The results also shows that very low charge density enables a coiled structure (at low pH), where monomers were neutral but stretches out at higher pH due to enhanced dissociation of carboxyl group at the PAA backbone, with diffused counter-ion (H^+) in the aqueous phase. In this case, with increase in pH, the H_d of E_{PAA250} and E_{PAA450} emulsion increased with increasing pH from 230 nm (at pH ~ 3) to 290 nm (at pH ~ 12), whereas E_{PAA15} emulsion, the size of the emulsion droplets remains constant at all pH. These results indicate that only high molar mass PAA adsorbed at the oil-water interface exhibit measurable pH dependent coil to globule transition.

4.4 Conclusions

The behavior of adsorbed weak polyelectrolyte (polyacrylic acid) at the oil-water interfaces is systematically studied under different environmental conditions such as ions of different valences, pH and molecular weight. The role of molecular weight and pH on the conformational changes are studied using this approach and are compared with direct intermolecular force, dynamic light scattering and zeta potential measurements. The results show that, in the absence of salt, adsorbed PAA undergo a reversible conformational change from compact globule at low pH to highly extended conformation at high pH due to electrostatic repulsion of backbone functional group, between the pH range of 3.0 and 11.8. The adsorbed PAA undergoes an extended conformation in the osmotic brush regime but collapses in the salted brush regime. The rate of swelling and shrinking in the presence of salt of different valence was found to be in good agreement with the theoretical predictions under some conditions. In the case of multivalent ions, the adsorbed polymer not only undergoes a sharp collapse at very low concentration of ions but also trigger irreversible aggregation, possibly due to bridged network like structure. The intermolecular force measurement for PAA of different molecular weight also showed that globule to extended transition is significant only for adsorbed PAA of molecular weight > 15 K. This study provides a new insights into the adsorbed macromolecule at O/W interface that enable improved stabilization of colloidal dispersion, enhanced oil recovery and targeting drug/protein delivery. Also, the experimental results provide new directions to probe macromolecular conformational changes at interfaces and provide novel ways of creating stimuli responsive nanostructures (e.g. pH, temperature, ion etc), lubrication, stabilization of colloids and drug delivery systems.

CHAPTER 5

Electro-steric interaction due to strong polyelectrolyte, poly(diallyldimethylammonium chloride) physisorbed at the oil-water interface under different environments: A comparison with weak polyelectrolyte

5.1. Introduction

Stimuli responsive functional materials find many technological applications in nano and micro level devices [86, 208-210]. Certain polymer brushes grafted or adsorbed on surfaces to control the overall behavior of the surface of interest by simply varying an environmental stimulus such as pH, temperature [211], ionic strength [204], electric field [212] etc. Controlling such surface behavior is important for applications in bio-medicine [213-215], lubrication [88, 216] etc. PE's coated lipid based complex capsules were shown to exhibit enhanced stability in organic solvent and proposed for controlled release applications [217]. Though the behavior of neutral polymers in bulk and interface is fairly well studied, the studies on the behavior of PE at interfaces are scarce [97]. It is known that the behavior of adsorbed PE on colloidal interfaces dictate the long term stability and rheology [218]. Natural polymers such as DNA, RNA, protein, polysaccrides etc belong to the family of PE's and thus an understanding of their behavior in bulk and interfaces [38, 56] under different environmental conditions not only enables to develop newer applications but also helps to understand the biologically important phenomenon such as protein aggragation [219], binding of protein, adsorption of DNA, protein folding [171], DNA condensation [172] etc.

The characteristics of adsorbed weak PE is different from strong PE in bulk under the same physio-chemical conditions such as pH, salt content, solvent medium, temperature [48, 50, 53, 56, 57] etc. For instance, the charge distribution and the fraction of charge over a weak

PE [50, 58](weak acid and base) are strongly dependant on solution pH and salt, thereby exhibiting coil to globule transition whereas strong acid or strong base display pH and salt insensitive behavior (up to particular salt concentration) [220]. Though it is known that PE behavior changes with physio-chemical conditions, studies show that their conformational changes can also depends on the molecular properties such as molecular weight [39], polydispersity [221] etc for weak PE. A recent study shows that the behavior of a strong PE can vary with solution pH [47, 222].

Though numerous studies have been carried out to understand the behavior of chemically anchored PE theoretically [32, 50, 51, 53, 56, 58, 182, 223, 224] as well as experimentally, [59, 60, 179, 180] the studies on physisorbed PE at liquid-liquid interface are scarce. The prime objective of the present study is to understand the behavior of a physisorbed strong PE at an oil-water interface and compare the results with that of a weak PE. The conformational changes of a physisorbed strong poly(diallyldimethylammonium chloride) - (PDDA) and weak poly(acrylic acid) - (PAA) at a magnetically polarizable oil-water interface under different pH, salt of concentrations and valences is studied here.

5.2. Materials

Magnetic nanoemulsions, E_{PAA450} and E_{PDDA} (PAA of 450 and PDDA of < 100 kg/mol stabilized emulsion, respectively) are used in this study. Material preparation and experimental setup are explained in Chapter II. Intermolecular interaction for E_{PAA450} and E_{PDDA} at different pH and salts of various concentrations and valances were measured using magnetic chaining technique.

5.3 Result and discussion

5.3.1 Hydrodynamic size and zeta potential of E_{PDDA} and E_{PAA450} emulsion

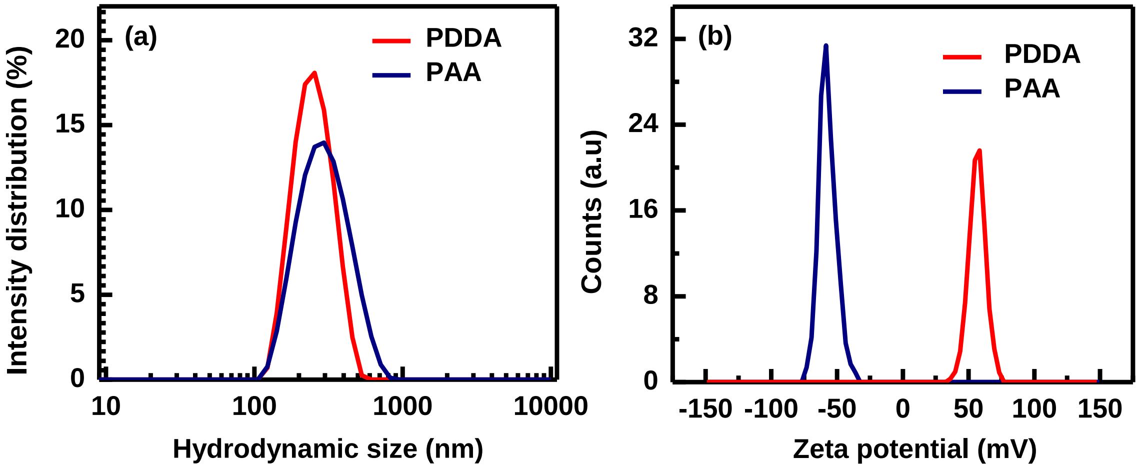

Figure 5.1: (a) Hydrodynamic diameter (H_d) and (b) zeta potential (ζ) of E_{PDDA} and E_{PAA450} emulsion. The average hydrodynamic diameter of E_{PDDA} and E_{PAA450} emulsion at pH = 7 were 270 and 255 nm, respectively. The ζ potentials values were + 58 mV and - 55 mV at pH = 7, for E_{PDDA} and E_{PAA450} emulsion respectively.

The hydrodynamic size (H_d) distribution and zeta potential (ζ) of E_{PDDA} and E_{PAA450} emulsion at pH 7 is shown in the **Figure 5.1 a & b,** respectively. The average H_d and ζ of E_{PDDA} emulsion at pH of 7 is found to be 250 nm and + 58 mV, respectively. The polydispersity index (PDI) of the E_{PDDA} emulsion is 0.1, indicating fairly good monodisperse nature of the emulsion. Adsorption of PDDA at the liquid-liquid interface results in a significant increase in emulsion droplet size to 250 nm and zeta potential to + 58 mV. Similarly, adsorption of PAA at emulsion interface increased the droplet size to 270 nm and the corresponding zeta potential changes to -55 mV at pH ~ 7. The polydispersity index of the E_{PAA450} emulsion was 0.2, indicating a lower monodispersity than the E_{PDDA} emulsion.

5.3.2 Effect of pH on interaction forces for E_{PDDA} and E_{PAA450} emulsion

The force profile of E_{PDDA} emulsion at different pH is shown in the **Figure 5.2a.** The force profiles in all cases were repulsive and decaying exponentially with distance, similar to the E_{PAA450} emulsion [113]. The force profiles here is described by an exponential function as $F(h) = K\exp(-\frac{h}{\lambda})$, where K is the pre-exponential factor, h is the interdroplet spacing and λ is the decay length, respectively [109, 198]. From the force profiles, decay length (λ) and first interaction distance ($2L_0$), are evaluated for E_{PDDA} and E_{PAA450}, as a function of pH (**Figure 5.2 b & c)**. Zeta potential of E_{PDDA} and E_{PAA450} emulsion at different pH is shown in the **Figure 5.2d**.

The PE mediated interactions arise from a combination of electrostatic, conformational entropy of polymer chain and steric interaction. Here, the electrostatic interactions are altered due to the variation in charge density over the PE backbone when they are exposed to different pH or ionic strength. In the present case, at pH 2.0, the onset of interaction in the force profile for E_{PDDA} emulsion begins at a higher interdroplet spacing and remains the same till the solution pH reaches 10.0 as shown in the **Figure 5.2a.** With further increase in pH (> 10), the onset of interaction decreases to a lower interdroplet spacing. But, the onset of interaction for E_{PAA450} emulsion begins at a lower interdroplet spacing that increases to a higher value with increase in pH [113]. To compare the behavior of PDDA and PAA, the force parameter values for PDDA and PAA are compared. For E_{PDDA} emulsion, λ was found to be ~ 17 nm between the solution pH 2.5 and 10.0 but with further increase in pH, λ decreases and reaches a value of 4 nm at a pH of 12.5, whereas for E_{PAA450} emulsion, λ was found to be 6.6 nm at pH 3.0, but increases with increase in pH and finally reaches a value of 28 nm at a pH of 11.8, with a total increase of 21.4 nm. The $2L_0$ for E_{PDDA} emulsion remains almost the same (64 nm) between the pH 2 to 10 but with further increase in pH, it decreases and reaches a value of 34 nm at pH 12.4. However, $2L_0$ increases from 60 to 175 nm as the pH increases from 3.0 to 11.8 for E_{PAA450} emulsion. The extended conformation of PE in the pH range 2-10 for E_{PDDA} emulsion was evident from the increased $2L_0$ (~ 64 nm) and λ (~ 18 nm) values of E_{PDDA} emulsion.

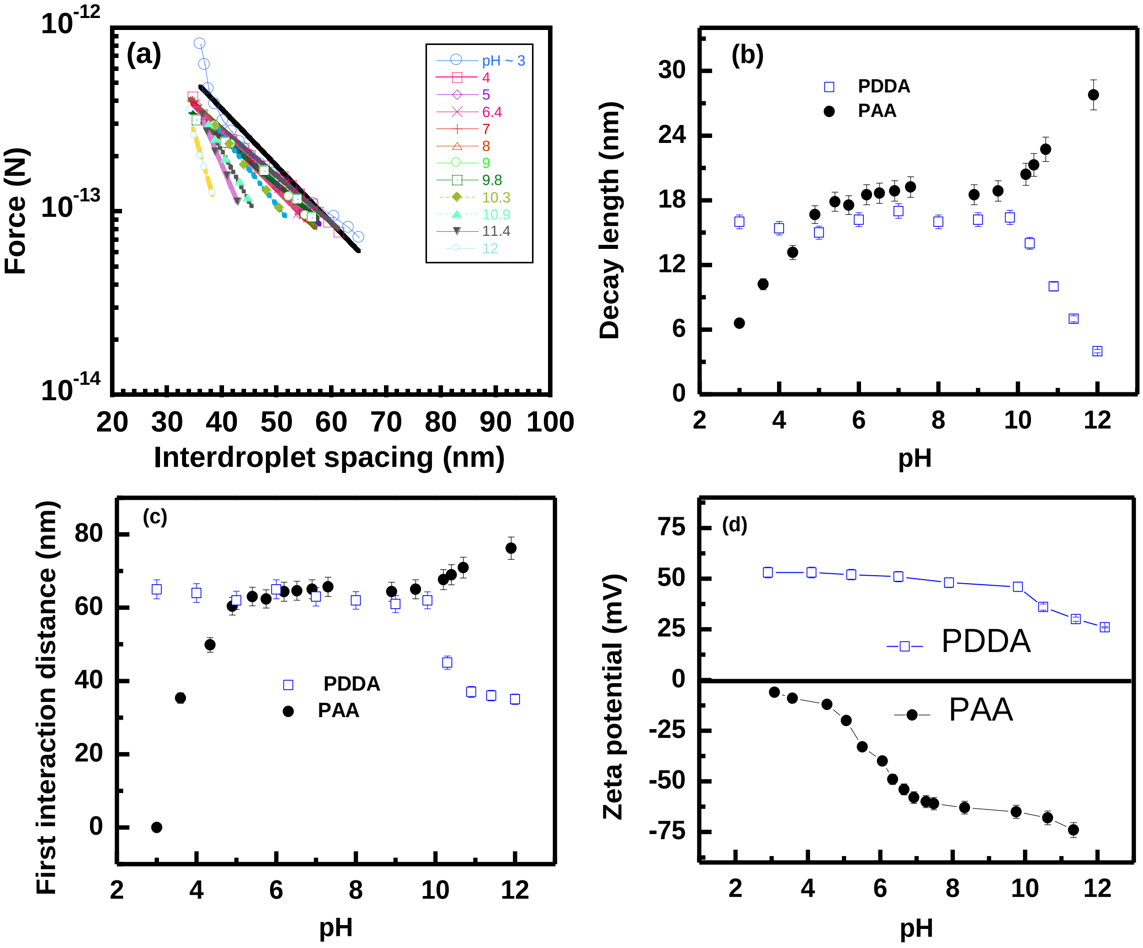

Figure 5.2: (a) Intermolecular force vs. distance for E_{PDDA} emulsion at various solution pH. (b) Decay length, (c) first interaction distance and (d) Zeta potential as a function of pH for E_{PDDA} and E_{PAA450} emulsion, respectively.

The increase in λ and $2L_0$ with pH for E_{PAA450} emulsion shows a globule to an extended conformation of the adsorbed PAA due to an increased electrostatic repulsion between the dissociated surface groups (COOH). The zeta potential of E_{PDDA} emulsion did not change (+ 56 mV) in the pH range between 2 and 10 but decreased to + 25 mV on increasing pH to 11.5 whereas for E_{PAA450} emulsion, zeta potential is found to increase with increase in pH (-10 mV at pH 3.0 and -74 mV at pH 11.5) as shown in the **Figure 5.2d**. Zeta potential measurement confirms the positively and negatively charged O/W interfaces due to the adsorption of strong cationic and weak anionic PE's, respectively **(Figure 5.2d**).

PDDA is water soluble cationic strong PE which dissociates by releasing Cl^- as counter ion while retaining quaternary ammonium group on the polymer backbone at all pH range. The force measurement shows that with increase in pH, the onset of interaction and λ remains the same for E_{PDDA} emulsion in the pH range 2 - 10 as shown in the **Figure 5.2 a & b.** With further increase in pH (between 10 and 12), the onset of interaction and extension of adsorbed PDDA decreases drastically. Though the behavior of the strong PE is considered as pH independent [45, 46], a recent study showed that the conformation, stiffness, hydration, adhesion, lubricity, protein adsorption of strong PE brush are pH dependent [222] because of the formation of inter chain hydrogen bonded network between the grafted chains and the rearrangement of chain conformation resulting from pH mediated adsorption of OH^- within the PE brush. The pH response of a strong PE, poly[2-(methacryloyloxy)ethyl trimethylammonium chloride], studied using quartz crystal microbalance showed that with increase in pH, the adsorption of OH^- on the outer part of strong PE is enhanced. The formation of such interchain hydrogen bonds between grafted brushes leads to cross-linking between the adsorbed brush structures and making them physically stiffer, resulting in a weakened electrostatic interaction. Moreover, it was also shown that the mole fraction of adsorbed OH^{-} on the strong PE brush vary with solution pH [47]. In the pH range of 2-7, only few OH^{-} groups were adsorbed on the brush but with increase in pH from 7-12 a strong adsorption of OH^{-} was noticed, particularly between the pH 10 and 12. The present experimental results are (pH independent behavior up to a pH 10 and the collapse of λ, zeta potential and $2L_0$ beyond pH 10) in very good agreement with the observations in poly[2-(methacryloyloxy) ethyl trimethylammonium chloride]. Above pH 10, λ decreases from16 to 4 nm, whereas $2L_0$ and ζ decreases from 64 to 22 nm and +52 to + 22 mV, respectively. All these results show that when pH > 10, a stronger adsorption of OH^{-} over the PDDA backbone increases, leading to a drop in the effective charge of PDDA.

Contrary to PDDA, PAA is a water soluble anionic weak PE carrying carboxylate anion group on the polymer backbone that ionizes into COO^{-} and H^{+} at pH > pK_a. At low pH, it is highly neutral and exhibits a compact structure but adopts an extended conformation at high pH due to deprotonation of the carboxyl groups. Though it was believed that at pH > pK_a + 1, weak acid dissociate completely, it is applicable only to monomers whereas polymer barely reaches 50 % ionization at this pH [225]. The fraction of deprotonated group on the backbone of the weak PE varies with pH as $f(pH) = \frac{1}{1+10^{(pKa-pH)}}$. Therefore, an enhanced fraction of deprotonated group occurs when the solution pH is increased above pK_a. When pH < pK_a, only 10% of the surface groups are ionized whereas around 90 % of the surface group are ionized when pH > pK_a. The pK_a of acrylic acid was found to be 4.54 [190].

In the present case, between pH 3.0 and 4.5, the zeta potential was quite low due to a fewer dissociated COOH group but in the pH range of 4.5 to 9, an enhanced dissociation of COOH group results in a huge increase in the zeta potential. As dissociation of PAA was almost complete at > pH 10, a little change in the zeta potential was observed between pH 10 and 12.

5.3.3 Influence of salt on the intermolecular forces for E_{PDDA} and E_{PAA450} emulsion

5.3.3.1 Trivalent ions

In addition to the electrostatic and steric interaction, the osmotic pressure due to counter-ion also plays an important role in swelling of the PE [50, 56, 58]. Unlike the association and dissociation of the surface groups of weak PE during pH change, the external salt plays a dual role of charge regulation at low concentration and screening of the surface groups at high concentration [50, 58, 60]. To understand the nature of conformational change of adsorbed PDDA and PAA in presence of salt, the intermolecular force measurement was carried out for E_{PDDA} and E_{PAA450} emulsion at a fixed pH (~5) but with varying salt concentration. The force-distance profiles, **Figure 5.3 a-d,** show that the intermolecular forces are repulsive in nature and decay exponentially with distance for both PDDA and PAA at all concentrations of trivalent ion. For E_{PDDA} emulsion, no variation in the onset of interaction in the force profile is observed at low concentration of Fe^{3+} (0.006 to 1.0 μM) but with further increase in Fe^{3+} (1.6 to 45 μM of Fe^{3+}), the onset of interaction decreases to a lower interdroplet spacing as shown in the **Figure 5.3 a & b.** But, for E_{PAA450} emulsion at low concentrations of Fe^{3+} (0.03 to 1.3 μM), the onset of interaction of the force profile increases to a higher interdroplet spacing as shown in the **Figure 5.3c** but decreases to a lower interdroplet spacing with further increase in Fe^{3+} concentration (2.7 to 270 µM of Fe^{3+}) as shown in the **Figure 5.3d.**

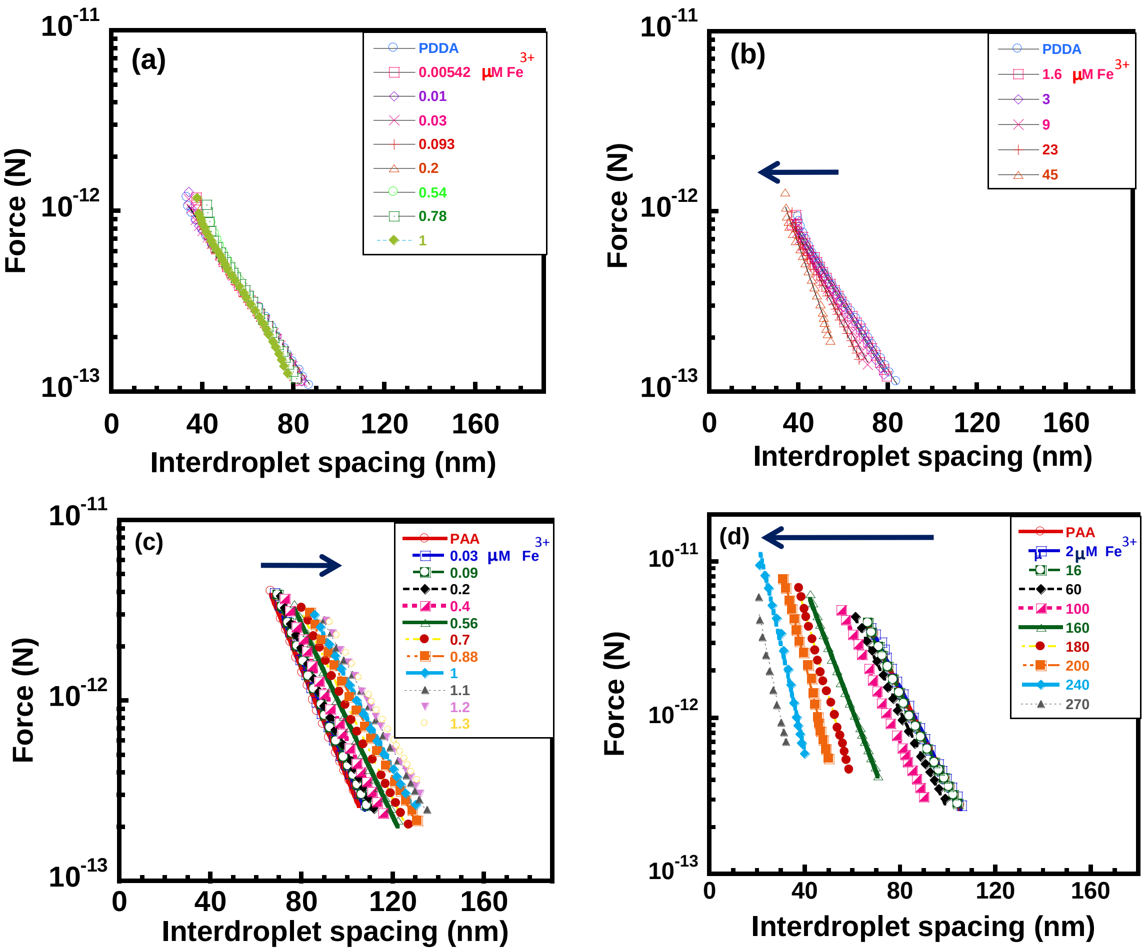

Figure 5.3: Force-distance profile for (a & b) E_{PDDA} emulsion at different concentrations of Fe^{3+} ion and (c & d) E_{PAA450} emulsion at different concentration of Fe^{3+} ion. The best fits are shown by the solid line.

The swelling and collapse of the PE brush in the presence of external salt concentration was theoretically predicted [49-51, 56, 58, 186, 226] and experimentally probed [55, 60, 205, 227]. To compare the behavior of PDDA and PAA, λ of both PE's at various concentration of Fe^{3+} is studied and the results are shown in **Figure 5.4 a & b.** λ remains the same at low concentration of Fe^{3+} for E$_{\mathrm{PDDA}}$ emulsion whereas for E$_{\mathrm{PAA450}}$ emulsion λ was found to increase with Fe^{3+} as λ$^{+0.07}$ in the same electrolyte concentration range. But, at high concentration of Fe^{3+} (2.7 to 270 μM) the corresponding λ variation is shown in the **Figure 5.4b** for both E$_{\mathrm{PDDA}}$ and E$_{\mathrm{PAA450}}$ emulsion, where λ scales with Fe^{3+} concentration as λ$^{-0.15}$ and λ$^{-0.165}$, respectively. Therefore, at low concentration of Fe^{3+}, extension of PDDA remains the same but a swelling is observed in the case of PAA. At high concentration of Fe $^{3+}$, both PDDA and PAA collapse.

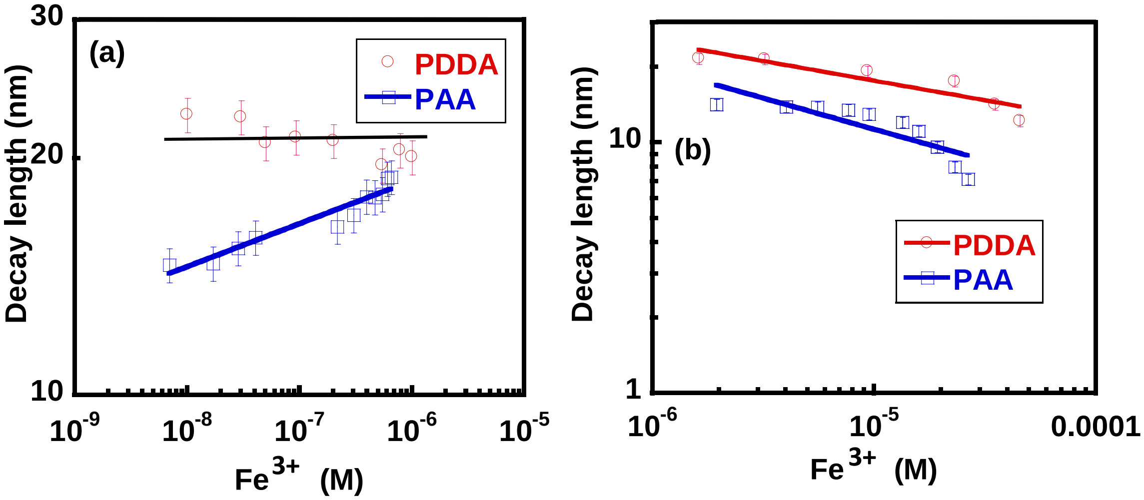

Figure 5.4: Decay length of E$_{\mathrm{PDDA}}$ and E$_{\mathrm{PAA450}}$ emulsion in the presence of (a) low concentration of Fe $^{3+}$ (b) high concentration of Fe^{3+}. The best fits are shown by the solid line. At low concentration, λ remains constant for E$_{\mathrm{PDDA}}$ emulsion whereas it increases with increase in Fe^{3+} concentration for E$_{\mathrm{PAA450}}$ emulsion, where λ ~ $\varphi_s^{0.07}$ (R^2 = 0.95). At high Fe^{3+} concentration, λ decreases for both E$_{\mathrm{PDDA}}$ and E$_{\mathrm{PAA450}}$ emulsions where λ scales with concentration of Fe^{3+} as ~ $\varphi_s^{-0.15}$ (R^2 = 0.91) and ~ $\varphi_s^{-0.16}$ (R^2 = 0.82), respectively.

Mean field and self consistent field theory [50, 58] predicts that the brush height of a strong PE does not change until the concentration of external ions is equal to the number of counter-ions inside the brush. The anomalous behavior (i.e. increase in PE brush height at low salt concentration) is a characteristics of weak PE but in case of strong PE, such a behavior was not observed [50, 58] where the brush height does not exhibit non-monotonic behavior as a function of salt concentration due to lack of potential gradient of ions between the surface and bulk. At very low salt concentration, the brush height of the quenched PE does not vary with addition of salt and the PE conformation remains unaltered (only slight variation in PE charge distribution was noticed) [45, 228]. The cross-over from osmotic (low salt concentration) to a salted brush regime (high salt concentration) was explained on the basis of two parameters [228]: Debye length (κ^{-1}) and ξ (the length scale over which a test charge is neutralized within the brush). When κ^{-1} x ξ <<1, the salt contribution is weak and the brush height was unaltered whereas κ^{-1} x ξ >>1, the counter-ions in the brush is modified that results in collapse of the brush height. Therefore, at high salt concentration, the brush enters salted brush (SB) regime where the quenched PE brush height collapse with increased salt content. The collapse continues due to decrease in osmotic pressure of the counter-ions and PE brush neutralizes completely and enters a quenched neutral brush (QNB) regime where it behaves like a neutral polymer brush. The observation of λ variation for E_{PDDA} emulsion with increasing Fe^{3+} was found to be quite similar to theoretically predicted variation for strong PE, where the PE chain extension remains unaltered at low concentration of Fe^{3+} ions. Between 0.006 to 1 μM of Fe^{3+}, λ is found to vary between 22 and 20 nm whereas further increasing Fe^{3+} concentration leads to a collapse of PDDA extension with a decay rate of $\lambda \sim \varphi_s^{-0.15}$, which is quite comparable to the decay rate of E_{PAA450} emulsion.

The addition of higher concentration (> 0.1 mM) of divalent and trivalent salt in E_{PDDA} and E_{PAA450} emulsion is found to cause a rapid phase separation where the flocculated oil droplets are phase separated from the aqueous phase. But, no such flocculation was observed in the presence of monovalent ions of high concentrations. A study showed that [229] at a lower concentration of trivalent ion ($EuCl_3$), the spherical PE brush (polystyrene sulfonate) adopts a more extended conformation whereas at higher trivalent concentrations a collapse of PE brush was observed due to partial neutralization of surface charge. Similarly, Farina et al. [230] studied structure and properties of the end-tethered anionic strong PE (polysodium styrenesulfonate) brush using surface force apparatus and showed that in the presence of trivalent ions (ruthenium hexamine - $Ru(NH_3)_6{}^{3+}$), the extended brush structure completely collapsed due to replacement of sodium ions with trivalent ions as a result of adhesion between the surfaces. A few other studies also showed that the addition of external ions can condense over PE backbone, thereby reducing the translational entropy of counter-ions and osmotic pressure inside the brush leading to a reduction in the brush height [205]. The addition of trivalent ions seems to replace the charges along PE backbone by forming strong ion pairs that collapse the adsorbed PE, followed by bridging attraction and flocculation of emulsion droplets. Though, the collapse of end-tethered PE was reported with a formation of adhesive interaction [55, 179] in the presence of multivalent ion, yet a proper understanding of such phenomenon is lacking. An earlier study showed that the collapse of PE was due to lowering of osmotic pressure in the brush layer where several monovalent counter-ions were replaced by a single multivalent ion and a strong multivalent counter-ions condensation can induce an effective charge neutralization [205]. Though, the osmotic pressure difference hypothesis is able to explain the collapse of PE in the presence of multivalent ions, the formation of adhesive interaction between the surfaces remains poorly understood. To account for this, new models were proposed to describe the collapse transition of PE followed by electrostatic attraction from bridging that gives rise to an adhesive interaction [53, 54, 201]. Another important observation, in the present case, is that the swelling and collapse of PE is seen at very low concentration of trivalent ion as compared to the monovalent and divalent ions.

The decay length measurement (**Figure 5.4b**) suggest that, at low salt concentration (i.e. osmotic brush regime), physically adsorbed PAA at oil-water interface swells with increasing salt concentration due to penetration of counter-ions in the bulk solution into the PE brush, driven by Donnan potential [199, 231], which result in an increase in osmotic pressure within the PE layer, a region called Osmotic brush (OsB) regime. This behavior was predicted theoretically for end-tethered annealed PE [50] where brush height underwent a swelling and collapse that depends on the amount of external salt content. This anomalous behavior was attributed to the increase in ionization of chains forming the brush with increase in salt content as $\alpha = [\frac{\alpha_b}{1-\alpha_b} a_{mon}\sigma(C_H^* + \varphi_s]^{2/3}$, where σ and a_{mon} are the grafting density of PE and the monomer size.

In our case, the rate of swelling of PAA was found to be $\lambda^{0.07}$ (which is quite low) as compared to the swelling of end-tethered brush height (H) with salt concentration that goes as, $H^{0.33}$. This discrepancy arises due to non-inclusion of some factors in the theory of PE brush such as steric interaction [59]. Studies also showed that the discrepancy might have originated from non-inclusion of hydrophobicity of polymer backbone, polydispersity of the chains and three body interaction at higher grafting density [202]. The non-monotonic dependence of brush height as a function of salt concentrations was also observed for chemically grafted hydrogel comprised of weak acids whose thermodynamics was studied using molecular theory[232]. Such non-monotonic brush height variation with change in pH is a characteristic of weak PE.

Once, the equilibrium between brush and bulk is established (when the concentration of mobile ions inside and outside the PE chains becomes equal) the degree of dissociation of the brush (α) attains the same value as that of the bulk α_b i.e. $\alpha \approx \alpha_b$, then brush enters another regime called salted brush (SB) regime where annealed PE brush height collapses with increasing salt content due to screening of the charges on the chains. The collapse continues till annealed PE neutralizes completely and finally entering a quenched neutral brush (QNB) regime where they display a neutral polymer brush characteristic. Here, for physically adsorbed PAA at oil-water interface, further addition of trivalent salt (> 1 μM) resulted in a collapse of adsorbed PE as $\lambda^{-0.15}$.

For E_{PDDA} emulsion, the collapse of adsorbed PE in presence of trivalent ions happens due to the exchange of monovalent ions with trivalent ions over the PE backbone [205]. This exchange and binding process results in the reduction of number of monovalent ions on the PE backbone and screening of the surface group [229]. The swelling dynamics of end-anchored PAA adsorbed on mica under varying salt concentration studied using AFM [194] showed that PAA undergoes a swelling at very low salt concentration due to dissociation of surface group but collapses at higher salt concentrations $L = C_s^{-0.17}$ at a pH 9. Since the brush structure was found to be highly protonated below pH 6, the brush height was found to be independent of salt concentrations. Although PAA has a pK_a of 4.2-5.5, the experimental condition in the above study was carried out such that the surface anchored PAA dissociates only above pH 6.

5.3.3.2 Mono and divalent ions

In this section, the behavior of the adsorbed PDDA and PAA at oil-water interface as a function of monovalent (Na^+) and divalent (Ca^{2+}) salt at a fixed pH (~ 5.0) is discussed. The λ obtained from the intermolecular force measurement for E_{PDDA} and E_{PAA450} emulsion at low and high concentrations of salt are shown in the **Figure 5.5 a & b.** As observed in the case of trivalent ions, at low monovalent salt concentration (between 0.04 to 10 mM), λ was found to be nearly constant (between 18 and 16) for E_{PDDA} emulsion, indicating that no change in extension of PDDA occurs. However, for E_{PAA450} emulsion, λ increases from 13 to18 nm and varies with φ_s as $\lambda \sim \varphi_s^{0.062}$ as shown in the **Figure 5.5a.** At high salt content, λ decreases from 16 to 4 nm as $\lambda \sim \varphi_s^{-0.4}$ for E_{PDDA} emulsion and 15 to 5.5 nm and decay as $\lambda \sim \varphi_s^{-0.27}$ for E_{PAA450} emulsion as shown in the **Figure 5.5b**. Similarly, in the case of divalent ions at low salt concentration, λ remains the same for E_{PDDA} emulsion but it increases from 15 to 19 nm as $\lambda \sim \varphi_s^{0.042}$ for E_{PAA450} emulsion as shown in the **Figure 5.5c**. At high divalent concentration, λ was found to decrease as $\lambda \sim \varphi_s^{-0.19}$ for E_{PDDA} emulsion and $\lambda \sim \varphi_s^{-0.21}$ for E_{PAA450} emulsion (**Figure 5.5d**).

As observed earlier, here also the extension of strong PE (PDDA) was found to be unaltered at low salt content of mono and divalent salt but swelling of adsorbed PAA (due to charge regulation) was observed in the same salt concentration range due to screening of surface groups that was observed for both strong and weak PE. But, the rate of decay for E_{PDDA} emulsion (-0.42) is quite high as compare to the rate of decay of end-tethered PE [50] where the brush height fell as H ~ $\varphi_s^{-0.33}$. In the case of strong PE , the collapse of the adsorbed PDDA occurs due to condensation of electrolyte ions over backbone of PDDA [41], thereby reducing electrostatic interaction. Though the surface group of the adsorbed PE neutralizes in the presence of high salt content, the brush height remains stable due to the excluded volume interaction [203]. The zeta potential of the E_{PDDA} emulsion in the presence of very high salt content (0.7 M NaCl) was found to be +8 mV, yet emulsion stability was extremely good in the presence of monovalent salt environment. This showed that for E_{PDDA} emulsion, with increasing NaCl concentration, the extension of PDDA decreases due to condensation of electrolyte ions followed by neutralization of surface group which was evident from the decrease in ζ.

Tamashiro et al.[230] derived an expression for the compressed normal force for quenched PE brush under various concentration of monovalent salt and monitored the brush height in the same salt environment. At high salt concentration, both experimental profile and theoretical prediction were quite similar where the brush height collapse was found to with salt concentration. A similar results of the collapse of a strong PE, poly([2-(methacryloyloxy)-ethyl]trimethylammonium chloride), grafted on silica particle, in the presence of monovalent salt was observed in an optical tweezer based study [233] where it was found that the Debye length (κ^{-1}) and surface potential (ψ_0) decreases with increasing monovalent salt concentrations due to screening of electrostatic interactions of the adsorbed PE by NaCl.

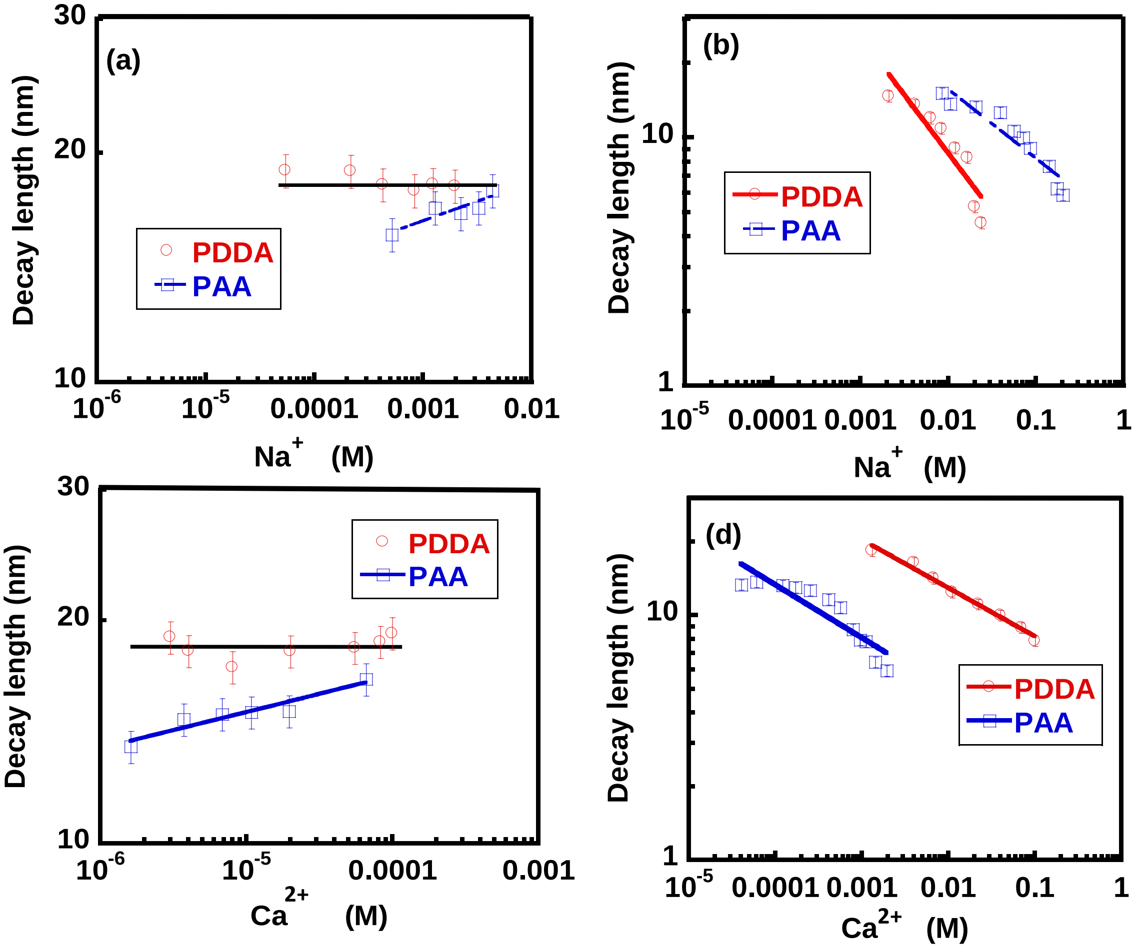

Figure 5.5: Variation of λ for E_{PDDA} and E_{PAA450} emulsion in the presence of low and high concentration of (a & b) Na $^{+}$ (c & d) Ca $^{2+}$, respectively. The best fits are shown by the solid lines. At low concentration of Na^{+}, λ remains constant for E_{PDDA} emulsion whereas it increases with Na^{+} for E_{PAA450} emulsion as, $\lambda \sim \varphi_s^{0.062}$ (R^2 = 0.89). At high salt concentration, λ decreases with increase in of Na^{+} as $\lambda \sim \varphi_s^{-0.4}$ (R^2 = 0.9) for E_{PDDA} emulsion and as $\lambda \sim \varphi_s^{-0.27}$ (R^2 = 0.94) for E_{PAA450} emulsion. At low concentration of Ca^{2+}, λ remains constant for E_{PDDA} emulsion whereas it increases with increase in Ca^{2+} for E_{PAA450} emulsion as, $\lambda \sim \varphi_s^{0.042}$ (R^2 = 0.95). λ decreases with further increase in Ca^{2+} for E_{PDDA} and E_{PAA450} emulsion as $\lambda \sim \varphi_s^{-0.19}$ (R^2 = 0.99) and $\lambda \sim \varphi_s^{-0.21}$ (R^2 = 0.88), respectively.

Although an enhanced swelling of strong end-tethered brush structure before it collapse at high salt concentration was reported [234], the present study reveals that the extension of the strong physisorbed PE remains almost the same before it begins to collapse at a high salt concentration. Similarly, theory showed that the strong PE brush does not undergo expansion at low salt concentration [50, 58] at all pH level but a study by Xiao chu et al. [234] observed an enhanced swelling of strong PE brush before it begins to collapse from ellipsometry, QCM-D and AFM measurements. The observed swelling of the PE at low salt content was explained on the basis of penetration of counter-ion which breaks up the multiplets already formed due to ion pairs and dipole-dipole interactions. According to the above study, strong PE dissociates at all pH level with confinement of the counter-ions inside the brush and the ion-pairs were formed due to dipole-dipole interaction in multiplets that restrict the complete stretching of the strong PE brush. When external salt concentration is increased, penetration of ions inside the brush and breaking of the existing multiplet structures results in further stretching of the strong PE brush.

A study by Beaman et al.[189] showed that the addition of divalent ion (Ca^{2+} and Mg^{2+}) to PAA adsorbed at oil-water interface enhances the screening of surface group much more than the monovalent ion of the same concentrations. Their study also showed that the presence of divalent ion can increase the adsorption of PAA at oil-water interface. Interestingly, in our case the PE brush height collapse was observed at a very low concentration of multivalent ions (0.1 mM for trivalent and 1 mM for divalent ion) as compared to monovalent ion (10 mM). Surprisingly, irrespective of the salt concentrations and valance, the swelling and collapse of physisorbed PE at the oil-water interface was remarkably similar to the theoretical predictions of end-tethered PE, though the nature of interface is completely different in the present study.

5.3.4 Zeta potential measurement of E_{PDDA} and E_{PAA450} emulsion as a function of salt

Figure 5.6a shows the ζ potential of E_{PDDA} emulsion as a function of mono, di and trivalent salt concentration. In the absence of electrolyte, the zeta potential was + 48 mV. But, the addition of salt neutralizes the charges on the adsorbed PE and decrease in zeta potential. As observed for E_{PAA450} emulsion, the addition of monovalent salt concentration decreases the zeta potential with a rate of scales as $\varphi_s^{-0.37}$ whereas for divalent and trivalent ions the rate of decay was found follow, $\varphi_s^{-0.20}$ and $\varphi_s^{-0.16}$, respectively. Again, as the valence of the salt increases even at lower concentration of salt, surface charge neutralization of emulsion droplets occurs as compared to monovalent salts of very high salt concentrations. This observation was consistent with our force measurement results.

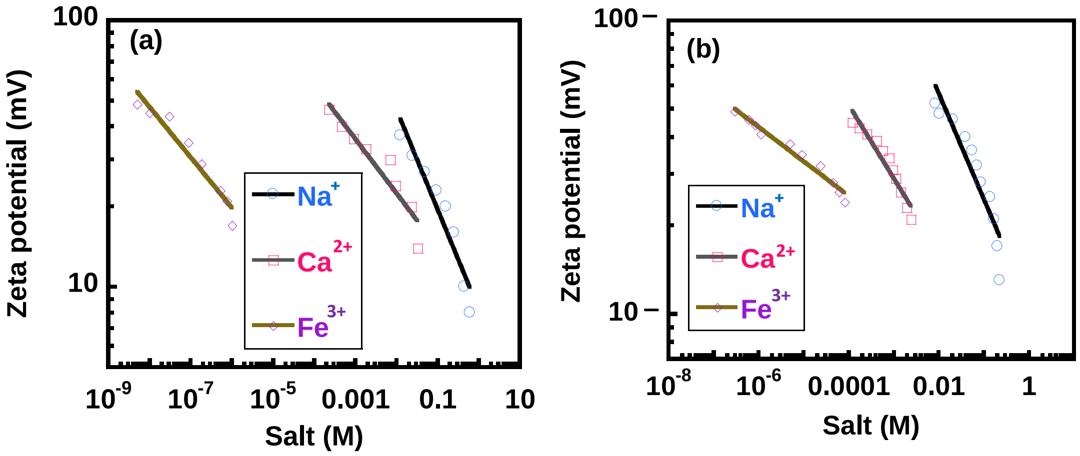

Figure 5.6: Zeta potential of (a) E_{PDDA} and (b) E_{PAA450} emulsion, as a function of salt concentration. The best fits are shown by the solid lines. The zeta potential for E_{PDDA} emulsion decays as $\varphi_s^{-0.37}$, $\varphi_s^{-0.20}$ and $\varphi_s^{-0.16}$ for mono, di and trivalent salt, respectively. The

decay of zeta potential as a function of salt for E_{PDDA} emulsion scales with concentration as $\varphi_s^{-0.36}$, $\varphi_s^{-0.25}$ and $\varphi_s^{-0.11}$ for mono, di and trivalent ions, respectively.

Figure 5.6b shows the zeta potential of E_{PAA450} emulsion with increasing salt concentration of mono, di and trivalent ions. In the absence of electrolyte, the zeta potential of E_{PAA450} emulsion was found to be -48 mV at a pH = 7. With the addition of salt decrease in the zeta potential occurs due to neutralization of PAA backbone charge carrier (COO^-). In the presence of monovalent salt concentration of 0.004 - 0.2 M, the zeta potential decreases as $\varphi_s^{-0.36}$ whereas for divalent and trivalent ion concentration it decays as $\varphi_s^{-0.25}$ and $\varphi_s^{-0.11}$, respectively. The rate of decay of surface charge for E_{PAA450} emulsion were found to follow $\varphi_s^{-0.36}$, $\varphi_s^{-0.25}$ and $\varphi_s^{-0.11}$ for mono, di and trivalent ions, respectively. It is clearly seen from the profile that as the valence of the salt increases the neutralization of the charged moieties happens at a lower concentration. Hoffman et al. [229] reported such collapse of PE brush at high Eu^{3+} concentration due to partial neutralization of surface charge. Our observation on the rate of collapse of adsorbed PAA with increasing valance of ion was consistent with other reported results.

Table 5.1: Comparisons of scaling relations of λ and ζ as a function of salt concentrations of different valances for E_{PDDA} and E_{PAA450} emulsion.

S. No.	**E_{PDDA} emulsion**		**E_{PAA450} emulsion**	
Salt	**Decay length (λ)**	**Zeta potential (ζ)**	**Decay length (λ)**	**Zeta potential (ζ)**
Monovalent (NaCl)	$\lambda \sim \varphi_s^{-0.4}$	$\zeta \sim \varphi_s^{-0.37}$	$\lambda \sim \varphi_s^{-0.27}$	$\zeta \sim \varphi_s^{-0.36}$
Divalent ($CaCl_2$)	$\lambda \sim \varphi_s^{-0.19}$	$\zeta \sim \varphi_s^{-0.20}$	$\lambda \sim \varphi_s^{-0.2}$	$\zeta \sim \varphi_s^{-0.25}$
Trivalent ($Fe_2(SO_4)_3$)	$\lambda \sim \varphi_s^{-0.15}$	$\zeta \sim \varphi_s^{-0.16}$	$\lambda \sim \varphi_s^{-0.16}$	$\zeta \sim \varphi_s^{-0.11}$

Table 5.1 shows the dependence of λ and ζ on different salt concentration for mono, di and trivalent ions for E_{PDDA} and E_{PAA450} emulsion. The scaling relation shows similar rate of collapse for physisorbed PDDA and PAA.

5.3.5 Reversibility in adsorption and release of added ions on PE backbone

To quantify whether external electrolyte adsorbed on the PE backbone is reversible, intermolecular force measurement is carried out for E_{PAA450} emulsion in the presence of higher salt concentration and valance, till the adsorbed PAA collapse completely. Then emulsion is further washed with lower concentration of NaCl (10 mM) and left it to equilibrate for two days.

Figure 5.7 a & b shows force-distance curves and the corresponding λ of E_{PAA450} emulsion with increasing concentration of NaCl (0.2 M) and after washing it with 10 mM NaCl. In the absence of NaCl, the force profile showed long range repulsion, arising due to electric double layer repulsion of dissociated carboxylate group where λ was found to be ~ 20 nm. With addition of NaCl, the onset of interaction in the force profile decreases and a complete collapse of adsorbed PAA were observed at 0.23 M NaCl, where the force profile shifted to a lower interdroplet spacing with λ ~ 5 nm with a zeta potential of -15 mV, indicating the collapse of PAA and neutralization of the surface groups. However, after washing the emulsion with very low concentration of NaCl, the onset of force profile shifted to a higher interdroplet spacing with a λ of 21 nm and the corresponding ζ of -54 mV, indicating that the adsorbed PAA reverted to its original extended structure. These results showed that the condensed ions on PAA backbone got desorbed on washing, thereby enabling PAA to regain its original extended conformation.

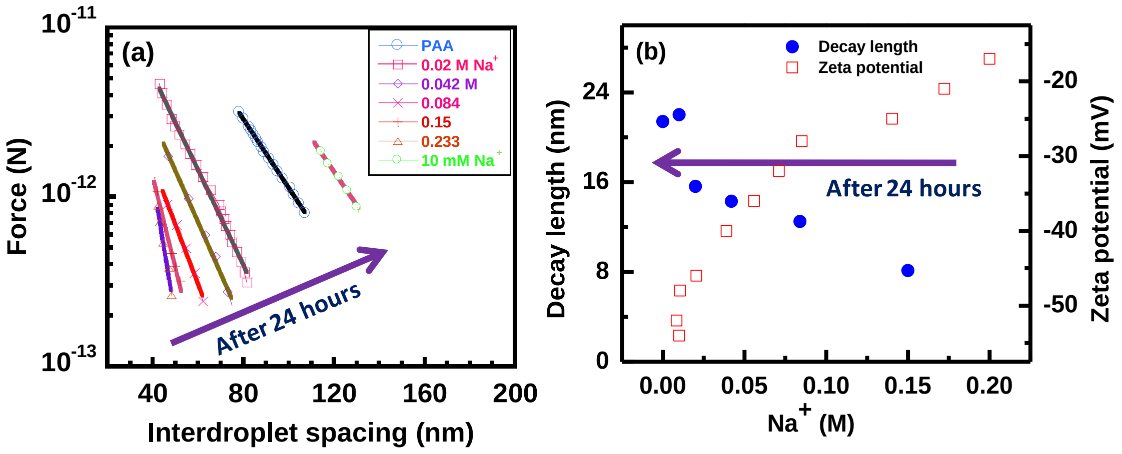

Figure 5.7: (a) Force-distance curves for E_{PAA450} emulsion at different NaCl concentration and washed it again with a lower salt (NaCl) concentration (10 mM). (b) Decay length and zeta potential for the same.

Similar results were reported earlier [235] with poly([2-(methacryloyloxy)ethyl] trimethylammonium chloride) brushes on glass surface. The PE brush was highly swollen with 0.05 mM NaCl a long range electrostatic repulsion was noted and the measured interaction and decay length were reduced on increasing the concentration of NaCl due to screening of electrostatic interaction. On changing the brush environment with a lower concentration of NaCl (0.05 mM), the brush height was restored to its original value, indicating the reversible brush conformation.

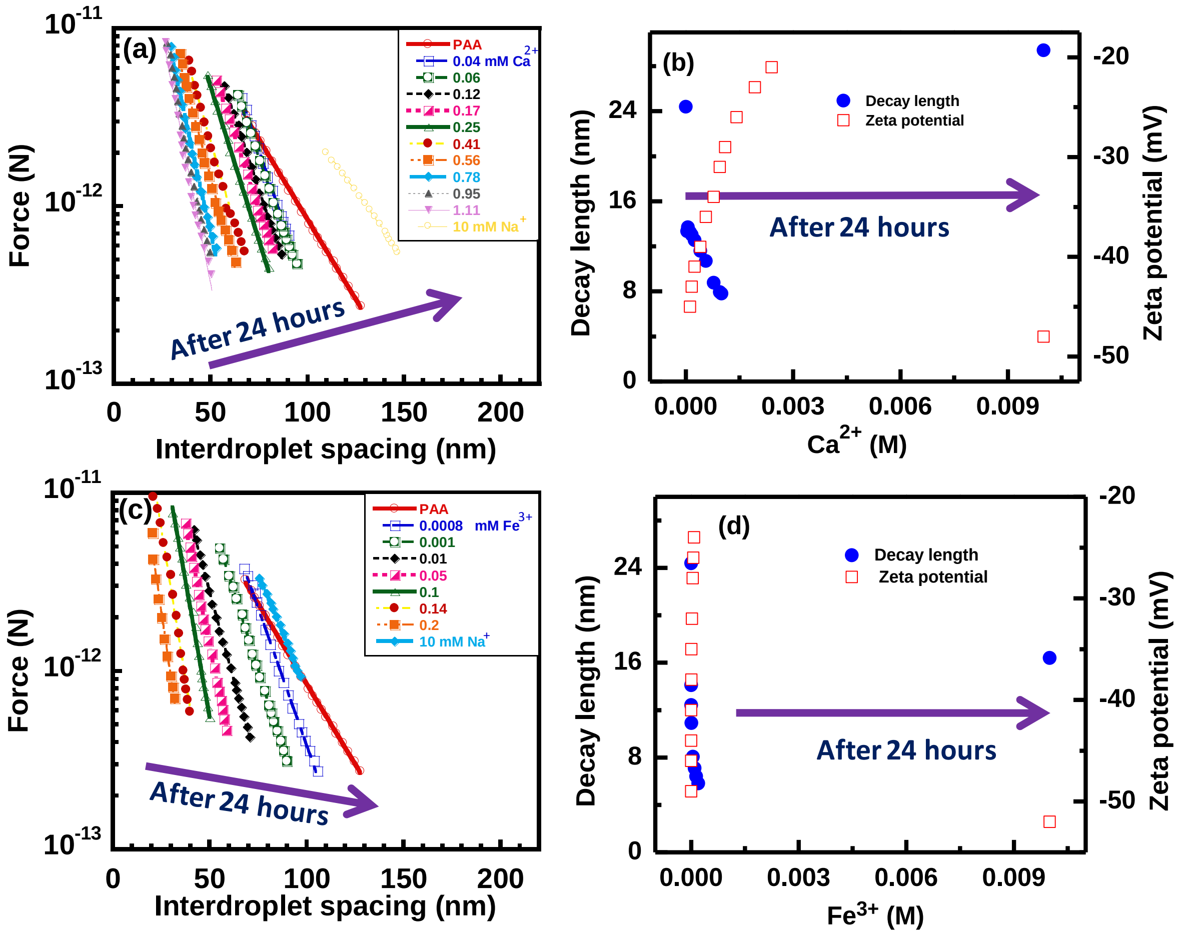

Figure 5.8: (a & c) Force-distance profile for E_{PAA450} emulsion at different Ca^{2+} and Fe^{3+} concentration and after washing it with a lower salt concentration of NaCl (b &d) Decay length and zeta potential for the same.

Figure 5.8 a-d shows force-distance curve and the corresponding λ variation for E_{PAA450} emulsion with increasing concentration of Ca^{2+} (0.04 to 1 mM) and Fe^{3+} (0.0008 to 0.2 mM) and the emulsion was washed with lower concentration of NaCl (0.01 M). In the presence of 1 mM Ca^{2+} and 0.2 mM Fe^{3+}, the onset of interaction decreases dramatically due to collapse of adsorbed PAA. The force profile shifted to a lower interdroplet spacing with a λ value of ~ 5 − 6 nm and a ζ of -22 to -24 mV due to screening of surface group. However, after emulsion was further washed with very low concentration of NaCl (10 mM), the onset of interaction shifted to a higher interdroplet spacing and the corresponding λ increased to 28 and 18 nm and ζ increased to -48 and -52 mV for Ca^{2+} and Fe^{3+}, respectively, indicating that the adsorbed PAA resumes to its original extended conformation. These results show that the condensed ions (Ca^{2+} and Fe^{3+}) over the adsorbed PAA can be removed by simply washing emulsion with a lower salt concentration.

Such a reversal of brush collapse and adhesion was also observed by Farina et al. [179, 230] in strong PE brush - (Poly(t-butyl styrene)$_{20}$ – poly(styrene)$_{420}$) on hydrophobically modified mica. Here, the brush height was found to be highly extended in a dilute concentration of trivalent ions (La^{3+} or $Ru(NH_3)_6^{3+}$) but collapsed at higher concentration. Their result showed that 99 % of the adsorbed $Ru(NH_3)_6^{3+}$ over PSS brush were released when collapsed and adhesive brush was remains monovalent salt solution. This showed that the diffusion of monovalent ion to the PE backbone can replace the condensed divalent trivalent ions. The present study confirms such reversible swelling of PAA at O/W interface. Though, the reversible swelling and collapse is observed in presence of salt in other strong PE's [55, 179, 235], such reversibility in PDDA system was not observed. In the case of strong

PE, the emulsion was destabilized completely while washing with a lower concentration of NaCl.

5.4 Conclusions

The behavior of strong polyelectrolyte, poly(diallyldimethylammonium chloride) - PDDA adsorbed at oil-water interfaces is studied using intermolecular force measurement, zeta potential and hydrodynamic measurement and the results are compared with the behavior of weak polyelectrolyte, poly(acrylic acid) - PAA. The study showed that at low salt concentration the adsorbed PDDA possess an extended conformation. In the presence of very high salt content, a complete collapse of the PDDA was noticed due to enhanced neutralization of the surface group. With multivalent salt, PDDA collapse occurred at lower salt concentration and the rate of collapse was rapid with increasing valence of the electrolyte. In the case of E_{PAA450} emulsion, in the absence of salt, PAA underwent a globule to extended transition in the pH ranges of $3 - 11$. But at constant pH, PAA displayed extended conformation at lower salt concentration but collapsed at higher salt concentration. Interestingly, the rate of swelling and collapse of PDDA and PAA was in good agreement with the theoretical predictions of end grafted PE. The collapse of PDDA and PAA was in agreement with electrophoretic measurement where increasing the salt concentration is found to decrease in the ζ due to enhanced neutralization of surface groups. However, irrespective of the nature of adsorbed ions over PAA, desorption of condensed ions is observed on washing. Though the interface and adsorption mechanism is entirely different with respect to end grafted PE, the rate of swelling and collapse of the adsorbed weak and strong PE was found to be remarkably similar. Also, the rate of collapse of adsorbed PE in both cases (PDDA and PAA) was found to be same as that of the rate of charge neutralization observed from electrophoretic measurement. These results are very useful to obtain insights into the behavior of biological macromolecules adsorbed at cell membrane-fluid interface.

CHAPTER 6

Competitive adsorption of bovine serum albumin at the oil-water interface in the presence of polyelectrolyte

6.1 Introduction

The protein adsorption at an interface is a complex process that involves various forces such as hydrophobic, van der Waals, electrostatic and hydrogen bond [236, 237]. The adsorption of protein at interfaces has an important implications in drug delivery [238], selective binding[239], biosensors [240], colloidal assembly [241, 242] and food industry [243]. Protein adsorption on nanoparticles or substrates [244] enhance stabilization of colloidal products [243, 245], increase biocompatibility of substrates [244] and improving bioactivity of implanted biomaterials.

Proteins are amphoteric polyelectrolyte (PE) [246] that are extensively used in industrial applications because of its low toxicity. The surface activity of protein enables them to adsorb over surfaces or interfaces [247]. The adsorption depends on the structure of protein and nature of substrate [62, 244]. For example, they act as emulsifiers [243, 245, 246] where adsorption of protein reduces the interfacial tension and forms a thin viscoelastic film through non-covalent intermolecular interaction that impart stability to the oil droplet against coalescence [248]. This aspect is exploited in pharmaceutical, personnel care and food products. The organization of proteins at interfaces influence the stability of the emulsion [19]. Protein adsorption is also used to make biocompatible surfaces and artificial scaffolds [9]. However, in marine and biomedical implants, the adsorption of protein on substrates [249] or nanostructured materials [27] is considered as an undesirable effect [28], as it results in biofouling on the materials [250-252] that reduces the functioning of the material (e.g. heat transfer efficiency, reduced flow rates, bacterial influenced corrosion). Irrespective of the importance of protein adsorption, a clear understanding on the mechanism behind this process is still elusive.

Understanding the mechanism of interaction and the right condition for macromolecule or protein adsorption at an interface is essential in fine tuning their properties and stability of colloidal systems [253]. BSA is one of the most extensively studied model globular proteins that belong to the class of serum albumin. It is synthesized in the liver of mammals, having half life of 19 days. It is the most abundant protein in blood plasma, responsible for maintaining osmotic pressure, blood pH as well as involves in the transport of cations, fatty acid, therapeutic drug, steroid [254] etc. At pH 7.4, BSA exhibits heart like shape, transforms to cigar like structure at pH 3.5 and denatures into fully expanded (E) structure at solution pH less than 2.8. The isoelectric point of BSA lies between pH 4.7 and 5.2 [255]. The secondary structure of BSA contains predominantly α-helix (73 %) and β-sheet (2 %) that changes with the solution pH. It is widely believed that the primary structure of protein is not changed when it is adsorbed at the air-water interface but the secondary structure changes in the presence of denaturants such as urea. Moreover, when BSA adsorbs at the oil-water interface, the percentage of secondary structure was found to change significantly. The adsorption of protein was determined from the change in solution pH [256] and studies showed that adsorption is maximum at the isoelectric point [7, 84]. Physio-chemical parameters such as pH, temperature, ionic strength etc alters the thermodynamic properties of the protein [257] and affects its adsorption over a surface [11]. Though it was believed that the protein adsorption at an interface was diffusion controlled [258, 259], in general the adsorption of protein at air-liquid and liquid-liquid interface depends on the energetic of interaction of protein with an interface [260]. The co-adsorption of protein with other PE's and lipids at emulsion interface is also important in improving the shelf life and performance of emulsion based products [63, 261]. Such interfacial engineering where combination of many surface active moieties is used to improve the quality of emulsions [8, 12, 247].

Since the behavior of adsorbed PE shows different behavior under different physio-chemical conditions [49, 50, 113], an understanding of interaction between the adsorbed PE and protein at different charge density of PE at oil-water interface is important. Though the macromolecular interactions at solid-liquid interfaces are studied extensively [262], such studies on liquid-liquid interface are scarce [263]. Using a combination of intermolecular force and electrophoretic measurements, we study the competitive adsorption of proteins at oil-water interface at different solution pH in the presence of a strong or weak PE. The questions that are addressed in the present work are the following: (a) is it possible to displace the adsorbed weak (annealed) or strong (quenched) PE over oil droplets by protein molecules? (b) What is the resultant colloidal stability at different solution pH? (c) Does competitive adsorption effective when surface charge density is high? To answer these questions, magnetically polarizable oil-in-water nanoemulsion stabilized with strong PE, PDDA (E_{PDDA} emulsion) and weak PE, PAA (E_{PAA450} emulsion) is prepared and studied the intermolecular interaction with BSA of different concentration at various solution pH. To validate the force data, electrophoretic measurements are also done under the above conditions.

6.2 Materials

Magnetic nanoemulsions, E_{PAA450}, E_{PDDA} and E_{BSA} (BSA stabilized emulsion) are used in this study. Material preparation and experimental setup are explained in Chapter 2. The average droplet size and nature of surface charge of the magnetically polarizable nanoemulsion was characterized using a Malvern Nanosizer (Zetasizer Nano-S). Intermolecular interactions for E_{PAA450} and E_{PDDA} emulsion in the presence of BSA were measured using magnetic chaining technique.

6.3 Results and discussion

6.3.1 Size and zeta potential of E_{BSA} emulsion

The average hydrodynamic size and zeta potential of E_{PAA450} and E_{PDDA} emulsion is discussed in chapter 2. The average hydrodynamic size (H_d) of E_{BSA} emulsion was 230 nm and zeta potential was highly positive (+ 38 mV) at low pH, which is found to decrease with increase in pH and reaches zero at pH ~ 5.2, where the net charge of various charged groups of BSA balances. Above pH 5.2, zeta potential was negative and the magnitude increases as solution pH approaches high alkaline condition, which confirms the amphoteric behavior of BSA.

The charge and conformation of the BSA changes abruptly with change in solution pH [264]. In the pH range of 4 to 7.5, it adopts F-form with a globular structure whereas between 4.5 and 4.0, normal-fast structures are seen. On lowering the pH further (< 4.0) results in an expanded structure. At high alkaline medium, basic structure with maximum extension and asymmetry occurs. The uneven distribution of charged patches across BSA is found to vary with solution pH. In acidic medium, the net charge of the protein is highly positive but in alkaline medium it is highly negative with isoelectric point between pH 4.7 and 5.2 [254, 265-267].

6.3.2 PDDA-BSA interaction

To understand the complex interactions of PDDA covered droplets in the presence of BSA, we performed the intermolecular force measurements. Force vs. distance curve for E_{PDDA} emulsion at various concentrations of BSA is shown in the **Figure 6.1a.** The force profiles were repulsive in nature and decay exponentially with interdroplet spacing, h as $F(h) = K \exp(-\frac{h}{\lambda})$ [113]. From force-distance profiles, the force parameters such as force constant - K, decay length - λ and first interaction distance - $2L_0$ are derived. In the absence of BSA the λ and ζ of E_{PDDA} emulsion at pH 5.4 was found to be 19 nm and + 56 mV, respectively. With increasing concentration of protein, the force profiles were less repulsive and the onset of force profile shifted to a lower h spacing at high concentration (0.5 wt %) of BSA, where λ and ζ were 6 nm and + 5 mV, respectively in the same solution pH (**Figure 6.1b)**. With increasing BSA concentration, the $2L_0$ decreases while K increases as shown in the **Figure 6.1 c & d,** respectively.

The onset of interaction in the force profile and extension of adsorbed PDDA was found to be independent of pH between 2 and 10 for E_{PDDA} emulsion alone. This finding was consistent with the previous work where the brush height of a strong PE was found to be the same for a wide range of solution pH [220]. Since the pH of the BSA solution and

E_{PDDA} emulsion was maintained at the same value, the observed decrease in decay length and first interaction distance is attributed to the adsorption of BSA at O/W interface.

Now the question is: Why force profiles change drastically on addition of BSA to an E_{PDDA} emulsion? The onset of interaction, decay length and zeta potential was found to decrease with increase in BSA concentration. The drastic reduction in the onset of interaction in the force profile and decay length suggests a collapse of the extended PDDA, probably due to the complexation with BSA and the subsequent replacement of adsorbed PDDA by BSA. The decrease in zeta potential suggests that the BSA-PDDA complexes are desorbed from oil-water interface and remained in the continuous phase.

Earlier studies on interaction of end-anchored PE with BSA showed a strong adsorption of protein over PE brush at low ionic strength and a protein inhibition at high ionic strength due to steric repulsion of neutralized PE [268-270]. The protein adsorption was high when the charge of protein was opposite that of the PE [270]. In the former case, a directed motion of protein into the PE layers was reported [271]. If BSA is complexed with the adsorbed PDDA the onset of interaction would have been increased significantly and the zeta potential would not have decreased drastically. But, the observed decrease in decay length and zeta potential suggests that the addition of BSA competitively displaced the adsorbed PDDA at oil-water interface.

E_{PDDA} emulsion was highly stable in the presence of BSA even at different environmental pH condition. The zeta potential of E_{PDDA} emulsion (without BSA) at pH 5.4 was + 58 mV but it decreases with increasing concentration of BSA and finally reaches + 5 mV at 0.5 wt % of BSA in the same physiological pH condition. The magnitude of zeta potential at this value was found to be similar to the zeta potential of E_{BSA} emulsion. This observation unambiguously confirms that the adsorbed PDDA is displaced from the oil-water interfaces and the droplet interface is covered with BSA. Interestingly, the addition of BSA causes a five order increase in the force magnitude (K), which further confirms the protein adsorption over emulsion droplets. The protein adsorption at an interface is a result of three dynamic process: (a) diffusion of protein from the aqueous phase to the interface (b) penetration and interfacial unfolding of protein (c) structural rearrangement of the adsorbed protein at an interface and the formation of a viscoelastic monolayer [272].

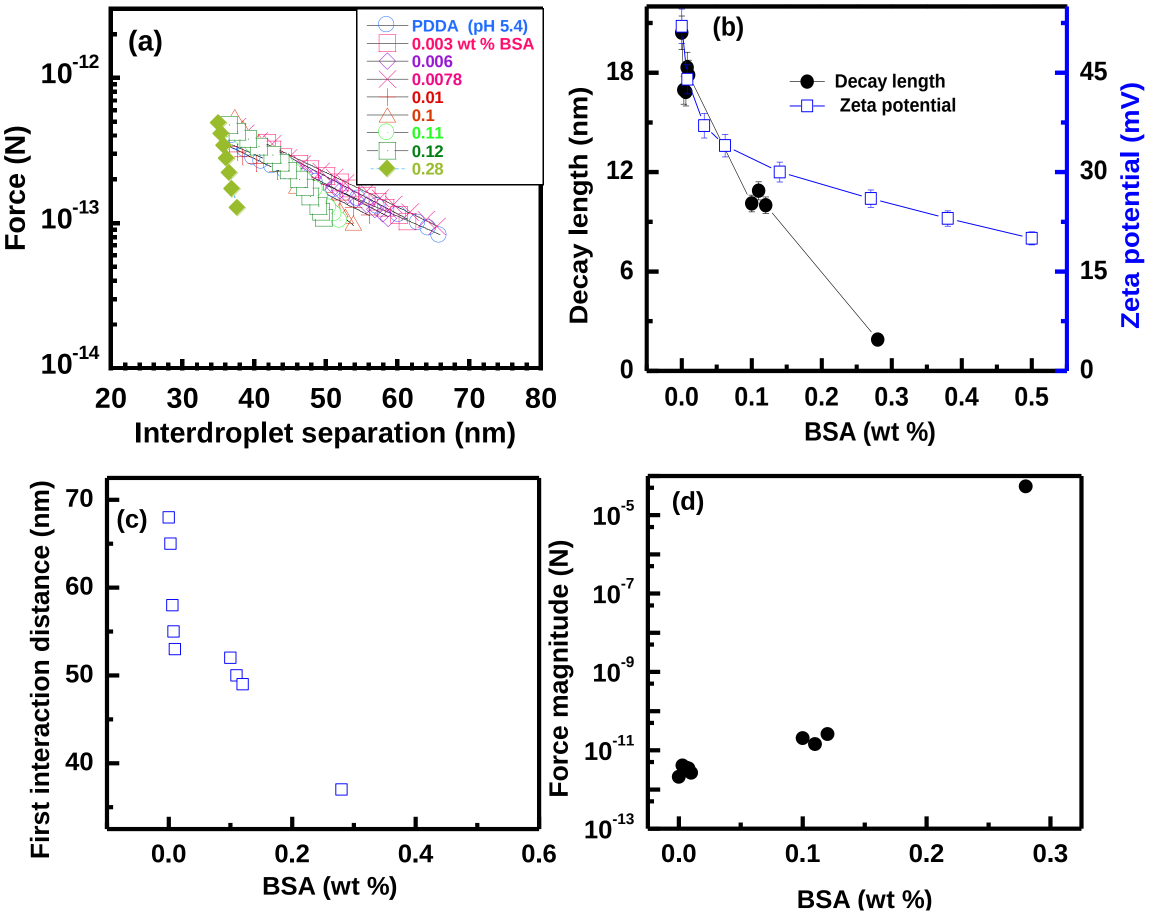

Figure 6.1: (a) Intermolecular force vs. distance for E_{PDDA} emulsion at various concentration of BSA at pH 5.2. (b) Decay length, λ and zeta potential, ζ for E_{PDDA} emulsion at different concentration of BSA (c & d) first interaction distance, $2L_0$ and force magnitude, K for E_{PDDA} emulsion at different concentration of BSA.

In bulk solution, conformation of BSA and hence its stability depends on the solution pH [254, 265, 273, 274] and concentration [275] . Aggregation of BSA at the air-water interface was noticed immediately at concentration > 8 ppm where unfolding of protein happened with varying concentration. At neutral pH, it exhibit normal heart like structure (N-isoform) but with decreasing pH it transforms to F-form and exhibits a cigar like structure at pH 3.5. During this N – F transition, helical content decreases and carboxylate group becomes titrable. It denatures into highly expanded structure (E-isoform) at pH 2.7 where no changes in helical structure occur. But, in alkaline condition it exhibits a basic state at pH 8.0 and aged state at pH > 8.0 [254]. During these transitions, the structure of BSA was also found to alter completely where the α-helical structure was less while secondary and tertiary structures were more. The transition of the proteins at various pH level determines its stability where the reduction of pH unfolds the protein with increased β-sheet that reduces the stability of BSA [276]. The changes in structure of BSA were found to be different than bulk solution. Reports showed that the structure of protein was found to be altered upon adsorption [256, 277, 278] that depends on the nature of surface and types of protein [64].

Meng et al. [279] reported from Raman spectroscopy that adsorption of protein at mineral oil/water interface results in alternation of tertiary structure and exposure of hydrophobic residues of protein but no changes in secondary structure (α-helix and β-sheet). Jorgensen et al. [4] reported a significant change in secondary structure when BSA was adsorbed at water/oil interface. The changes in secondary structure was found to vary with the polarity of oil phase [5]. The tertiary structure of BSA was also found to vary with adsorption [5]. Dickinson et al. [280] proposed that protein adopts a molten globular structure based on the loss of tertiary structure with only fewer changes in secondary structure of protein. Courthaudon et al. [281] showed that protein does not exhibit a single conformational state upon adsorption at oil-water interface but depending upon the history of the protein prepared, the conformation of the adsorbed protein changes. The denaturation of adsorbed protein at the oil-water interface and the consequent destabilization of emulsion were reported in the presence of salt due to electrostatic screening of surface charge. [282] Reports showed that heat can denatures BSA due to loss of tertiary and secondary structure [283]. Since, the measurements were performed at room temperature, no emulsion destabilization was noticed.

The force vs. distance curve for E_{PDDA} emulsion at pH 7.0 in the presence of BSA (maintaining at same solution pH) is shown in the **Figure 6.2a.** It is observed that the addition of BSA decreases the onset of interaction in the force profile and collapse in λ is observed as shown in the **Figure 6.2b**. In the absence of BSA, the λ and ζ of E_{PDDA} emulsion were found to be 18 nm and + 58 mV, respectively. With increasing concentration of protein, the force profiles were found to be less repulsive and the onset of force profile shifted to lower interdroplet spacing at high concentration (0.5 wt %) of BSA where λ and ζ were 6 nm and -10 mV, respectively in the same solution pH as shown in the **Figure 6.2b**. As observed earlier, the zeta potential of E_{PDDA} emulsion at pH 7.0 was found to be + 56 mV but with addition of BSA its magnitude decreased to -10 mV (at 0.5 wt % of BSA), which was close to the zeta potential of E_{BSA} emulsion (-16 mV). This suggests that the adsorbed PDDA was fully displaced from the oil droplets and is replaced by BSA. The competitive adsorption of BSA was also noticed when the solution pH was changed. In the presence of BSA at physiological pH of 7.0, the magnitude of zeta potential decreased dramatically and it was same as that of E_{BSA} emulsion. The change in zeta potential of competitively adsorbed BSA arise due to dissociation of carboxylate groups of BSA, which becomes highly negative at high pH (> isoionic point).

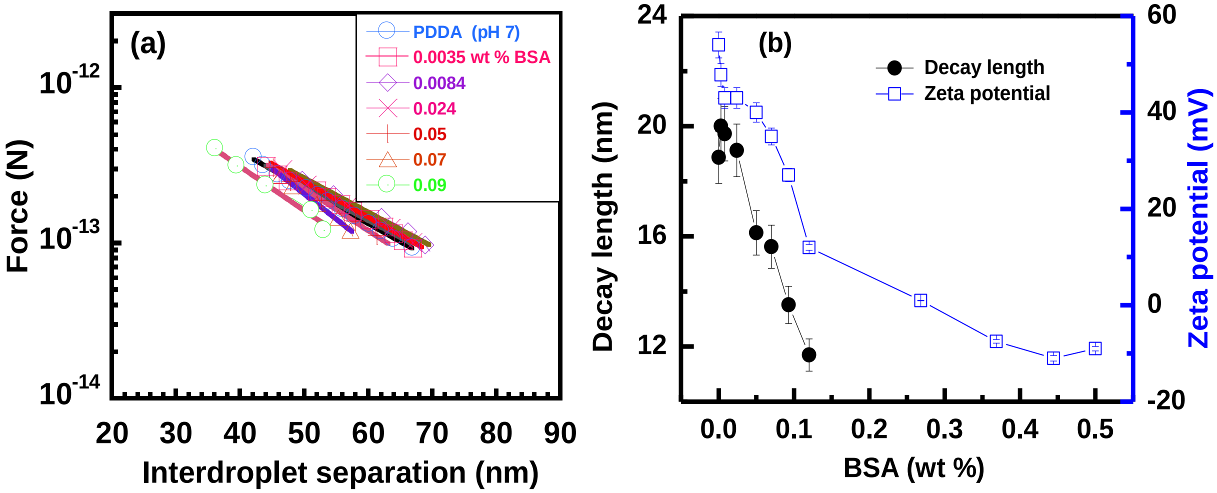

Figure 6.2: (a) Intermolecular force vs. distance for E_{PDDA} emulsion at various concentration of BSA at pH 7.0. (b) Decay length, λ and zeta potential, ζ for the same.

Though BSA is more hydrophilic in nature and its tendency to adsorb at oil phase at neutral pH and above is less likely, yet we observed a complete displacement of the PDDA followed by the adsorption of BSA at oil–water interface. This observation show that the hydrophobicity of protein is not the only parameter that promotes the adsorption of protein at an interface but a combination of various forces of interaction such as electrostatic, van der Waals, etc as reported in literature [236, 237, 260]. Earlier study showed that the adsorption of BSA onto the oil-water interface leads to an enhanced stability with increasing concentration of BSA due to high surface coverage [272, 284]. Such adsorption also leads to structural reorganization of the adsorbed proteins [283].

Studies have carried out in solid-liquid interface where BSA makes complexes with the end-grafted polyelectrolytes in which the ionic strength is found to play an important role in determining the complexation of protein with grafted polyelectrolytes. However, a study by Satulovsky et al. [248] showed that polymers on hydrophobic surfaces can be displaced by proteins. It should be noted that in the present case the polyelectrolytes are adsorbed at hydrophobic interface and our findings of the displacement of adsorbed PAA and PDDA by BSA from oil-water interface is in good agreement with Satulovsky et al. The zeta potential values of emulsion stabilized with BSA in presence of PAA and PDDA is also pointing the fact that the polyelectrolytes are displaced from the interface (Figs. 6.4 and 6.5). Furthermore one of the force parameters – force magnitude obtained from force vs. distance curves shows a dramatic increase, which is possible only if the added moieties go to the interface.

6.3.3 PAA-BSA interaction

The intermolecular force as a function of distance for E_{PAA450} emulsion at pH 3.5 for different BSA concentration is shown in **Figure 6.3a** where the force profiles for E_{PAA450}

emulsion (without BSA), was repulsive and decay exponentially with distance [113]. The force-distance profile was fitted with an exponential function as $F(h) = K\exp(-\frac{h}{\lambda})$, where h is the interdroplet spacing.

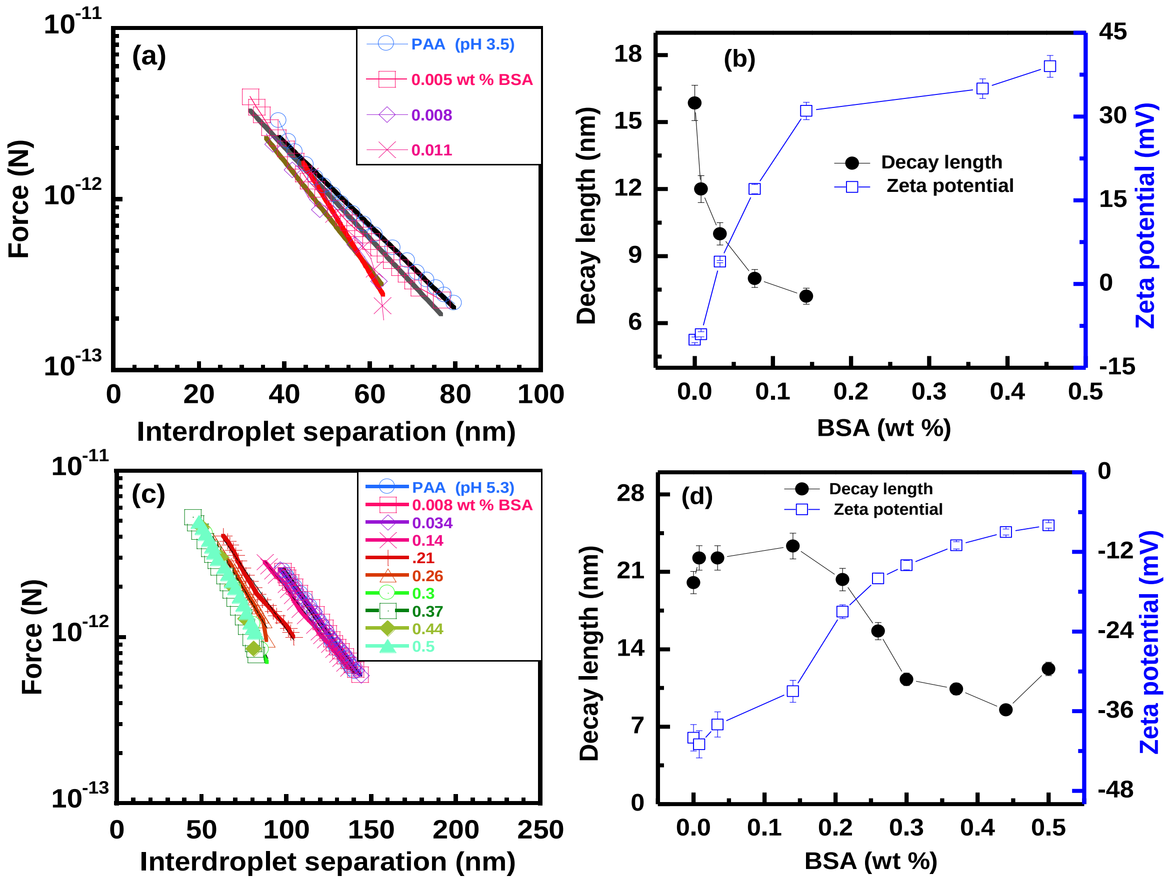

Figure 6.3: (a & c) Intermolecular force vs. distance for E_{PAA450} emulsion at various concentration of BSA at pH 3.5 and 5.2 (b & d) Decay length and zeta potential as a function of concentration of BSA at pH 3.5 and 5.2.

In the absence of BSA, the decay length and zeta potential of E_{PAA450} emulsion at pH 3.5 was found to be 15 nm and –10 mV, respectively. In the presence of protein, the range of intermolecular force was less and with increasing concentration of BSA, decay length decreases to 6 nm, whereas the zeta potential becomes + 38 mV (**Figure 6.3b)**. Similarly, the intermolecular force vs. distance for E_{PAA450} emulsion at various concentrations of BSA at pH 5.2 is shown in the **Figure 6.3c.** The variation in the decay length and zeta potential as a function of BSA concentration at pH 5.2 is shown in **Figure 6.3d**. In the absence of BSA, the decay length and zeta potential of E_{PAA450} emulsion was found to be 20 nm and – 40 mV, respectively but reached 10 nm and -6 mV, respectively in the presence of 0.5 wt % BSA.

Here, the addition of BSA results in reduction in the onset of interaction in the force profile and collapse of the adsorbed PAA (as evident from the reduced decay length variation) at pH 3.5 and 5.2. But, the zeta potential measurement showed that the sign of E_{PAA450} emulsion is changed completely with 0.5 wt % BSA. In the absence of BSA, the zeta potential of E_{PAA450} emulsion at pH 3.5 was – 10 mV, which was changed to + 40 mV in the presence of 0.5 wt % of BSA. The sign change of emulsion in the presence of BSA points the fact that adsorbed PAA was fully displaced from the oil droplets through competitive adsorption of BSA. The variation of effective charge of BSA with solution pH originates from the dissociation of various groups on the backbone of BSA [266]. At low pH ($pH < pK_a$) the carboxylate groups are protonated but the amine groups are positively charged. Therefore, the net charge of the protein is positive under high acidic condition [265, 267, 276].

The complete replacement of anionic PE by BSA from oil droplets at a very small concentration (at low pH ~ 3.5) could be because of increased hydrophobicity of BSA with decrease in pH [276]. Similarly, the magnitude of the zeta potential decreased drastically for E_{PAA450} emulsion at pH 5.2 and reaches -6 mV in the presence of 0.5 wt % BSA at the same physiological pH. Previous report showed that BSA exhibit isoelectric point around pH 4.7 and 5.6 [255, 276]. Depending upon the amount of salt content, the isoelectric point of BSA varies. Since the ionic strength is zero in the present case, the isoelectric point is around pH 5.2 where zeta potential reaches nearly zero, which is consistent with the previous works [7, 255].

Earlier study showed that the charge of BSA was found to be highly positive at pH below isoionic point. But with increasing solution pH, the charge contribution due to carboxylate and amine group balances such that the total charge on the BSA was found to be balanced at isoelectric point. The structure of protein at an interface was completely different from its bulk counterpart [277] where the secondary structure was found to change drastically when oil-water interface was adsorbed with a thick layer of protein.[285, 286] The adsorbed BSA was also found to denaturate upon adsorption on oil (hexane) phase [286]. The maximum in the adsorption of BSA was observed at isoelectric point due to reduced electrostatic interaction, which allows large number of protein molecules to pack at an interface.

6.3.4 Zeta potential of E_{PDDA} and E_{PAA450} emulsion as a function of BSA

To confirm the competitive adsorption of BSA over emulsion droplets we have compared the zeta potential measurement of E_{BSA} emulsion (at zero salt concentration) and competitively adsorbed BSA over emulsion droplets at different solution pH (3.5, 5.2 and 7.0). The net charge of BSA was found to vary with solution pH, which is determined from the balance of various charged groups [266]. The zeta potential of E_{BSA} emulsion display an isoelectric point at pH ~ 5.4, below which the zeta potential was positive due to dominance of amine groups whereas at pH > 5.4 negative charge develops due to dominance of carboxylate group **(Figure 6.4a)**. With increase in pH > pK_a, the zeta potential of E_{PAA450} emulsion increase due to increased dissociation of surface carboxylate group of PAA where the zeta potential was found to be -10, -40 and -65 mV at pH 3.5, 5.4 and 7.0, respectively **(Figure 6.4b)**. But the addition of BSA changes zeta potential to + 38, -2 and -20 mV at pH 3.5, 5.2 and 7.0, respectively (**Figure 6.4b**) which was quite same as that of the zeta potential of E_{BSA} emulsion and also consistent with the previous reports [276]. The zeta potential of E_{PDDA} emulsion was + 50 mV between pH 2 and 10 but changes to + 38, -1 and – 10 mV in the presence of BSA at pH 3.5, 5.4 and 7.0, respectively, which was also consistent with the previous measurements [276]. Therefore, the intermolecular force and electrophoteic measurement showed that the addition of BSA to emulsion stabilized with a weak anionic or strong cationic PE results in the competitive displacement of adsorbed PE and adsorption of protein molecules. Although such competitive displacement and adsorption was observed earlier [111, 261, 287, 288] in the presence of adsorbed neutral macromolecule, the present study shows such competitive adsorption occur in the case of PE's too.

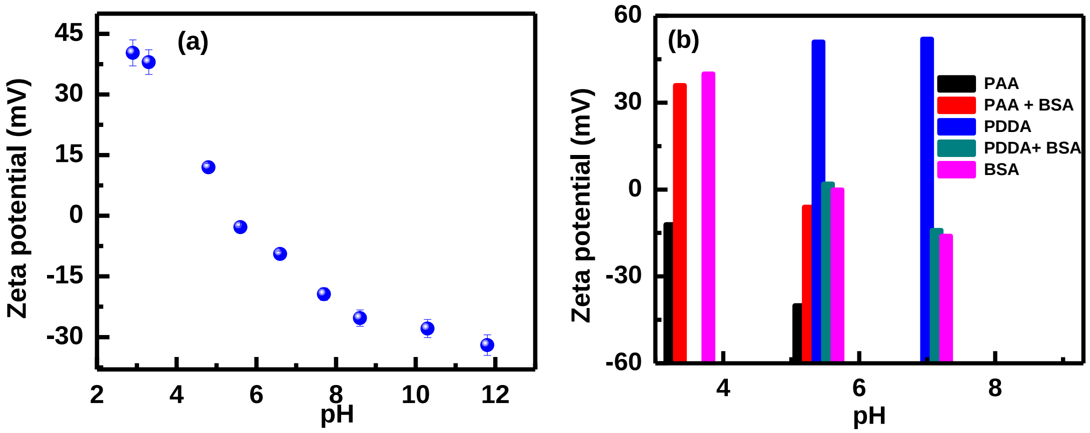

Figure 6.4: (a) Zeta potential of E_{BSA} emulsion as a function of pH. (b) Zeta potential of E_{PAA450} and E_{PDDA} emulsion in the presence of 0.5 wt. % BSA at pH 3.5, 5.2 and 7.0. Addition of BSA results in complete displacement of the adsorbed PAA and PDDA where the zeta potential of E_{PAA450} and E_{PDDA} emulsion in the presence of BSA was found to be the same as that of E_{BSA} emulsion.

To further confirm the competitive adsorption of BSA, the zeta potential of E_{PAA450}, E_{BSA}, E_{PAA450} + BSA and E_{PDDA} + BSA emulsion at various pH levels are compared as shown in the **Figure 6.5 a & b**. Due to fraction of deprotonated group on the backbone of PAA, the zeta potential of E_{PAA450} emulsion varies with pH but was nearly zero under high acidic condition (pH ~ 3.0). It increases with increase in pH due to an enhanced dissociation of surface carboxyl group (-75 mV at pH 11.5) as shown in the **Figure 6.5a**. The fraction of deprotonated group on the backbone is ~ 10% of the surface groups when pH < pK_a but increased dramatically when pH > pK_a. The increase in PAA charge density was consistent with the zeta potential measurement where it was found to be very low (~ 10 mV) between pH 3.0 and 4.5 due to undissociated COOH group. As dissociation of PAA was complete above pH 10, no change in zeta potential was observed above pH 10. Similarly, the zeta potential of E$_{BSA}$ emulsion shows an amphoteric behavior where under high acidic condition the zeta potential was found to be positive (+ 40 mV at pH 3.0) and highly negative under high alkaline condition (-34 mV at pH 12.0) with an isoelectric point of ~ pH 5.2. The zeta potential of competitively adsorbed BSA over emulsion droplets at various pH shows that under acidic condition it was + 25 mV, 0 mV at pH ~ 5.0 and finally reached -50 mVat pH ~ 12.0. This observation confirms the competitive adsorption of BSA over emulsion droplets under varying pH. The observed increase in zeta potential (-50 mV) might be because of limited number of PAA molecules at interface.

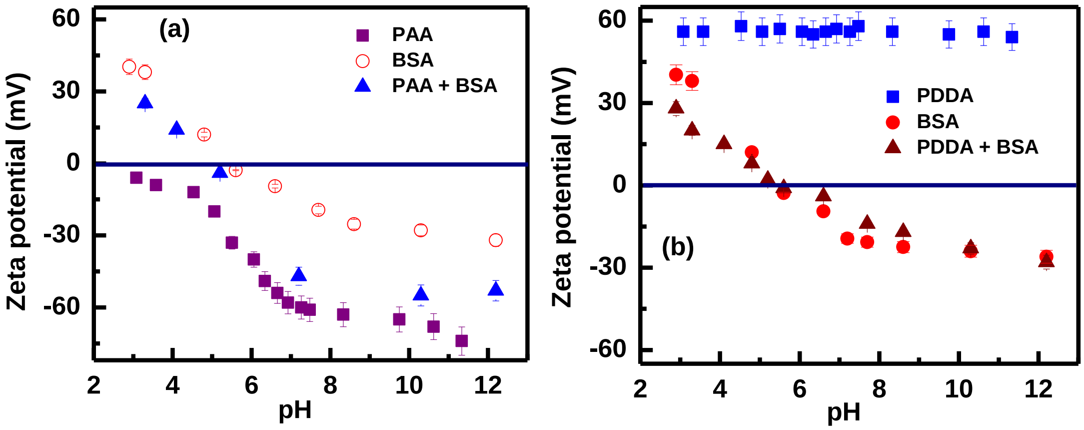

Figure 6.5: (a) Comparison study of zeta potential measurement for (a) E$_{PAA450}$, E$_{BSA}$ and E$_{PAA450}$ + BSA emulsion (b) E$_{PDDA}$, E$_{BSA}$ and E$_{PDDA}$ + BSA emulsion at different solution pH.

Similarly, the zeta potential of the E$_{PDDA}$ emulsion is highly positive, which is independent of pH in the range 2 to 10. When BSA (at pH 7.5) is added to the E$_{PDDA}$

emulsion in the same pH condition, it displaces PDDA and adsorbs over emulsion droplets (zeta potential -10 mV). The adsorbed BSA over emulsion droplets at various pH shows that under acidic condition (pH ~ 3.0) the zeta potential was + 30 mV, 0 mV ~ pH 5.0 and finally -34 mV under high alkaline medium (pH ~ 12.0). This observation further confirms the competitive adsorption of BSA over emulsion droplets.

Based on the intermolecular force and zeta potential measurement, the possible scenario of the interaction of adsorbed PAA and PDDA with BSA at pH 5.4 is schematically represented in **Figure 6.6**. When the emulsion droplets are covered with PAA where the solution pH > pK_a (~ 5.4), a long range electro-steric repulsion was noticed due to dissociated carboxylate group that makes the chain to adopt a highly extended structure. The globule to extended transition of adsorbed PAA was reversible with solution pH. The addition of a small amount of BSA competitively displaces the adsorbed PAA and hence the interface is decorated with both PAA and BSA. With further increase in BSA content (0.5 wt %) the adsorbed PAA is completely displaced and the interface is fully covered with BSA.

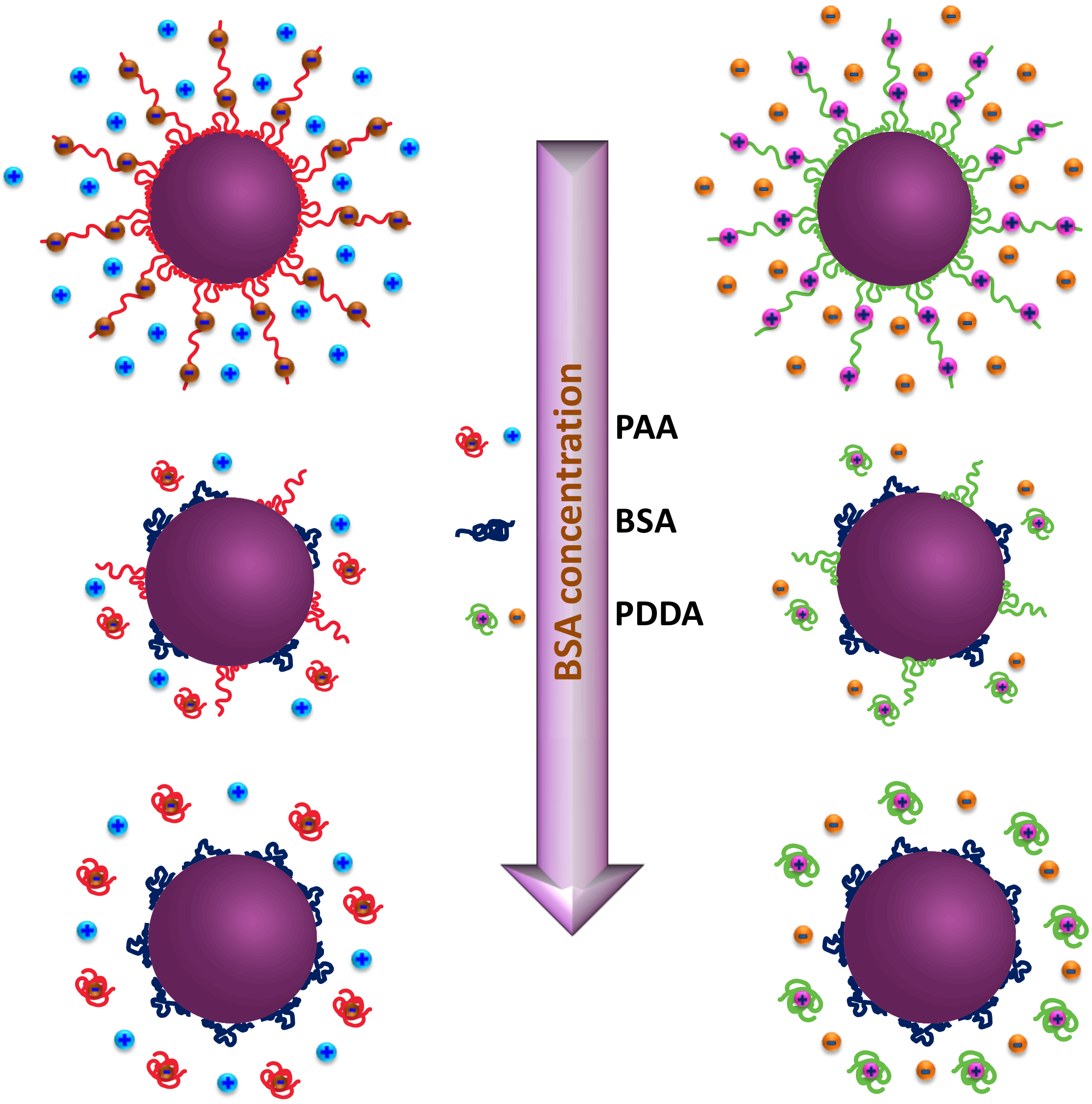

Figure 6.6: Schematic representation of the competitive adsorption of BSA at the oil-water interface covered with PAA (left) and PDDA (Right) at solution pH ~ 5.4. Low to high concentration of BSA is shown by the arrow from top to bottom. (top-left) Emulsion droplets covered with PAA possessing negative charge over PE backbone and counter-ions (H^+) in the aqueous phase. (middle-left) E_{PAA450} emulsion with protein molecule partially displaces the adsorbed PAA (bottom-left) complete displacement of adsorbed PAA upon

increased concentration of BSA. (top-right) emulsion droplets covered with PDDA with positive charge over PE backbone and counter-ions (Cl^-) in the aqueous phase. (middle-right) E_{PDDA} emulsion with BSA where partial displacement of adsorbed PDDA with BSA is shown (bottom-right) and complete displacement of adsorbed PDDA upon addition of high concentration of BSA.

When the emulsion droplets are covered with PDDA, a long range pH independent electro-steric repulsion was noticed due to dissociated quaternary ammonium groups that make the chain to adopt a highly extended structure. But, the extension of PDDA was found to be unaltered due to dissociation of surface groups at all solution pH. Though the adsorbed PDDA was dissociated completely, addition of small amount of BSA leads to a partial displacement of PDDA, where the interface is decorated with PDDA and BSA complexes. But, with further increase in BSA concentration, the adsorbed PDDA was displaced completely and the interface is fully covered with BSA.

The adsorption kinetics of protein at air-water and oil-water interface was studied extensively [237, 260, 283, 289-291]. Though earlier studies speculated that the adsorption of protein to an interface was diffusion controlled [258, 259], subsequent studies showed that the protein adsorption to an interface is not just a simple function of concentration gradient of protein between bulk and interface but rather it is the sum of interaction potential of the protein and the interface [237, 260, 291]. The interaction arises from the contribution due to electrostatic (μ_{elec}), van der Waals interaction (μ_{vdW}), hydrophobic interaction ($\mu_{h\varphi}$) of the protein with the force field generated at the interface. Therefore, the total chemical potential of protein at any distance from the interface can be expressed as $\mu = \mu_{ideal} + \mu_{conf} + \mu_{h\varphi} + \mu_{elec} + \mu_{vdW}$. Here, μ_{ideal} is the chemical potential due to concentration gradient, μ_{elec} comprised of coulomb interaction between the protein and its image charge in low dielectric media (oil phase) as well as electric double layer due to protein and interface and μ_{vdW} corresponds to van der Waals interaction, which comprised of Debye-Keesom and London dispersion. Also, the adsorption of protein depends on the nature of interface (air-water or oil-water) and also the type and magnitude of interaction [237].

Though hydrophobic interaction is considered as one of the major driving forces for the adsorption of protein at liquid-liquid interface ($E_{h\varphi} = -84\, R \exp(-\frac{d}{d_0})$), the uneven distribution of hydrophilic and hydrophobic patches (where only 50 % of the globular protein is hydrophobic) over protein backbone indicates that only half of the interaction energy contributes to the adsorption of protein. At oil-water interface, the London dispersion and Debye-Keesom interaction were found to be attractive for protein molecule (BSA, lysozyme and β-casein) [237]. As protein approaches the interface, the electric double layer of protein and interface can overlap, that can result in a net attractive or repulsive interaction, depending upon the sign of the charges of an interface and protein. When the interface and protein backbone bears opposite charge the net interaction becomes attractive whereas when the charge of interface and protein are similar the net electrostatic contribution becomes attractive at short distances.

Studies on the adsorption of BSA showed that equilibrium concentrations of BSA over oil-water interface were higher compared to their bulk diffusion coefficients, but the adsorption and equilibrium concentration of the same at air-water interface was found to be lower [260]. The adsorption of protein over an oil-water interface depends on the energetics of interaction of the various molecular forces of the proteins with the interfaces. The sum of interaction energy for the protein at oil-water interface was found to be attractive, which was larger for BSA than other protein molecules such as lysozyme, β-casein etc [237].

Our study also showed that within a time scale of ~ 30 minutes, the adsorbed weak anionic and strong cationic PE was quickly displaced by the added BSA which is consistent with the earlier reports. Particularly, for E_{PAA450} emulsion at low pH (~ 3.5) when the hydrophobicity of the BSA was quite high, immediate adsorption is noticed, which is further confirmed from the zeta potential measurement where the sign of the zeta potential changes to positive with addition of 0.02 % BSA and the magnitude of zeta potential increases dramatically with further increase in BSA concentration. Though the nature and the charge density of PEs are completely different in the present case, the displacement of adsorbed PDDA and PAA by BSA was noticed at all the pH values, which shows the universal nature of competitive displacement of PE's from oil-water interface.

6.4 Conclusion

The role of bovine serum albumin (BSA) with quenched polyelectrolyte (PE), poly(diallyldimethylammonium chloride) – PDDA, and annealed PE, poly(acrylic acid) – PAA, adsorbed at oil-water interfaces is studied using intermolecular force and electrophoretic measurements. The competitive adsorption of protein at O/W interface shows that irrespective of the nature of adsorbed PE, they are displaced by small molecules of BSA at all solution pH. In the absence of BSA, emulsion droplets covered with PDDA or PAA exhibits a long range electro-steric repulsive interaction, where the former exhibits a pH independent and latter shows pH dependent behavior. The addition of BSA to E_{PDDA} emulsion at pH 5.2 results in a decrease in the onset of interaction in the force profile, followed by the replacement of PDDA by BSA at oil-water interface. The sign of the zeta potential of E_{PDDA} emulsion was found to change upon competitive adsorption of BSA. Competitive adsorption of BSA over emulsion droplets was also observed at pH ~ 7.0 when the surface was initially covered with PDDA. For the E_{PAA450} emulsion, addition of BSA decreases the onset of interaction force profile, due to replacement of PAA by BSA molecules in the pH range 3.5 and 5.2. The reversal of the sign and the change in the magnitude of zeta potential indicates the displacement of PDDA and PAA by BSA molecules at the oil-water (O/W) interface, which was in agreement with the findings of Satulovsky et.al. [Proc. Natl. Acad. Sci. 97 (2000) 9037–9041] that polymers on hydrophobic surfaces are not effective in preventing protein adsorption, indicate the displacement of macromolecule of very large molecular weight and preferential adsorption of small macromolecules at the O/W interfaces, irrespective of the nature of adsorbed PE's (strong or weak, anionic or cationic with high or low charge density). These results should find interesting applications in industrial products (food and pharmaceutical) where different types of stabilizing entities are used during storage and applications. Further, these results are also useful to understand the behavior of biologically important macromolecules adsorbed at cell membrane-fluid interface as the oil-water interface covered with charged polymer mimics cell membrane-fluid interface adsorbed with protein, polysaccrides etc.

Chapter 6

CHAPTER 7

Novel application of magnetic nanofluid stabilized with macromolecules

7.1 Non-enzymatic detection of urea using magnetic nanoemulsion

7.1.1 Importance of urea sensing

Urea[$(NH_2)_2CO$], is extensively used as a nitrogen-release fertilizer in agriculture and animal feed additive and in consumer products such as detergents and cleaning products [292]. The estimated worldwide production of urea is 208 metric tons by 2020, of which major chunk (~90%) will be used in fertilizers [293]. The urea from the human body is excreted into the urine, is a predominant metabolite of nitrogenous compounds [294]. Urea denatures proteins[295] and also affects in vitro activity of enzymes [296]. The carbonylation of proteins in renal cell [297] leads to severe protein damage, that can cause diseases such as diabetes, chronic renal failure, chronic lung disease and sepsis [298]. The presence of high level of urea damages cellular DNA by developing oxidative stress and proteins of renal inner medullary cells of mouse[297]. DNA damages include breaking of single strand and alternation of bases. The normal level of urea in blood serum is in the range of 2.7–7.5 mM (15-40 mg/dL) [299]. The amount of urea in serum of the patients suffering from renal insufficiency is in the range of 30-80 mM. Patients suffering from heart failure and renal dysfunction were found to have an abnormal urea level [300]. Similarly, the urea concentration in cow milk is used as an indicator of protein-feeding efficiency, assessing the quality of ethyl carbamate (urethane) in wine, marine-nitrogen cycle etc [294]. Therefore, knowledge of urea concentration in body fluids is very important in diagnosing renal and liver diseases and also for environmental monitoring and in food science.

Although there are several analytical approaches for the measurement of urea, no single technique covers the large concentration range. This warrants the need to develop a simple, fast, cost effective, reliable and robust approach for real time monitoring of urea. There are several direct [39, 292, 294] and indirect [301-304] analytical techniques for the measurement of urea. The indirect techniques rely on the enzymatic degradation of urea before its detection whereas direct techniques use absorbance or calorimetric. Though much work were done on enzymatic degradation of urea, where immobilized urea on the surface of the material (e.g. metal oxide) often alters the structural conformation of the urease that can encounter problems in the accurate detection of urea. Moreover, the modification of electrode with an enzyme is a complicated immobilization procedure that has poor stability besides complex operating procedure and high cost. In case of direct technique such as calorimetric, pre-treatment of the sample is required which is considered as one of the major disadvantages, besides having difficulties in field monitoring. Many new nanomaterial based sensors have been attempted in recent years for quantifying the level of urea [305-310].

In recent years, stimuli responsive magnetic materials are finding great interest because of their applications in sensors [83], heat transfer [74], hyperthermia [311] optical devices [312], bio implants [120] etc. Magnetic nanoemulsions are kinetically stable system, stabilized with surface active molecules at the oil-water (O/W) interface. They respond to a magnetic field and exhibit a significant change in their optical properties [313]. Depending upon the type of adsorbed moieties and physio-chemical properties, their optical properties are tuned [43, 314]. Response stimuli smart polymers are shown to have applications in gas sensing [315].

In this work, a simple, easy to use and selective detection of urea sensor is developed using magnetically responsive nanofluids. The response time of the present approach is very fast (~ 100 times faster compared to 3D crystals), and is highly cost effective. By suitably adjusting the concentration of the oil droplets, the nanoemulsion exhibits a color change in the presence of urea which enables visual naked eye detection of urea. Moreover, the current method is non-enzymatic and detects a wide range of concentrations of urea.

7.1.2 Materials and methods

Magnetic nanoemulsions, E_{SDS}, E_{PLURO}, and E_{PAA450} are used in this study. Intermolecular interactions for E_{SDS}, E_{PLURO}, and E_{PAA450} in the presence of various concentrations of urea were measured using magnetic chaining technique. Material preparation and experimental setup are explained in Chapter 2.

7.1.3. Results and discussion

7.1.3.1 Dependence of Bragg peak position on the concentration of urea

Bragg peak spectra for E_{SDS}, E_{PAA450} and E_{PLURO} at fixed magnetic field but at different urea concentration is shown in the **Figure 7.1 (a-c)**. A constant magnetic field of 110 G was used to create the grating with a 'd' spacing of 260 and 280 nm for E_{SDS} and E_{PLURO} emulsion whereas 320 G was used to fix the grating distance of 340 nm for E_{PAA450} emulsion (without urea). In the absence of urea, the Bragg peak was formed at 760 & 780 nm for E_{SDS} and E_{PLURO} emulsion, respectively whereas for E_{PAA450} emulsion it formed at

900 nm. The Bragg peak was shifted to a lower wavelength as the concentration of urea increases (shown by the arrow). The Bragg peak position for E_{SDS} emulsion was shifted to 618 nm from 760 nm at a concentration of 0.6 g/L. For E_{PAA450} emulsion, the Bragg peak position in the absence of urea was 880 nm, which is shifted to 656 nm at a urea concentration of 33.3 g/L. For E_{PLURO} emulsion, the Bragg peak position in the absence of urea was 776 nm, which was shifted to 598 nm for a urea concentration of 324 g/L. Even at very high concentrations of urea, the Bragg peak has not collapsed, indicating the excellent stability of the emulsion.

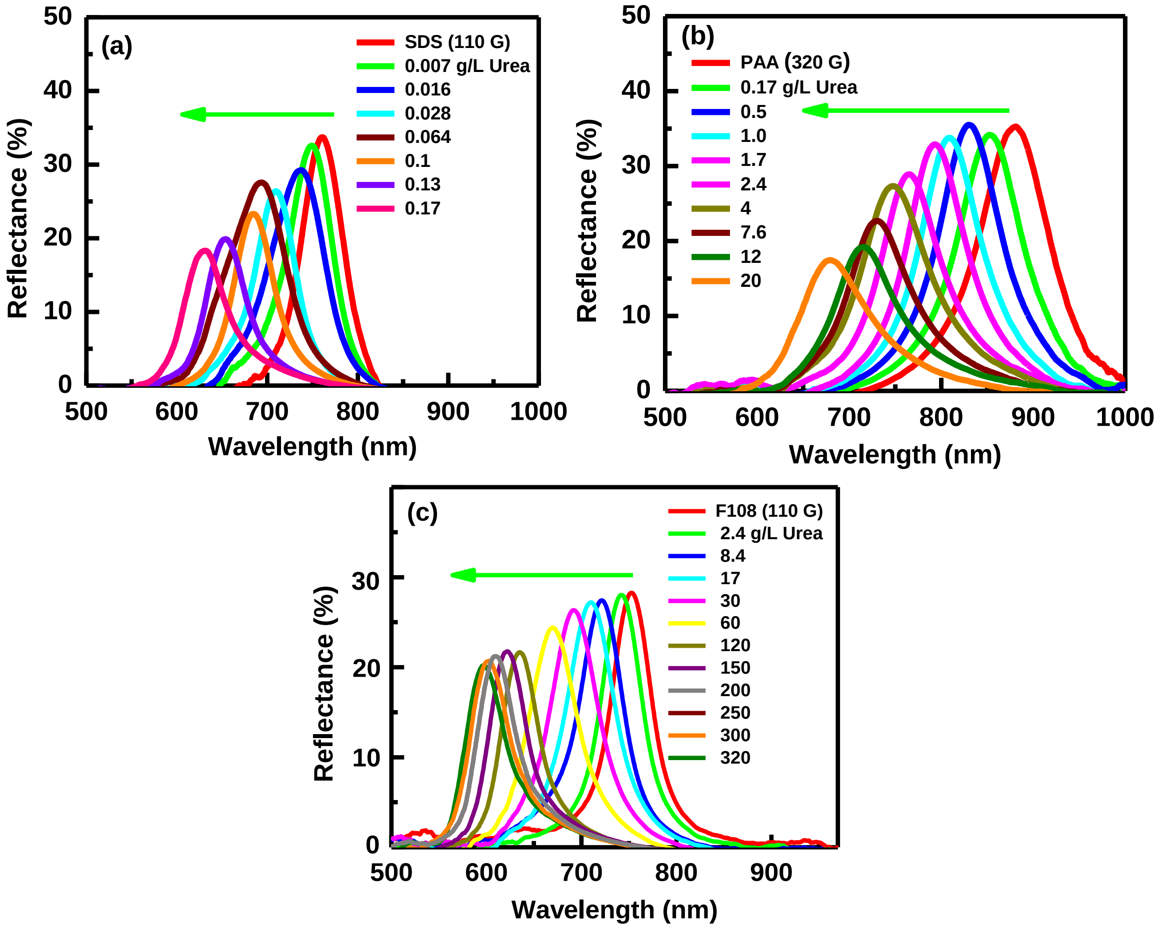

Figure 7.1: Bragg peak spectra at different urea concentrations ranging from 0.007 g/L to 320 g/L for (a) E_{SDS} (b) E_{PAA450} and (c) E_{PLURO} emulsion.

Figure 7.2 (a & b) shows the Bragg peak wavelength and the corresponding change in wavelength for various concentration of urea for E_{SDS}, E_{PAA450} and E_{PLURO} emulsion. In the urea concentration range of 0.003-0.6 g/L, the Bragg peak wavelength change in E_{SDS} emulsion was 760-618 nm, with a total $\Delta\lambda_{peak}$ change of 142 nm. In the case of E_{PAA450} and E_{PLURO} emulsions, for the urea level of 0.18-33.3 g/L and 2.4-334 g/L, the Bragg peak wavelength change was 880-656 nm and 776-598 nm, respectively, corresponding to a total $\Delta\lambda_{peak}$ change of 224 and 178 nm, respectively. These results show that the linear detection range of urea can be extended dramatically by using macromolecular functional groups of larger molecular weights.

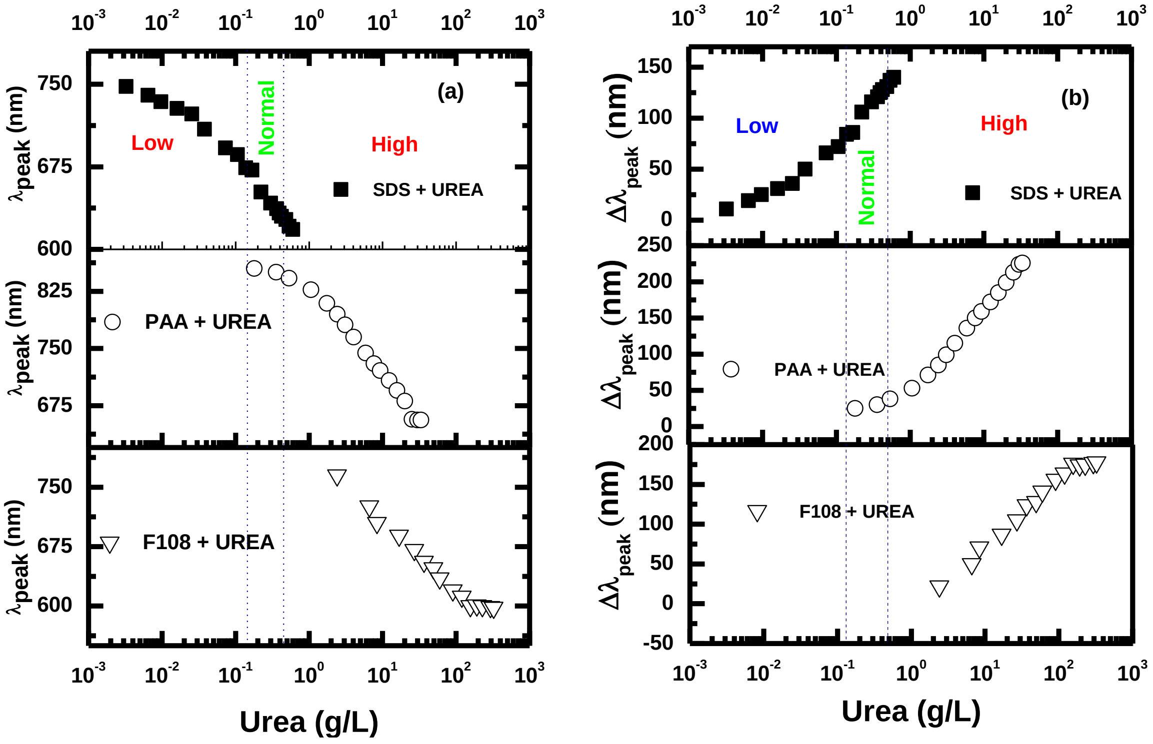

Figure 7.2: (a) Bragg peak wavelength (λ_{peak}) Vs urea concentration for E_{SDS}, E_{PAA450} and E_{PLURO} emulsion (Top to bottom) (b) the corresponding change in Bragg peak wavelength ($\Delta\lambda_{peak}$).

The normal urea level in serum is 0.14-0.4 g/L. For the lower to normal urea detection range, E_{SDS} emulsion is found to be suitable. The E_{PAA450} and E_{PLURO} emulsion are found to be ideal for the detection of higher concentrations of urea. Both E_{SDS} and E_{PAA450} emulsion shows a linear detection range for the normal urea level (0.14 to 0.4 g/L) whereas for E_{PLURO} emulsion, detection of very high concentration of urea (2-320 g/L) was possible, with an excellent linear variation up to 120 g/L. Since, the response time of the nanoemulsion is about a second, this method offers a rapid detection of urea.

7.1.3.2 Mechanism of interaction of urea with functional moieties

To understand the reason for the observed large shift in Bragg peak upon addition of urea, the molecular interactions between the emulsion droplet is studied. The details of the force measurement technique is discussed in previous publications [101, 109]. **Figure 7.3 (a-c)** shows the force-distance profile for E_{SDS}, E_{PAA450} and E_{PLURO} emulsions at various concentrations of urea. Overall, the force profiles were found to be repulsive and decay exponentially with distance. With increasing urea concentration, the range of repulsive force is reduced in all the cases. For electrostatically stabilized colloidal systems, interaction forces in the presence of electric double layer was repulsive and decay exponentially with distance[159, 160]. Similarly, the interaction force due to polymer or weak polyelectrolyte covered surface also decay exponentially with distance which is expressed as $F(h) = K \exp\left(-\frac{h}{\lambda}\right)$, where the pre-exponential factor, K is the force constant, h is the inter droplet spacing and λ is the decay length of the polymer.

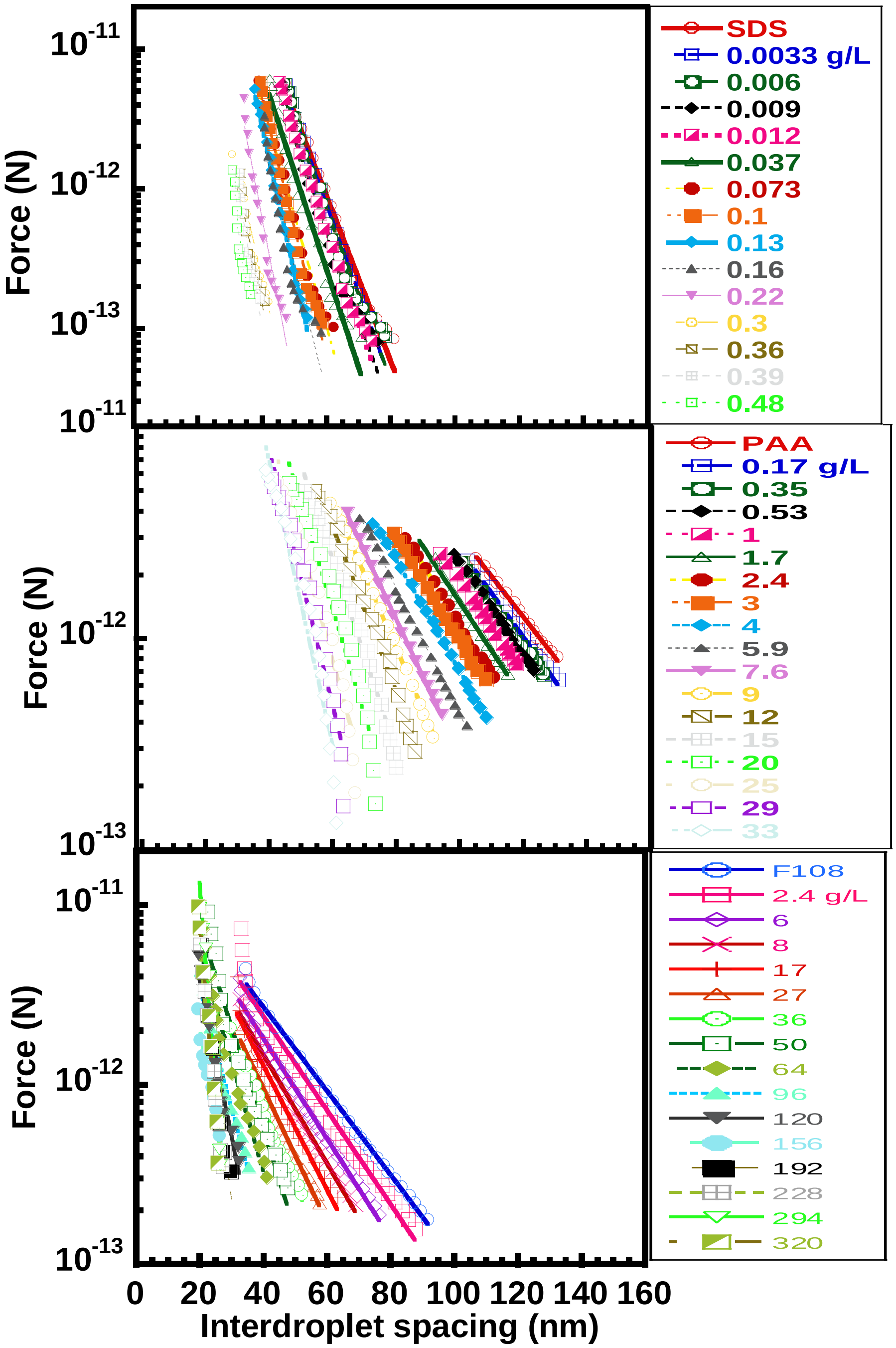

Figure 7.3: Force vs. distance for (a) E_{SDS} (b) E_{PAA450} and (c) E_{PLURO} at different concentrations of urea. The solid line represents the best fit of the experimental data with an exponential function.

From the force profiles, the Debye- κ^{-1} or decay length -λ, first interaction distance $2L_0$ and the magnitiude of force K are obtained for different concentrations of urea. The κ^{-1} or λ for charged or polymer stabilized emulsion is obtained from the slope of the force-distance profile. The force parameters obtained for the three cases at different urea concentrations are shown in the **Figure 7.4 a-d.**

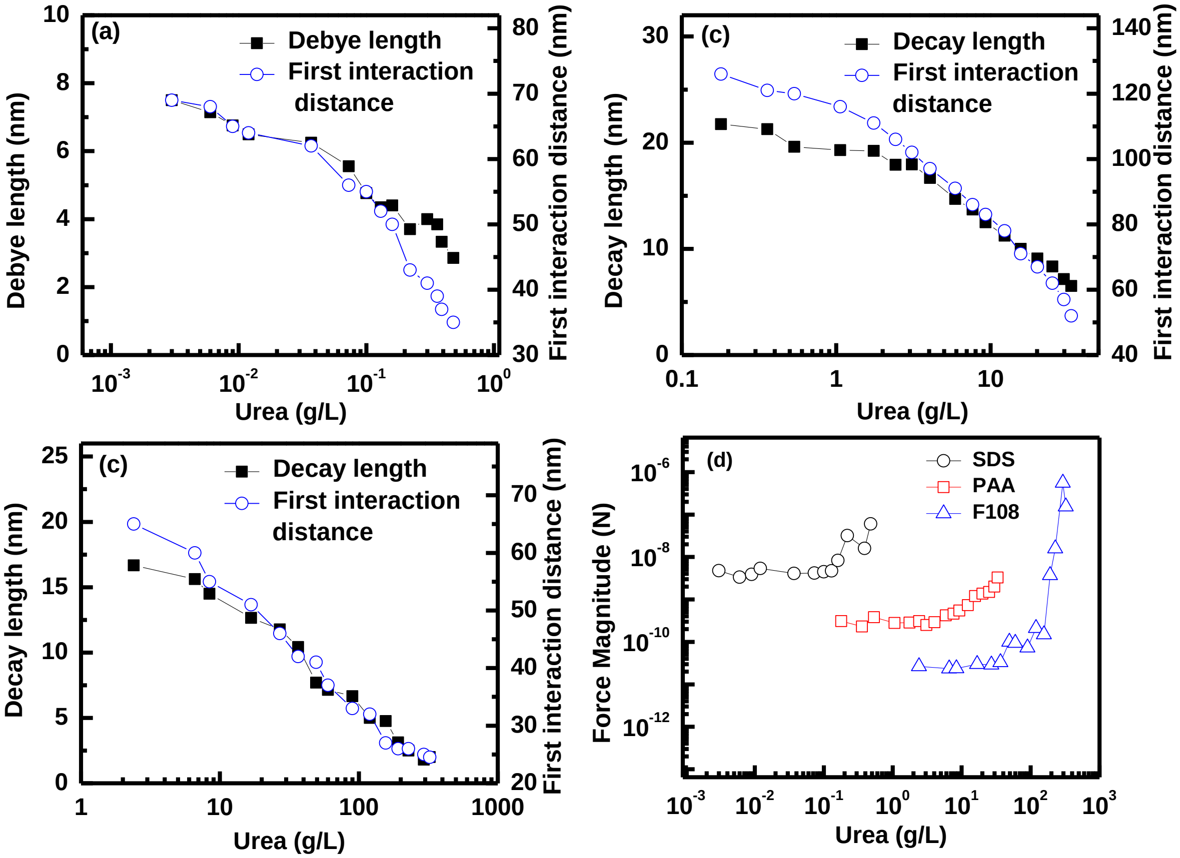

Figure 7.4: Variation of force parameters (Debye or decay length and first interaction distance $2L_0$) as a function of concentration of urea for (a) E_{SDS} (b) E_{PAA450} and (c) E_{PLURO} emulsion and (d) force magnitiude, K as a function of concentration of urea for E_{SDS}, E_{PAA450} and E_{PLURO} emulsions.

The κ^{-1} of E_{SDS} emulsion decreased from 9 to 2.8 nm as the concentration of urea is increased from 0.003 to 0.6 g/L. In the same urea concentration, the $2L_0$ reduced from 71 to 35 nm, with an order of magnitude increase in K. For E_{PAA450} emulsion, the λ is reduced from 22 to 6.5 nm as the concentration of urea is increased from 0.17 to 33 g/L. In the above concentration range, the $2L_0$ changes from 131 to 52 nm and K increased by one order of magnitude. For E_{PLURO} emulsion, the λ and $2L_0$ is reduced from 17 to 2.5 nm and 64 to 24 nm as the concentration of urea is increased from 2.4 to 334 g/L. Surprisingly, K increased by four orders of magnitude for E_{PLURO} emulsion at high concentrations of urea.

7.1.3.3 Urea - sodium do-decyl sulphate (SDS) Interaction

It is well established that urea is an effective denaturants of proteins and modify the hydrophobic-hydrophilic interactions of surfactants [316]. Therefore, it can affect micellar properties by modifying the delicate hydrophobic-hydrophilic balance. Earlier studies on the interaction of urea with ionic surfactant using electron spin resonance spectroscopy showed that urea interacts with the polar headgroups of the ionic surfactant micelles, penetrates below the surfactant polar headgroups by replacing some water molecules that solvate the hydrophobic chain and the polar headgroup of the amphiphile, and strongly increases the microviscosity of the micelle interface [317]. Their study also confirms the direct interaction between urea and probe molecules at concentrations below the CMC of SDS. Therefore, SDS - urea interaction is expected to screen micellar surface charge and weaken the hydrophobic interactions. In another study by Carnero Ruiz et al. [318] also confirmed the direct interaction of urea with SDS where a decrease in SDS micellar size with increase in urea concentration is reported. Aswal et al. [319] showed that the addition of urea can cause an increase in CMC of SDS due to enhanced solubilization of alkyl chain.

Further, their study also confirms that the repulsion between the head group of the Gemini surfactant decreases with increasing concentrations of urea. This finding of the reduction in the κ^{-1} and $2L_0$ of E_{SDS} emulsion in the presence of urea is in good agreement with the previous findings on direct interaction of urea with the polar head groups of the SDS micelles. The penetration of urea to the surfactant polar head groups and the strong increase in the micro viscosity of the micelle interface leads to a reduced electrostatic repulsion between the head groups and reduce the spatial extension of the double layer.

7.1.3.4 Urea - poly(ethylene oxide)-poly(propylene oxide)-poly(ethylene oxide) (F-108) interaction

As the concentration of F-108 polymer in the present study is well above CMC (7 g/l) [320], it is expected that the triblock micelles are adsorbed at the liquid interface. The observed λ of E_{PLURO} emulsion (17 nm) is comparable to the hydrodynamic size of F108 micelle ~17 ± 2.5 nm obtained by Kabonov et al.[321]. An earlier study showed that the presence of urea affect the formation of polymeric micelle by altering the balance between hydrophilic and hydrophobic block of triblock polymers [322]. A similar study also showed that urea is known to interact directly with PEO as well as PPO [323]. The two plausible mechanisms of action of urea in aqueous solutions are: hydration of non-polar solutes by behaving as a structure-breaker and replacement of some of the water molecules in the hydration shell of the solute and its final self association [324]. There is also a report that urea does not behave as a water “structure breaker” [302]. In a recent study, Uttam Anand et al. [323] showed from red edge excitation shift (REES) experiments that both PPO and PEO regions are hydrated heavily by urea, and the PPO region is easily dehydrated. They also observed that the temperature counteracts the effect of urea and the counteraction effect is more prominent in the core region and urea reduces the viscosity of the core and corona regions. From ^{1}H NMR technique Jun-he Ma et al. [325] had shown that urea interact selectively with the PEO blocks of the block copolymer (PEO-PPO-PEO), and the interaction sites changes with increasing temperature. Such interaction also increases the hydration of PPO segment of the block copolymers and increases critical micellization temperature (CMT). The observed reduction in the $2L_0$ and λ in the force profile for E_{PLURO} emulsion clearly shows the strong interaction of urea with the pluronics micelles. With increased concentrations of urea, the micellar size decreases and eventually the de-micellization occur. If the micellar structure remains intact, the $2L_0$ values would have remained the same or decreased slightly.

7.1.3.5 Urea - poly(acrylic acid) (PAA) Interaction

PAA is a water soluble anionic polyelectrolyte that undergoes drastic conformational changes (coil to globule) by varying the pH of the medium. At low pH, it is neutral and exhibit coiled structure whereas at high pH, it swells due to ionization of carboxyl group at the backbone of the polyelectrolyte. Since, the experiment was carried out at pH 7, the polyelectrolyte is highly charged and exhibits an extended conformation, which is evident from the decay length (~ 23 nm) and zeta potential (-47 mV). Eritsyan et al. [326] studied the formation of PAA and urea complexes using IR spectroscopy and showed that the intra and intermolecular interactions between the acrylic acid (COO^-) of PAA and ammonium ion of urea (NH_3^+), results in the formation of salt. The formation of FTIR band between 1560 and 1640 cm^{-1} showed the presence of ammonium ion and carboxylic acid, whereas the occurrence of bands between 1695 and 1705 cm^{-1} was attributed to the formation of amide group ($-C=O-N-H-R-$) due to interaction between $-COOH$ and $-NH_2$.

Fernandes et al. [327] also showed that amino group of urea react with carboxylic group of acrylic acid.

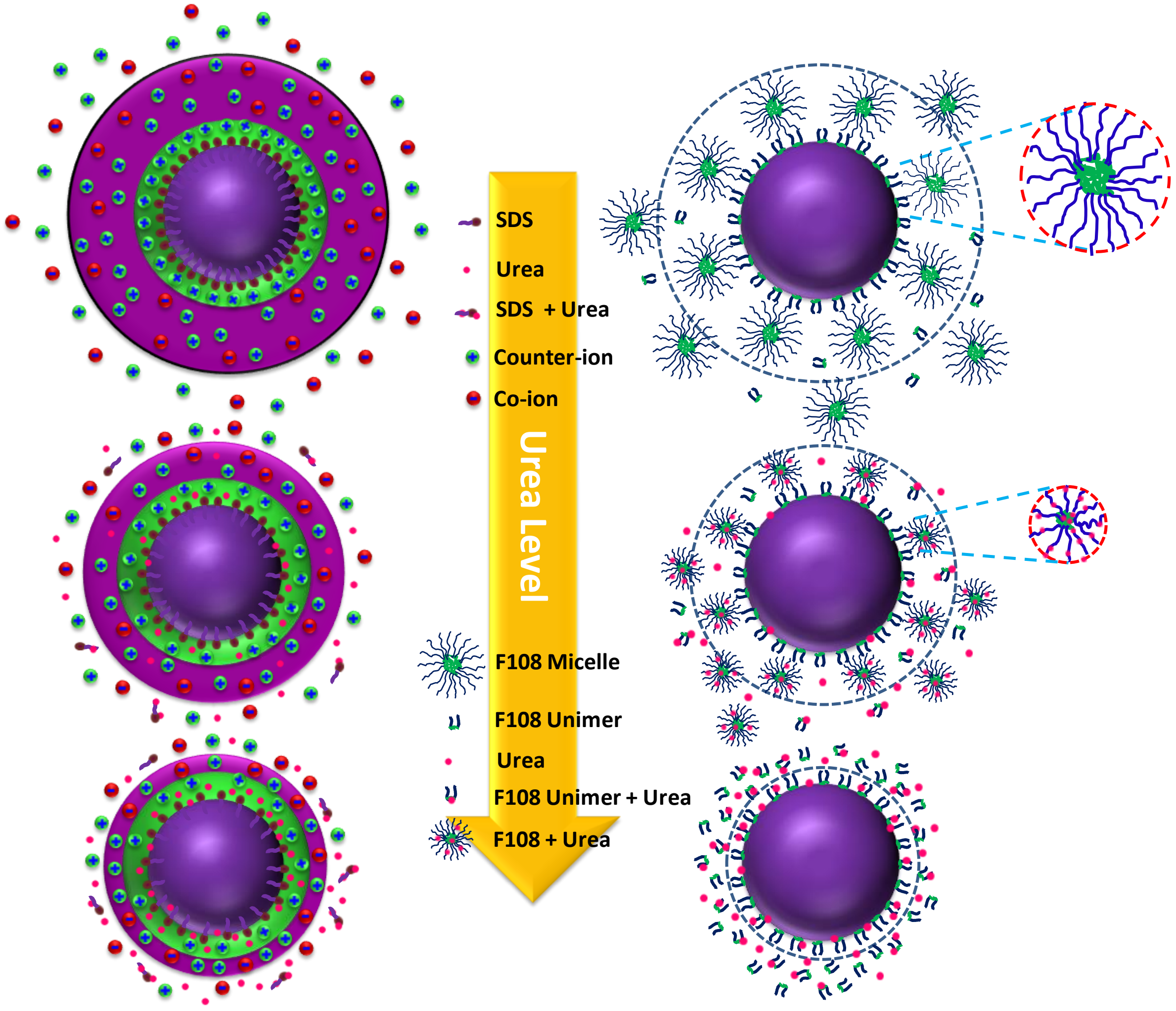

Figure 7.5: Schematic representation of the interaction of urea with the surface active moieties (left) and pluronics (right) at different concentrations of urea and its effect on the electrical double layer and polymeric conformation. Low to high concentration of urea is shown from top to bottom.

The zeta potential measurements of the E_{PAA450} emulsion in the presence of different concentration of urea were carried out. In the absence of urea, the observed zeta potential was - 47 mV at neutral pH. As the concentration of the urea increases, zeta potential decreases steadily and reaches -14 mV at 30 g/L of urea which supports the force measurement data, where the λ was found to decrease in the presence of urea by neutralizing adsorbed COO^- by amine group (NH_3^+) due to enhanced interaction between PAA and urea. Based on the experimental results from force, hydrodynamic diameter, zeta potential and Bragg peak measurements, the interaction of urea with the surface active moieties (left) and pluronics (right) at different concentrations of urea (low to high from top to bottom) and the corresponding changes in the electrical double layer (left) and polymeric conformational changes (right) are shown schematically in **Figure 7.5**.

7.1.3.6 Interference of polyacrylic acid (PAA) stabilized emulsion with biologically important ions

The blood contains different type's ions in addition to red blood cell (RBC), white blood cell (WBC), platelets etc. The amount of Na^+, and Ca^{2+} in the serum is ~ 130 mM [328] and 2-2.5 mM [329], respectively. In order to test the selectivity of the sensor in the presence of biologically important cations, the spectral response of the sensor in the presence of NaCl of 130 mM and $CaCl_2$ of 2.5 mM is measured, where E_{PAA450} emulsion was used. Here, the urea concentration was varied from 0-30 g/l. Initially, the pH of the E_{PAA450} emulsion is increased to ~ 9, before the addition of salts in the system, in order to stretch the PAA by increasing dissociation of COOH group on the polymer backbone.

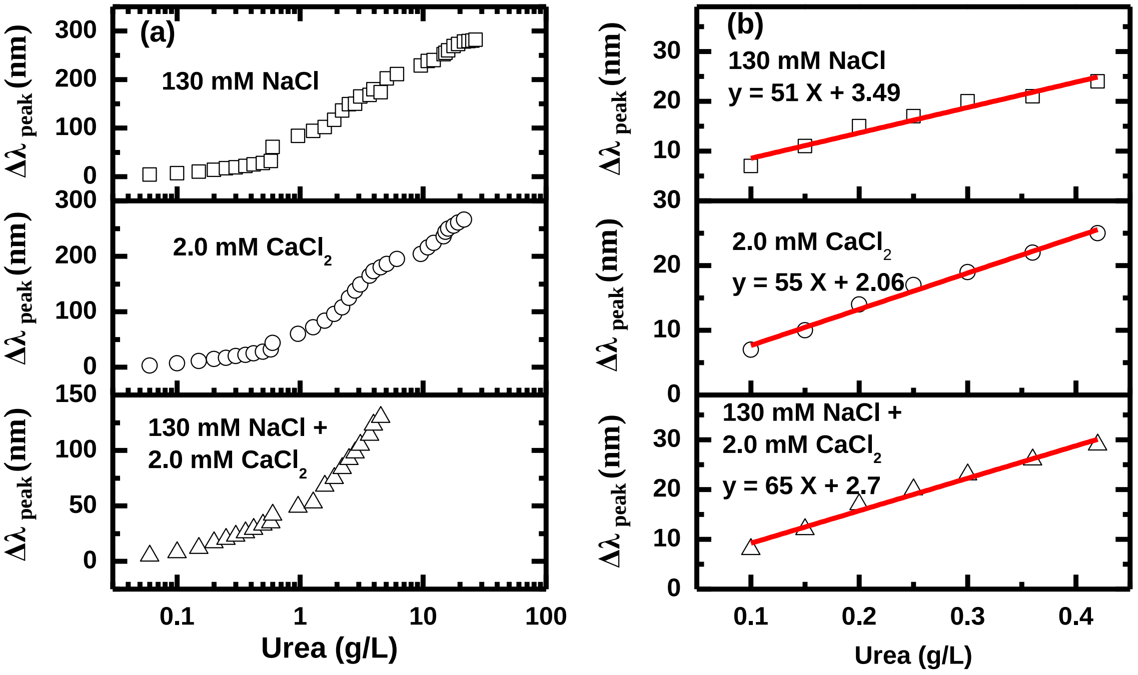

Figure 7.6: Change in Bragg peak wavelength for E_{PAA450} emulsion vs. urea in the concentration range of (a) 0 – 30 g/L and (b) 0.1-0.45 g/L in the background salt concentrations of 130 mM NaCl, 2.0 mM $CaCl_2$ and mixture of both (From top to bottom). The solid lines in the figure represent the best fit on the experimental data.

The change in Bragg peak wavelength for an E_{PAA450} emulsion in the presence of urea of varying concentration in the background salt concentration of NaCl (130 mM), $CaCl_2$ (2.0 mM) and a mixture of both are shown in the **Figure 7.6 a & b**. The Bragg peaks are formed at 990 nm for salt free emulsion shifts to 865 nm, 900 nm and 710 nm in the presence of NaCl, $CaCl_2$ and mixture of both. Here, the Bragg peak is blue-shifted in the presence of urea. The variation in the Bragg peak was found to be linear in the normal urea concentration range, which shows the selectivity of the sensor in the presence of other ions. The change in the Bragg peak wavelength in the presence of urea is 266 nm, 282 nm and

130 nm for 130 mM NaCl, 2.0 mM $CaCl_2$ and mixtures of both, respectively. From the observed difference between the Bragg spectra, the normal and abnormal urea level in the serum can be detected directly in the presence of background electrolytes. Therefore, for practical application, the E_{PAA450} emulsion is found to be ideal. By modifying the suitable functional molecules with a desired pH level, the possibility of extending the sensitivity and selectivity in the presence of other ions is possible and such studies are planned.

7.2 Temperature and pH Sensing using Functionalized Magnetic Nanofluid

7.2.1 Importance of temperature and pH sensing

Temperature and pH are important parameters which play critical role in metabolic activity in human [330], environmental factors [331] and many other chemical processes. Abnormal intracellular pH leads to biological malfunction that results in the disruption of cardiac function [332], progression of cancer [333] etc. Certain metabolic reaction happen only in particular physio-chemical conditions. For instance, the pH of the extra cellular fluid and tissues, including blood are very sensitive to acid-base balance [334] and any deviation from the normal pH leads to a worsening of biological function and development of diseases such as acute contractile depression [335], triggering of electrical arrhythmia [336] etc. The change in pH of the body fluid can result in several disorders and even neuronal activity causes significant changes in pH of brain. The patients suffering from diabetes, renal and respiratory causes are found to have abnormal pH level; e.g., abnormal pH in urine indicates the renal dysfunction [337]. Temperature is another important physiological condition to be monitored to assess malfunctioning of certain organs and diseases in humans. The normal body temperature of humans lies between 35 and 38 °C [338]. The body temperature above the normal causes hyperthermia whereas body temperature below the normal causes hypothermia. The minor disorders in the elevation of body temperature include headache, nausea, vomiting and weakness etc. The heart rate increases 10 beats per minute for each 1 °C rise in temperature, above the normal limit for children [339]. Hypothermia may cause vigorous shivering, cold dieresis, amnesia and bradycardia and can result in cardiac arrest and hallucination [222]. This warrants the need to monitor the pH and temperature precisely in body fluids using cost effective and portable devices.

To overcome the limitations of existing pH sensing techniques (glass blub based and spectroscopic approaches) , several new materials have been attempted where the factors often weighed are cost, sensitivity, reliability, portability, miniaturization, ease of fabrication, biocompatibility etc. Much attention was paid to fluorescence based sensor [340] but the disadvantage is that the intensity based fluorescence is affected by fluctuation in excitation source, detector drift and changes in light path through sensor film. Though several other types of pH and temperature sensors were developed in the past, there has been increased interest in the development of simple and cost effective optical sensors for pH [341, 342] and temperature measurements [343]. The optical sensors were developed by utilizing the properties of materials such as fluorescence [344], luminescence [340] and absorbance [345] etc. The techniques such as fiber Bragg grating [346], colorimetric [347], tilted fiber Bragg grating [348], surface plasmon resonance [349], lossy mode resonance [346] etc were used to measure the pH values. Though independent monitoring of pH [350, 351] and temperature [343, 352, 353] were achieved by many techniques, only a few works were reported in monitoring of both temperature and pH [354-356] and other physical or chemical parameters [357, 358] simultaneously.

Among various materials, in recent years, stimuli responsive materials are getting much attention due to their significant change in optical properties in the presence of external stimuli like temperature, electric and magnetic field. Stimuli responsive polymers also find numerous applications in drug delivery [359], gated ionic channel [89], rheology modifier [360], multi-parameter sensor [209, 343] and actuators [175]. The limitations of glass bulb based pH sensors includes errors in obtaining accurate data at high acidic and basic environment whereas the pH measurement based on spectroscopy (fluorescence and absorption), microelectrodes, nuclear magnetic resonance etc, are neither portable systems nor cost effective. In this work, it is shown that the optical properties of magnetic nanofluid can be modulated suitably by functionalizing them with stimuli responsive moieties for real time applications. A new optical probe by coupling magnetic nanoemulsion with a temperature or pH responsive macromolecules for sensing temperature and pH is developed. Owing to its optical detection mode, it has advantages over conventional electrochemical techniques like, immunity to electrical interferences, miniature nature, remote sensing ability, non-invasive or minimally invasive and disposable features. The unique feature and novelty of this approach includes, faster response time, broad temperature and pH sensing range. Accurate monitoring of pH and temperature are achieved here by simply measuring the shift in Bragg peak position.

7.2.2 Materials

Magnetic nanoemulsions, E_{PVA}, E_{PAA450} and E_{PAA250} are used in this study. Intermolecular interaction for E_{PVA}, E_{PAA450} and E_{PAA250} emulsion at different temperature and pH were measured using magnetic chaining technique. Material preparation and experimental setup are explained in Chapter 2.

7.2.3 Results and discussion

7.2.3.1 Dependence of Bragg peak position with temperature in E_{PVA} emulsion

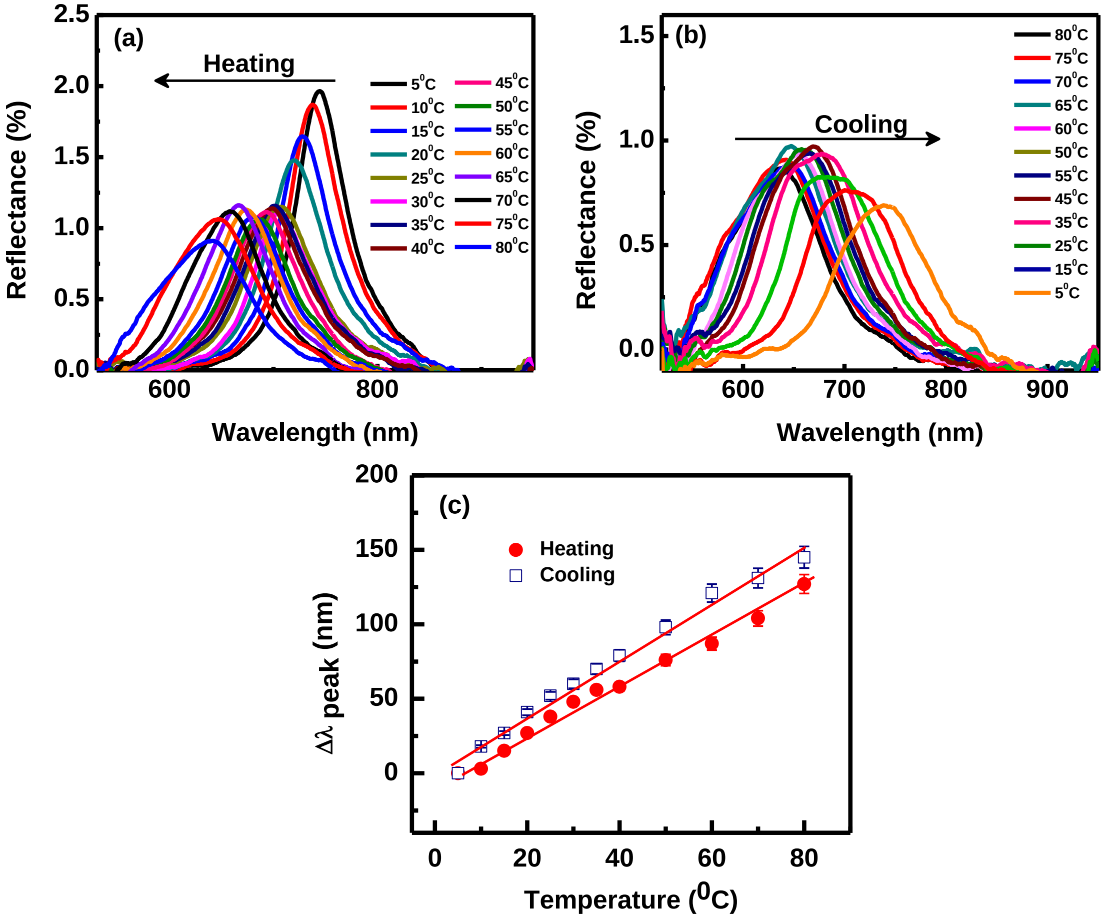

Figure 7.7: Bragg peak spectra for an E_{PVA} emulsion at different temperature range from 5 to 75 °C during (a) heating (b) cooling, respectively at a magnetic field of 130 G. (c) Change in Bragg peak wavelength ($\Delta\lambda_{peak}$) vs. temperature for the same at magnetic fields of 130 G. The solid lines represent the best linear fit on the experimental data. For a magnetic field strength of 130 G, the slopes were 1.68 and 1.9 ($R^2 = 0.99$ and 0.98) during heating and cooling cycles, respectively.

To monitor the response of the nanofluid with change in temperature, a constant magnetic field of 130 G was applied such that a grating with a fixed ‘d’ spacing is formed. **Figure 7.7 a & b** shows the Bragg spectra observed in E_{PVA} emulsion as a function of temperature during heating and cooling, respectively. As temperature increased, the Bragg peak is blue-shifted to lower wavelengths as shown by the arrow in the **Figure 7.7a**. When temperature decreased from 75 to 5 °C, a red-shift in the Bragg peak was observed as shown in the **Figure 7.7b.** The peak shift was found to be reversible with a little hysteresis. The change in the Bragg peak wavelength ($\Delta\lambda_{peak}$) for E_{PVA} emulsion during heating and cooling at a magnetic field strength of 130 G is shown in the **Figure 7.7c** respectively. The total variation in $\Delta\lambda_{peak}$ were 120 and 140 nm during heating and cooling, respectively, with slopes of 1.2 and 1.3, at a magnetic field of 130 G.

7.2.3.2 Dependence of Bragg peak position with temperature for PVA-Vac + borax emulsion

Figure 7.8a shows the variation in Bragg spectra for E_{PVA}+ Borax emulsion in the presence of borax of 10 mM as a function of temperature during heating. For a constant magnetic field strength of 130 G, the ‘d’ spacing was 300 nm (λ_{peak} = 800 nm) at 5 °C. As the temperature increased, the Bragg spectra were blue-shifted to a lower wavelength of 644 nm at 90 ºC. As observed in the previous case, here too the behavior was found to be reversible with negligible hysteresis. A total variation in Bragg spectra ($\Delta\lambda_{peak}$) of 156 nm is observed in the temperature range between 5 and 90 °C with slopes of 1.72 and 1.78 during heating and cooling, respectively as shown in the **Figure 7.8b**. It should be noted that the addition of 10 mM borax increased the temperature response of the nanofluid up to 90 °C, with an excellent linearity and negligible hysteresis. Since the nanofluid used was water based, the upper temperature detection limit was limited to the boiling point of the continuous phase. Efforts are being made in developing the non-aqueous based magnetic fluids for extending the temperature range of the sensor.

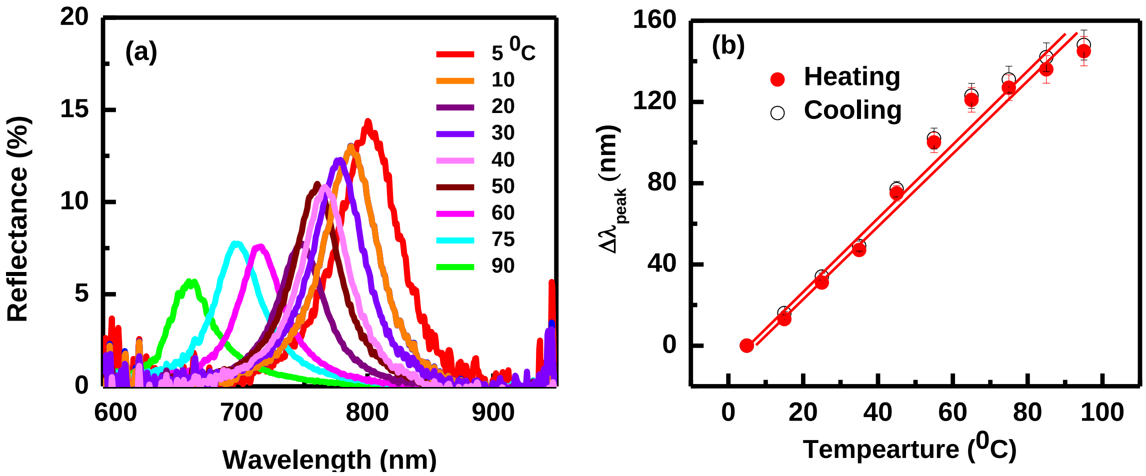

Figure 7.8: (a) Variation of Bragg spectra with temperature for E_{PVA}+ Borax emulsion. (b) Change in peak wavelength during heating and cooling, respectively. The solid line represents the best fit on the experimental data with a linear function (Y = mX + C). For a magnetic field strength of 130 G, the slopes were 1.72 and 1.78 ($R^2 = 0.97$) during heating and cooling, respectively.

7.2.3.3 Mechanism of Bragg peak shift with temperature

To understand the mechanism behind the observed large Bragg peak shift upon varying temperature, the intermolecular force between the emulsion droplet is studied. **Figure 7.9a** shows the force-distance profile for E_{PVA} emulsion at different temperatures. Overall, the force profiles were found to be repulsive and decay exponentially with distance. With an increasing temperature, the onset of interaction decreases and the range of repulsive forces were found to decrease. The interaction force between polymer or weak polyelectrolyte covered surfaces is given by $F(h) = K \exp\left(-\frac{h}{\lambda}\right)$, where the pre-exponential factor, K is the force constant, h is the inter droplet spacing and λ is the decay length.

From the force profiles, λ, $2L_0$ and K are obtained for different temperatures as shown in the **Figure 7.9 b - d**. The λ of E_{PVA} emulsion decreases from 12 to 2.4 nm as the temperature is increased from 5 to 75 °C (**Figure 7.9b)**. In the same temperature range, $2L_0$ is reduced from 55 to 22 nm as shown in the **Figure 7.9c** but K increased by almost three orders of magnitude as shown in the **Figure 7.9d**. For E_{PVA} emulsion, the experimental λ was found to be 12 nm, which was comparable to the radius of gyration (R_g) of free polymer in solution, measured by viscometry (i.e. 16 nm). The increase in K in the temperature range 5 and 90 ºC is attributed to the increased adsorption of polymer on emulsion droplets at elevated temperature.

For PVA solution, the hydrogen bond exist between the polar hydroxyl group (–OH) of PVA and water [177]. Briscoe et al. [181] showed from viscosity measurement that with an increasing temperature, the extend of hydrogen bond breaks down leading to a reduction in solvent quality. It was also shown that inter and intra hydrogen bond breaks down with increasing thermal energy. However, as the temperature decreases, the hydrogen bonds between water and –OH group reforms again. Even for a polymer with transition temperature around room temperature, e.g. PNIPAM above LCST [136], the complete dehydration is not possible. This should be the reason for the hysteresis observed during heating and cooling.

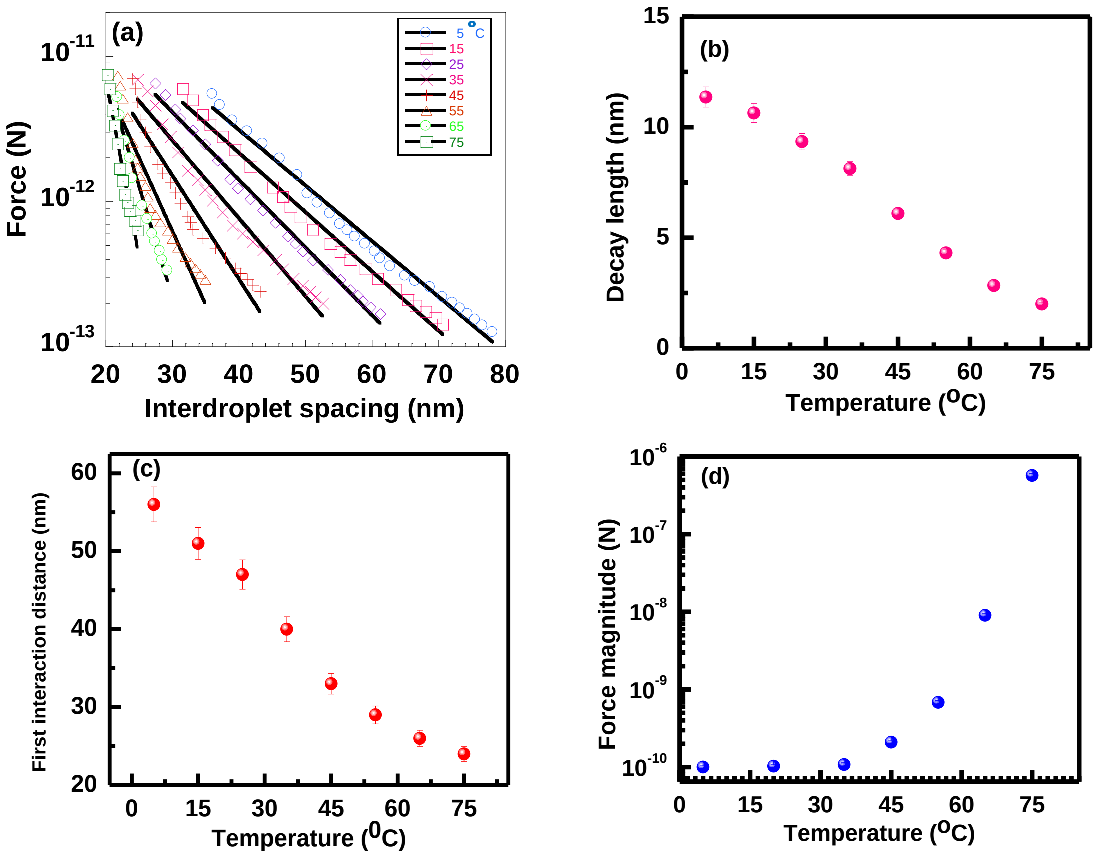

Figure 7.9: (a) Interaction forces between E_{PVA} emulsion droplets at different temperatures. The solid line represents the best fit on the experimental data (b) Decay length (c) first interaction distance and (d) Force magnitude as a function of temperature.

Cosgrove et al. [177] studied the characteristics of the adsorbed polymer on a polystyrene latex with an increase in temperature using small angle neutron scattering (SANS). They found that the thickness of the polymer layer contracts with increase in temperature. The same study also revealed that the adsorbed amount of polymer (PEO and PVA-vac) and the volume fraction of the polymer segments on the polystyrene latex increases with worsening of solvency condition i.e. with increase in temperature. The present result on increase in K with temperature in E_{PVA} emulsion is consistent with the above reports. Since the magnitude of K depends on the adsorbed amount of polymer at an interface, the increase in K and decrease in λ with an increase in temperature suggests that the extension of PVA-vac decreases but the amount of PVA-vac adsorption at liquid-liquid interface increases due to compaction of PVA over emulsion droplets, with increase in temperature. The peak broadening during cooling arises possibly because of increased amount of PVA-Vac at O/W interfaces at higher temperatures. Therefore, the observed changes in the interdroplet spacing and force parameters are in excellent agreement with the reported results on solid-liquid interfaces [177] .

7.2.3.4 Mechanism of interaction of PVA-Vac with borax at different temperature

Figure 7.10 a & b shows the intermolecular force-distance curves and the corresponding force parameter (λ and $2L_0$) for E_{PVA} emulsion in the presence of borax of various concentration. With increasing borax concentration, the onset of interaction increases and the force profile shifts to a higher interdroplet distance. **Figure 7.10 c & d** shows the intermolecular force-distance curves and the corresponding force parameters for E_{PVA}+ Borax emulsion at different temperatures. With increasing temperature, the onset of interaction decreases and the force profile shifts to a lower droplet distance. The interaction forces in the above two cases follows exponential decay. In all these cases the force between the droplets are repulsive in nature and decays exponentially.

The λ and $2L_0$ of E_{PVA} emulsion increases from 11 to 14 nm and 80 to 120 nm, respectively as the borax concentration is increased from 0.3 to 10 mM. In the presence of high concentration of borax (10 mM), with increase in temperature from 5 to 95 °C, λ and $2L_0$ decreases from 14 to 10 nm and 95 to 55 nm, respectively. Therefore, the onset of interaction and force parameters increases with increase in borax concentration at fixed temperature whereas it decreases with increase in temperature for a fixed PVA + borax concentration.

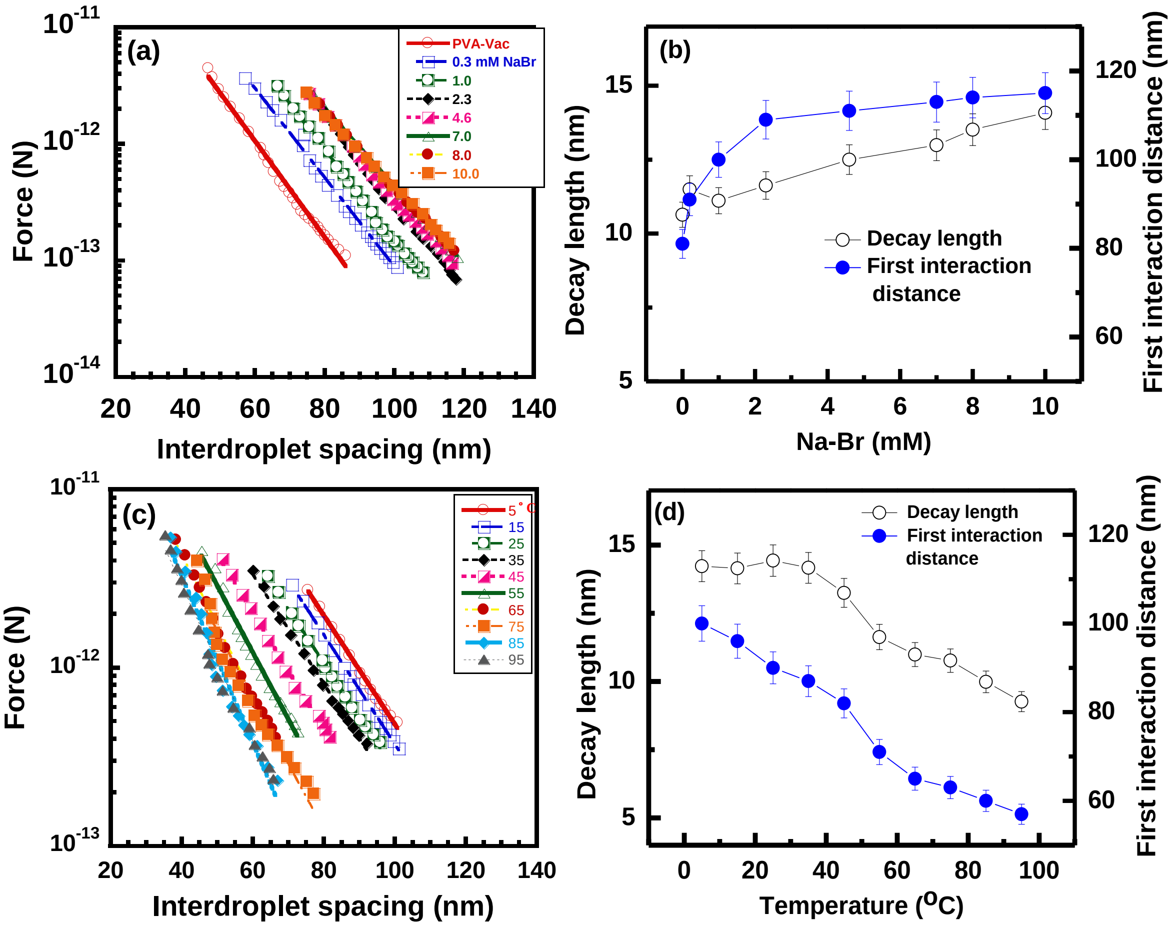

Figure 7.10: (a) Force-distance profile and (b) variation of force parameters (decay length and first interaction distance) as a function of borax concentration in E_{PVA} emulsion. (c) Force-distance profile and (d) variation of force parameters as a function of temperature for E_{PVA} + borax emulsion at various temperature. The solid line in the force profile represents the best fit of the experimental data. The solid lines on other graphs are guide to the eye.

The interaction between PVA and borax is well described in the literature [361, 362]. In general, borax, also known as sodium borate, is a good buffer, dissociate into boric and monoborate ion with sodium (Na^+) as a counter-ion [361]. For a very long time, it has been known that monoborate ions make complex with organic polyols. PVA and borax makes complex either in 1:1 or 2:1 ratio and such complexation would be either monodiol or cross linking (also known as di-diol) depending upon the concentration of borax. When the stoichiometric ratio of polymer/borax was 2:1, cross liking of polymers results in gelling, which is often called di-diol complexation whereas for 1:1 ratio, the dissociated borate ions complex with the polymer chain, thus makes a neutral polymer (PVA) into polyelectrolyte like structure [362]. Sinton et al. [361] showed from ^{11}B NMR spectra that 2:1 intra-chain complexes dominate at low concentration of borax and PVA but with an increase in borax concentration, it switches to 1:1 ratio where the loops in the polymer chain breaks down and the neutral polymer is transformed into a highly charged structure. Such interaction between the charged complexes on the polymer chain is expressed in terms of coulomb energy as $U/_{kT} = \frac{Q}{b_e}\exp(-\kappa b_e)$, where κ is the inverse Debye length and b_e is the spacial distance between the two charges [114].Therefore, the addition of borate ions into PVA molecules induces electrostatic charges on the backbone of PVA chains which expands the polymer. Such complexation is evident from the changes in force parameters and zeta potential results.

The force measurement shows that λ of E_{PVA} emulsion increase with increasing borax concentration. The zeta potential was found to be ~ 0 mV in the absence of borax but in the presence of 10 mM borax, it increased to -17 mV. The electrostatic repulsion and intra-molecular crosslinks dictate the chain dimension and structure of complexes. The conformation of the polymer complexes depends on the balance in the excluded volume of polymers, the electrostatic repulsion among the charged complexes bound on polymeric chains and the shielding effect of free Na^+ ions on the charged complexes. With addition of borax, the adsorbed neutral polymer becomes a weakly charged polyelectrolyte because of the complexation with borax. The electrostatic contribution becomes stronger with increase in borax concentration, thus the adsorbed polymer expands with increasing borax concentration and hence increase in inter-droplet separation.

It was reported that for 2:1 ratio of PVA and borax, a visco-elastic network is formed. Kazhugi koga et al. [363] showed that the intrinsic viscosity of PVA and borax complex decreases with increase in temperature due to breakdown of the same di-diol complexes. The dynamic light scattering and dynamic viscoelasticity studies showed that with increase in temperature, the relaxation time (τ_m) of the network structure of PVA and borax decreases, indicating a collapse of network structure and an increase in dynamic correlation length (ξ_H) of the same, indicating the shortening of network structure as well as lifetime of the complexes [363]. Earlier work reported a decrease in intrinsic viscosity of PVA-borax complex with increasing temperature till 80 °C along with a transformation of the opaque visco-elastic to a transparent solution in the same condition [364].

Other reasons for the decrease of λ in PVA-borax complex with increase in temperature could be due to the increased dissociation of borate ion, which effectively shields the existing polyelectrolyte complex and decrease in PVA chain size in the PVA-borax complex [363]. The intrinsic viscosity of PVA was not altered in the presence of borax. Therefore, the observed change in PVA-borax complex with rise in temperature can also be attributed to the breakdown of hydrogen bond between water and PVA. The above reported results are consistent with the observed behavior in the intermolecular force measurements.

7.2.4 pH sensing using nanoemulsion

7.2.4.1 Dependence of Bragg peak position with pH

Figure 7.11 a & b shows the Bragg spectra and the corresponding change in maximum peak wavelength for E_{PAA250} emulsions as a function of pH at room temperature and **Figure 7.11 c & d** shows the Bragg spectra and the corresponding change in maximum peak wavelength for E_{PAA450} emulsion as a function of pH. To monitor the response of the nanofluid to pH, a constant magnetic field of 400 G was applied such that Bragg peak is formed in the visible wavelength at a low pH. The Bragg peak is formed at 650 nm at pH 3.0 but is red-shifted to a higher wavelength with increase in pH as shown by the arrow. At pH 11.5, the Bragg spectra are shifted to the red end of the spectrum. The behavior was found to be reversible with a little hysteresis where decrease in pH brings back the Bragg peak to its original state**.** A reversible response to pH was seen below the emulsion pH of 12. When emulsion pH was $\geq$ 12, counter-ion condensation takes place, which results in the irreversible aggregation of emulsion droplets. The change in peak position $\Delta\lambda_{peak}$ of the Bragg spectra for E_{PAA250} emulsion (at a magnetic field of 400 G) with increase in pH is shown in the **Figure 7.11b**. At pH 3.0, the λ_{peak} was formed at 650 nm, corresponds to a 'd' spacing of 248 nm, which is red-shifted to 950 nm, when pH reaches ~11.0, and the corresponding grating spacing was 357 nm.The Bragg spectra and the corresponding $\Delta\lambda_{peak}$ for E_{PAA450} emulsions is shown in the **Figure 7.11 c & d.** As observed with E_{PAA250} emulsion, a similar behavior was found in this case too. The response to pH was found to be reversible when pH $\leq$ 12.

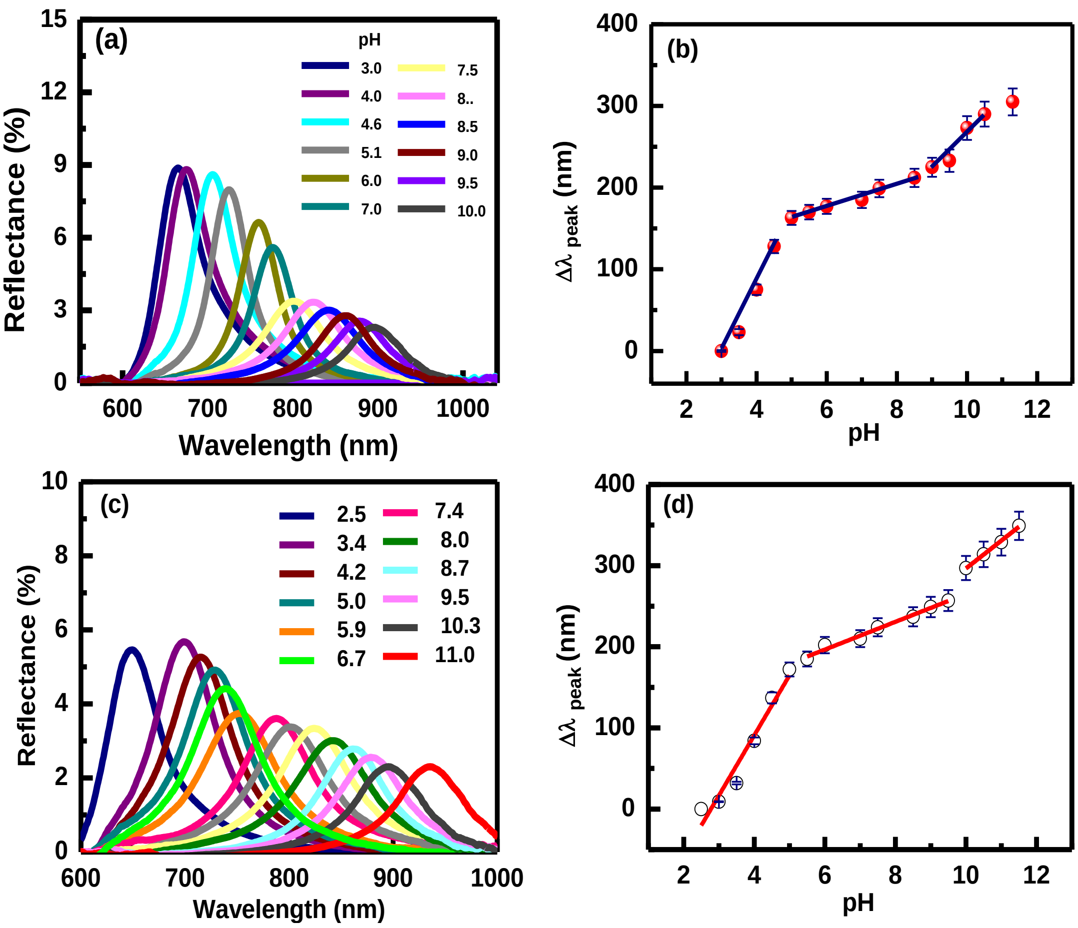

Figure 7.11: Bragg peak and the corresponding change in Bragg peak wavelength for (a & b) E_{PAA250} and (c & d) E_{PAA450}, respectively as a function of pH. For a magnetic field strength of 400 G, three different linear regions are observed in the $\Delta\lambda_{peak}$ curve in the pH range 2.5-6, 6-9 and 9-11.5. The slopes of above three regions were 74, 17 and 38 (with $R^2 = 0.94, 0.98$ and 0.82) with increase in pH for E_{PAA250} emulsion. For E_{PAA450} emulsion, the slopes were 70, 13 and 47 ($R^2 = 0.97, 0.98$ and 0.99) with increase in pH , respectively.

For a magnetic field strength of 400 G, Bragg peak was formed at 660 nm, corresponding to diffraction grating spacing of 240 nm at a pH ~ 3.0. With increase in pH, the Bragg spectra shifted to a higher wavelength as shown by the arrow. At a pH of 11, the Bragg spectra move towards the red end of the spectrum and the behavior was found to be reversible with a little hysteresis. $\Delta\lambda_{peak}$ values were 300 and 350 nm for E_{PAA250} and E_{PAA450} emulsion, respectively when pH is increased from 3.0 to 11.5. $\Delta\lambda_{peak}$ with pH showed three different slopes of 74, 17 and 38 in the pH range of 2.5 to 6, 6 to 9 and 9 to 11.3, respectively, with a good linearity for each regimes (**Figure 7.11b)** for E_{PAA250} emulsion. With increasing the molecular weight of the adsorbed PAA also display almost the same behavior where slopes were of 70, 13 and 47 at different pH ranges **(Figure 7.11d)**.

Based on the experimental results from the Bragg peak, intermolecular force and zeta potential measurement, the change in conformation of the adsorbed PVA-vac + borax with increasing temperature and PAA with increasing pH is represented schematically in **Figure 7.12 (a-c) and (d-f**), respectively**.** At low temperature (5 ºC) but at a fixed pH and magnetic field, the swelling of PVA-vac + borax complex adsorbed at oil-water interface causes the oil droplets to interact at larger spacing where the λ_{peak} of the Bragg spectrum is formed at a higher wavelength (750 nm) as shown in the **Figure 7.12a**. As the temperature increases to 40 ºC, the adsorbed polymer-borax complexes collapses due to dehydration and breakdown of hydrogen bond between aqueous phase and PVA, leading to a decrease in the interdroplet spacing and hence the Bragg spectra as shown in the **Figure 7.12b**. With further increase in temperature to 90 °C, enhanced dehydration results in the complete collapse of the adsorbed PVA-vac + borax so that λ_{peak} of the Bragg spectra is blue-shifted as shown in the **Figure 7.12c**.

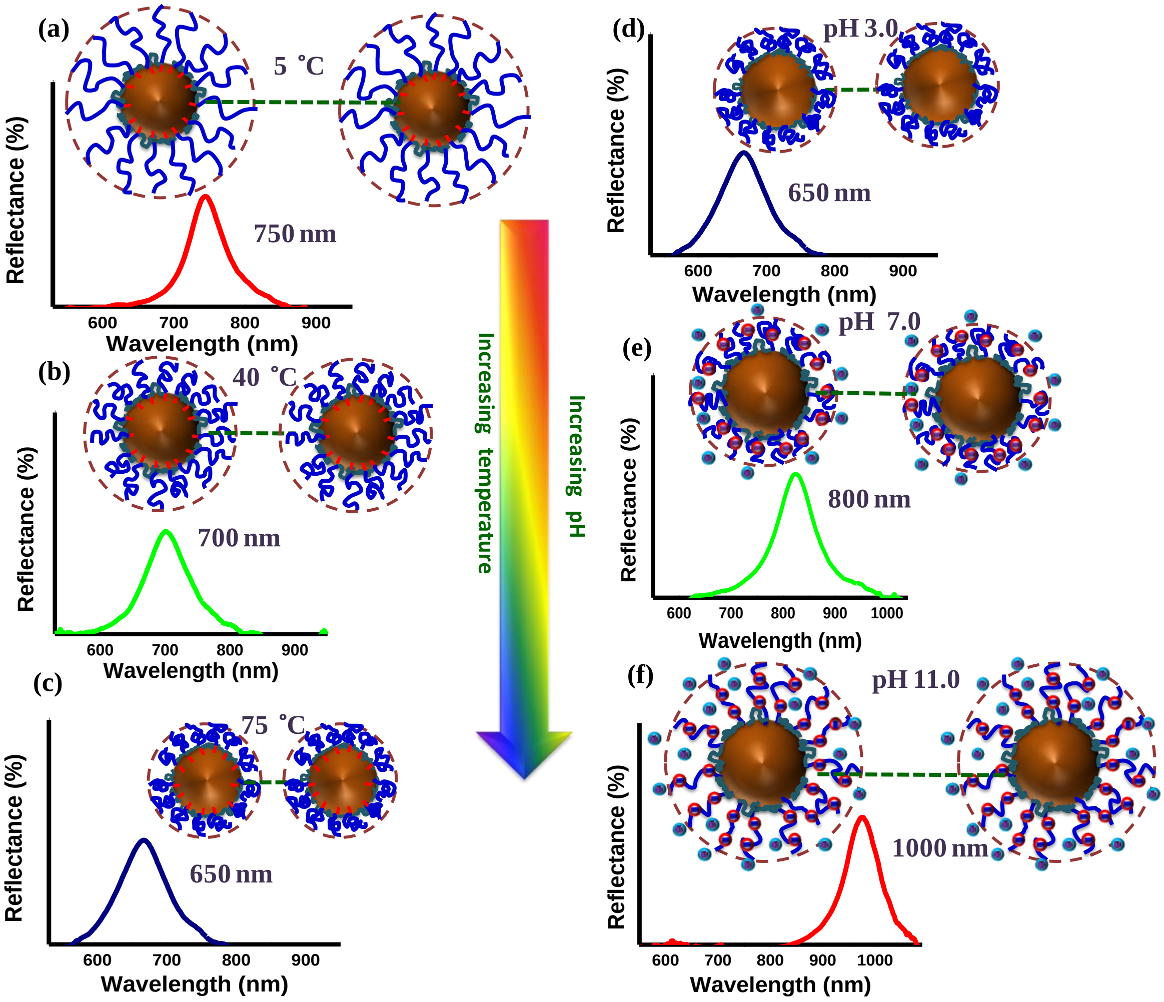

Figure 7.12: Schematic representation of the conformational change of the adsorbed macromolecule at oil-water interface and the change in Bragg peak position with change in temperature and pH. (Top to bottom) Lower to higher temperature or pH. (a-c) Change in conformation of the adsorbed neutral macromolecule complexes (PVA-vac + Borax), Bragg peak and interdroplet separation of emulsion droplets at a constant magnetic field but at different temperature of 5, 40 and 90 ˚C. (d-f) Change in conformation of adsorbed anionic polyelectrolyte (PAA), Bragg peak and interdroplet separation of emulsion droplets at a constant magnetic field but at pH 3, 7 and 11.0.

For E_{PAA450} emulsion, at low pH (~3.0) and at room temperature, the anionic polyelectrolyte PAA adsorbed at oil-water interface is neutral in nature and exhibits a compact globule structure with a collapsed conformation as shown in the **Figure 7.12d**. Therefore, the emulsion droplets begin to interact at a lower interdroplet spacing, which is reflected in the formation of λ_{peak} at 650 nm. **Figure 7.12e** shows that with increasing pH to 7.0, the adsorbed polyelectrolyte swells due to the ionization of surface groups where the λ_{peak} is shifted to 800 nm. Finally when the pH is increased to 11.0, almost complete dissociation of the adsorbed PAA occurs that leads to an enhanced swelling with huge increase in the interdroplet spacing (λ_{peak} is shifted to 1000 nm) as shown in the **Figure 7.12f**.

7.2.4.2 Influence of temperature on pH response of E_{PAA450} emulsion

For practical application of this new platform, pH response should be insensitive to the change in other environmental conditions such as temperature, ionic species etc. To test the non-interfering behavior of the new platform, the temperature response of E_{PAA450} emulsion is studied at pH ~ 7.0. The Bragg spectra variation for E_{PAA450} emulsion in the temperature range from 5 to 85 °C is also shown in the **Figure 7.13a**. To examine the effect of temperature towards pH sensing, the total variation in $\Delta\lambda_{peak}$ in the temperature range of 5 to 85 °C (at constant pH) and in the pH range of 3 to 11.5 is measured and plotted in the **Figure 7.13b**. It is clear that $\Delta\lambda_{peak}$ variations in the wide temperature range of 5 to 85 °C (**Figure 7.13 b)** was ~10% as compared to the $\Delta\lambda_{peak}$ variation with change in pH at room temperature (35 nm against 350 nm with pH). This shows that the pH sensing using E_{PAA450} emulsion is almost independent of the temperature. Similarly with neutral macromolecules, temperatures sensing is not affected with changes in pH of the medium.

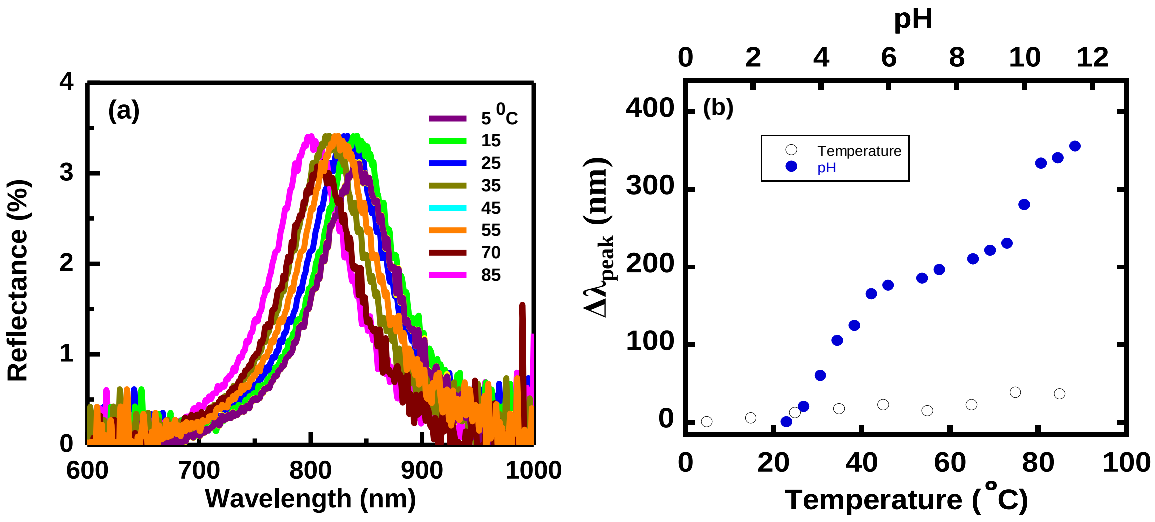

Figure 7.13: (a & b) Temperature response on Bragg spectra for E_{PAA450} emulsion at pH ~ 7.0 and the corresponding $\Delta\lambda_{peak}$ for the same. The total variation in $\Delta\lambda_{peak}$ in the temperature range between 5 and 85 ºC was 35 nm as compared to the $\Delta\lambda_{peak}$ variation of 350 nm for the pH range 3 - 11.5.

7.2.4.3 Response time, reversibility and reproducibility

Figure 7.14 a & b shows the Bragg peak change at different time interval for E_{PVA} emulsion at constant temperature (5 °C) and E_{PAA450} at constant pH (~ 7.0), respectively. The changes in Bragg peak position at constant temperature and pH at different time interval (up to 20 minutes) in each case shows negligible change in the Bragg peak position. The subtle changes in the Bragg peak position in the above time interval was within the peak position detection error. Therefore, temperature or pH measurement through Bragg peak has negligible time dependence.

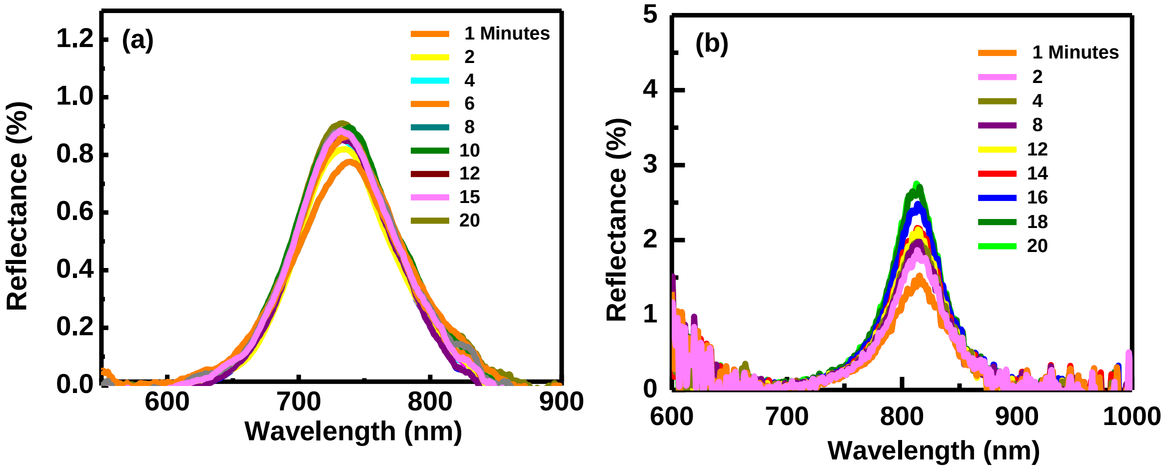

Figure 7.14: Time dependence of Bragg peak position (a) at constant temperature (5 °C) for E_{PVA} emulsion (b) at constant pH (~ 6.0) for E_{PAA450} emulsion.

The reversibility in sensing of the emulsion was assessed by measuring the change in Bragg peak position on increasing and decreasing the temperature and pH. In the case of E_{PVA} emulsion, the nanofluid exhibited a perfect reversibility with a minor hysteresis during heating and cooling cycles. In case of E_{PAA450} emulsion the reversibility in pH monitoring was possible up to pH 12. The reproducibility of the emulsion towards temperature and pH was checked by repeating the experiment for three times, which gave a similar result with insignificant deviation. **Table 7.1** shows the sensing capability of magnetic nanoemulsion is found to be better for monitoring both temperature and pH over a broad range in the fastest time as compared to other approaches. Moreover, the present technique has the advantage, owing to optical mode of detection. With suitable functional moieties and modification of emulsion properties, it should be possible to visually manifest the temperature and pH changes. Further work is being done to achieve visual manifestation of temperature and pH.

Table 7.1: Established sensing techniques used for monitoring pH, temperature and both, materials used, range of detection, response time and reference. Among various sensing techniques, magnetic nanoemulsion based sensor has a broader range and faster response time.

Materials	Measured parameter	pH Range	Temp. range (˚C)	Response time (sec.)	Ref.
pH sensor					
pH dependent fluorophore	Fluorescent Intensity	1 - 9.5	---	< 90	344
Eu $^{3+}$ functionalized UiO-67-bpydc	Fluorescent Intensity	1.06-10.9	---	---	340
Polyaniline-coated tilted fiber Bragg gratings	Transmitted amplitude spectrum	2-12	---	8 – 67	348
Fluorophore linked phospholipid	Fluorescent Intensity	3 -8 and 7 – 11	---	---	350
Congo red immobilized triacetyl cellulose	Absorption spectrum	0 – 4.5	---	150	345
Prussian blue deposited multimode optical fiber	Average time constant of optrode	2-8	---	---	365
Temperature sensor					
Zinc oxide film coated Hollow core fiber	Transmittance spectra	---	20 - 460	---	352
Laminated pouch	Luminescennce		2 – 45	---	353

	lifetime				
Sagnac interferometer with photonic crystal fiber	Transmittance spectra	---	23-35	---	[366]
CdS:SiO_2 nanocomposite	Photolumininescence intensity	---	293-883	---	[367]
Graphene nanowall/polydimethyl siloxane	Resistance change	---	20-120	---	[368]
Er^{3+} doped $SnSrO_3$	Fluorescence intensity	---	20-100	---	[369]
pH and temperature sensors					
Reduced graphene oxide (rGO)	Open circuit potential between potentiostat and galvastat	4-10	25 - 43		[355]
Rhodamine and fluorescein isothiocyanate	Fluorescent intensity	5 – 8	32 – 38	---	[356]
pH and temperature terpolymer labeled with aminofluorescein (l_{42} – D_{50} – S_8 –FL)	Transmittance of light	6.4-8.4	30 - 46	---	[370]
Polymer fluorescent sensor	Fluorescence intensity	4 – 10	25 - 37	---	[354]
NaYF4: Yb^{3+}, Er^{3+} nanocrystals	Luminescence	3 – 12	10 - 80	---	[371]
NBD-P(OEGMA-co-DEGMA)-RhB_2,	Fluorescence intensity	2 – 10	20 – 50	---	[372]
Magnetic nanoemulsion	Reflected Bragg spectra	3-11.5	5 – 90	≤ 1	Present work

7.3 Conclusion

A simple, non-enzymatic, nanofluid based optical sensor for the detection of very low to high urea concentration in the range of 10^{-3} to 10^{2} g/L is developed. The nanofluid used here is an oil-in-water magnetic nanoemulsion containing superparamagnetic iron oxide nanoparticles of size ~10 nm. Under a constant magnetic field (~90 Gauss), the magnetic emulsion forms a one dimensional Bragg diffraction grating with a fixed interparticle spacing. In the presence of urea, the probe showed a large wavelength shift in the visible wavelength range of 880-600 nm, due to complexation of urea with the functional moieties that dramatically changes the electrostatic repulsion between emulsion droplets or conformation of adsorbed polymer. The functional moieties, E_{SDS}, E_{PAA450} and E_{PLURO} emulsion are found to be suitable for the measurement of urea in the concentrations range 0.003-0.6, 0.18-33.3 and 2.4-334 g/L, respectively. E_{PAA450} emulsion is found to be suitable for the selective detection of urea in the presence of biologically important cations such as Na^+ and Ca^{2+}. The fast response time of the sensor (less than a second) and the wide urea detection capability are the unique features of the new sensor.

Also, a magnetic nanofluid based optical sensor capable of monitoring both temperature and pH is also developed. The interdroplet distance changes with temperature or pH stimuli are manifested spectroscopically. E_{PVA} emulsion was found to have a linear temperature sensing range of 5- 75 °C whereas E_{PVA} + borax emulsion showed an improved temperature measuring capability in the range of 5 - 90 °C. By using a functional group of PAA, pH monitoring is achieved in the range of 3 - 11.5. The fast response time (~ 1 second), multi stimuli options, minimum cross interference with other environmental condition, simple to use, and inexpensive nature of emulsion makes this new platform attractive for monitoring of pH and temperature. Further, this new platform also has a potential to visually monitoring the environmental changes by observing the color changes by suitable functionalization.

CHAPTER 8

Conclusion and recommendation for future work

8.1 Conclusion

The conformational change of neutral and charged macromolecules at the oil-water interfaces is systematically studied under various physio-chemical conditions using in-house developed intermolecular force measurement technique and the key results are given below:

Intermolecular interaction due to a thermoresponsive polymer, Poly (N-isopropylacrylamide) (PNIPAM) adsorbed at the oil-water interface under different temperatures and anionic surfactant concentration showed a repulsive steric interaction and temperature tunable interdroplet separation below the lower critical solution temperature (LCST) due to reversible swelling and collapse of adsorbed PNIPAM at the O/W interface where decay length (λ) decreases from 12.6 to 7 nm with increase in temperature. Above the LCST (> 35 ºC), a strong attractive forces is found to operate between adsorbed PNIPAM layers, causing a bridging of PNIPAM covered droplets. In the presence of a small amount of 2 mM sodium do-decyl sulphate (SDS), LCST is increased by 3 ºC and therefore λ varied between 16.6 and 12.7 nm as the temperature increased from 5 to 38 ºC due to strong association of PNIPAM and SDS.

New insights are obtained in conformational change of adsorbed weak polyelectrolyte - (polyacrylic acid) - PAA at the oil-water interfaces under different environmental conditions such as ions of different valences, pH and molecular weight. In the absence of salt, adsorbed PAA undergoes a reversible conformational change from compact globule at low pH (3.0) where λ was found to be 6.6 nm to a highly extended conformation at high pH (11.8) where λ reached 28 nm due to electrostatic repulsion of backbone functional group. With addition of salt, the adsorbed PAA undergoes an extended conformation in the osmotic brush regime where λ scales with concentration of salt as ~ φ_s^x with the exponent x was found to be 0.068, 0.049 and 0.072 for Na^+, Ca^{2+} and Fe^{3+}, respectively but collapses in the salted brush regime where λ scales as ~ φ_s^{-y} and the exponent y were found to be 0.3, 0.26 and 0.17 for Na^+, Ca^{2+} and Fe^{3+}, respectively. The rate of swelling and shrinking in the presence of salt of different valence was found to be in good agreement with the mean field and self-consistent field theoretical predictions. The intermolecular force measurement for PAA of different molecular weight showed that globule to extended transition is significant only for adsorbed PAA of molecular weight > 15 Kg/mol.

The behavior of a strong polyelectrolyte, poly(diallyldimethylammonium chloride) - PDDA adsorbed at the oil-water interfaces studied using magnetic chaining technique, showed that the adsorbed PDDA adopts an extended conformation at the oil-water interface at zero salt concentration where λ was found to be ~ 17 nm that remains unchanged in the pH range from 2 to 10 but collapses completely to 4 nm at a pH of 11.5 due to interchain hydrogen bonding between adsorbed PDDA chains. At low salt concentration, the adsorbed PDDA possesses an extended conformation where λ remains the same but collapse of the PDDA was noticed at a very high salt content with a rate of decay of $\varphi_s^{-0.4}$, $\varphi_s^{-0.19}$ and $\varphi_s^{-0.15}$, for Na^+, Ca^{2+}, and Fe^{3+} respectively due to an enhanced neutralization of the surface group. Interestingly, the rate of swelling and collapse of PDDA and PAA was in good agreement with the theoretical predictions for end grafted strong PE. The collapse of PDDA and PAA was in agreement with the electrophoretic results where an increasing the salt concentration is found to decrease the zeta potential due to an enhanced neutralization of surface groups. Also, the rate of collapse of adsorbed PDDA and PAA was found to be the same as that of the rate of charge neutralization, observed from the electrophoretic measurement.

The role of lower molecular weight protein (BSA) into E_{PDDA} and E_{PAA450} emulsion is studied at different solution pH conditions showed that the addition of BSA to E_{PDDA} emulsion results in the displacement of PDDA from the oil-water interface by BSA under different pH conditions. The λ and ζ of E_{PDDA} emulsion was found to be 19 nm and + 56 mV, respectively that changes to 6 nm and + 5 mV at pH 5.2 and 6 nm and -10 mV at pH 7.0 in the presence of BSA. A similar competitive displacement of PAA by BSA was observed in E_{PAA450} emulsion when the solution pH condition is altered where λ and ζ of E_{PAA450} emulsion at pH 3.5 was 15 nm and – 10 mV in the absence of BSA, respectively but changes to 5 nm and + 38 mV when BSA was present at the interfaces. These results confirmed the preferential adsorption of small molecules through competitive displacement of larger molecules at liquid-liquid interfaces, irrespective of the nature of adsorbed PE's (strong or weak, anionic or cationic, high or low charge density).

The sensing ability of magnetic nanoemulsion functionalized with different functional moieties for detecting urea, pH and temperature of the fluids is studied. The study showed a selective detection of urea of wide concentration range of 10^{-3} to 10^{2} g/L is possible using E_{SDS}, E_{PAA450} and E_{PLURO} emulsion. E_{SDS} emulsion shows a change in Bragg peak wavelength ($\Delta\lambda_{peak}$) of 142 nm that detects urea in the concentration range of 0.003-0.6 g/L whereas E_{PAA450} and E_{PLURO} emulsion showed the $\Delta\lambda_{peak}$ of 224 and 178 nm that detects urea level of 0.18-33.3 g/L and 2.4-334 g/L, respectively. E_{PAA450} emulsion is found to be suitable for the selective detection of urea in the presence of biologically important cations of 130 mM NaCl and 2 mM $CaCl_2$. Similarly, temperature and pH sensing ability of E_{PVA} and E_{PAA450} emulsion is studied. The study showed that E_{PVA} emulsion has linear temperature sensing capability in the range of 5 - 75 °C, whereas E_{PVA} + Borax emulsion has an improved temperature measuring capability in the range of 5 - 90 °C. Finally, the pH monitoring in the range of 3 - 11.5 is achieved, using E_{PAA450} and E_{PAA250} emulsion.

8.2 Recommendation for future work:

- To study the synergistic conformational changes of neutral and charged macromolecules in the presence of surfactant.
- To study the role of nanoparticles at emulsion interface under different environmental conditions.
- To understand the nature of colloidal interaction in the presence of linear and branched polymers.
- To understand the behaviour of proteins at emulsion interface under different environmental conditions.
- Testing of urea detection ability in serum samples.

References:

1. Doi, M., *Soft matter physics*. Oxford univeristy press: New York, 2013.

2. Hiemenz, P. C.; Rajagopalan, R., *Principles of Colloid and Surface Chemistry*. Marcel Dekker: New York, 1997.

3. Maji, S.; Cesur, B.; Zhang, Z.; Geest, B. G. D.; Richard; Hoogenboom, Poly(N-isopropylacrylamide) coated gold nanoparticles as colourimetric temperature and salt sensors. *Polym. Chem.* **2016,** *7*, 1705-1710.

4. Jorgensen, L.; Weert, M. V. D.; Vermehren, C.; Bjerregaard, S.; Frokjaer, S., Probing structural changes of proteins incorporated into water-in-oil emulsions. *J.Pharm.Sci.* **2004,** *93*, 1847-1859.

5. Husband, F. A.; Garrood, M. J.; Mackie, A. R.; Burnett, G. R.; Wilde, P. J., Adsorbed protein secondary and tertiary structures by circular dichroism and infrared spectroscopy with refractive index matched emulsions. *J. Agric. Food Chem.* **2001,** *49*, 859–866.

6. Leal-Calderon, F.; Schmitt, V.; Bibette, J., *Emulsion science : Basic principles*. Second ed.; Springer: New Yok, US, 2007; p 236.

7. Jachimska, B.; Pajor, A., Physico-chemical characterization of bovine serum albumin in solution and as deposited on surfaces. *Bioelectrochemistry* **2012,** *87* 138–146.

8. Song, N.; Wang, A.-j.; Li, J.-m.; Zhu, Z.; Shi, H.; Maa, X.-l.; Sun, D., Study on influencing factors of pickering emulsions stabilized by hydroxyapatite nanoparticles with nonionic surfactants. *Soft Matter* **2018,** *14*, 3889-3901.

9. Ge, L.; Mohwald, H.; Li, J., Polymer-stabilized phospholipid vesicles formed on polyelectrolyte multilayer capsules. *Biochem. Biophys. Res. Commun.* **2003,** *303*, 653–659.

10. Fernandez, P.; André, V.; Rieger, J.; Kühnle, A., Nano-emulsion formation by emulsion phase inversion. *Colloids Surf.A:Physiochem. Eng. Aspects* **2004,** *251*, 53-58.

11. Kavok, N.; Grygorova, G.; Klochkov, V.; Yefimova, S., The role of serum proteins in the stabilization of colloidal LnVO4:Eu3+ (Ln = La, Gd, Y) and CeO2 nanoparticles. *Colloids Surf.A:Physiochem. Eng. Aspects* **2017,** *529*, 594–599.

12. María I. Moran-Valero; Víctor M. Pizones Ruiz-Henestrosa; Pilosof, A. M. R., Synergistic performance of lecithin and glycerol monostearate in oil/water emulsions. *Colloids Surf., B* **2017,** *151*, 68–75.

13. Ge, L.; Mohwald, H.; Li, J., Biointerfacing polyelectrolyte microcapsules. *ChemPhysChem* **2003,** *4*, 1351 - 1355.

14. Patino, J. M. R.; Pilosof, A. M. R., Protein–polysaccharide interactions at fluid interfaces. *Food Hydrocolloids* **2011,** *25*, 1925-1937.

15. Friberg, S.; Jansson, P. O.; Cederberg, E., Surfactant association structure and emulsion stability. *J. Colloid Interface Sci.* **1976,** *55*, 614-623.

16. Leal-Calderon, F.; Stora, T.; Mondain Monval, O.; Bibette, J., Direct measurement of colloidal forces. *Phys. Rev. Lett.* **1994,** *72*, 2959.

17. Mondain-Monval, O.; Espert, A.; Omarjee, P.; Bibette, J.; Leal-Calderon, F.; Philip, J.; Joanny, J. F., Polymer-induced repulsive forces: Exponential scaling. *Phys. Rev. Lett.* **1998,** *80*, 1778-1781.

18. Philip, J.; Mondain-Monval, O.; Leal-Calderon, F.; Bibette, J., Colloidal force measurements in the presence of a polyelectrolyte. *J. Phys. D: Appl. Phys.* **1997,** *30* 2798.

19. Schroder, A.; Berton-Carabin, C.; Venema, P.; Cornacchia, L., Interfacial properties of whey protein and whey protein hydrolysates and their influence on o/w emulsion stability. *Food Hydrocolloids* **2017,** *73* 129-140.

20. Verwey, E. J. W.; Overbeek, J. T. G., *Theory of stability of lyophobic colloids. The interaction of sol particles having an electric double layer*. Elsevier: Amsterdam, 1948.
21. Israelachvili, J. N., *Intermolecular and surface forces*. Academic Press: San Diego, 1985.
22. McPherson, T.; Kidane, A.; Szleifer, I.; Park, K., Prevention of protein adsorption by tethered poly(ethylene oxide) layers: experiments and single-chain mean-field analysis. *Langmuir* **1998,** *14*, 176-186.
23. Chapman, D. L., LI. A contribution to the theory of electrocapillarity. *The london, edinburgh, and dublin philosophical magazine and journal of science* **1913,** *25*, 475-481.
24. Debye, P.; Hückel, E., De la theorie des electrolytes. I. abaissement du point de congelation et phenomenes associes. *Phys. Z.* **1923,** *24*, 185-206.
25. Stern, H. O., Zur theorie der elektrolytischen doppelschicht. *Z. Elektrochem. Angew. Phys. Chem.* **1924,** *30*, 508-516.
26. Hunter, R. J., *Foundations of colloidal science*. Oxford Universiy Press: Great Britain, 2001; p 640.
27. Stepien, G.; Moros, M.; Pérez-Hernández, M.; Monge, M.; Gutiérrez, L.; Fratila, R. M.; Heras, M. d. l.; Guillén, S. M.; Lanzarote, J. J. P.; Solans, C.; Pardo, J.; Fuente, J. M. d. l., Effect of surface chemistry and associated protein corona on the long-term biodegradation of iron oxide nanoparticles in vivo. *ACS Appl. Mater. Interfaces* **2018,** *10* 4548–4560.
28. Pan, S.; Zhang, H.; Liu, W.; Wang, Y.; Pang, W.; Duan, X., Biofouling removal and protein detection using a hypersonic resonator. *ACS Sens.* **2017,** *2*, 1175–1183.
29. Milner, S. T.; Witten, T. A.; Cates, M. E., Theory of the grafted polymer brush. *Macromolecules* **1988,** *21*, 2610-2619.
30. Gennes, P. G. d., Conformations of polymers attached to an interface. *macromolecule* **1980,** *13*, 1069-1075.
31. Gennes, P. G. D., Polymers at an interface. 2. Interaction between two plates carrying adsorbed polymer layers. *Macromolecules* **1982**, 492–500.
32. Gong, P.; Wu, T.; Genzer, J.; Szleifer, I., Behavior of surface-anchored poly(acrylic acid) brushes with grafting density gradients on solid substrates: 2. Theory. *Macromolecules* **2007,** *40*, 8765-8773.
33. Guo, X.; Zhao, K., Insight into the electrical properties and chain conformation of spherical polyelectrolyte brushes by dielectric spectroscopy. *J. Phys.: Condens. Matter* **2017** *29*, 055102
34. Morishima, Y.; Ohgi, H.; Kamachi, M., Effect of counterion condensation on the fluorescence quenching of phenanthrene-labeled sodium salt of poly(acry1ic acid-co-acrylamide) in salt-free solution *Macromolecules* **1993,** *26*, 4293-4297
35. Tom, A. M.; Vemparala, S.; Rajesh, R.; Brilliantov, N. V., Mechanism of chain collapse of strongly charged polyelectrolytes. *Phys.Rev.Lett.* **2016,** *117*, 147801
36. Jayasree, K.; Ranjith, P.; Rao, M.; Kumar, P. B. S., Equilibrium properties of a grafted polyelectrolyte with explicit counterions. *J.Chem.Phys.* **2009,** *130*, 094901
37. Tom, A. M.; Vemparala, S.; Rajesh, R.; Brilliantov, N., Regimes of strong electrostatic collapse of a highly charged polyelectrolyte in a poor solvent. *Soft Matter* **2017**.
38. Kundagrami, A.; Muthukumar, M., Effective charge and coil-globule transition of a polyelectrolyte chain. *Macromolecules* **2010,** *43*, 2574–2581.
39. Swift, T.; Swanson, L.; Geoghegan, M.; Rimmer, S., The pH-responsive behaviour of poly(acrylic acid) in aqueous solution is dependent on molar mass. *Soft Matter* **2016,** *12*, 2542-2549.
40. Yadav, V.; Harkin, A. V.; Robertson, M. L.; Conrad, J. C., Hysteretic memory in pH-response of water contact angle on poly(acrylic acid) brushes. *Soft Matter* **2016,** *12*, 3589-3599.

41. Arnold, R., The titration of polymeric acid. *J.Colloid.Sci.* **1957,** *12*, 549-556.

42. Fleer, G.; Cohen Stuart, M.; Scheutjens, J.; Cosgrove, T.; Vincent, B., *Polymer at interfaces* Chapman and Hal: London, 1993.

43. Zaibudeen, A. W.; Philip, J., Multi-stimuli responsive nanofluid with easy-to-visualize structural color patterns. *Colloids Surf., A* **2017,** *8*, 98–108.

44. Bohmer, M. R.; Evers, O. A.; Scheutjens, J. M. H. M., Weak polyelectrolytes between two surfaces: Adsorption and stabilization *Macromolecucles* **1990,** *23*, 2288-2301

45. Lee, D. H.; Bae, Y.; Kim, Y. N.; Sung, J. Y.; Han, S. W.; Kang, D. P., Counterion-induced control of the colloidal state of polyamic acid nanoparticles for electrophoretic deposition. *Langmuir* **2018,** *34*, 219–227.

46. Barrat, J.-L.; Joanny, J.-F., Theory of polyelectrolyte solutions. *Adv.Chem.Phys* **1996,** *94*, 1–66.

47. Zhang, J.; Kou, R.; Liu, G., Effect of salt concentration on the pH responses of strong and weak polyelectrolyte brushes. *Langmuir* **2017,** *33* 6838–6845.

48. Israels, R.; Leermakers, F. A. M.; Fleer, G. J.; Zhulina, E. B., Charged polymeric brushes: Structure and scaling relations *Macromolecules* **1994,** *27*, 3249-3261.

49. Lyatskaya, Y. V.; Leermakers, F. k. M.; Fleer, G. J.; Zhulina, E. B.; Birshteint, T. M., Analytical self-consistent-field model of weak polyacid brushes *Macromolecules* **1995,** *28*, 3562-3569

50. Zhulina, E. B.; Birshtein, T. M.; Borisov, V., Theory of ionizable polymer brushes *Macromolecules* **1995,** *28*, 1491-1499

51. Zhulina, E. B.; Borisov, O. V., Poisson boltzmann theory of pH-sensitive (annealing) polyelectrolyte brush. *Langmuir* **2011,** *27*, 10615–10633.

52. Zhulina, E. B.; Rubinstein, M., Lubrication by polyelectrolyte brushes. *Macromolecules* **2014,** *47*, 5825–5838.

53. Brettmann, B.; Pincus, P.; Tirrell, M., Lateral structure formation in polyelectrolyte brushes induced by multivalent ions. *Macromolecucles* **2017,** *50*, 1225–1235.

54. Brettmann, B. K.; Laugel, N.; Hoffmann, N.; Pincus, P.; Tirrell, M., Bridging contributions to polyelectrolyte brush collapse in multivalent salt solutions. *J. Polym. Sci., Part A: Polym. Chem.* **2016,** *54*, 284–291.

55. Farina, R.; Laugel, N.; Pincus, P.; Tirrell, M., Brushes of strong polyelectrolytes in mixed mono- and tri-valent ionic media at fixed total ionic strengths. *Soft Matter* **2013,** *9*, 10458–10472.

56. Pincus, P., Colloid stabilization with grafted polyelectrolytes. *Macromolecules* **1991,** *24*, 2912–2919.

57. Tamashiro, M. N.; Herna´ndez-Zapata, E.; Schorr, P. A.; Balastre, M.; Tirrell, M.; Pincus, P., Salt dependence of compression normal forces of quenched polyelectrolyte brushes. *J. Chem. Phys.* **2001,** *115*, 1960-1969.

58. Israels, R.; Leermakers, F. A. M.; Fleer, G. J., On the theory of grafted weak polyacids *Macromolecules* **1994,** *27*, 3087-3093

59. Currie, E. P. K.; Sieval, A. B.; Fleer, G. J.; Stuart, M. A. C., Polyacrylic acid brushes: Surface pressure and salt-induced swelling. *Langmuir* **2000,** *16*, 8324-8333.

60. Wu, T.; Gong, P.; Szleifer, I.; Vicek, P.; Subr, V.; Genzer, J., Behavior of surface anchored poly(acrylic acid) brushes with grafting density gradients on solid substrates : 1. Experiement. *Macromolecules* **2007,** *40*, 8756-8764.

61. Shimada, R. T.; Fonseca, M. S.; Petri, D. F. S., The role of hydroxypropyl methylcellulose structural parameters on the stability of emulsions containing Spirulina biomass. *Colloids Surf.A:Physiochem. Eng. Aspects* **2017,** *529*, 137–145.

62. Qiao, X.; Miller, R.; Sun, K., Interfacial adsorption, viscoelasticity and recovery of silk fibroinlayers at different oil/water interface. *Colloids and Surfaces A: Physicochem. Eng. Aspects* **2017,** *519*, 179–186.

63. Liu, H.; Li, Y.; Diao, X.; Kong, B.; Liu, Q., Effect of porcine bone protein hydrolysates on the emulsifying and oxidative stability of oil-in-water emulsions. *Colloids Surf.A:Physiochem. Eng. Aspects* **2018,** *538*, 757–764.

64. Cheetangdee, N.; Fukada, K., Protein stabilized oil-in-water emulsions modified by uniformity of size by premix membrane extrusion and their colloidal stability. *Colloids and Surfaces A: Physicochem. Eng. Aspects* **2012,** *403*, 54– 61.

65. Derjaguin, B.; Kussakov, M., Anamolous properties of thin polymolecular films. *Acta Physicochimica.URSS* **1939,** *10*.

66. Peters, T., *All about albumin*. Elsevier: New York, 1995.

67. Odenbach, S., *Colloidal magneitc fluids, basics, development and application of ferrofluids*. Springer-Verlag: Berlin, 2009.

68. Laskar, J. M.; Philip, J.; Raj, B., Light scattering in a magnetically polarizable nanoparticle suspension. *Phys. Rev. E* **2008,** *78*, 031404.

69. Laskar, J. M.; Philip, J.; Raj, B., Experimental investigation of magnetic-field-induced aggregation kinetics in nonaqueous ferrofluids. *Phys. Rev. E* **2010,** *82*, 021402.

70. Zaibudeen, A. W.; Philip, J., Thermally tunable grating using thermo-responsive magnetic fluid. *Opt. Mater.* **2017,** *66*, 117-121.

71. Laskar, J. M.; Philip, J.; Raj, B., Experimental evidence for reversible zippering of chains in magnetic nanofluids under external magnetic fields. *Phys. Rev. E* **2009,** *80*, 041401.

72. Felicia, L. J.; Philip, J., Probing of field-induced structures and their dynamics in ferrofluids using oscillatory rheology. *Langmuir* **2014,** *30*, 12171−12179.

73. Shima, P. D.; Philip, J.; Raj, B., Magnetically controllable nanofluid with tunable thermal conductivity and viscosity. *Appl. Phys. Lett.* **2009,** *95*, 133112.

74. Shima, P. D.; Philip, J.; Raj, B., Role of microconvection induced by Brownian motion of nanoparticles in the enhanced thermal conductivity of stable nanofluids. *Appl. Phys. Lett.* **2009,** *94* (22), 223101-223101-3.

75. Liu, T.; Chen, X.; Di, Z.; Zhang, J.; Li, X.; Chen, J., Tunable magneto-optical wavelength filter of long-period fiber grating with magnetic fluids. *Appl. Phys. Lett.* **2007,** *91*, 121116.

76. Mahendran, V.; Philip, J., Nanofluid based optical sensor for rapid visual inspection of defects in ferromagnetic materials. *Appl. Phys. Lett.* **2012,** *100*, 073104.

77. Mahendran, V.; Philip, J., Sensing of Biologically important cations such as Na^+,K^+,Ca^{2+},Cu^{2+} and Fe^{3+} using magnetic nanoemulsions. *Langmuir* **2013,** *29*, 4252−4258.

78. Philip, J.; Shima, P. D.; Raj, B., Nanofluid with tunable thermal properties. *Appl. Phys. Lett.* **2008,** *92*, 043108.

79. Wang, B.; Wang, B.; Wei, P.; Wang, X.; Lou, W., Controlled synthesis and size-dependent thermal conductivity of Fe_3O_4 magnetic nanofluids. *Dalton Trans.* **2012,** *41*, 896-899.

80. Espinosa, A.; Corato, R. D.; Kolosnjaj-Tabi, J.; Flaud, P.; Pellegrino, T.; Wilhelm, C., Duality of iron oxide nanoparticles in cancer therapy: Amplification of heating efficiency by magnetic hyperthermia and photothermal bimodal treatment. *ACS Nano* **2016,** *10*, 2436–2446.

81. Hallali, N.; Clerc, P.; Fourmy, D.; Gigoux, V.; Carrey, J., Influence on cell death of high frequency motion of magnetic nanoparticles during magnetic hyperthermia experiments. *Appl. Phys. Lett.* **2016,** *109*, 032402.

82. Mahendran, V.; Philip, J., Influence of ag+ interaction on 1d droplet array spacing and the repulsive forces between stimuli-responsive nanoemulsion droplets. *Langmuir* **2014,** *30*, 10213−10220.

83. Mahendran, V.; Philip, J., Non-enzymatic glucose detection using magnetic nanoemulsions. *Appl. Phys. Lett.* **2014,** *105*, 123110.

84. Jachimska, B.; Tokarczyk, K.; Łapczynska, M.; Agnieszka; Puciul-Malinowska; Zapotoczny, S., Structure of bovine serum albumin adsorbed on silica investigated by quartz crystal microbalance. *Colloids Surf., A* **2016,** *489*, 163–172.

85. Mahendran, V.; Philip, J., A methanol sensor based on stimulus-responsive magnetic nanoemulsions. *Sens. Actuators B* **2013,** *185*, 488– 495.

86. Wang, H.-C.; Grolman, J. M.; Rizvi, A.; Hisao, G. S.; Rienstra, C. M.; Zimmerman, S. C., pH-triggered release from polyamide microcapsules prepared by interfacial polymerization of a simple diester monomer. *ACS Macro.Lett* **2017,** *6*, 321-325.

87. Costa, M. C. M.; Silva, S. M. C.; Antunes, F. E., Adjusting the low critical solution temperature of poly(N-isopropyl acrylamide) solutions by salts, ionic surfactants and solvents: A rheological study. *J.Mol.Liq.* **2015,** *210*, 113–118.

88. Kang, T.; Banquy, X.; Heo, J.; Lim, C.; Lynd, N. A.; Lundberg, P.; Oh, D. X.; Lee, H.-K.; Hong, Y.-K.; Hwang, D. S.; Waite, J. H.; Israelachvili, J. N.; Hawker, C. J., Mussel-Inspired anchoring of polymer loops that provide superior surface lubrication and antifouling properties. *ACS Nano* **2016,** *10*, 930–937.

89. Zhao, Y.; Janot, J.-M.; Balanzat, E.; Balme, S., Mimicking pH-gated ionic channels by polyelectrolyte complex confinement inside a single nanopore. *Langmuir* **2017,** *33*, 3484-3490.

90. F.J. Schmitt, C. P., J. Simon, H. Ringsdorf, and J. Israelachvili, Direct surface force and contact angle measurements of an adsorbed polymer with a lower critical solution temperature. *Langmuir* **1998,** *14*, 2838 2845.

91. Plunkett, M. A.; Claesson, P. M.; Ernstsson, M.; Rutland, M. W., Comparison of the adsorption of different charge density polyelectrolytes: a quartz crystal microbalance and x-ray photoelectron spectroscopy study. *Langmuir* **2003,** *19*, 4673-4681.

92. Liu, G.; Zhang, G., Collapse and swelling of thermally sensitive poly(N-isopropylacrylamide) brushes monitored with a quartz crystal microbalance

J. Phys. Chem.B **2005,** *109*, 743-747.

93. Ruiz-Cabello, F. J. M.; Trefalt, G.; Maroni, P.; Borkovec, M., Electric double-layer potentials and surface regulation properties measured by colloidal force-probe atomic force microscopy. *Phys. Rev. E* **2014,** *90*, 012301.

94. Conboy, J. C.; Messmer, M. C.; Richmond, G. L., Investigation of surfactant conformation and order at the liquid liquid interface by total internal reflection sum-frequency vibrational spectroscopy. *J. Phys. Chem.* **1996,** *100*, 7617-7622.

95. Kleshchanok, D.; Lang, P. R., Steric repulsion by adsorbed polymer layers studied with total internal reflection microscopy. *Langmuir* **2007,** *23*, 4332-4339.

96. Wong, T. C.; Liu, C. S.; Poon, C. D.; Kwoh, D., Nuclear magnetic resonance study of polymer-surfactant interaction. Carbon-13 NMR study of polymer-induced non-Newtonian to Newtonian transition in a viscoelastic micellar system. *Langmuir* **1992,** *8*, 460–463.

97. Beaman, D. K.; Robertson, E. J.; Richmond, G. L., Ordered polyelectrolyte assembly at the oil–water interface. *Proc. Natl. Acad. Sci* **2012,** *28*, 3226–3231.

98. Robertson, E. J.; Richmond, G. L., Molecular insights in the structure and layered assembly of polyelectrolytes at the oil/water interface. *J. Phys. Chem. C* **2014,** *118*, 28331−28343.

99. Hofl, S.; Zitzler, L.; Hellweg, T.; Herminghaus, S.; Mugele, F., Volume phase transition of ‘‘smart’’ microgels in bulk solution and adsorbed at an interface a combined afm, dynamic light, and small angle neutron scattering study. *Polymer* **2007,** *48*, 245-254.

100. Singh, P. K.; Kumbhakar, M.; Ganguly, R.; Aswal, V. K.; Pal, H.; Nath, S., Time-resolved fluorescence and small angle neutron scattering study in pluronics-surfactant supramolecular assemblies. *J. Phys. Chem. B* **2010,** *114*, 3818–3826.

101. Philip, J.; Gnanaprakash, G.; Jayakumar, T.; Kalyanasundaram, P.; Raj, B., Three distinct scenarios under polymer, surfactant, and colloidal interaction. *Macromolecules* **2003,** *36*, 9230-9236.

102. Philip, J.; Gnanaprakash, G.; Jaykumar, T.; Kalyanasundaram, P.; Mondain-Monval, O.; Raj, B., Interaction between emulsion droplets in the presence of polymer−surfactant complexes. *Langmuir* **2002,** *18*, 4625-4631.

103. Dreyfus, R.; Lacoste, D.; Bibette, J.; Baudry, J., Measuring colloidal forces with the magnetic chaining technique. *Eur. Phys. J. E* **2009,** *28*, 113-123.

104. Shima, P. D.; Philip, J.; Raj, B., Synthesis of aqueous and nonaqueous iron oxide nanofluids and study of temperature dependence on thermal conductivity and viscosity. *J. Phys. Chem. C* **2010,** *114*, 18825−18833.

105. Ayyappan, S.; Gnanaprakash, G.; Panneerselvam, G.; Antony, M. P.; Philip, J., Effect of surfactant monolayer on reduction of Fe_3O_4 nanoparticles under vacuum. *J. Phys. Chem. C* **2008,** *112*, 18376.

106. Gnanaprakash, G.; Ayyappan, S.; Jayakumar, T.; Philip, J.; Raj, B., Magnetic nanoparticles with enhanced γ -Fe_2O_3 to α-Fe_2O_3 phase transition temperature. *Nanotechnology* **2006,** *17*, 5851-5857.

107. Cullity, B. D., *Elements of x ray diffraction*. Addison-wesley publishing company inc.: 1956

108. Silverstein, R. M.; Webster, F. X.; Kiemel, D. J., *Spectrometric identification of organic compounds*. John wiley & sons Inc., 2005.

109. Philip, J.; Jaykumar, T.; Kalyanasundaram, P.; Raj, B.; Mondain-Monval, O., Effect of polymer-surfactant association on colloidal force. *Phys. Rev. E* **2002,** *66*, 011406.

110. Bibette, J., Depletion interactions and fractionated crystallization for polydisperse emulsion purification. *J. Colloid Interface Sci.* **1991,** *147*, 474-478.

111. Mahendran, V.; Sangeetha, J.; Philip, J., Probing of competitive displacement adsorption of casein at oil-in-water interface using equilibrium force distance measurements. *J. Phys. Chem. B* **2015,** *119*, 6828–6835.

112. Zaibudeen, A. W.; Philip, J., Magnetic nanofluid based non-enzymatic sensor for urea detection. *Sens. Actuators, B.* **2018,** *255*, 720–728.

113. Zaibudeen, A. W.; Philip, J., A spectroscopic approach to probe macromolecular conformational changes at interface under different environmental conditions: A case study with PAA adsorbed at oil-water Interface. *J.Mol.Liq.* **2018,** *252*, 30–39.

114. Zaibudeen, A. W.; Philip, J., Behavior of a weak polyelectrolyte at oil-water interfaces under different environmental conditions. *Colloids Surf.A:Physiochem. Eng. Aspects* **2018,** *538*, 610–621.

115. Berne, B. J.; Pecora, R., *Dynamic light scattering: with applications to biology, chemistry and physics*. John Wiley: New York, 1976.

116. Hunter, R. J., *Zeta potential in colloid science: Principles and applications*. Academic Press: London, 1981.

117. Zhang, H.; Widom, M., Field-induced forces in colloidal particle chains. *Phys. Rev. E* **1995,** *51*, 2099-2103.

118. H.M.Kwambaa; J.W.Goodwin; R.W.Hughes; P.A.Reynolds, Viscosity, molecular weight and concentration relationship at 298K of low molecular weight cis-ispropene in good solvent. *Colloids and surface A:Physiochem.Engg.Aspects* **2007,** *294*, 14-19.

119. Guarrotxena, N.; Quijada-Garrido, I., Optical and swelling stimuli-response of functional hybrid nanogels: feasible route to achieve tunable smart core@shell plasmonic@polymer nanomaterials. *Chem.Mater.* **2016,** *28*, 1402–1412.

120. Gargava, A.; Arya, C.; Raghavan, S. R., Smart hydrogel-based valves inspired by the stomata in plants. *ACS Appl. Mater. Interfaces* **2016,** *8*, 18430–18438.

121. Shi, K.; Liu, Z.; Wei, Y.-Y.; Wang, W.; Ju, X.-J.; Xie, R.; Chu, L.-Y., Near-infrared light-responsive poly(n-isopropylacrylamide)/graphene oxide nanocomposite hydrogels with ultrahigh tensibility. *ACS Appl. Mater. Interfaces* **2015,** *7*, 27289–27298.

122. Higashiguchi, K.; Imai, J.; Matsuda, K., Structural Colored Balloons Responsive to pH Change. *Langmuir* **2016,** *32*, 4945–4951.

123. Wang, Y.; Michel, F. M.; Levard, C.; Choi, Y.; Eng, P. J.; Gordon E. Brown, J., Competitive sorption of Pb(II) and Zn(II) on polyacrylic acid-coated hydrated aluminum-oxide surfaces. *Environ. Sci. Technol.* **2013,** *47*, 12131−12139.

124. Duan, X.; Zhang, R.; Li, Y.; Shi, T.; An, L.; Huang, Q., Monte carlo study of polyelectrolyte adsorption on mixed lipid membrane. *J.Phy.Chem B* **2013,** *117*, 989−1002.

125. Patrick, M. J.; Janjic, J. M.; Teng, H.; O'Hear, M. R.; Brown, C. W.; Stokum, J. A.; Schmidt, B. F.; Ahrens, E. T.; Waggoner, A. S., Intracellular pH measurements using perfluorocarbon nanoemulsions. *J. Am. Chem. Soc.* **2013,** *135*, 18445−18457.

126. P.A.Pincus; C.J.Sandroff; T. A.Witten, J., Polymer adsorption on colloidal particles. *J. Physique* **1984,** *45*, 725-729

127. Hu, J.; Dai, L.; Liu, S., Analyte-reactive amphiphilic thermoresponsive diblock copolymer micelles-based multifunctional ratiometric fluorescent chemosensors. *Macromolecule* **2011,** *44*, 4699–4710.

128. Kusolkamabot, K.; Sae-ung, P.; Niamnont, N.; Wongravee, K.; Sukwattanasinitt, M.; Hoven, V. P., Poly(N-isopropylacrylamide)-stabilized gold nanoparticles in combination with tricationic branched phenylene-ethynylene fluorophore for protein identification. *Langmuir* **2013,** *29* 12317−12327.

129. Mura, S.; Nicolas, J.; Couvreur, P., Stimuli response nanocarriers for drug delivery. *Nat.Mater* **2013,** *12*, 991-1003.

130. Kang, Y.; Ma, Y.; Zhang, S.; Ding, L.-S.; Li, B.-J., Dual-stimuli-responsive nanoassemblies as tunable releasing carriers. *ACS Macro.Lett* **2015,** *4*, 543-547.

131. Zeltner, M.; Schätz, A.; Heftia, M. L.; Stark, W. J., Magnetothermally responsive C/Co@PNIPAM-nanoparticles enable preparation of self-separating phase-switching palladium catalysts. *J. Mater. Chem.* **2011,** *21*, 2991-2996.

132. Halperin, A.; Kroger, M., Collapse of thermoresponsive brushes and the tuning of protein adsorption. *Macromolecules* **2011,** *44*, 6986–7005.

133. Ringsdorf, H.; Simon, J.; Winnik, F. M., Hydrophobically modified poly(N-sopropylacrylamides) in water: A look by fluorescence techniques at the heat-induced phase transition. *Macromolecule* **1992,** *25*, 7306-731.

134. Chee, C. K.; Rimmer, S.; Soutar, I.; Swanson, L., Time-resolved fluorescence anisotropy studies of the temperature-induced intramolecular conformational transition of poly(N-isopropylacrylamide) in dilute aqueous solution. *Polymer* **1996,** *38*, 483-486

135. Wu, C.; Zhou, S., First observation of the molten globule state of a single homopolymer chain. *Phys.Rev.Lett* **1996,** *77*, 3053-3055.

136. Wang, X.; Qiu, X.; Wu, C., Comparison of the coil-to-globule and the globule-to-coil transitions of a single poly(N-isopropylacrylamide) homopolymer chain in water. *Macromolecule* **1998,** *31*, 2972-2976.

137. Katsumoto, Y.; Tanaka, T.; Ihara, K.; Koyama, M.; Ozaki, Y., Contribution of intramolecular C=O H-N hydrogen bonding to the solvent induced reentrant phase separation of poly(n-isopropylacrylamide). *J. Phys. Chem. B* **2007,** *111*, 12730 -12737.

138. Baulin, V. A.; Halperin, A., Signatures of a concentration-dependent flory x parameter: Swelling and collapse of coils and brushes. *Macromol. Theory Simul.* **2003,** *12* (549–559).

139. Deshmukh, S. A.; Sankaranarayanan, S. K. R. S.; Mancini, D. C., Vibrational spectra of proximal water in a thermo-sensitive polymer undergoing conformational transition across the lower critical solution temperature. *J. Phys. Chem. B* **2012,** *116*, 5501−5515.

140. Du, H.; Wickramsinghe, R.; Qian, X., Effects of salt on lower critical solution temperature of poly(n-isopropylacrylamide). *J. Phys. Chem.B* **2010,** *114*, 16594-16604.

141. Walter, R.; Ričko, J.; Quellet, C.; Nyffenegger, R.; Binkert, T., Coil-globule transition of poly(N-isopropylacrylamide): A study of polymer-surfactant association. *Macromolecule* **1996,** *29*, 4019-4028.

142. Meewes, M.; Ricka, J.; Silva, M. d.; Nyffenegger, R.; Binkert, T., Coil-globule transition of poly (N-isopropylacrylamide):A study of surfactant effects by light scattering. *Macromolecule* **1991,** *24*, 5811-5816.

143. Kumar, A. C.; Erothu, H.; Bohidar, H. B.; Mishra, A. K., Bile salt induced aggregation of poly(n-isopropylacrylamide) and lowering of the low critical solution temperature in aqueous solutions. *J.Phy.Chem.B* **2011,** *115*, 433–439.

144. Lu, Y.; Ye, X.; Zhou, K.; Shi, a. W., A comparative study of urea-induced aggregation of collapsed poly(n-isopropylacrylamide) and poly(N,N- diethylacrylamide) chains in aqueous solutions. *J.Phy.Chem.B* **2013,** *117*, 7481-7488.

145. Zhu, P. W.; Napper, D. H., Effects of anionic surfactant on the coil-to-globule transition of interfacial poly(N-isopropylacrylamide). *Langmuir* **1996,** *12*, 5992 5998.

146. Chen, J.; Gong, X.; Yang, H.; Yao, Y.; Xu, M.; Chen, Q.; Cheng, R., NMR study on the effects of sodium n-dodecyl sulfate on the coil-to-globule transition of poly(n-isopropylacrylamide) in aqueous solutions. *Macromolecule* **2011,** *44*, 6227–6231.

147. Zhu, P. W., Effects of sodium dodecyl sulfate on structures of poly(N-isopropylacrylamide) at particle surface. *J.Phy.Chem B* **2015,** *119*, 359-371.

148. Wu, C.; Wang, X., Globule to coil transition of a single homopolymer chain in solution. *Phys.Rev.Lett* **1998,** *80*, 4092-4094.

149. Winnik, F. M., Fluorescence studies of aqueous solutions of poly(N-isopropylacrylamide) below and above their lcst. *Macromolecule* **1990,** *23*, 233-242.

150. Haupt, B. J.; Senden, T. J.; Sevick, E. M., AFM evidence of rayleigh instability in single polymer chains. *Langmuir* **2002,** *18*, 2174-2182.

151. Ishida, N.; Biggs, S., Direct observation of the phase transition for a poly(n-isopropylacryamide) layer grafted onto a solid surface by AFM and QCM-D. *Langmuir* **2007,** *23*, 11083-11088.

152. Kidoaki, S.; Ohya, S.; Nakayama, Y.; Matsuda, T., Thermoresponsive structural change of a poly(n-isopropylacrylamide) graft layer measured with an atomic force microscope. *Langmuir* **2001,** *17*, 2402 2407.

153. Chen, H.; Ruckenstein, E., Micellar structures in nanoparticle-multiblock copolymer complexes. *Langmuir* **2014,** *30*, 3723−3728.

154. Qiao, J.; Mua, X.; Qi, L., A versatile method for the preparation of polyacrylamide derivative functionalized thermo-responsive gold nanoparticles. *J. Mater. Chem. B* **2013,** *1*, 5756–5761.

155. Philipp, M.; Aleksandrova, R.; Mulle, U.; Ostermeyer, M.; Sanctuary, R.; Muller-Buschbaum, P.; Baulin, J. K. K.; A., V., Molecular versus macroscopic perspective on the demixing transition of aqueous PNIPAM solutions by studying the dual character of the refractive index. *Soft Matter* **2014,** *10*, 7297–7305

156. Cheng, H.; Shen, L.; Wu, C., LLS and FTIR studies on the hysteresis in association and dissociation of poly(n-isopropylacrylamide) in water. *Macromolecule* **2006,** *39*, 2325-2329.

157. Chen, J.; Xue, H.; Yao, Y.; Yang, H.; Li, A.; Xu, M.; Chen, Q.; Cheng, R., Effect of surfactant concentration on the complex structure of poly(n-isopropylacrylamide)/sodium n-dodecyl sulfate in aqueous solutions. *Macromolecule* **2012,** *45*, 5524–5529.

158. Chen, J.; Gong, X.; Yang, H.; Yao, Y.; Xu, M.; Chen, Q.; Cheng, R., NMR study on the effects of sodium n-dodecyl sulfate on the coil-to-globule transition of poly(N-isopropylacrylamide) in aqueous solutions. *Macromolecules* **2011,** *44*, 6227–6231.

159. Derjaguin, B., On the repulsive force between charged colloidal particles and on the theory of slow coagulation and stability of lyophobe sols. *Trans.Faraday.Soc* **1940,** *35*, 203-215.

160. Derjaguin, B. V.; Rabinovich, Y. I.; Churaev, N. V., Direct measurement of molecular forces. *Nature* **1978,** *272*, 313-318.

161. Zhu, P. W.; Napper, D. H., Conformational transitions of poly(N-isopropylacrylamide) chains loopily absorbed at the surfaces of poly(N-tert-butylacrylamide) latex particles in water. *J. Phys. Chem. B* **1997,** *101*, 3155-3160.

162. Semenov, A. N.; Bonet-Avalos, J.; Johner, A.; Joanny, J. F., Adsorption of polymer solutions onto a flat surface. *Macromolecule* **1996,** *29*, 2179-2196.

163. Ding, Y.; Ye, X.; Zhang, G., Can coil-to-globule transition of a single chain be treated as a phase transition? *J. Phys. Chem.B* **2008,** *112*, 8496–8498.

164. Svitova, T. F.; Radke, C. J., AOT and pluronic F68 coadsorption at fluid/fluid tnterfaces: a continuous-flow tensiometry study. *Ind. Eng. Chem. Res.* **2005,** *44*, 1129-1138.

165. Walter, R.; Ricka, J.; Quellet, C.; Nyffenegger, R.; Binkert, T., Coil-globule transition of poly(N-isopropylacrylamide): A study of polymer-surfactant association. *Macromolecule* **1996,** *29*, 4019-4028.

166. Lee, L.-T.; Cabane, B., Effects of surfactants on thermally collapsed poly(N-isopropylacrylamide) macromolecules. *Macromolecule* **1997,** *30*, 6559-6566.

167. Jia, H.; Wildes, A.; Titmuss, S., Structure of ph-responsive polymer brushes grown at the gold− water interface: dependence on grafting density and temperature. *Macromolecule* **2011,** *45*, 305−312.

168. Ogaki, R.; Andersen, O. Z.; Jensen, G. V.; Kolind, K.; Kraft, D. C.; Pedersen, J. P.; Foss, M., Temperature induced ultradense peg polyelectrolyte surface grafting provides effective long term bioresistance against mamalina cells, serum and whole blood. *Biomacromolecule* **2012,** *13*, 3668-3677.

169. Napper, D. H., *Polymeric stabilization of colloidal dispersions*. Academic press: New York, 1983; p 441.

170. Higaki, Y.; Kobayashi, M.; Murakami, D.; Takahara, A., Anti-fouling behavior of polymer brush immobilized surfaces. *Polymer* **2016,** *48* 325-331.

171. Maity, H.; Reddy, G., Folding of protein L with implications for collapse in the denatured state ensemble. *J. Am. Chem. Soc.* **2016,** *138*, 2609–2616.

172. Jorge, A. F.; Dias, R. S.; Pereira, J. C.; Pais, A. A. C. C., DNA condensation by pH-responsive polycations. *Biomacromolecules* **2010,** *11*, 2399–2406.

173. Kim, B.-H.; Jung, J.-H.; Hong, S.-H.; Joo, J.; Epstein, A. J.; Mizoguchi, K.; Kim, J. W.; Choi, H. J., Nanocomposite of polyaniline and Na^+–montmorillonite clay. *Macromolecules* **2002,** *35* 1419–1423.

174. Hostnik, G.; Cerar, J., On describing the equilibria in mixed solutions of polyelectrolytes and simple salts using the law of mass action. *J.Mol.Liq.* **2017,** *228*, 96-102.

175. Ionov, L., Polymeric actuators. *Langmuir* **2015,** *31*, 5015–5024.

176. Jardat, M.; Dahirel, V.; Carnal, F., Dynamics of ions in model charged porous media: Influence of polyelectrolytes. *J.Mol.Liq.* **2017,** *228*, 224–229.

177. Cosgrove, T.; Crowley, T. L.; Ryan, K.; Webster, J. R. P., The effects of solvency on the structure of an adsorbed polymer layer and dispersion stability`. *Colloids Surf.* **1990,** *51*, 255-269.

178. Hehmeyer, O. J.; Arya, G.; Panagiotopoulos, A. Z., Monte Carlo simulation and molecular theory of tethered polyelectrolytes. *J.Chem.Phys* **2007,** *126*, 244902.

179. Farina, R.; Laugel, N.; Yu, J.; Tirrell, M., Reversible adhesion with polyelectrolyte brushes tailored via the uptake and release of trivalent lanthanum ions. *J. Phys. Chem. C* **2015,** *119*, 14805–14814.

180. Sparks, D. J.; Romero-Gonzalez, M. E.; El-Taboni, E.; Freeman, C. L.; Hall, S. A.; Kakonyi, G.; Swanson, L.; Banwart, S. A.; Harding, J. H., Adsorption of poly acrylic acid onto the surface of calcite: an experimental and simulation study. *Phys.Chem.Chem.Phys* **2015,** *17*, 27357-27365.

181. Briscoe, B.; Luckham, P.; Zhu, S., The effects of hydrogen bonding upon the viscosity of aqueous poly(vinyl alcohol) solutions. *Polymer* **2000,** *41*, 3851–3860.

182. Xie, F.; Lu, H.; Nylander, T.; Wagberg, L.; Forsman, J., Theoretical and experimental investigations of polyelectrolyte adsorption dependence on molecular weight. *Langmuir* **2016,** *32*, 5721-5730.

183. Swavola, J. C.; Edwards, T. D.; Bevan, M. A., Direct measurement of macromolecule-coated colloid−mucus interactions. *Langmuir* **2015,** *31*, 9076-9085.

184. Riley, J. K.; An, J.; Tilton, R. D., Ionic surfactant binding to pH-responsive polyelectrolyte brush grafted nanoparticles in suspension and on charged surfaces. *Langmuir* **2015,** *31*, 13680-13689.

185. Guptha, V. S.; Hsiao, P.-Y., Polyelectrolyte brushes in monovalent and multivalent salt solutions. *Polymer* **2014,** *55*, 2900-2912.

186. O.Lebedeva, I.; Zhulina, E. B.; Borisov, O., Self-consistent field theory of polyelectrolyte brush with finite chain extensibility. *J.Chem.Phys* **2017,** *146*, 214901.

187. Mehrdad, A.; Taleb-Abbasi, M., Influence of some inorganic salts on the intrinsic viscosity of poly(acrylic acid) in aqueous solutions. *J.Mol.Liq.* **2016,** *223*, 699–706.

188. Sarkar, D.; Somasundaran, P., Conformational dynamics of poly(acrylic acid). A study using surface plasmon resonance spectroscopy. *Langmuir* **2004,** *20*, 4657-4664.

189. Beaman, D. K.; Robertson, E. J.; Richmond, G. L., Metal ions: Driving the orderly assembly of polyelectrolytes at a hydrophobic surface. *Langmuir* **2012,** *28*, 14245−14253`.

190. Mathieson, A. R.; McLaren, J. V., Potentiometric study of the conformational transition in poly(acrylic acid) *J. Polym. Sci., Part A: Polym. Chem.* **1965,** *3*, 2555-2565

191. Mahendran, V.; Philip, J., Spectral response of magnetic nanofluid to toxic cations. *Appl. Phys. Lett.* **2013,** *102*, 163109.

192. Biggs, S.; Proud, A. D., Forces between silica surfaces in aqueous solutions of a weak polyelectrolyte. *Langmuir* **1997,** *13*, 7202-7210.

193. Laguecir, A.; Ulrich, S.; Labille, J.; Fatin-Rouge, N.; Stoll, S.; Buffle, J., Size and pH effect on electrical and conformational behavior of poly(acrylic acid): Simulation and experiment. *Eur. Polym. J.* **2006,** *42*, 1135–1144.

194. Lego, B.; Skene, W. G.; Giasson, S., Swelling study of responsive polyelectrolyte brushes grafted from mica substrates: Effect of pH, salt, and grafting density. *Macromolecules* **2010,** *43*, 4384–4393.

195. Nnebe, I. M.; Tilton, R. D.; Schneider, J. W., Direct force measurement of the stability of poly(ethyleneglycol)–polyethylenimine graft films. *J.Coll&Inter.Scien* **2004,** *276*, 306–316.

196. Dobrynin, A. V.; Deshkovski, A.; Rubinstein, M., Adsorption of polyelectrolytes at an oppositely charged surface. *Phys.Rev.Lett* **2000,** *84*, 3101-3104.

197. Brilliantov, N. V.; Kuznetsov, D. V.; Klein, R., Chain collapse and counterion condensation in dilute polyelectrolyte solutions. *Phys.Rev.Lett* **1998,** *81*, 1433-1436.

198. Philip, J.; Gnanaprakash, G.; Jaykumar, T.; Kalyanasundaram, P.; Raj, B., Stretching and collapse of neutral polymer layers under association with ionic surfactants. *Phys. Rev. Lett.* **2002,** *89*, 268301.

199. Zhulina, E. B.; Borisov, O. V.; Birshtein, T. M., Polyelectrolyte brush interaction with multivalent ions. *Macromolecucles* **1999,** *32*, 8189-8196.

200. He, S.-Z.; Merlitz, H.; Chen, L.; Sommer, J.-U.; Wu, C.-X., Polyelectrolyte brushes: MD simulation and SCF Theory. *Macromolecules* **2010,** *43*, 7845–7851.

201. Liu, L.; Pincus, P. A.; Hyeon, C., Heterogeneous morphology and dynamics of polyelectrolyte brush condensates in trivalent counterion solution. *Macromolecules* **2017,** *50*, 1579–1588.

202. Zhang, H.; Ruhe, J., Swelling of poly(methacrylic acid) brushes: Influence of monovalent salts in the environment. *Macromolecules* **2005,** *38*, 4855-4860.

203. Jia, H.; Grillo, I.; Titmuss, S., Small angle neutron scattering study of polyelectrolyte brushes grafted to well-defined gold nanoparticle interfaces. *Langmuir* **2010,** *26*, 7482–7488.

204. Yu, J.; Mao, J.; Yuan, G.; Satija, S.; Jiang, Z.; Chen, W.; Tirrell, M., Structure of polyelectrolyte brushes in the presence of multivalent counterions. *Macromolecules* **2016,** *49*, 5609–5617.

205. Mei, Y.; Lauterbach, K.; Hoffmann, M.; Borisov, O. V.; Ballauff, M.; Jusufi, A., Collapse of spherical polyelectrolyte brushes in the presence of multivalent counterions. *Phys.Rev.Lett* **2006,** *97*, 158301.

206. Alexander, S., Adsorption of chain molecules with a polar head a scaling description. *J. Phys. France* **1977,** *38*, 983 - 987.

207. Melo, J. S. d.; Costa, T.; Francisco, A.; Macanita, A. L.; Gago, S.; Goncalves, I. S., Dynamics of short as compared with long poly(acrylic acid) chains hydrophobically modified with pyrene, as followed by fluorescence techniques. *Phys. Chem. Chem. Phys.* **2007,** *9*, 1370–1385.

208. O'Neal, J. T.; Dai, E. Y.; Zhang, Y.; Clark, K. B.; Wilcox, K. G.; George, I. M.; Ramasamy, N. E.; Enriquez, D.; Batys, P.; Sammalkorpi, M.; Lutkenhaus, J. L., QCM-D investigation of swelling behavior of layer-by-layer thin films upon exposure to monovalent ions. *Langmuir* **2018,** *34*, 999–1009.

209. Lee, H.-Y.; Tiwari, K. R.; Raghavan, S. R., Biopolymer capsules bearing polydiacetylenic vesicles as colorimetric sensors of pH and temperature. *Soft Matter* **2011,** *7*, 3273–3276.

210. Pu, S.; Chen, X.; Chen, L.; Liao, W.; Y.Chen; Y.Xia, Tunable magnetic fluid grating by applying a magnetic field. *Appl. Phys. Lett.* **2005,** *87*, 021901.

211. Wang, J.; Ayano, E.; Maitani, Y.; Kanazawa, H., Tunable surface properties of temperature-responsive polymer-modified liposomes induce faster cellular uptake. *ACS Omega* **2017,** *2*, 316–325.

212. Ashraf, K. M.; Khan, M. R. K.; Higgins, D. A.; Collinson, M. M., pH and surface charge switchability on bifunctional charge gradients. *Langmuir* **2018,** *34*, 663–672.

213. Tergolina, V. B.; Santos, A. P. d., Effect of dielectric discontinuity on a spherical polyelectrolyte brush. *J.Chem.Phys* **2017,** *147*, 114103.

214. Padwal, P.; Bandyopadhyaya, R.; Mehra, S., Polyacrylic acid-coated iron oxide nanoparticles for targeting drug resistance in mycobacteria. *Langmuir* **2014,** *30*, 15266−15276.

215. Kavitha, T.; Kang, I.-K.; Park, S.-Y., Poly(acrylic acid)-grafted graphene oxide as an intracellular protein carrier. *Langmuir* **2014,** *30*, 402−409.

216. Faivre, J.; Shrestha, B. R.; Xie, G.; Delair, T.; David, L.; Matyjaszewski, K.; Banquy, X., Unraveling the correlations between conformation, lubrication, and chemical stability of bottlebrush polymers at interfaces. *Biomacromolecules* **2017,** *18*, 4002–4010.

217. Sletmoen, M.; Maurstad, G.; Nordg, C. T.; Draget, K. I.; Stokke, B. T., Oligoguluronate induced competitive displacement of mucin–alginate interactions: relevance for mucolytic function. *Soft Matter* **2012,** *8*, 8413–8421.

218. Aaron P.R. Eberle; Norman J. Wagner; Castaneda-Priego, R., Dynamical arrest transition in nanoparticle dispersions with short range interactions. . *Phys. Rev. Lett.* **2011,** *106*, 105704

219. Tabatabai, A. P.; Weigandt, K. M.; Blair, D. L., Acid-induced assembly of a reconstituted silk protein system. *Phys.Rev.E* **2017,** *96*, 022405.

220. Forch, R.; Schonherr, H.; Jenkins, A. T. A., *Surface design: applications in bioscience and nanotechnology*. Wiley-VCH Verlag GmbH & Co. KGaA: 2009.

221. Szuttor, K.; Roy, T.; Hardt, S.; Holm, C.; Smiatek, J., The stretching force on a tethered polymer in pressure-driven flow. *J.Chem.Phys* **2017,** *147*, 034902.

222. Wu, B.; Wang, X.; Yang, J.; Hua, Z.; Tian, K.; Kou, R.; Zhang, J.; Ye, S.; Luo, Y.; Craig, V. S. J.; Zhang, G.; Liu1, G., Reorganization of hydrogen bond network makes strong polyelectrolyte brushes pH-responsive. *Sci. Adv.* **2016,** *2*, 1600579.

223. Mitra, S.; Kundagrami, A., Kinetics of swelling and collapse of a single polyelectrolyte chain. *Macromolecucles* **2017,** *50* 2504–2517.

224. Gong, P.; Genzer, J.; Szleifer, I., Phase behavior and charge regulation of weak polyelectrolyte grafted layers. *Phys.Rev.Lett.* **2007,** *98*, 018302.

225. Yu, M.; Qian, L.; Cui, S., Reentrant variation of single-chain elasticity of polyelectrolyte induced by monovalent salt. *J. Phys. Chem. B* **2017,** *121*, 4257–4264.

226. Zhulina, E. B.; Rubinstein, M., Ionic strength dependence of polyelectrolyte brush thickness. *Soft Matter* **2012,** *8*, 9376-9383.

227. Biesalski, M.; Johannsmann, D.; Ruheb, J., Synthesis and swelling behavior of a weak polyacid brush. *J.Chem.Phys* **2002,** *117*, 4988-4994.

228. Lebedeva, I. O.; Zhulina, E. B.; Borisov, O. V., Self-consistent field theory of polyelectrolyte brushes with finite chain extensibility. *J.Chem.Phys* **2017,** *146*, 214901.

229. Hoffmann, M.; Jusufi, A.; Schneider, C.; Ballauff, M., Surface potential of spherical polyelectrolyte brushes in the presence of trivalent counterions. *J.Coll&Inter.Scien* **2009** *338* 566–572.

230. Tamashiro, M. N.; Hernandez-Zapata, E.; Schorr, P. A.; Balastre, M.; Tirrell, M.; Pincus, P., Salt dependence of compression normal forces of quenched polyelectrolyte brushes. *J. Chem. Phys.* **2001,** *115*, 1960-1969.

231. Maarel, J. R. C. v. d.; Groenewegen, W., Salt-induced contraction of polyelectrolyte diblock copolymer micelles. *Langmuir* **2000,** *16*, 7510-7519.

232. Longo, G. S.; Cruz, M. O. d. l.; Szleife, I., Non-monotonic swelling of surface grafted hydrogels induced by pH and/or salt concentration. *J.Chem.Phys* **2014,** *141*, 124909.

233. Murakami, D.; Takenaka, A.; Kobayashi, M.; Jinnai, H.; Takahara, A., Measurement of the electrostatic interaction between polyelectrolyte brush surfaces by optical tweezers. *Langmuir* **2013,** *29*, 16093−16097.

234. Chu, X.; Yang, J.; Liu, G.; Zhao, J., Swelling enhancement of polyelectrolyte brushes induced by external ions. *Soft Matter* **2014,** *10*, 5568–5578.

235. Wei, X.; Ngai, T., Ion-induced hydrophobic collapse of surface-confined polyelectrolyte brushes measured by total internal reflection microscopy. *Polym. Chem.* **2012,** *3*, 2121-2128.

236. Stilin, V.; Weetall, H.; Vanderah, D. J., SPR studies of the nonspecific adsorption kinetics of human IgG and bsa on gold surfaces modified by self-assembled monolayers (SAMs). *J. Colloid Interface Sci.* **1997,** *185*, 94–103.

237. Sengupta, T.; Damodaran, S., Role of dispersion interactions in the adsorption of proteins at oil-water and air-water interfaces. *Langmuir* **1998,** *14*, 6457-6469.

238. Panja, S.; Khatua, D. K.; Halder, M., Investigations on the effect of fatty acid additives on casein micelles: role of ethylenic unsaturation on the interaction and structural diversity. *ACS Omega* **2018,** *3*, 821-830.

239. Panja, S.; Khatua, D. K.; Halder, M., Simultaneous binding of folic acid and methotrexate to human serum albumin: insights into the structural changes of protein and the location and competitive displacement of drugs. *ACS Omega* **2018,** *3*, 246–253.

240. Biswas, A.; Banerjee, S.; Gart, E. V.; Nagaraja, A. T.; McShane, M. J., Gold nanocluster containing polymeric microcapsules for intracellular ratiometric fluorescence biosensing. *ACSOmega* **2017,** *2*, 2499−2506.

241. Obana, M.; Silverman, B. R.; Tirrell, D. A., Protein-mediated colloidal assembly *J. Am. Chem. Soc.* **2017,** *139*, 14251–14256.

242. Fu, X.; Wang, Y.; Zhong, W.-H.; Cao, G., A multifunctional protein coating for self-assembled porous nanostructured electrodes. *ACS Omega* **2017,** *2*, 1679−1686.

243. Tang, C.-H.; Shen, L., Role of conformational flexibility in the emulsifying properties of bovine serum albumin. *J. Agric. Food Chem.* **2013,** *61*, 3097−3110.

244. Khakalo, A.; Filpponen, I.; Rojas, O. J., Protein adsorption tailors the surface energies and compatibility between polylactide and cellulose nanofibrils. *Biomacromolecules* **2017,** *18*, 1426–1433.

245. Bonoli-Carbognin, M.; Cerretani, L.; Bendini, A.; Almajano, M. P.; Gordon, M. H., Bovine serum albumin produces a synergistic increase in the antioxidant activity of virgin olive oil phenolic compounds in oil-in-water emulsions. *J. Agric. Food Chem.* **2008,** *56*, 7076–7081.

246. Romero, A.; Beaumal, V.; David-Briand, E.; Cordobes, F.; Guerrero, A.; Anton, M., Interfacial and oil/water emulsions characterization of potato protein isolates. *J. Agric. Food Chem.* **2011,** *59*, 9466–9474.

247. Athas, J. C.; Jun, K.; McCafferty, C.; Owoseni, O.; John, V. T.; Raghavan, S. R., An effective dispersant for oil spills based on food-grade amphiphiles. *Langmuir* **2014,** *30*, 9285−9294.

248. Satulovsky, J.; Carignano, M. A.; Szleifer, I., Kinetic and thermodynamic control of protein adsorption. *Proc. Natl. Acad. Sci.* **2000,** *97*, 9037–9041.

249. Lu, Z.; Chen, Z.; Guo, Y.; Ju, Y.; Liu, Y.; Feng, R.; Xiong, C.; Ober, C. K.; Dong, L., Flexible hydrophobic antifouling coating with oriented nanotopography and non-leaking capsaicin. *ACS Appl. Mater. Interfaces.* **2018**.

250. Ma, C.; Zhang, W.; Zhang, G.; Qian, P.-Y., Environmentally friendly antifouling coatings based on biodegradable polymer and natural antifoulant. *ACS Sustainable Chem. Eng.* **2017,** *5*, 6304–6309.

251. Lockhart, J. N.; Spoonmore, T. J.; McCurdy, M. W.; Rogers, B. R.; Guelcher, S. A.; Harth, E., Poly(glycidol) coating on ultrahigh molecular weight polyethylene for reduced biofilm growth. *ACS Appl. Mater. Interfaces* **2018,** *10*, 4050–4056.

252. Giamblanco, N.; Marletta, G.; Graillot, A.; Bia, N.; Loubat, C.; Berret, J.-F., Serum protein-resistant behavior of multisite-bound poly(ethylene glycol) chains on iron oxide surfaces. *ACS Omega* **2017,** *2*, 1309–1320.

253. Helgeson, M. E., Colloidal behavior of nanoemulsions: Interactions, structure,and rheology. *Curr. Opin. Colloid Interface Sci.* **2016,** *25*, 39–50.

254. Sadler, P. J.; Tucker, A., pH-induced structural transitions of bovine serum albumin histidine pK, values and unfolding of the n-terminus during the n to f transition. *Eur. J. Biochem.* **1993,** *212*, 811-817.

255. Salis, A.; Bostrom, M.; Medda, L.; Cugia, F.; Barse, B.; Parsons, D. F.; Ninham, B. W.; Monduzzi, M., Measurements and theoretical interpretation of points of zero charge/potential of bsa protein. *Langmuir* **2011,** *27*, 11597–11604.

256. Xu, Z.; Grassian, V. H., Bovine serum albumin adsorption on TiO_2 nanoparticle surface: effects of ph and co-adsorption of phosphate on protein-surface interactions and protein structure. *J.Phy.Chem.C* **2017,** *121*, 21763–21771.

257. Platten, F.; Valadez-Pérez, N. E.; Castañeda-Priego, R.; Egelhaaf, S. U., Extended law of corresponding states for protein solutions. *J.Chem.Phys* **2015,** *142*, 174905

258. Graham, D. E.; Phillips, M. C., Proteins at liquid interfaces I. kinetics of adsorption and surface denaturation. *J. Colloid Interface Sci.* **1979,** *70*, 403-414.

259. Graham, D. E.; Phillips, M. C., Proteins at liquid interfaces Ill. molecular structures of adsorbed films. *J. Colloid Interface Sci.* **1979,** *70*, 427-439.

260. Sengupta, T.; Razumovsky, L.; Damodaran, S., Energetics of protein-interface interactions and its effect on protein adsorption. *Langmuir* **1999,** *15*, 6991-7001.

261. Chang, Y.; Hu, Y.; McClements, D. J., Competitive adsorption and displacement of anionic polysaccharides (fucoidan and gum arabic) on the surface of protein-coated lipid droplets. *Food Hydrocolloids* **2016,** *52* 820-826.

262. Jin, H.; Wang, W.; Chang, H.; Shen, Y.; Yu, Z.; Tian, Y.; Yu, Y.; Gong, J., Effects of salt-controlled self-assembly of triblock copolymers F68 on interaction forces between oil drops in aqueous solution. *Langmuir* **2017,** *33*, 14548–14555.

263. Yang, F.; Wu, W.; Chen, S.; Gan, W., The ionic strength dependent zeta potential at the surface of hexadecane droplets in water and the corresponding interfacial adsorption of surfactants. *Soft Matter* **2017,** *13*, 638-646.

264. Leggio, C.; Galantini, L.; Pavel, N. V., About the albumin structure in solution: cigar expanded form versus heart normal shape. *Phys. Chem. Chem. Phys.* **2008,** *10*, 6741–6750.

265. Taxford, C.; Swanson, S. A.; Shore, W. S., Hydrogen ion equilibria of bovine serum albumin. *J. Am. Chem. Soc.* **1955,** *77*, 6414-6421.

266. Bohme, U.; Scheler, U., Effective charge of bovine serum albumin determined by electrophoresis NMR. *Chem.Phys.Lett* **2007,** *435*, 342–345.

267. Medda, L.; Barse, B.; Cugia, F.; Boström, M.; Parsons, D. F.; Ninham, B. W.; Monduzzi, M.; Salis, A., Hofmeister challenges: ion binding and charge of the bsa protein as explicit examples. *Langmuir* **2012,** *28*, 16355−16363.

268. Wittemann, A.; Ballauff, M., Interaction of proteins with linear polyelectrolytes and spherical polyelectrolyte brushes in aqueous solution. *Phys.Chem.Chem.Phys* **2006,** *8*, 5269–5275.

269. Inoue, Y.; Ishihara, K., Reduction of protein adsorption on well-characterized polymer brush layers with varying chemical structures. *Colloids Surf., B* **2010,** *81*, 350–357.

270. Yao, X.; Nie, K.; Chen, Y.; Jiang, F.; Kuang, Y.; Yan, H.; Fang, Y.; Yang, H.; Nishinari, K.; Phillips, G. O., The influence of non-ionic surfactant on lipid digestion of gum arabic stabilized oil-in-water emulsion. *Food Hydrocolloids* **2018,** *74*, 78-86.

271. Henzler, K.; Rosenfeldt, S.; Wittemann, A.; Harnau, L.; Finet, S.; Narayanan, T.; Ballauff, M., Directed motion of proteins along tethered polyelectrolytes. *Phys.Rev.Lett* **2008,** *100*, 158301.

272. Tang, C.-H.; Shen, L., Dynamic adsorption and dilatational properties of BSA at oil/water interface: role of conformational flexibility. *Food Hydrocolloids* **2015,** *43*, 388-399.

273. Bloomfield, V., The structure of bovine serum albumin at low pH. *Biochemistry* **1966,** *2*, 684-689.

274. Baler, K.; Martin, O. A.; Carignano, M. A.; Ameer, G. A.; Vila, J. A.; Szleifer, I., Electrostatic unfolding and interactions of albumin driven by pH changes: a molecular dynamics study. *J. Phys. Chem. B.* **2014,** *118*, 921−930.

275. He, S.; Huang, M.; Ye, W.; Chen, D.; He, S.; Ding, L.; Yao, Y.; Wan, L.; Xu, J.; Miao, S., Conformational change of bovine serum albumin molecules at neutral pH in ultra-diluted aqueous solutions. *J.Phy.Chem B* **2014**.

276. Li, R.; Wu, Z.; Wangb, Y.; Ding, L.; Wang, Y., Role of pH-induced structural change in protein aggregation in foam fractionation of bovine serum albumin. *Biotechnology Reports* **2016,** *9*, 46–52.

277. Lee, S.-H.; Lefevre, T.; Subirade, M.; Paquin, P., Changes and roles of cecondary structures of whey protein for the formation of protein membrane at soy oil/water interface under high-pressure homogenization. *J. Agric. Food Chem.* **2007,** *55*, 10924–10931.

278. Liu, Y.; Yadav, M. P.; Yin, L., Enzymatic catalyzed corn fiber gum-bovine serum albumin conjugates: Their interfacial adsorption behaviors in oil-in-water emulsions. *Food Hydrocolloids* **2018,** *77*, 986-994.

279. Meng, G.; Chan, J. C. K.; Rousseau, D.; Li-Chan, E. C. Y., Study of protein−lipid interactions at the bovine serum albumin/oil interface by raman microspectroscopy. *J. Agric. Food Chem.* **2005,** *53*, 845–852.

280. Dickinson, E., Mixed proteinaceous emulsifiers: review of competitive protein adsorption and the relationship to food colloid stabilization. *Food Hydrocolloids* **1986,** *1*, 3-23.

281. Courthaudon, J.-L.; Dickinson, E.; Matsumura, Y.; Clark, D. C., Competitive adsoprtion of β lactoglobulin + tween 20 at the oil-water interface. *Colloids Surf.* **1991,** *56*, 293-300.

282. Kim, H.-J.; Decker, E. A.; McClements, D. J., Impact of protein surface denaturation on droplet flocculation in hexadecane oil-in-water emulsions stabilized by β-lactoglobulin. *J. Agric. Food Chem.* **2002,** *50*, 7131–7137

283. Day, L.; Zhai, J.; Xu, M.; Jones, N. C.; Hoffmann, S. V.; Wooster, T. J., Conformational changes of globular proteins adsorbed at oil-in-water emulsion interfaces examined by synchrotron radiation circular dichroism. *Food Hydrocolloids* **2014,** *34*, 78-87.

284. Al-Malah, K. I.; Azzam, M. O. J.; Omari, R. M., Emulsifying properties of bsa in different vegetable oil emulsions using conductivity technique. *Food Hydrocolloids* **2000,** *14*, 485–490.

285. Meng, G.; Chan, J. C. K.; Rousseau, D.; Li-Chan, E. C. Y., Study of protein−lipid interactions at the bovine serum albumin/oil interface by raman microspectroscopy. *J. Agric. Food Chem.* **2005,** *53*, 845−852

286. Campana, M.; Hosking, S. L.; Petkov, J. T.; Tucker, I. M.; Webster, J. R. P.; Zarbakhsh, A.; Lu, J. R., Adsorption of bovine serum albumin (bsa) at the oil/water interface: a neutron reflection study. *Langmuir* **2013,** *31*, 5614−5622.

287. Jiang, J.; Jin, Y.; Liang, X.; Piatko, M.; Campbell, S.; Lo, S. K.; Liu, Y., Synergetic interfacial adsorption of protein and low-molecular-weight emulsifiers in aerated emulsions. *Food Hydrocolloids* **2018,** *81*, 15-22.

288. Ho, K. K. H. Y.; Schroen, K.; Martín-Gonzalez, M. F. S.; Berton-Carabin, C. C., Synergistic and antagonistic effects of plant and dairy protein blends on the physicochemical stability of lycopene-loaded emulsions. *Food Hydrocolloids* **2018,** *81*, 180-190.

289. Barbosa, L. R. S.; Ortore, M. G.; Spinozzi, F.; Mariani, P.; Bernstorff, S.; Itri, R., The importance of protein-protein interactions on the ph-inducedcconformational changes of bovine serum albumin: a small-angle x-ray scattering study. *Biophys. J .* **2010** *98*, 147–157.

290. Szleifer, Protein adsorption on surfaces with grafted polymers: a theoretical approach. *Biophys. J .* **1997,** *72*, 595-612.

291. Xu, S.; Damodaran., S., The role of chemical potential in the adsorption of lysozyme at the air-water interface. *Langmuir* **1992,** *8*, 2021-2027.

292. Bianchi, R. C.; Silva, E. R. d.; Dall'Antonia, L. H.; Ferreira, F. F.; Alves, W. A., A nonenzymatic biosensor based on gold electrodes modified with peptide self-assemblies for detecting ammonia and urea oxidation. *Langmuir* **2014,** *30*, 11464–11473.

293. Heffer, P.; Prud'homme, M., Fertilizer Outlook 2016-2020. In *84th IFA Annual Conference*, Moscow 2016.

294. Francis, P. S.; Lewis, S. W.; Lim, K. F., Analytical methodology for the determination of urea: current practice and future trends. *Trends Anal. Chem.* **2002,** *21*, 389-400.

295. Canchi, D. R.; Paschek, D.; García, A. E., Equilibrium study of protein denaturation by urea. *J. Am. Chem. Soc.* **2010,** *132*, 2338–2344.

296. Yancey, P.; Clark, M.; Hand, S.; Bowlus, R.; Somero, G., Living with water stress: Evolution of osmolyte systems. *Science* **1982,** *217*, 1214-1222.

297. Zhang, Z.; Dmitrieva, N. I.; Park, J.-H.; Levine, R. L.; Burg, M. B., High urea and NaCl carbonylate proteins in renal cells in culture and in vivo, and high urea causes 8-oxoguanine lesions in their DNA. *Proc. Natl. Acad. Sci. USA* **2004,** *101*, 9491–9496.

298. Dalle-Donne, I.; Giustarini, D.; Colombo, R.; Rossi, R.; Milzani, A., Protein carbonylation in human diseases. *Trends Mol. Med.* **2003,** *9*, 169-176.

299. Dhawan, G.; Sumana, G.; Malhotra, B. D., Recent developments in urea biosensors. *Biochem. Eng. J.* **2009,** *44*.

300. Pan, M.; Heinecke, G.; Bernardo, S.; Levitt, J., Urea: A comprehensive review of the clinical literature. *Dermatol Online J.* **2013,** *19*, 20392.

301. Reshetilov, A. N.; Plekhanova, Y. V.; Dubrovskii, A. V.; Tikhonenko, S. A., Detection of urea using urease and paramagnetic Fe_3O_4 particles incorporated into polyelectrolyte microcapsules *Process Biochem.* **2016,** *51*, 277–281.

302. Breslow, R., Hydrophobic effects on simple organic reactions in water. *Acc. Chem. Res.* **1992,** *24*, 159–164.

303. Kaushika, A.; Solanki, P. R.; Ansari, A. A.; Sumanaa, G.; Ahmad, S.; Malhotraa, B. D., Iron oxide-chitosan nanobiocomposite for urea sensor. *Sens. Actuators, B* **2009,** *138*, 572–580.

304. Ansari, S. G.; RizwanWahab; Ansari, Z. A.; Kima, Y.-S.; Khang, G.; Al-Hajryd, A.; Shina, H.-S., Effect of nanostructure on the urea sensing properties of sol–gel synthesized ZnO. *Sens. Actuators, B* **2009,** *137*, 566–573.

305. Wu, Z.; Fu, X.; Wang, Y., Click synthesis of a triphenylamine-based fluorescent methanol probe with a unique D-π-A structure. *Sens. Actuators, B* **2017,** *245*, 406–413.

306. Ding, H.; Li, B.; Pu, S.; Liu, G.; Jia, D.; Zhou, Y., A fluorescent sensor based on a diarylethene-rhodamine derivative for sequentially detecting Cu^{2+} and arginine and its application in keypad lock. *Sens. Actuators, B* **2017,** *247*, 26–35.

307. Wang, H.; Wang, J.; Wang, J.; Zhu, R.; Shen, Y.; Xu, Q.; Hu, X., Spectroscopic method for the detection of 2,4-dichlorophenoxyacetic acid based on its inhibitory effect towards catalase immobilized on reusable magnetic Fe3O4-chitosan nanocomposite. *Sens. Actuators, B* **2017,** *247* 146–154.

308. Kumara, D.; Umrao, S.; Mishrab, H.; Srivastava, R. R.; Srivastava, M.; Srivastava, A.; Srivastava, S. K., Eu:Y_2O_3 highly dispersed fluorescent PVA film as turn off luminescent probe for enzyme free detection of H_2O_2. *Sens. Actuators, B* **2017,** *247*, 170–178.

309. Gu, P.; Liu, X.; Tian, Y.; Zhang, L.; Huang, Y.; Su, S.; Feng, X.; Fan, Q.; Huang, W., A novel visible detection strategy for lysozyme based on gold nanoparticles and conjugated polymer brush. *Sens. Actuators, B* **2017,** *246*, 78–84.

310. Wu, S.; Guo, H.; Wang, L.; Xin, Y.; Cheng, Y.; Fan, W., An ultrasensitive electrochemical biosensing platform for fructose and xylitol based on boronic acid-diol recognition. *Sens. Actuators, B* **2017,** *245*, 11–17.

311. Lahiri, B. B.; Muthukumaran, T.; Philip, J., Magnetic hyperthermia in phosphate coated iron oxide nanofluids. *J. Magn. Magn. Mater.* **2016,** *407*, 101-113.

312. Luo, L.; Pu, S.; Tang, J.; Zeng, X.; Lahoubi, M., Highly sensitive magnetic field sensor based on microfiber coupler with magnetic fluid. *Appl. Phys. Lett.* **2015,** *106*, 193507.

313. Laskar, J. M.; Raj, B.; Philip, J., Enhanced transmission with tunable Fano-like profile in magnetic nanofluids. *Phys. Rev. E* **2011**.

314. Kurzhals, S.; Zirbsand, R.; Reimhult, E., Synthesis and magneto-thermal actuation of iron oxide core–PNIPAM shell nanoparticles. *ACS Appl. Mater. Interfaces* **2015,** *7*, 19342–19352.

315. Ma, Y.; Promthaveepong, K.; Li, N., Responsive polymer-functionalized Au nanoparticles for CO_2 sensor. *Anal.Chem.* **2016,** *88*, 8289−8293.

316. Tanford, C., Isothermal unfolding of globular proteins in aqueous urea solutions. *J.Ame.Chem.Soc* **1963,** *86*, 2050-2059.

317. Baglioni, P.; Rivara-Minten, E.; Dei, L.; Ferronis, E., ESR study of sodium dodecyl sulfate and dodecyltrimethylammoium bromide micellar solutions. Effect of urea *J. Phys. Chem.* **1990,** *94*, 8218-8222

318. Ruiz, C. C., A photophysical study of the urea effect on micellar properties of sodium dodecylsulfate aqueous solutions *Colloid. Polym. Sci.* **1995** *273*, 1033-1040.

319. Kaur, R.; Kumar, S.; Aswal, V. K.; Mahajan, R. K., Influence of headgroup on the aggregation and interactional behavior of twin-tailed cationic surfactants with pluronics. *Langmuir* **2013,** *29*, 11821−1183.

320. Wu, C.; Liu, T.; White, H.; Chu, B., Atomic force microscopy study of $E_{99}P_{69}E_{99}$ triblock chains on silicon surface. *Langmuir* **2000,** *16*, 656-661.

321. Kabanov, A. V.; Nazarova, I. R.; Astafieva, I. V.; Batrakova, E. V.; Alakhov, V. Y.; Yaroslavov, A. A.; Kabanov, V. A., Micelle formation and solubilization of fluorescent probes in poly(oxyethylene-b-oxypropylene-b-oxyethylene) solutions. *Macromolecules* **1995,** *28*, 2303–2314.

322. Watlaufer, D. B.; Malik, S. K.; Stoller, L.; Coffin, R. L., Nonpolar group participation in the denaturation of proteins by urea and guanidinium salts. Model compound studies. *J. Am. Chem. Soc.* **1964,** *86* 508–514.

323. Anand, U.; Mukherjee, S., Microheterogeneity and microviscosity of f127 micelle: The counter effects of urea and temperature. *Langmuir* **2014,** *30*, 1012−1021.

324. Alexandridis, P.; Athanassiou, V.; Hatton, T. A., Pluronic-P1O5 PEO-PPO-PEO block copolymer in aqueous urea solutions: Micelle formation, structure, and microenvironment *Langmuir* **1995,** *11*, 2442-2450

325. Ma, J.-h.; Guo, C.; Tang, Y.-l.; Chen, L.; Bahadur, P.; Liu, H.-Z., Interaction of urea with pluronic block copolymers by 1 H NMR spectroscopy. *J. Phys. Chem. B* **2007,** *111*, 5155-5161.

326. M.L.Eritsyan; L.A.Gyurdzhyan; L.T.Melkonyan; G.V.Akopyan, Copolymers of acrylic acid with urea. *Russ. J. Appl. Chem.* **2006,** *79*, 1666-1668.

327. Fernandes, B. S.; Pinto, J. C.; Cabral-Albuquerque, E. C. M.; Fialho, R. L., Free-radical polymerization of urea, acrylic acid and glycerol in aqueous solutions. *Polym. Eng. Sci.* **2015,** *55*, 1219-1229.

328. Cametti, C., Does electrical of linear polyelectrolytes in aqueous solutions follow the dynamic scaling laws? A critical review and a summary of the key relations *Polymers* **2014,** *6*, 1207-1231.

329. Bizzarri, A. R.; Cametti, C.; Biasio, A. D., Counterion accumulation in rod-like polyelectrolyte solutions with added salt and manning's condensation theory. *Ber. Bunsenges. Phys. Chem* **1988,** *92*, 17-21.

330. Grasso, G.; Satriano, C.; Milardi, D., A neglected modulator of insulin-degrading enzyme activity and conformation: The pH. *Biophys. Chem.* **2015,** *203–204*, 33–40.

331. Lin, H.; Li, G.; Dong, Y.; Li, J., Effect of pH on the release of heavy metals from stone coal waste rocks. *Int. J. Miner. Process.* **2017,** *165*, 1–7.

332. Vaughan-Jones, R. D.; W.Spitzer, K.; Swietach, P., Intracellular pH regulation in heart. *J. Mol. Cell. Cardiol.* **2009,** *46*, 318-331.

333. A. Webb, B.; Chimenti, M.; P. Jacobson, M.; L. Barber, D., Dysregulated pH: a perfect storm for cancer progression. *Nat. Rev. Cancer* **2011,** *11*, 671–677.

334. Bischof, G.; Cosentini, E.; Hamilton, G.; Riegler, M.; Zacherl, J.; Telekya, B.; Feil, W.; Schiessel, R.; E.Machen, T.; Wenzl, E., Effects of extracellular pH on intracellular pH-regulation and growth in a human colon carcinoma cell-line. *Biochim. Biophys. Acta* **1996,** *1282*, 131-139.

335. Harrison, S. M.; Frampton, J. E.; McCall, E.; Boyett, M. R.; Orchard, C. H., Contraction and intracellular Ca2+, Na+, and H+ during acidosis in rat ventricular myocytes. *Am. J. Physiol., Cell Physiol.* **1992,** *262* 348–357.

336. Orchard, C. H.; Cingolani, H. E., Acidosis and arrhythmias in cardiac muscle. *Cardiovasc. Res.* **1994,** *28*, 1312–1319.

337. NM, M.; MA, C.; OW, M.; B, A.-H.; K., S., Low urine pH: a novel feature of the metabolic syndrome. *Clin. J. Am. Soc. Nephrol.* **2007,** *2(5):* , 883-888.

338. Bernheim, H. A., The regulation of body temperature in fever. *The Reticuloendothelial System* **1985,** *7B*, 339-353.

339. Pearson, A. C.; Linford, M. R.; Harb, J. N.; Davis, R. C., Dual patterning of a poly(acrylic acid) layer by electron-beam and block copolymer lithographies. *Langmuir* **2013,** *29*, 7433−7438.

340. Zhang, X.; Jiang, K.; He, H.; Yue, D.; Zhao, D.; Cui, Y.; Yang, Y.; Qian, G., A stable lanthanide-functionalized nanoscale metal-organic framework as a fluorescent probe for pH. *Sens. Actuators, B* **2018,** *254*, 1069–1077.

341. Schyrr, B.; Pasche, S.; Scolan, E.; Ischer, R.; Ferrario, D.; Porchet, J.-A.; Voirin, G., Development of a polymer optical fiber pH sensor for on-body monitoring application. *Sens. Actuators, B* **2014,** *194*, 238–248.

342. Wong, W. C.; Chan, C. C.; Hu, P.; Chan, J. R.; Low, Y. T.; Dong, X.; Leong, K. C., Miniature pH optical fiber sensor based on waist-enlarged bitaper and mode excitation. *Sens. Actuators, B* **2014,** *191* 579–585.

343. Lee, S.; Kim, J.-Y.; Chen, X.; Yoon, J., Recent progress in stimuli-induced polydiacetylenes for sensing temperature, chemical and biological targets. *Chem. Commun.* **2016** *52*, 9178--9196.

344. Wang, X.-Y.; Huang, D.-W.; Niu, C.-G.; Guo, L.-J.; Cui, J.-J.; Hu, L.-Y.; Zeng, G.-M., An internal reference fluorescent pH sensor with two pH-sensitive fluorophores carrier. *Sens. Actuators, B* **2016,** *234* 593–601.

345. G.K., M. S.; G.H.Rounaghi; M.Chamsaz, An optical sensor for determination of low pH values based on covalent immobilization of Congo red on triacetyl cellulose films via epichlorohydrin. *Sens. Actuators B: Chem.* **2018,** *254*, 177-181.

346. Zubiate, P.; Zamarreno, C. R.; Villar, I. D.; Matias, I. R.; Arregui, F. J., Tunable optical fiber pH sensors based on TE and TM lossy mode resonances (LMRs). *Sens. Actuators, B* **2016,** *231*, 484–490.

347. He, L.; Xin, J. H.; Chen, S., Robust and low cytotoxic betaine-based colorimetric pH sensors suitable for cancer cell discrimination. *Sens. Actuators, B* **2017,** *252* 277–283.

348. Aldaba, A. L.; González-Vila, Á.; Debliquy, M.; Lopez-Amo, M.; Caucheteur, C.; Lahem, D., Polyaniline-coated tilted fiber Bragg gratings for pH sensing. *Sens. Actuators, B* **2018** *254*, 1087–1093.

349. Joshi, G. K.; Johnsonb, M. A.; Sardar, R., Novel pH-responsive nanoplasmonic sensor: Controlling polymer structural change to modulate localized surface plasmon resonance response. *RSC Adv.* **2014,** *4*, 15807–15815

350. Kemmer, G. C.; Bogh, S. A.; Urban, M.; Palmgren, M. G.; Vosch, T.; Schillerd, J.; Pomorski, T. G., Lipid-conjugated fluorescent pH sensors for monitoring pH changes in reconstituted membrane systems. *Analyst* **2015,** *140*, 6313–6320

351. Long, L.; Li, X.; Zhang, D.; Meng, S.; Zhang, J.; Sun, X.; Zhang, C.; Zhou, L.; Wang, L., Amino-coumarin based fluorescence ratiometric sensors for acidic pH and their application for living cells imaging. *RSC Adv.* **2013,** *3*, 12204–12209.

352. Sun, H.; Luo, H.; Wu, X.; Liang, L.; Wang, Y.; Ma, X.; Zhang, J.; Hu, M.; Qiao, X., Spectrum ameliorative optical fiber temperature sensor based on hollow-core fiber and inner zinc oxide film. *Sens. Actuators, B* **2017** *245*, 423–427.

353. Koren, K.; Kühl, M., A simple laminated paper-based sensor for temperature sensing and imaging. *Sens. Actuators, B* **2015,** *210*, 124–128.

354. Yin, L.; He, C.; Huang, C.; Zhu, W.; Wang, X.; Xu, Y.; Qian, X., A dual pH and temperature responsive polymeric fluorescent sensor and its imaging application in living cellsw. *Chem.Commun.* **2012,** *48*, 4486–4488.

355. Salvo, P.; Calisi, N.; Melai, B.; Cortigiani, B.; Mannini, M.; Caneschi, A.; Lorenzetti, G.; Paoletti, C.; Lomonaco, T.; Paolicchi, A.; Scataglini, I.; Dini, V.; Romanelli, M.; Fuoco, R.; Francesco, F. D., Temperature and pH sensors based on graphenic materials. *Biosens. Bioelectron.* **2017,** *91*, 870–877.

356. Liu, H.; Maruyama, H.; Masuda, T.; Honda, A.; Arai, F., Multi-fluorescent micro-sensor for accurate measurement of pH and temperature variations in micro-environments. *Sens. Actuators, B* **2014,** *203*, 54–62.

357. Rosace, G.; Trovato, V.; Colleoni, C.; Caldara, M.; Re, V.; Brucale, M.; Piperopoulos, E.; Mastronardo, E.; Milone, C.; Luca, G. D.; Plutino, M. R., Structural and morphological characterizations of MWCNTs hybrid coating onto cotton fabric as potential humidity and temperature wearable sensor. *Sens. Actuators, B* **2017,** *252*, 428–439.

358. Lee, K.; Asher, S. A., Photonic crystal chemical sensor-pH and ionic strength. *J. Am. Chem. Soc* **2000,** *122* (39), 9534-9537.

359. Peng, L.; Liu, S.; Feng, A.; Yuan, J., Polymeric nanocarriers based on cyclodextrins for drug delivery: Host–guest interaction as stimuli responsive linker. *Mol. Pharmaceutics* **2017,** *14*, 2475–2486.

360. Wang, J.; Feng, Y.; Agrawald, N. R.; Raghavan, S. R., Wormlike micelles versus water-soluble polymers as rheology-modifiers: similarities and differences. *Phys. Chem. Chem. Phys.* **2017,** *19*, 24458-24466.

361. Sinton, S. W., Complexation chemistry of sodium borate with poly(vinyl alcohol) and small diols. A ^{II}B NMR study. *Macromolecules* **1987,** *20*, 2430-2441.

362. Shibayama, M.; Sato, M.; Kimura, Y.; Fujiwara, H.; Nomura, S., 'IB n.m.r, study on the reaction of poly(vinyl alcohol) with boric acid. *Polymer* **1988,** *29*, 336-340.

363. Koga, K.; Takada, A.; Nemoto, N., Dynamic light scattering and dynamic viscoelasticity of poly(viny lalcohol) in aqueous borax solutions. 5. temperature effects. *Macromolecucles* **1999,** *32*, 8872-8879.

364. Takada, A.; Nishimura, M.; Koike, A.; Nemoto, N., Dynamic light scattering and dynamic viscoelasticity of poly(vinyl alcohol) in aqueous borax solutions. 4. further investigation on polymer concentration and molecular weight dependencies. *Macromolecules* **1998,** *31*, 436-443.

365. Khorami, H. A.; PeterWild; G.Brolob, A.; Djilali, N., pH-Dependent response of a hydrogen peroxide sensing probe. *Sens. Actuators B: Chem.* **2016,** *237*, 113-119.

366. Liu, Q.; Li, S.-G.; Chen, H., Enhanced sensitivity of temperature sensor by a PCF with a defect core based on Sagnac interferometer. *Sens. Actuators B: Chem.* **2018,** *254*, 636–641.

367. Saxena, N.; Kumara, P.; Gupta, V., CdS:SiO_2 nanocomposite as a luminescence-based wide range temperature sensor. *RSC Adv.* **2015,** *5* 73545-73551.

368. Yang, J.; Wei, D.; Tang, L.; Song, X.; Luo, W.; Chu, J.; Gao, T.; Shi, H.; Dua, C., Wearable temperature sensor based on graphene nanowalls. *RSC Adv.* **2015,** *5*, 25609-25615

369. Cortes-Adasme, E.; Vega, M.; Martin, I. R.; Llanos, J., Synthesis and characterization of SrSnO3 doped with Er^{3+} for up-conversion luminescence temperature sensors. *RSC Adv.* **2017,** *7*, 46796–46802.

370. Guo, Y.; Wang, D.; Yang, L.; Liu, S., Nanoscale monolayer adsorption of polyelectrolytes at the solid/liquid interface observed by quartz crystal microbalance. *Polymer* **2017,** *49*, 543–548

371. Liu, D.; Xu, X.; Wang, F.; Zhou, J.; Mi, C.; Zhang, L.; Lu, Y.; Ma, C.; Goldys, E.; Lince, J.; Jin, D., Emission stability and reversibility of upconversion nanocrystals. *J. Mater. Chem. C* **2016,** *4*, 9227-9234

372. Wan, X.; Liu, S., Fluorescent water-soluble responsive polymers site-specifically labeled with FRET dyes possessing pH- and thermo-modulated multicolor fluorescence emissions as dual ratiometric probes. *J. Mater. Chem.* **2011,** *21*, 10321-10329